Evaluation of the effects of varying fuel quality on solid oxide fuel cell systems

Doctoral Thesis

to be awarded the degree

Doctor of Engineering (Dr.-Ing.)

submitted by

Martin Hering

from Schweinfurt

approved by the Faculty of Energy and Economic Sciences,

Clausthal University of Technology,

Date of oral examination

25.07.2018

Dean
Prof. Dr. rer. nat. habil. Bernd Lehmann

Chairperson of the Board of Examiners
Prof. Dr.-Ing. Norbert Meyer

Supervising tutor
Prof. Dr.-Ing. Otto Carlowitz

Reviewer
Prof. Dr. techn. Wolfgang Winkler

Acknowledgment

I would like to express my deepest acknowledgment to my supervising Professors - Prof. Dr.-Ing. Otto Carlowitz and Prof. Dr. techn. Wolfgang Winkler - for their steady and ongoing support, as well as their suggestions and constructive criticism throughout the process of my dissertation. Moreover, I would especially like to thank them for supporting the work on my dissertation at the Corporate Research Department of the *Robert Bosch GmbH*. Furthermore, I would like to thank one of my former university supervisors, Professor Jacob Brouwer, Ph.D., for his feedback and constructive discussions in regard to my dissertation topic and the entire field of solid oxide fuel cells, as well as his personal advice.

Additionally, I would particularly like to thank my internal supervisors Stefanie and Peter for their extensive time investment in discussions and feedback, as well as the exceptional support, which ultimately allowed for the implementation and testing of the developed ideas. I would also like to express my grateful acknowledgment to Stefanie for her detailed corrections and feedback on the written part of the dissertation, as well as her constant positive reinforcement.

Special thanks to my *Bosch* coworkers Tania, Thomas, René, Maxime, Timo, Julia and Ana for their personal support, guidance and help throughout the entire process. Many thanks for integrating me into the team and giving me the opportunity to learn and work on topics, which were beyond the scope of my dissertation.

Moreover, I would like to thank Thomas Grohmann and the complete team of *AIRTECH Europe GmbH*, as well as Kathy Heidebrecht, Joel Oakman and Ski Milburn of *VAIREX* for their support, suggestions, constructive criticism and feedback in regards to the development and testing of the characteristic compressor map modeling.

Many thanks to Jesper Bruun of *Energinet.dk*, Eric Van Gysel and Quentin Degroote of *Fluxys Belgium* and József Balla of *FGSZ* for supplying temporally resolved natural gas data sets. Additionally, I would like to thank my student Sandrine Rodosik for acquiring the data set from the *Bosch Thermotechnologie* location in Saint-Thegonnec.

Furthermore, I would like to thank the entire department *CR/AEB* of the *Robert Bosch GmbH* for giving me the opportunity to work on my dissertation in an inspiring and exceptionally co-operative environment. Moreover, I gratefully acknowledge the financial support of the *German Federal Ministry for Economic Affairs and Energy* (*BMWi*), which provided partial support for the research presented in this dissertation.

In addition, I would like to express my deepest thanks to my entire family: Especially my partner Hannah for her ongoing and exceptional support throughout my complete dissertation, as well as for moving to center our life in Germany; and my parents and siblings Elisabeth, Rudolf, Verena and Matthias for their long-term personal support, for keeping up with my way of life and for their valuable life advice and guidance.

Lastly, a shout-out to everyone I did not specifically mention in the acknowledgment, who gave any personal or scientific support.

Abstract

This dissertation outlines the effects of fluctuating natural gas quality on solid oxide fuel cell systems with anode exhaust gas recirculation by implementing and testing two control approaches in a natural gas fueled test rig. For this purpose, the principles of solid oxide fuel cell systems and the governing system equations are introduced for a system with anode exhaust gas recirculation.

Additionally, the fundamentals of natural gas and fluctuating natural gas quality, as well as the current European regulatory frame work are presented. Eight temporally resolved European natural gas data sets are evaluated and compared, outlining that the natural gas quality in Europe is highly volatile with variable magnitudes in different locations. Methane and ethane fractions are the most volatile components in the evaluation, due to the 95 % confidence domains ranging from 86.5 to 97.5 % and 0.9 to 10.2 %, respectively. The derived natural gas coefficients provide the basis for an exact classification and clustering of different natural gas mixtures in regard to the corresponding fuel cell system responses. Furthermore, the governing system equations are simplified by replacing all natural gas composition constraints with the corresponding natural gas coefficient.

Furthermore, the development, validation and testing of the basic control scheme and black box modeling approach are outlined. The conducted literature review highlights that the effects of fluctuating natural gas quality on solid oxide fuel cell systems are not frequently addressed in literature. Additionally, the implemented basic control strategy in the 13 kW solid oxide fuel cell test rig keeps the natural gas mass flow rate and reformer inlet volume flow rate constant in relation to a defined reference natural gas composition. Consequently, for fluctuating natural gas quality, the designated fuel utilization factor and oxygen-to-carbon ratio set points can not be ideally realized. For the chosen test rig location in Renningen, the model predicted fluctuations of the fuel utilization factor and oxygen-to-carbon ratio from 0.7129 to 0.8046 and 1.926 to 2.098 for set points of 0.75 and 2, respectively. Additionally, during the experimental evaluation at nominal operation, the estimated fluctuation magnitudes of the fuel utilization factor and oxygen-to-carbon ratio are approximately verified, due to the corresponding matching spreads of the measured domains between 0.6823 and 0.7633, as well as 1.822 and 2.109. Consequently, with the basic control approach, the carbon deposition risk is temporarily too high, due to the frequently occurring low oxygen-to-carbon ratios. However, the risk of irreversible stack damage, due to the partial depletion of fuel inside single cells of the stack, is low during the testing period.

Consequently, an advanced control logic is developed, which relies on the detection of a single natural gas quality indicator to adjust the system flow rates in relation to the detected natural gas state. For the chosen test rig location in Renningen, the advanced control scheme achieves superior simulation results with predicted fluctuations of the fuel utilization factor and oxygen-to-carbon ratio from 0.7495 to 0.7502 and from 1.993 to 2.017 for set points of 0.75 and 2, respectively. Furthermore, the exceptional simulation results are verified during the experimental evaluation at nominal operation, due to the small spreads of the fuel utilization factor and oxygen-to-carbon ratio domains from 0.7543 to 0.7630 and 1.969 to 2.030, respectively. The corresponding simulation results of the basic control scheme in the identical time frame yield distinctly extended domains from 0.7030 to 0.7607 and 1.906 to 2.021, respectively. Consequently, the advanced control logic successfully prevents excessively low oxygen-to-carbon ratios and limits the risks of carbon deposition. Additionally, more stable fuel utilization factor progressions are achieved, outlining the superior performance of the advanced control scheme.

In summary, this dissertation highlights that a solid oxide fuel cell system with anode exhaust gas recirculation can be advantageously operated with natural gas using an advanced control scheme, which is reactive to the current natural gas state. Therefore, the system can be stably operated and the lifetime can be extended.

Table of Contents

List of Tables

List of Figures

Nomenclature

List of Latin symbols

Symbol	Unit	Description
A	m^2	Area
a	-	Coefficient of the linear / quadratic / power or multiple linear regression
B	Variable	Regression coefficient of characteristic blower map modeling
C	Variable	Regression coefficient of characteristic blower map modeling
c_p	J kg^{-1} K^{-1}	Specific heat capacity
$c_{p,mol}$	J mol^{-1} K^{-1}	Molar heat capacity
E	V	Voltage
F	A s mol^{-1}	Faraday constant
$\triangle g$	J mol^{-1}	Gibbs free energy of reaction
$\dot{H}$	J s^{-1}	Enthalpy flow rate
h	J mol^{-1}	Molar enthalpy
h_i	J mol^{-1}	Molar lower heating value
h_s	J mol^{-1}	Molar higher heating value
$\tilde{h}_s$	J m^{-3}	Volumetric higher heating value
I	A	Electric current
j	A m^{-2}	Electric current density
K_C	-	Carbon gas coefficient
K_{e^-}	-	Electron gas coefficient
K_H	-	Hydrogen gas coefficient
K_M	kg mol^{-1}	Molar mass to electron coefficient ratio
K_N	-	Nitrogen gas coefficient
K_{NG}	-	Natural gas coefficients
K_O	-	Oxygen gas coefficient
$K_{\triangle an}$	-	Change in molar quantity coefficient of anode point of view
$K_{\triangle mix}$	-	Change in molar quantity coefficient of combustion point of view
K_λ	-	Stoichiometric combustion coefficient
K_Φ	-	Oxygen-to-carbon ratio dependent combined gas coefficient

Symbol	Unit	Description
M	kg mol^{-1}	Molar mass
$\dot{m}$	kg s^{-1}	Mass flow rate
N	-	Number
n	s^{-1}	Rotational speed
$\dot{n}$	mol s^{-1}	Molar flow rate
P	W	Power
p	Pa	Pressure
$\dot{Q}$	J s^{-1}	Heat flow rate
R	J mol^{-1} K^{-1}	Molar universal gas constant
r	-	Recirculation ratio
S	-	Scaling coefficient
s	-	Individual uncertainty
T	K	Absolute temperature
U	-	Utilization factor
u	-	Standard uncertainty
$\dot{V}$	m^3 s^{-1}	Volume flow rate
v_m	m^3 mol^{-1}	Molar volume
w	J m^{-3}	Wobbe-index
x	mol mol^{-1}	Mole fraction
y	- / K^{-1} / K^{-2} / K^{-3} / K^{-4}	Coefficient for calculation of molar heat capacity
Z	Ω	Resistance

List of Greek symbols

Symbol	Unit	Description
α	Variable	Coefficient of quadratic equation
β	Variable	Coefficient of quadratic equation
γ	Variable	Coefficient of quadratic equation
ϑ	°C	Temperature
η	-	Efficiency
κ	-	Charge transfer coefficient

Symbol	Unit	Description
λ	-	Air-to-fuel equivalence ratio
ρ	kg m^{-3}	Density
Λ	-	Placeholder for subscripts
Υ	mol mol^{-1}	Steam-to-carbon ratio
Φ	mol mol^{-1}	Oxygen-to-carbon ratio
Ψ	%	Valve position

List of subscripts

Subscript	Description
a	Air
Act	Activation polarization
AEGR	Anode exhaust gas recirculation
amb	Ambient
AM_1	Anode outlet mass flow rate control scheme 1
AM_2	Anode outlet mass flow rate control scheme 2
an	Anode
AV_3	Anode outlet volume flow rate control scheme 3
bu	Burner
BG	Bio gas
BOP	Balance-of-plant
bp	Bypass
C	Carbon atom
ca	Cathode
calc	Calculated
CH_4	Methane
CO	Carbon monoxide
Conc	Concentration polarization
CO_2	Carbon dioxide
CPOX	Catalytic partial oxidation
C_2H_6	Ethane

Subscript	Description
C_3H_8	Propane
C_4H_{10}	Butane
des	Designated
e^-	Electron
el	Electric
eq	Equilibrium
eqv	Equivalent
EWS	External water supply
ex	Exchange
Exh	Exhaust
F	Fluctuating state
f	Fuel
GC	Quantified with gas chromatography system
GT	Gas turbine
H	Hydrogen atom
H_2	Hydrogen
H_2O	Water vapor
i	Species
IC_0	Ideal control scheme
in	Inlet
ini	Initial
lim	Limiting
LR	Linear regression
max	Maximal / Maximum
MFC	Mass flow controller
MLR	Multiple linear regression
min	Minimal / Minimum
mix	Mixture
Msd	Measured
N	Nitrogen atom

Subscript	Description
NC_0	Natural gas electron coefficient control scheme
NDIR	Quantified with nondispersive infrared sensors
N_2	Nitrogen
NG	Natural gas
NM_1	Natural gas mass flow rate control scheme 1
O	Oxygen atom
out	Outlet
O_2	Oxygen
PoE	Propagation of error
PR	Power regression
PV	Process value
QR	Quadratic regression
R	Reference state
rec	Recirculation
ref	Reformer
rev	Reversible
R_iV_1	Reformer inlet volume flow rate control scheme 1
S	Stack
Sim	Simulated
SOFC	Solid oxide fuel cell
SP	Set point
Std	Standard conditions
sto	Stoichiometric
Sys	System
sbu	Start up burner
tr	Transferred
uti	Utilized

List of abbreviations

Abbreviation	Description
AC	Alternating current
ASC	Anode supported cell
AEGR	Anode exhaust gas recirculation
BE	Belgium
BG	Bio gas
CM 2014	Campo Maior 2014 natural gas data set
CPOX	Catalytic partial oxidation
CRR	Complete reforming reaction
CS	Control scheme
CSC	Cathode supported cell
EG 2014	Egtved 2014 natural gas data set
ESC	Electrolyte supported cell
EWS	External water supply
DC	Direct current
DE	Germany
DK	Denmark
FI	Finland
FR	France
GC	Gas chromatography system
GCD	Gadolinium doped ceria
GE 2014	Gent 2014 natural gas data set
GPC	Generalized predictive control
GPU	Gas processing unit
GT	Gas turbine
HEX	Heat exchanger
HU	Hungary
HU 2014	Hungarian 2014 natural gas data set
H-gas	High calorific natural gas
IM 2014	Imatra 2014 natural gas data set

Abbreviation	Description
LSCF	Lanthanum strontium cobaltite ferrite
LSCM	Lanthanum strontium chromite manganite
LSF	Lanthanum strontium ferrite
LSM	Lanthanum strontium manganite
Max	Maximum
MFC	Mass flow controller
MFM	Mass flow meter
Min	Minimum
MPC	Model predictive control
NDIR	Nondispersive infrared sensor unit
NG	Natural gas
Ni-YSZ	Nickel-zirconia cermet
NNPC	Neural network predictive controller
P	Proportional
PI	Proportional integral
PID	Proportional integral differential
PRR	Partial reforming reaction
PT	Portugal
P&ID	Piping and instrumentation diagram
REF	Reformer
Rng 2013	Renningen 2013 natural gas data set
Rng 2016	Renningen 2016 natural gas data set
ScSZ	Scandium stabilized zirconia
SG	Syngas
Sim	Simulation / Simulated
SOFC	Solid oxide fuel cell
SP	Set point
ST 2014	Saint-Thegonnec 2014 natural gas data set
WGSR	Water-gas-shift reaction
YSZ	Yttrium stabilized zirconia

List of control scheme abbreviations

Abbreviation	Control scheme description
AM_1	Anode outlet mass flow rate control scheme 1
AM_2	Anode outlet mass flow rate control scheme 2
AV_1	Anode outlet volume flow rate control scheme 1
AV_2	Anode outlet volume flow rate control scheme 2
AV_3	Anode outlet volume flow rate control scheme 3
AV_4	Anode outlet volume flow rate control scheme 4
IC_0	Ideal control scheme
NC_0	Natural gas electron coefficient control scheme
NM_1	Natural gas mass flow rate control scheme 1
NM_2	Natural gas mass flow rate control scheme 2
NM_3	Natural gas mass flow rate control scheme 3
NM_4	Natural gas mass flow rate control scheme 4
NV_1	Natural gas volume flow rate control scheme 1
NV_2	Natural gas volume flow rate control scheme 2
NV_3	Natural gas volume flow rate control scheme 3
NV_4	Natural gas volume flow rate control scheme 4
NV_5	Natural gas volume flow rate control scheme 5
R_iV_1	Reformer inlet volume flow rate control scheme 1
R_iV_2	Reformer inlet volume flow rate control scheme 2
RV_1	Reformer outlet volume flow rate control scheme 1
RV_2	Reformer outlet volume flow rate control scheme 2
RV_3	Reformer outlet volume flow rate control scheme 3
RV_4	Reformer outlet volume flow rate control scheme 4
RV_5	Reformer outlet volume flow rate control scheme 5
RV_6	Reformer outlet volume flow rate control scheme 6

1 Introduction

Beginning in 2015, 156 states signed and later ratified the Paris Agreement, creating a worldwide understanding that action against the anthropogenic climate change must take place. The major goal of the agreement is to maintain the global average temperature increase 2 K below the pre-industrial value. To reach this objective, greenhouse gas emissions have to be significantly reduced throughout the member states. Consequently, highly developed industrial countries are taking the lead and setting ambiguous goals. For instance, Germany is aiming to reduce their greenhouse gas emissions by 55 % from the 1990 levels by 2030 [1, 2, 3].

Nevertheless, the worldwide consumption of natural gas is still predicted to increase by approximately 2 % annually until 2030, emphasizing the still rising significance of this conventional resource [4, 5, 6, 7]. Additionally, due to the combination of natural gas from different origins inside highly interconnected gas grids, the natural gas composition at the final point of consumption can vary significantly over time [7, 8, 9, 10, 11].

Furthermore, renewable synthetic natural gas, bio gas and hydrogen are considered promising future energy carriers, due to the similarity and possible interchangeability with current conventional gaseous energy sources [10, 12, 13, 14, 15, 16, 17, 18]. However, with rising hydrogen injections into the natural gas grid, natural gas quality fluctuations may significantly increase, ultimately intensifying the challenges for connected devices [19].

High temperature solid oxide fuel cell (SOFC) systems present a promising solution to bridge the gap between the age of conventional natural gas and a hypothetical pure hydrogen era, due to the inherent fuel flexibility of SOFCs. Additionally, SOFC technology has several advantages compared to conventional energy converters, such as motors or gas turbines. For instance, SOFCs have higher electrical efficiencies, lower carbon dioxide and criteria air pollutant emissions, as well as reduced noise levels [8, 20, 21, 22]. As a result, SOFC systems can be implemented to replace conventional converters, ultimately significantly reducing greenhouse gas emissions and supporting the objectives of the Paris Agreement. However, the influences of fluctuating natural gas quality on SOFCs have not been frequently addressed in literature. Consequently, this dissertation focuses on the evaluation of the effects of varying fuel quality on solid oxide fuel cell systems and the development, application and experimental testing of feasible control strategies. The main objective of this dissertation is the design of an adaptive control logic, which is able to maintain stable system conditions during natural gas composition fluctuations. For this purpose, this work is divided into four main chapters.

The principles of solid oxide fuel cell systems are explained in chapter 2. First, the technological background is presented. Second, three different system approach options are compared, where the anode exhaust gas recirculation option is chosen for further evaluation, due to the superior efficiency potential and abandonment of a water supply unit during nominal operation. Third, the governing system equations are introduced for an SOFC system with anode exhaust gas recirculation. Lastly, the electrochemical constraints and efficiency calculations are outlined.

The fundamentals of natural gas and fluctuating natural gas quality, as well as the current European regulatory frame work are presented in chapter 3. Eight temporally resolved European natural gas data sets are evaluated and compared, providing a data base of approximately 35000 gas measurements. Based upon the chemical composition of natural gas, five general natural gas coefficients are derived. The natural gas coefficients allow for an exact classification and clustering of different natural gas mixtures in regard to the corresponding fuel cell system responses. The interrelations of the natural gas coefficients and the corresponding relations to other natural gas properties are further used to derive general constraints and correlations. The chapter is concluded with an evaluation of the thermodynamic effects of varying natural gas quality on SOFC systems, focusing on the specific reformer heat flow rate, the ideal reversible and Nernst voltages, as well as the carbon deposition region.

Chapter 4 is divided in five sections, focusing primarily on the development, validation and testing of the control scheme (CS) and modeling approach. First, a literature review focusing on the control and operating strategies of SOFC systems is conducted, providing the baseline for the definition of the objectives of this dissertation, which are subsequently presented in the introduction. Second, the SOFC test rig setup and the details of the applied control strategy are outlined, including an analytic derivation of the designated basic CS with a constant natural gas mass flow rate and reformer inlet volume flow rate during natural gas operation. Third, a black box system model is developed, allowing for the evaluation of the basic CS and the ideal CS using the temporally resolved natural gas data base. Then, the results of the SOFC test rig during natural gas operation are outlined, allowing for verification of the chosen basic CS and validation of the model. Lastly, the basic control approach is further evaluated via a sensitivity analysis in the modeling environment, increasing the significance of the assessment.

The derivation, development and evaluation of the modified control schemes are presented in chapter 5. In total, 22 modified control schemes are analytically derived, based upon the combination of two leading flow rate control variables. Additionally, an advanced CS is developed, which uses the determination of a single natural gas coefficient, in relation with the natural gas coefficient regressions, to closely reproduce the ideal CS performance. All derived control schemes are included in the modeling approach, allowing for a comparison and performance evaluation for the temporally resolved natural gas data base. Additionally, all control scheme options are rated, using six defined criteria, including natural gas robustness, implementation feasibility and projected cost ratings. The highest rated CS option, which is the advanced CS, is then selected for an extended evaluation via a sensitivity analysis in the modeling environment and experimental testing in the SOFC test rig. In the final step, the adjustments to the SOFC test rig control logic and the experimental results of the advanced CS are presented.

In summary, the objectives of this dissertation include the following contents, which are excluded or only minorly addressed in the identified, relevant literature outlined in section 4.1:

1. The use of measured, temporally resolved natural gas data as a basis for the evaluation of the effects of varying natural gas quality on SOFC systems, including an anode exhaust gas recirculation. Therefore, real natural gas conditions at a specific point of consumption are represented. (Addressed in sections 3.3, 3.5 and 4.3.)

2. The development, implementation and long term testing of a complete system control strategy for an SOFC test rig fueled with natural gas from the grid. The strategy fulfills the main identified control objectives, with an open loop control for the anode and a closed loop control for the cathode constraints. (Addressed in sections 4.2 and 4.4.)

3. The detailed quantification of the naturally occurring fluctuations of the natural gas composition at the chosen SOFC test rig location. (Addressed in sections 3.3.3 and 4.4.)

4. The model based validation and verification of the experimentally recorded data samples, where the model is able to reproduce the behavior of the system for the developed control approach. (Addressed in sections 4.3 and 4.4.)

5. The extension of the model to compare 23 different control approaches, based upon the ideal realization of flow rate set points at variable system locations in accordance to designated reference natural gas compositions. (Addressed in sections 5.1 and 5.3.)

6. The evaluation of the effect of hydrogen addition to the natural gas data base to assess the robustness of the derived strategies. (Addressed in sections 4.5.3, 5.3.3.2 and 5.4.)

7. The application of the derived natural gas data constraints to develop, implement and test a control logic, which can achieve ideal system behavior based solely upon the determination of a single natural gas coefficient. (Addressed in sections 3.4.3, 5.2 and 5.5.)

2 Solid oxide fuel cell system principles

The following chapter outlines the fundamentals and principles of different solid oxide fuel cell system designs, with focus on systems including an anode exhaust gas recirculation. Additionally, this chapter highlights the introduction of the major governing system equations and constraints, which are used in combination with chapter 3 as a basis for model and control scheme development and implementation. For a more general overview of high temperature fuel cells, including history, material setups, designs, manufacturing, applications and modeling, the reader is referred to Kendall and Kendall [20], Larminie and Dicks [8], Huang and Goodenough [21], Milewski et al. [23] and Boaro and Salvatore [24].

2.1 Background of technology

2.1.1 Functional principle of a solid oxide fuel cell

The principle of an SOFC is schematically shown in Figure 2.1. The cathode channel of the SOFC is supplied with air, whereas the anode channel is fed with a hydrogen rich fuel. At the cathode, molecular oxygen is reduced forming oxygen ions, which are transferred through the ion conducting ceramic electrolyte to the anode. There, hydrogen or carbon monoxide are oxidized releasing electrons in the process, which are conducted through the external circuit to the cathode. In summary, the hydrogen or carbon monoxide are converted, with the help of the transferred oxygen ions, in an electrochemical reduction-oxidation reaction to water vapor or carbon dioxide, respectively [8, 20, 21, 23, 24].

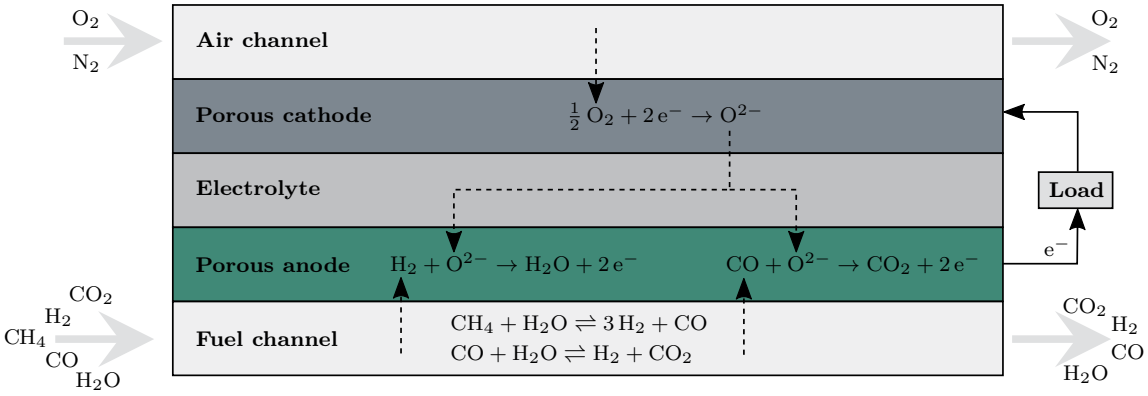

Figure 2.1: Simplified schematic principle of an SOFC

The anode and cathode half reactions, as well as the complete electrochemical conversion reactions are outlined in Table 2.1. As shown in Figure 2.1, the hydrogen rich fuel can be comprised of a mixture of hydrogen, carbon monoxide, carbon dioxide, methane and water vapor due to the reforming of natural gas. The process is described in further detail in section 2.1.3. Theoretically, methane can also be directly electrochemically oxidized at the anode, however the internal conversion reaction to hydrogen and carbon monoxide in the presence of water vapor is by orders of magnitude faster and is therefore, favored [20, 23, 24]. Hydrogen has the highest diffusion and reaction affinity and is therefore, the primary electrochemically converted component of the fuel. Carbon monoxide and hydrogen are related by the water-gas-shift reaction, converting carbon monoxide to hydrogen and carbon dioxide in the presence of water vapor. The equilibrium of the water-gas-shift reaction is steadily disturbed due to the electrochemical consumption of hydrogen and corresponding formation of water vapor. Both disturbances lead

to a shift of the reaction towards the product side, ultimately increasing the hydrogen content. In summary, compared to hydrogen, the direct electrochemical conversion of carbon monoxide is negligible small, due to the higher reaction affinity of hydrogen and the quickness of the water-gas-shift reaction [20]. As also indicated in Figure 2.1, an SOFC can neither completely deplete the oxygen in air nor all potent parts of the fuel since low concentrations are connected with sharp cell voltage drops, as outlined in section 2.2.3.

Table 2.1: Anode and cathode reactions

	Half reaction	Sum reaction
Cathode	$\frac{1}{2}\,O_2 + 2\,e^- \rightarrow O^{2-}$	-
Anode	$H_2 \rightarrow 2\,H^+ + 2\,e^-$	$2\,H^+ + O^{2-} \rightarrow H_2O$
	$CO \rightarrow CO^{2+} + 2\,e^-$	$CO^{2+} + O^{2-} \rightarrow CO_2$

2.1.2 Cell and stack design

The ceramic electrolyte is usually composed of yttrium stabilized zirconia (YSZ), gadolinium doped ceria (GCD) or scandium stabilized zirconia (ScSZ). The materials can be manufactured in very thin layers and are stable in both reducing and oxidizing atmospheres at the anode and cathode, respectively. In addition, the materials are electronic insulators. However, oxygen ion conduction is possible at elevated temperatures, between 500 and 1000 °C, due to defects in the crystal structure of the materials. Typical anode materials are comprised of a porous ceramic supporting structure combined with a catalytic active metallic material, providing a close match to the thermal expansion properties of the electrolyte, high electronic and ionic conductivity, as well as a fast mass transport to the reaction area. Metallic nickel or copper is used as a catalyst in the combined metal and ceramic compound, for both the internal reforming of methane and the electrochemical oxidation of hydrogen and carbon monoxide. Nickel-zirconia cermet (Ni-YSZ) is one of the most popular anode materials. Alternatively, ceramic perovskite oxides, such as lanthanum strontium chromite manganite (LSCM), with mixed ionic and electronic conductivity, are used. Common porous cathode materials include mixed ionic and electronic conducting setups, such as lanthanum strontium manganite (LSM), lanthanum strontium ferrite (LSF), lanthanum strontium cobaltite ferrite (LSCF) or composites of LSM and YSZ. Additional properties of the cathode are identical to the previous listed features of the anode [8, 20, 21, 24].

As previously shown, a single fuel cell is comprised of an anode, an electrolyte and a cathode layer, which can be arranged in a stacked formation or in a concentric circular layout, for instance the planar or tubular cell geometry. Both the tubular and the planar geometry have several subcategories, like microtubes and closed-one-end tubes or rectangular and circular plates. Individual cells are further categorized as anode (ASC), cathode (CSC), electrolyte (ESC), interconnect or substrate supported cells, in reference to the structural supporting layer of the cell. For the formation of a fuel cell stack, multiple cell arrangements are connected using interconnects, which are ceramic or metallic materials with high electronic conductivity and thermal expansion coefficients matching cell properties. In case of a planar SOFC, the flow field is usually integrated in the interconnect, providing gas transport to the adjacent anode and cathode, as well as gas-tight sealing between both channels [8, 20]. In regard to the SOFC test rig and evaluated experimental results presented in chapters 4 and 5, the focus is a planar rectangular ESC stack design. It should be noted, that the general equations for SOFC systems, including an anode exhaust gas recirculation, presented and derived in this chapter are valid independently from the designated cell and stack design and layout.

2.1.3 System approach options

As shown in Figure 2.2, an SOFC system can be schematically divided into balance-of-plant components, for instance blowers, and two main subsystems, the gas processing unit (GPU) and the SOFC module. Additionally, three conceptual approaches are outlined, including a system with catalytic partial oxidation (CPOX), external water supply (EWS) and anode exhaust gas recirculation (AEGR).

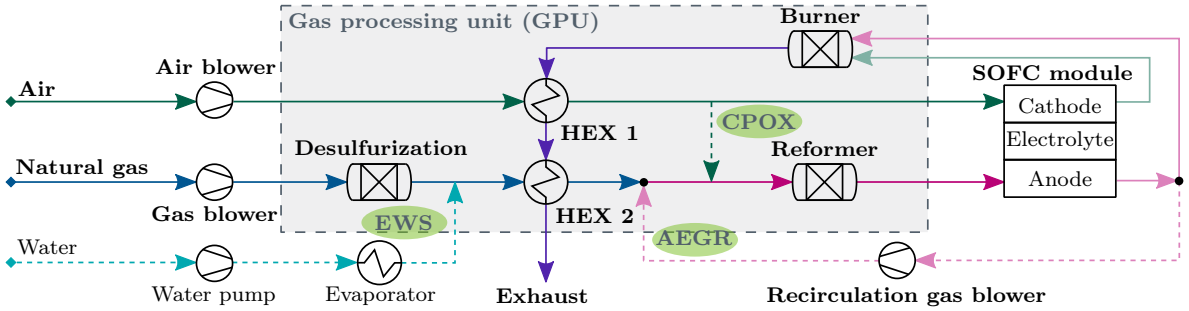

Figure 2.2: Simplified schematic SOFC system overview

The SOFC module includes at least one SOFC stack, which consists of an assembly of several individual cells connected using an interconnect. Inside a module, the fuel and air channel of several SOFC stacks can be connected with the help of module manifolds. However, the internal structure of an SOFC module, and the benefits and challenges of different fuel and air flow path interconnection possibilities are beyond the scope of this work. Interconnection possibilities, their benefits and challenges, as well as the effect of uneven distribution of fuel inside a module assembly are evaluated by Wahl [25] and Hering [26]. The interconnection of the fuel and air flow path, between different stacks in a module is considered parallel in this work and possible unequal distributions of fuel and air are neglected. Therefore, each stack of a module can be considered as a comparable entity, meaning no distinction between individual stacks has to be taken into account.

The purpose of the GPU is to heat up the fuel and air to match the anode and cathode inlet operating conditions, and the preconditioning of natural gas. Fresh ambient air is supplied to the system using an air blower. Prior to its entrance to the cathode, the air is heated in heat exchanger 1 (HEX 1), with the help of the burner exhaust gas. The burner is supplied with a mixture of anode and cathode exhaust gas, containing partially depleted fuel and air. A gas blower is used to supply natural gas to the desulfurization unit. There, the amount of catalyst poisoning sulfur containing species in natural gas is reduced below harmful thresholds. The effects of sulfur containing species in natural gas on SOFC systems are briefly addressed in section 3.1. Downstream of the desulfurization unit, the fuel is preheated in heat exchanger 2 (HEX 2) and further conditioned in a reformer, forming a hydrogen rich fuel. In general, the conversion of natural gas to hydrogen rich gas can be achieved either via steam reforming, due to the supply of water vapor, or by catalytic partial oxidation, due to the supply of oxygen. The corresponding chemical reactions of the partial (PRR) and complete (CRR) reaction steps for a general alkane molecule (C_nH_{2n+2}) and the related water-gas-shift reaction (WGSR) are outlined in Table 2.2 [8, 20, 21, 23, 24].

As highlighted with dotted lines in Figure 2.2, there are three different options for supplying the reformer with either oxygen or water vapor:

1. CPOX - the reformer is supplied with a mixture of oxygen and fuel using an air bypass
2. EWS - the reformer is supplied with a mixture of water vapor and fuel using an external evaporator unit

3. AEGR - the reformer is supplied with a mixture of water vapor rich recirculation gas and fuel using a recirculation gas blower

Table 2.2: Chemical equations of partial and complete reforming reactions, and water-gas-shift reaction for steam reforming and catalytic partial oxidation

	Steam reforming	Catalytic partial oxidation
PRR	$C_nH_{2n+2} + n\,H_2O \rightleftharpoons (2\,n+1)\,H_2 + n\,CO$	$C_nH_{2n+2} + \frac{n}{2}\,O_2 \rightleftharpoons (n+1)\,H_2 + n\,CO$
CRR	$C_nH_{2n+2} + 2\,n\,H_2O \rightleftharpoons (3\,n+1)\,H_2 + n\,CO_2$	$C_nH_{2n+2} + \frac{3\,n+1}{2}\,O_2 \rightleftharpoons (n+1)\,H_2O + n\,CO_2$
WGSR	$CO + H_2O \rightleftharpoons H_2 + CO_2$	

The CPOX option usually leads to a simple system design, with low complexity and good start up capabilities, due to the straightforward control of the fuel-to-air ratio and the exothermic nature of the reforming reaction. However, in comparison to steam reforming, the CPOX option yields low net electrical system efficiency, up to approximately 30 % due to the lower hydrogen yield of the PRR. Additionally, the undesirable CRR leads to a complete depletion of utilizable parts of the fuel, as outlined in Table 2.2 [20, 24].

A system with EWS needs an additional subsystem containing an evaporation unit to supply water vapor to the system. Additionally, the evaporation system usually uses deionized water, which needs to be generated from either a fresh water source or condensed from the water vapor rich exhaust gas of the system or anode. Therefore, compared to the CPOX option, the system complexity is higher and additional effort is necessary for the water vapor supply, ultimately yielding an intermediate net electrical system efficiency up to approximately 55 %. It should be noted, that both the evaporation of water, and the endothermic steam reforming need to be supplied with external heat. The thermal integration of neither the evaporation nor the reformer unit are shown in Figure 2.2. However, the reformer can alternatively be heated with the cathode exhaust prior to entering the burner or with the burner exhaust prior to entering HEX 1. The evaporator could be integrated downstream of HEX 1 or HEX 2. Additionally, the fresh water supply could also be replaced by a condensing unit, which extracts water from the humid anode or system exhaust gas [20, 24].

The third system option includes recirculation of a fraction of the anode exhaust gas, containing a partially depleted, water vapor rich fuel. Therefore, the reformer unit is supplied with water vapor and the remaining utilizable parts of the anode exhaust gas are recycled, ultimately increasing the fuel utilization factor and the overall net electrical efficiency up to 60 %. However, the system complexity and thermal interactions are high and the control constraints and start up capabilities are more sophisticated, but an external water vapor providing subsystem is unnecessary. Analogous to the EWS case, a thermal integration of the reformer unit is also necessary. Additionally, the recirculation gas blowers inlet temperature might be limited. Therefore, the recycled portion of the anode exhaust gas has to be cooled down to fulfill the blower temperature requirement, underlining the increased system complexity [20, 24]. Although the AEGR option has several challenges, due to increased system complexity, high thermal interactions and sophisticated control constrains, it is chosen as the evaluated system approach in this work. The AEGR option was selected, based upon the superior efficiency potential and abandonment of an external water supply unit during nominal operation.

The gross electrical efficiency potential of the three system design options versus the fuel utilization factor of the stack ($U_{f,S}$), which is introduced in subsection 2.2.1.3, is outlined in Figure 2.3[1] for a pure methane feed and typical cell voltage boundaries in a stack ranging between 0.75 and 0.85 V. For the AEGR and CPOX option, the oxygen-to-carbon ratio (Φ),

[1] The calculation constraints are shown in appendix A.

which is introduced in subsection 2.2.1.1, is set to fixed values of 2 and 0.85, respectively. Figure 2.3 clarifies the superior efficiency potential of the AEGR option due to the recycling of the anode exhaust gas. The EWS option is only touching the AEGR domain for very high fuel utilization factors of the stack and cell voltages. The CPOX option has an overall lower efficiency potential due to the reduced hydrogen yield of the reforming reaction.

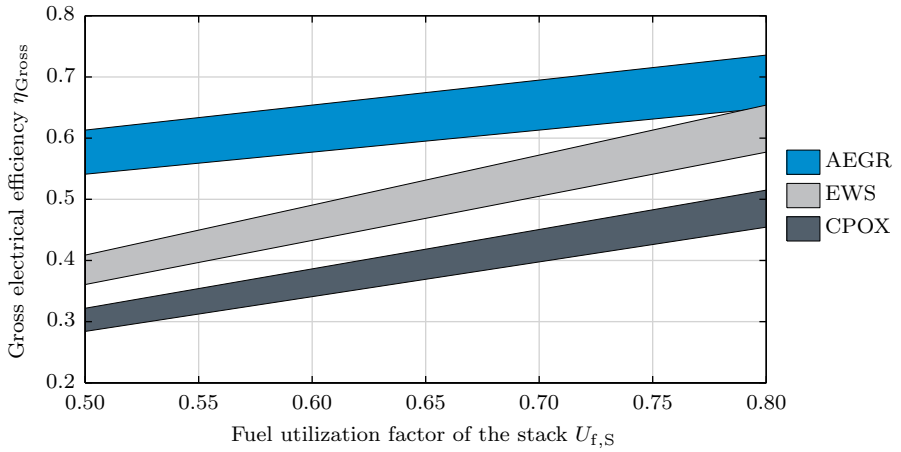

Figure 2.3: Gross electrical efficiency domains related to the lower heating value for AEGR with $\Phi_{\mathrm{AEGR}} = 2$, EWS and CPOX option with $\Phi_{\mathrm{CPOX}} = 0.85$ for a pure methane feed with cell voltages between 0.75 and 0.85 V[1]

2.2 Governing system equations

In an SOFC system, the governing characteristic system variables are the fuel utilization factor of the stack and the oxygen-to-carbon ratio in the reformer. The former needs to fall below a specific threshold value to prevent fuel starvation inside the stack, whereas the latter has to be sufficiently high to prevent carbon deposition inside the reformer, as outlined in section 3.5. In correspondence to the natural gas feed, both characteristic variables can be applied to calculate the ideal necessary amount of recirculated anode exhaust gas or the recirculation ratio (r) to keep both $U_{\mathrm{f,S}}$ and Φ constant. In the following section, the governing system equations are linked to the relation of $U_{\mathrm{f,S}}$, Φ and r, together with the natural gas composition, expressed using the natural gas coefficients as defined in section 3.4.

2.2.1 Characteristic system parameters

2.2.1.1 Oxygen-to-carbon ratio

The oxygen-to-carbon ratio in the reformer is defined as the quotient of the molar flow rate of oxygen and carbon atoms, as shown in equation (2.1) [27]. The parameter Φ is one of the main control variables of an SOFC system. A too low value of Φ can result in carbon deposition, as outlined in section 3.5. Exceedingly high values of Φ result in an increased dilution of the gas, ultimately reducing the Nernst voltage, which is displayed in equation (2.36).

$$\Phi = \frac{\dot{n}_{\mathrm{O,ref}}}{\dot{n}_{\mathrm{C,ref}}} \tag{2.1}$$

2.2.1.2 Recirculation ratio

In a system including an anode exhaust gas recirculation, the recirculation ratio is defined as the splitting between the total mass or molar flow rate at the anode outlet and in the recirculation loop, as shown in equation (2.2). The mass and molar flow rate are interchangeable, since the gas composition at the anode outlet and in the recirculation loop are identical. Referring to Carré et al. [27] and Gallet Segarra [28], r can also be expressed using $U_{\mathrm{f,S}}$, Φ, as well as the carbon (K_{C}), oxygen (K_{O}) and electron coefficients ($K_{\mathrm{e^-}}$) of natural gas, which are introduced in section 3.4. The gas coefficients represent the weighted amount of carbon and oxygen atoms or potentially releasable electrons contained in the respective natural gas mixture.

$$r = \frac{\dot{m}_{\mathrm{rec}}}{\dot{m}_{\mathrm{an,out}}} = \frac{\dot{n}_{\mathrm{rec}}}{\dot{n}_{\mathrm{an,out}}} = \left(U_{\mathrm{f,S}} \left(\frac{K_{\mathrm{e^-}}}{2\,(\Phi\,K_{\mathrm{C}} - K_{\mathrm{O}})} - 1 \right) + 1 \right)^{-1} \tag{2.2}$$

2.2.1.3 Fuel utilization factor

The fuel utilization factor is defined as the ratio between the utilized and supplied flow rate of electrons [20, 21, 23, 24]. In a system with anode exhaust gas recirculation, the fuel utilization factor can be expressed in relation to the potential flow rate of releasable electrons at the system or anode inlet, yielding the fuel utilization factor of the system ($U_{\mathrm{f,Sys}}$) and stack, respectively. According to Carré et al. [27], both fuel utilization factors are connected solely by r, as shown in equation (2.3). By applying the definition of r, $U_{\mathrm{f,Sys}}$ can also be calculated using $U_{\mathrm{f,S}}$, Φ, as well as the carbon, oxygen and electron coefficients of natural gas.

$$U_{\mathrm{f,Sys}} = \frac{U_{\mathrm{f,S}}}{1 - r\,(1 - U_{\mathrm{f,S}})} = \frac{U_{\mathrm{f,S}}\,K_{\mathrm{e^-}} + 2\,(\Phi\,K_{\mathrm{C}} - K_{\mathrm{O}})\,(1 - U_{\mathrm{f,S}})}{K_{\mathrm{e^-}}} \tag{2.3}$$

2.2.1.4 Relation between characteristic system parameters

The relation between the fuel utilization factor of the stack, oxygen-to-carbon ratio and recirculation ratio, as well as fuel utilization factor of the system is shown in Figure 2.4 for a system with a pure methane feed[2]. For a designated Φ and $U_{\mathrm{f,S}}$ the corresponding r and $U_{\mathrm{f,Sys}}$ can be uniquely determined. Additionally, a high $U_{\mathrm{f,Sys}}$ is achieved by increasing both $U_{\mathrm{f,S}}$ and r. For r equal to zero, $U_{\mathrm{f,S}}$ and $U_{\mathrm{f,Sys}}$ are identical, resulting in a system layout without anode exhaust gas recirculation.

2.2.1.5 Flow rates of gas and air

The corresponding molar ($\dot{n}_{\mathrm{NG,in}}$) or mass flow rate of natural gas ($\dot{m}_{\mathrm{NG,in}}$) can be computed using the electric current (I), number of cells in the stack (N_{Cell}), $U_{\mathrm{f,Sys}}$, the Faraday constant (F) and electron natural gas coefficient, as shown in equation (2.4) [20, 27].

$$\dot{n}_{\mathrm{NG,in}} = \frac{I\,N_{\mathrm{Cell}}}{U_{\mathrm{f,Sys}}\,F\,K_{\mathrm{e^-}}} \rightarrow \dot{m}_{\mathrm{NG,in}} = \dot{n}_{\mathrm{NG,in}}\,M_{\mathrm{NG,in}} \tag{2.4}$$

Analogous to the molar or mass flow rate of natural gas, the flow rate of air ($\dot{n}_{\mathrm{a,in}}, \dot{m}_{\mathrm{a,in}}$) can be determined using the air utilization factor (U_{a}), characterized as the ratio between the transferred and total supplied amount of oxygen, as shown in equation (2.5) [20, 27]. In contrast

[2] The recirculation ratio expressed as a function of the fuel utilization factor of the system and stack or oxygen-to-carbon ratio is derived from equation (2.3) or by applying equation (2.3) to equation (2.2), respectively.

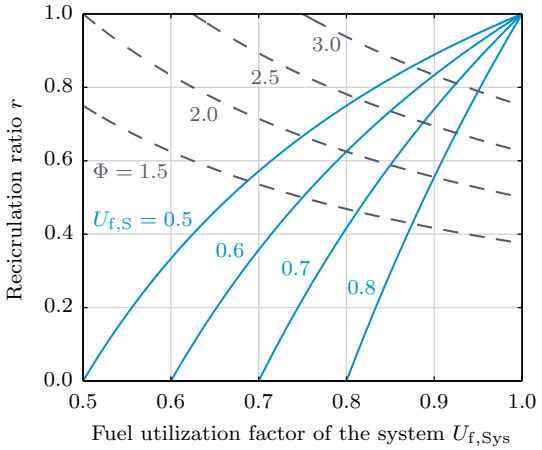

Figure 2.4: Relation between oxygen-to-carbon ratio, recirculation ratio, as well as fuel utilization factor of the stack and system for a pure methane feed

to the fuel flow path, no distinction is necessary between system and stack air utilization factor because the evaluated system does not include air recirculation.

$$\dot{n}_{\mathrm{a,in}} = \frac{I\,N_{\mathrm{Cell}}}{4\,U_{\mathrm{a}}\,F\,x_{\mathrm{a,O_2}}} \rightarrow \dot{m}_{\mathrm{a,in}} = \dot{n}_{\mathrm{a,in}}\,M_{\mathrm{a,in}} \tag{2.5}$$

2.2.1.6 Air-fuel-equivalence ratio

In general, the air-fuel-equivalence ratio for combustion (λ) is defined as the quotient of supplied to the stoichiometric necessary amount of oxygen. The stoichiometric amount of oxygen can be determined based upon the stoichiometric oxygen coefficients of the corresponding complete combustion reaction, which are outlined in Table 2.4. Therefore, a related stoichiometric combustion coefficient (K_λ) is defined based upon the respective mole fractions ($x_{\mathrm{bu,in},i}$) and stoichiometric oxygen number ($N_{\mathrm{O_2,bu,sto},i}$) of the combustible species at the burner inlet, as shown in equation (2.6), using the stoichiometric oxygen number listed in Table 2.3. Lastly, as outlined in equation (2.7), the coefficient can be implemented to express λ as a function of the air and fuel burner inlet flow rates, the corresponding oxygen content in the air and the stoichiometric combustion coefficient, respectively.

$$K_\lambda = \sum_i x_{\mathrm{bu,in},i}\,N_{\mathrm{O_2,bu,sto},i} \tag{2.6}$$

$$\lambda = \frac{\dot{n}_{\mathrm{O_2,bu,in}}}{\dot{n}_{\mathrm{O_2,bu,sto}}} = \frac{\dot{n}_{\mathrm{a,bu,in}}\,x_{\mathrm{bu,in,O_2}}}{\dot{n}_{\mathrm{f,bu,in}}\,K_\lambda} \tag{2.7}$$

Table 2.3: Stoichiometric oxygen number of the combustible species

Species i	CH_4	C_2H_6	C_3H_8	C_4H_{10}	H_2	CO
Stoichiometric oxygen number $N_{\mathrm{O_2,bu,sto},i}$	2.0	3.5	5.0	6.5	0.5	0.5

2.2.2 Conservation equations

2.2.2.1 Mass balance of system

The complete system mass balance of an SOFC system is schematically illustrated in Figure 2.5. The shown system includes a reformer, a stack divided into a cathode and anode flow channel, as well as an anode exhaust gas recirculation path and burner. The corresponding mass balance relations are displayed below as equations (2.8), (2.9), (2.10), (2.11) and (2.12). As outlined, each individual mass flow can be expressed using at least two of the following - the mass flow rate of natural gas and air at the system inlet, as well as the transferred mass flow rate of oxygen ($\dot{m}_{\mathrm{O_2,tr}}$) and r. As shown in equation (2.13), $\dot{m}_{\mathrm{O_2,tr}}$ can be calculated based upon the electric current and number of cells in the stack, or as function of $\dot{m}_{\mathrm{NG,in}}$, $U_{\mathrm{f,Sys}}$ and the electron gas coefficient, by applying equation (2.4).

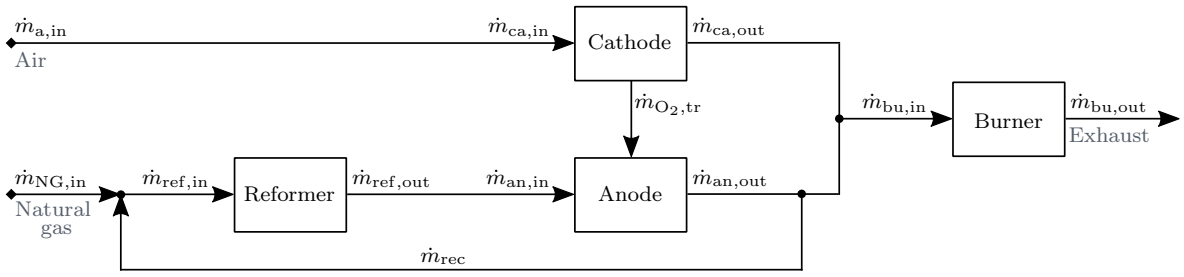

Figure 2.5: Simplified system overview with mass balance

$$\dot{m}_{\mathrm{ref,in}} = \dot{m}_{\mathrm{ref,out}} = \dot{m}_{\mathrm{an,in}} = \dot{m}_{\mathrm{NG,in}} + \dot{m}_{\mathrm{rec}} = \frac{\dot{m}_{\mathrm{NG,in}} + r\,\dot{m}_{\mathrm{O_2,tr}}}{1-r} \tag{2.8}$$

$$\dot{m}_{\mathrm{an,out}} = \dot{m}_{\mathrm{an,in}} + \dot{m}_{\mathrm{O_2,tr}} = \frac{\dot{m}_{\mathrm{NG,in}} + \dot{m}_{\mathrm{O_2,tr}}}{1-r} \tag{2.9}$$

$$\dot{m}_{\mathrm{rec}} = r\,\dot{m}_{\mathrm{an,out}} = \frac{r\,(\dot{m}_{\mathrm{NG,in}} + \dot{m}_{\mathrm{O_2,tr}})}{1-r} \tag{2.10}$$

$$\dot{m}_{\mathrm{ca,out}} = \dot{m}_{\mathrm{ca,in}} - \dot{m}_{\mathrm{O_2,tr}} = \dot{m}_{\mathrm{a,in}} - \dot{m}_{\mathrm{O_2,tr}} \tag{2.11}$$

$$\dot{m}_{\mathrm{bu,in}} = \dot{m}_{\mathrm{bu,out}} = (1-r)\,\dot{m}_{\mathrm{an,out}} + \dot{m}_{\mathrm{ca,out}} = \dot{m}_{\mathrm{NG,in}} + \dot{m}_{\mathrm{a,in}} \tag{2.12}$$

$$\dot{m}_{\mathrm{O_2,tr}} = \frac{I\,N_{\mathrm{Cell}}\,M_{\mathrm{O_2}}}{4\,F} = \frac{\dot{m}_{\mathrm{NG,in}}\,U_{\mathrm{f,Sys}}\,K_{\mathrm{e^-}}\,M_{\mathrm{O_2}}}{4\,M_{\mathrm{NG,in}}} \tag{2.13}$$

2.2.2.2 Molar balance of system

Analogous to the mass balance, the complete molar balance of the system is schematically illustrated in Figure 2.6.

In contrast to the mass balance, the molar flow rates are affected by the occurring reforming reactions of hydrocarbons in the reformer and anode, together with the combustion reaction inside the burner. According to Carré [29], assuming a complete conversion of all hydrocarbons

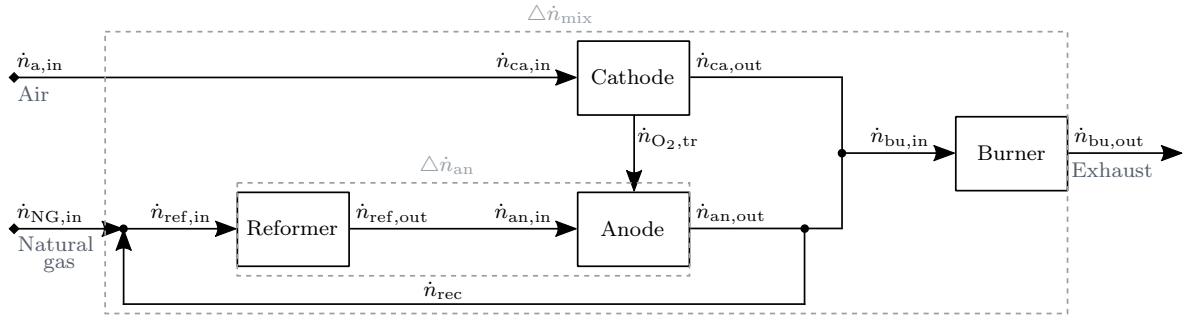

Figure 2.6: Simplified system overview with molar balance

at the anode outlet, the change in molar quantity can be calculated solely as a function of the molar flow rate and composition of natural gas. The corresponding formula is displayed in equation (2.14). The equation uses the change in molar quantity coefficients of the anode pathway of each individual species ($\triangle\dot{n}_{\mathrm{an},i}$), outlined in Table 2.4 including the considered chemical equation. Although the stoichiometry of the electrochemical conversion of hydrogen or carbon monoxide indicates a change in the molar quantity, both species are not affecting the molar flow rate in the anode flow path, because oxygen is transferred from the cathode channel [27, 29]. It should be noted that, oxygen is not included in Table 2.4. As outlined in chapter 3, natural gas at most contains traces of oxygen and extensive leakages from the cathode to the anode flow path are assumed to be negligible low. Consequently, oxygen is not considered a possible present species in the anode flow path.

By limiting the natural gas composition to methane, ethane, propane, butane, carbon dioxide, nitrogen and hydrogen, the change in molar quantity can also be related to the carbon and oxygen gas coefficient using the respective definition, introduced in section 3.4. As a result, the coefficient representing the change in molar quantity ($K_{\triangle\mathrm{an}}$) can be obtained, as depicted in equation (2.15)[3].

$$\triangle\dot{n}_{\mathrm{an}} = \dot{n}_{\mathrm{NG,in}} \sum_i x_{\mathrm{NG,in},i}\, \triangle\dot{n}_{\mathrm{an},i} \tag{2.14}$$

$$K_{\triangle\mathrm{an}} = \sum_i x_{\mathrm{NG,in},i}\, \triangle\dot{n}_{\mathrm{an},i} = 2\,K_{\mathrm{C}} - K_{\mathrm{O}} \tag{2.15}$$

The change in molar quantity between the natural gas and air inlet, and the exhaust outlet can be calculated using the theoretical complete mixture of the inlet gases and assuming a complete combustion reaction. The change in molar quantity can be calculated as outlined in equation (2.16) using the change in molar quantity coefficients of the combustion for each individual species ($\triangle\dot{n}_{\mathrm{bu},i}$), illustrated in Table 2.4 including the considered chemical equation. For the purpose of simplification, coefficient ($K_{\triangle\mathrm{mix}}$) is defined in equation (2.17), representing the change in molar quantity of the complete combustion reaction.

$$\triangle\dot{n}_{\mathrm{mix}} = (\dot{n}_{\mathrm{NG,in}} + \dot{n}_{\mathrm{a,in}}) \sum_i x_{\mathrm{mix},i}\, \triangle\dot{n}_{\mathrm{bu},i} \quad \text{with: } x_{\mathrm{mix},i} = \frac{x_{\mathrm{NG,in},i}\,\dot{n}_{\mathrm{NG,in}} + x_{\mathrm{a,in},i}\,\dot{n}_{\mathrm{a,in}}}{\dot{n}_{\mathrm{NG,in}} + \dot{n}_{\mathrm{a,in}}} \tag{2.16}$$

$$K_{\triangle\mathrm{mix}} = \sum_i x_{\mathrm{mix},i}\, \triangle\dot{n}_{\mathrm{bu},i} \tag{2.17}$$

[3]The relation of $K_{\triangle\mathrm{an}}$ to the individual species is shown in equation (3.13) in section 3.4.

Table 2.4: Molar quantity change coefficient of anode and combustion point of view

Species i	Main anode flow path reaction	Molar quantity coefficient of anode $\triangle\dot{n}_{\mathrm{an},i}$	Combustion reaction	Molar quantity coefficient of burner $\triangle\dot{n}_{\mathrm{bu},i}$
CH_4	$CH_4 + H_2O \rightleftharpoons CO + 3\,H_2$	+2	$CH_4 + 2\,O_2 \rightarrow CO_2 + 2\,H_2O$	0
C_2H_6	$C_2H_6 + 2\,H_2O \rightleftharpoons 2\,CO + 5\,H_2$	+4	$C_2H_6 + \frac{7}{2}\,O_2 \rightarrow 2\,CO_2 + 3\,H_2O$	+0.5
C_3H_8	$C_3H_8 + 3\,H_2O \rightleftharpoons 3\,CO + 7\,H_2$	+6	$C_3H_8 + 5\,O_2 \rightarrow 3\,CO_2 + 4\,H_2O$	+1
C_4H_{10}	$C_4H_{10} + 4\,H_2O \rightleftharpoons 4\,CO + 9\,H_2$	+8	$C_4H_{10} + \frac{13}{2}\,O_2 \rightarrow 4\,CO_2 + 5\,H_2O$	+1.5
CO_2	-	0	-	0
N_2	-	0	-	0
H_2	$H_2 + \frac{1}{2}\,O_2 \rightarrow H_2O$	0	$H_2 + \frac{1}{2}\,O_2 \rightarrow H_2O$	-0.5
CO	$CO + H_2O \rightleftharpoons CO_2 + H_2$	0	$CO + \frac{1}{2}\,O_2 \rightarrow CO_2$	-0.5
H_2O	-	0	-	0

The change in molar quantity coefficients are applied to express the molar balance solely as functions of the molar flow rate of natural gas and air at the system inlet, as well as r and the transferred molar flow rate of oxygen ($\dot{n}_{\mathrm{O_2,tr}}$). The resulting constraints are shown in equations (2.18), (2.19), (2.20), (2.21), (2.22) and (2.23). Analogous to the mass flow rate, the molar flow rate of transferred oxygen can be calculated based upon the electric current and number of cells in the stack, or as function of $\dot{n}_{\mathrm{NG,in}}$, $U_{\mathrm{f,Sys}}$ and the electron gas coefficient, as outlined in equation (2.24). Although the molar flow rate at the reformer outlet ($\dot{n}_{\mathrm{ref,out}}$) and anode inlet ($\dot{n}_{\mathrm{an,in}}$) are equal, neither can be expressed as an analytical function as long as an incomplete conversion of hydrocarbons in the reformer is assumed, due to the dependence of the molar flow rate on the equilibrium state.

$$\dot{n}_{\mathrm{ref,in}} = \dot{n}_{\mathrm{NG,in}} + \dot{n}_{\mathrm{rec}} = \frac{\dot{n}_{\mathrm{NG,in}}\,(1 + r\,K_{\triangle\mathrm{an}})}{(1-r)} \tag{2.18}$$

$$\dot{n}_{\mathrm{an,out}} = \dot{n}_{\mathrm{ref,in}} + \triangle\dot{n}_{\mathrm{an}} = \frac{\dot{n}_{\mathrm{NG,in}}\,(1 + K_{\triangle\mathrm{an}})}{(1-r)} \tag{2.19}$$

$$\dot{n}_{\mathrm{rec}} = r\,\dot{n}_{\mathrm{an,out}} = \frac{r\,\dot{n}_{\mathrm{NG,in}}\,(1 + K_{\triangle\mathrm{an}})}{(1-r)} \tag{2.20}$$

$$\dot{n}_{\mathrm{ca,out}} = \dot{n}_{\mathrm{ca,in}} - \dot{n}_{\mathrm{O_2,tr}} = \dot{n}_{\mathrm{a,in}} - \dot{n}_{\mathrm{O_2,tr}} \tag{2.21}$$

$$\dot{n}_{\mathrm{bu,in}} = \dot{n}_{\mathrm{ca,out}} + (1-r)\,\dot{n}_{\mathrm{an,out}} = \dot{n}_{\mathrm{a,in}} - \dot{n}_{\mathrm{O_2,tr}} + \dot{n}_{\mathrm{NG,in}}\,(1 + K_{\triangle\mathrm{an}}) \tag{2.22}$$

$$\dot{n}_{\mathrm{bu,out}} = \dot{n}_{\mathrm{NG,in}} + \dot{n}_{\mathrm{a,in}} + \triangle\dot{n}_{\mathrm{mix}} = (\dot{n}_{\mathrm{NG,in}} + \dot{n}_{\mathrm{a,in}})\,(1 + K_{\triangle\mathrm{mix}}) \tag{2.23}$$

$$\dot{n}_{\mathrm{O_2,tr}} = \frac{I\,N_{\mathrm{Cell}}}{4\,F} = \frac{\dot{n}_{\mathrm{NG,in}}\,U_{\mathrm{f,Sys}}\,K_{\mathrm{e^-}}}{4} \tag{2.24}$$

2.2.2.3 Electron balance of anode path

The molar flow rate of potentially releasable electrons in natural gas ($\dot{n}_{\mathrm{e^-,NG,in}}$) can be related to the electron gas coefficient, as shown in equation (2.25). Additionally, as introduced in section 2.2.1.3, the fuel utilization factor is defined as the ratio between the utilized ($\dot{n}_{\mathrm{e^-,S,uti}}$) and supplied flow rate of electrons at the anode inlet ($\dot{n}_{\mathrm{e^-,an,in}}$), as illustrated in equation (2.26). By applying both definitions, the molar balance of potentially releasable electrons at the reformer, anode and in the recirculation loop can be expressed as functions of $U_{\mathrm{f,S}}$, $\dot{n}_{\mathrm{e^-,NG,in}}$ and r, as outlined in equations (2.27), (2.28) and (2.29).

$$\dot{n}_{\mathrm{e^-,NG,in}} = \dot{n}_{\mathrm{NG,in}}\, K_{\mathrm{e^-}} \tag{2.25}$$

$$U_{\mathrm{f,S}} = \frac{\dot{n}_{\mathrm{e^-,S,uti}}}{\dot{n}_{\mathrm{e^-,an,in}}} \rightarrow \dot{n}_{\mathrm{e^-,S,uti}} = U_{\mathrm{f,S}}\, \dot{n}_{\mathrm{e^-,an,in}} = \frac{I\, N_{\mathrm{Cell}}}{F} \tag{2.26}$$

$$\dot{n}_{\mathrm{e^-,an,out}} = \dot{n}_{\mathrm{e^-,an,in}} - \dot{n}_{\mathrm{e^-,S,uti}} = (1 - U_{\mathrm{f,S}})\, \dot{n}_{\mathrm{e^-,an,in}} = \frac{\dot{n}_{\mathrm{e^-,NG,in}}\,(1 - U_{\mathrm{f,S}})}{1 - r\,(1 - U_{\mathrm{f,S}})} \tag{2.27}$$

$$\dot{n}_{\mathrm{e^-,rec}} = r\, \dot{n}_{\mathrm{e^-,an,out}} = \frac{r\, \dot{n}_{\mathrm{e^-,NG,in}}\,(1 - U_{\mathrm{f,S}})}{1 - r\,(1 - U_{\mathrm{f,S}})} \tag{2.28}$$

$$\dot{n}_{\mathrm{e^-,ref,in}} = \dot{n}_{\mathrm{e^-,ref,out}} = \dot{n}_{\mathrm{e^-,an,in}} = \dot{n}_{\mathrm{e^-,NG,in}} + \dot{n}_{\mathrm{e^-,rec}} = \frac{\dot{n}_{\mathrm{e^-,NG,in}}}{1 - r\,(1 - U_{\mathrm{f,S}})} \tag{2.29}$$

2.2.2.4 Element balance of anode path

The following element balance is based upon the conceptional assumption that every molecule can be disassembled into its constituting atoms using the related stoichiometric coefficients. For instance, a methane molecule can be split up into a carbon and four hydrogen atoms. The considered species of natural gas are composed of a combination of carbon, hydrogen, nitrogen and oxygen atoms. Additionally, only the flow rate of oxygen atoms is changing in the anode path, due to the electrochemical transfer of oxygen. As a result, the carbon, hydrogen and nitrogen balance can be obtained based upon r, $\dot{n}_{\mathrm{NG,in}}$ and the corresponding gas coefficient, as outlined in equations (2.30), (2.31) and (2.32). The oxygen element balance needs to be divided into two separate balances, due to the electrochemical transfer of oxygen inside the stack. The resulting balances, at the an anode outlet, and reformer or anode inlet, are shown in equations (2.33) and (2.34) using the molar flow rate of oxygen, previously defined in equation (2.24).

$$\dot{n}_{\mathrm{C,ref,in}} = \dot{n}_{\mathrm{C,ref,out}} = \dot{n}_{\mathrm{C,an,in}} = \dot{n}_{\mathrm{C,an,out}} = \frac{\dot{n}_{\mathrm{C,in}}}{1 - r} = \frac{\dot{n}_{\mathrm{NG,in}}\, K_{\mathrm{C}}}{1 - r} \tag{2.30}$$

$$\dot{n}_{\mathrm{H,ref,in}} = \dot{n}_{\mathrm{H,ref,out}} = \dot{n}_{\mathrm{H,an,in}} = \dot{n}_{\mathrm{H,an,out}} = \frac{\dot{n}_{\mathrm{H,in}}}{1 - r} = \frac{\dot{n}_{\mathrm{NG,in}}\, K_{\mathrm{H}}}{1 - r} \tag{2.31}$$

$$\dot{n}_{\mathrm{N,ref,in}} = \dot{n}_{\mathrm{N,ref,out}} = \dot{n}_{\mathrm{N,an,in}} = \dot{n}_{\mathrm{N,an,out}} = \frac{\dot{n}_{\mathrm{N,in}}}{1 - r} = \frac{\dot{n}_{\mathrm{NG,in}}\, K_{\mathrm{N}}}{1 - r} \tag{2.32}$$

$$\dot{n}_{\mathrm{O,an,out}} = \frac{\dot{n}_{\mathrm{O,in}} + \dot{n}_{\mathrm{O,tr}}}{1 - r} = \frac{\dot{n}_{\mathrm{NG,in}}\, K_{\mathrm{O}} + 2\, \dot{n}_{\mathrm{O_2,tr}}}{1 - r} = \frac{\dot{n}_{\mathrm{NG,in}}}{1 - r} \left(K_{\mathrm{O}} + \frac{U_{\mathrm{f,Sys}}}{2}\, K_{\mathrm{e^-}} \right) \tag{2.33}$$

$$\dot{n}_{\mathrm{O,ref,in}} = \dot{n}_{\mathrm{O,ref,out}} = \dot{n}_{\mathrm{O,an,in}} = \dot{n}_{\mathrm{O,an,out}} - \dot{n}_{\mathrm{O,tr}} = \dot{n}_{\mathrm{O,an,out}} - 2\,\dot{n}_{\mathrm{O_2,tr}}$$
$$= \frac{\dot{n}_{\mathrm{NG,in}}}{1-r}\left(K_{\mathrm{O}} + \frac{r\,U_{\mathrm{f,Sys}}}{2}\,K_{\mathrm{e^-}}\right) = \frac{\dot{n}_{\mathrm{NG,in}}}{1-r}\,\Phi\,K_{\mathrm{C}} \tag{2.34}$$

2.2.3 Electrochemical constraints - cell voltage

A generic voltage current curve of a fuel cell as a function of the current density (j) is shown in Figure 2.7a. The current density is the ratio between the electric current and active cell area ($A_{\mathrm{Cell,active}}$). As displayed in Figure 2.7a, the cell voltage (E_{Cell}) of a fuel cell is related to the reversible voltage (E_{rev}) by the deviation to ideal standard conditions, the change of the fuel composition due to the electrochemical conversion, and the ohmic loss and polarization inside of the cell [8, 20, 23, 24, 30].

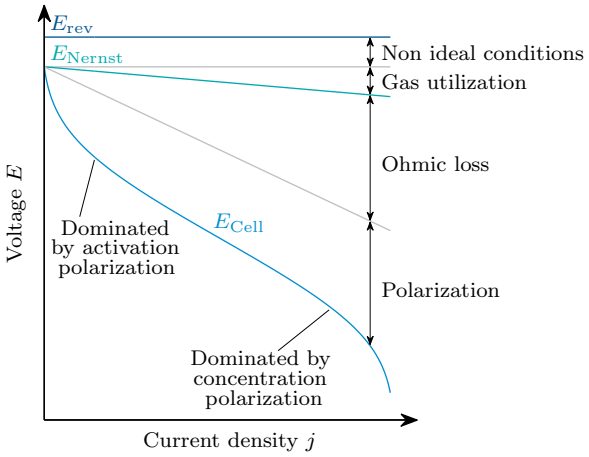

(a) Generic voltage current curve with individual voltage loss portions based upon Kendall and Kendall [20], Singhal and Kendall [30] and Milewski et al. [23]

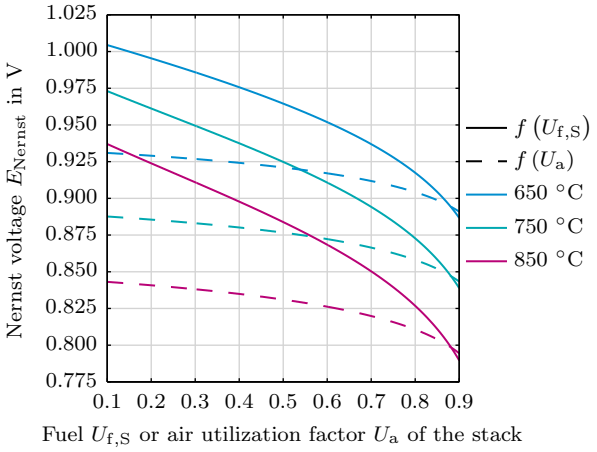

(b) Nernst voltage as a function of temperature and fuel or air utilization factor of the stack for a designated $\Phi = 2$ and fixed $U_{\mathrm{a}} = 0.25$ or $U_{\mathrm{f,S}} = 0.75$, respectively

Figure 2.7: Generic voltage current curve and Nernst voltage as a function of temperature and fuel or air utilization factor of the stack

The reversible voltage of a fuel cell can be calculated based upon the Gibbs free energy ($\triangle g$) of the electrochemical conversion reactions, the related number of releasable electrons ($N_{\mathrm{e^-}}$) and the Faraday constant, as outlined in equation (2.35). However, the Gibbs free energy is pressure and temperature dependent and therefore, for a constant pressure, the reversible voltage is decreasing with an increasing temperature [20, 23, 24].

$$E_{\mathrm{rev}} = -\frac{\triangle g(p,T)}{N_{\mathrm{e^-}}\,F} \tag{2.35}$$

Additionally, the reversible voltage is further reduced by considering the different partial pressures or concentrations of reactants at the anode and cathode, expressed using the Nernst equation (2.36) for the electrochemical conversion of hydrogen [20, 23, 24].

$$E_{\mathrm{Nernst}} = E_{\mathrm{rev}} - \frac{R\,T}{N_{\mathrm{e^-}}\,F}\,\ln\left(\frac{x_{\mathrm{H_2O}}}{x_{\mathrm{H_2}}\,\sqrt{x_{\mathrm{O_2}}}}\right) \tag{2.36}$$

Furthermore, losses due to the activation of the reactions, the ohmic resistance of the cell and the limitation of the gas transport to the electrodes have to be included. The activation polarization has a large influence for low current densities and yields a sharp non-linear voltage drop. The activation polarization (E_{Act}) can be computed using the Butler-Volmer equation (2.37) using the exchange current density (j_{ex}), the charge transfer coefficient (κ) and number of releasable electrons. The ohmic loss (E_{Ohmic}) includes ionic resistance of the electrolyte against the transfer of oxygen ions and the electronic resistances of the electrodes and interconnect to the transport of electrons. The ohmic loss can be calculated using Ohm's law and has a linear influence, as displayed in equation (2.38). The concentration polarization (E_{Conc}) has a sharp non-linear influence on the cell voltage for high current densities, due to limited diffusion of electrochemical active species to the reaction area resulting from the low total concentration of those species. The concentration polarization can be computed using the limiting current density at the anode or cathode $\left(j_{\mathrm{lim,an/ca}}\right)$ and the corresponding number of releasable electrons, as outlined in equation (2.39) [8, 20, 23, 24].

$$j = j_{\mathrm{ex}} \left(\exp\left(\frac{\kappa_1 \, N_{\mathrm{e^-}} \, F}{R \, T} \, E_{\mathrm{Act}} \right) - \exp\left(- \frac{(1-\kappa_2) \, N_{\mathrm{e^-}} \, F}{R \, T} \, E_{\mathrm{Act}} \right) \right) \tag{2.37}$$

$$E_{\mathrm{Ohmic}} = I \left(Z_{\mathrm{el}} + Z_{\mathrm{ionic}} \right) \tag{2.38}$$

$$E_{\mathrm{Conc}} = - \frac{R \, T}{N_{\mathrm{e^-}} \, F} \ln\left(1 - \frac{j}{j_{\mathrm{lim,an/ca}}} \right) \tag{2.39}$$

Finally, the cell voltage can be obtained by subtracting the three losses from the Nernst Voltage (E_{Nernst}), as outlined in equation (2.40) [8, 20, 23, 24].

$$E_{\mathrm{Cell}} = E_{\mathrm{Nernst}} - E_{\mathrm{Act}} - E_{\mathrm{Ohmic}} - E_{\mathrm{Conc}} \tag{2.40}$$

The influence of temperature, fuel and air utilization factor of the stack on the Nernst voltage is shown in Figure 2.7b for an atmospheric ideal SOFC system including AEGR with a fixed Φ of 2 and a corresponding constant U_{a} or $U_{\mathrm{f,S}}$ of 0.25 or 0.75, respectively[4]. As displayed in Figure 2.7b, $U_{\mathrm{f,S}}$ has a very high non linear impact on the Nernst voltage with extreme gradients for values higher than 0.8. The air utilization factor has a slight linear influence up to a value of around 0.4, whereas an increase beyond this utilization factor leads to an intermediate non linear decrease of the Nernst voltage. The variation in temperature yields an almost linear shift of the overall voltage level, due to the strong temperature dependence of the reversible voltage.

2.2.4 Efficiency

2.2.4.1 Electrical efficiency

In general, the gross electrical efficiency of a fuel cell system (η_{Gross}) is defined by the quotient of the electric power output of the stack (P_{el}) and the enthalpy flow rate of the supplied natural gas $\left(\dot{H}_{\mathrm{NG,in}}\right)$. The former can be expressed using the electric current, cell voltage and number of cells. The latter is the product of the molar flow rate of the supplied natural gas and the corresponding molar lower heating value ($h_{\mathrm{i,NG}}$). Additionally, by applying equation (2.4), the

[4] The result were generated based upon the ideal control scheme of the system model, which is presented in chapter 4, using the designated stack temperature and characteristic parameters to calculate the equilibrium composition for a pure methane system feed.

gross electrical efficiency can be expressed as a function of the fuel utilization factor of the system, as outlined in equation (2.41) [20, 24].

$$\eta_{\mathrm{Gross}} = \frac{P_{\mathrm{el}}}{\dot{H}_{\mathrm{NG,in}}} = \frac{E_{\mathrm{Cell}}\, I\, N_{\mathrm{Cell}}}{\dot{n}_{\mathrm{NG,in}}\, h_{\mathrm{i,NG}}} = \frac{E_{\mathrm{Cell}}\, U_{\mathrm{f,Sys}}\, F\, K_{\mathrm{e^-}}}{h_{\mathrm{i,NG}}} \tag{2.41}$$

Furthermore, the net electrical efficiency of the system (η_{Net}) can be calculated by including the power demand of all balance-of-plant components (P_{BOP}), depicted in equation (2.42). The balance-of-plant demand contains the power demand of the blowers, sensors, actuators and electronic control panels, along with the DC to AC or DC to DC conversion losses of the inverter to ensure grid parity [20, 24].

$$\eta_{\mathrm{Net}} = \frac{P_{\mathrm{el}} - P_{\mathrm{BOP}}}{\dot{H}_{\mathrm{NG,in}}} = \frac{E_{\mathrm{Cell}}\, I\, N_{\mathrm{Cell}} - P_{\mathrm{BOP}}}{\dot{n}_{\mathrm{NG,in}}\, h_{\mathrm{i,NG}}} \tag{2.42}$$

2.2.4.2 Thermal efficiency

In case of direct use of the waste heat of the SOFC system, the thermal efficiency (η_{Thermal}) can be defined in relation to the enthalpy flow rate of the supplied natural gas, as outlined in equation (2.43). The heat can, for instance, be extracted from the hot exhaust gas downstream of HEX 2, displayed in Figure 2.2. The extracted heat can be utilized for the heating or evaporation of fresh water, or for supplying an endothermic process [20].

$$\eta_{\mathrm{Thermal}} = \frac{\dot{Q}_{\mathrm{Thermal}}}{\dot{H}_{\mathrm{NG,in}}} = \frac{\dot{Q}_{\mathrm{Thermal}}}{\dot{n}_{\mathrm{NG,in}}\, h_{\mathrm{i,NG}}} \tag{2.43}$$

2.2.4.3 Total efficiency

Lastly, the sum of the net electrical and thermal efficiency can be used to describe the total system efficiency (η_{Total}), as shown in equation (2.44) [20].

$$\eta_{\mathrm{Total}} = \frac{P_{\mathrm{el}} - P_{\mathrm{BOP}} + \dot{Q}_{\mathrm{Thermal}}}{\dot{H}_{\mathrm{NG,in}}} = \eta_{\mathrm{Net}} + \eta_{\mathrm{Thermal}} \tag{2.44}$$

3 Natural gas quality

The following chapter outlines the regulatory background and the magnitudes of varying natural gas qualities in the European Union. The evaluation is based upon several temporally resolved natural gas data sets from different European locations. The data base is further used to compare the individual data sets and derive general constraints and correlations. The chapter concludes with an evaluation of the thermodynamic effects of varying natural gas quality on an ideal SOFC system including an AEGR.

3.1 Overview

In general, crude natural gas is a mixture of short-chained hydrocarbons, such as methane, ethane, propane, butane, and higher hydrocarbon compounds (C_{5+}), as well as inert contents, primarily carbon dioxide and nitrogen. Methane is the dominating species making up at least 75 % of the mixture. Ethane, propane, nitrogen and carbon dioxide contents are usually present in single-digits, up to a maximum of roughly 10 %, respectively. Butane can appear as unbranched or iso butane at a maximum of roughly 1 %. The C_{5+} compounds can be found in the form of unbranched, iso or neo pentane and even in traces of higher hydrocarbons, such as hexane isomers. However, the C_{5+} compounds are often shown as a sum because their added up total contents are usually lower than 0.5 %. Additionally, depending on origin, crude natural gas can also contain traces of oxygen, hydrogen, and rare gases, such as helium, argon, and sulfurous species, primarily present as hydrogen sulfide. Crude natural gas is gathered in a myriad of locations worldwide. After gas conditioning, including oil and contaminant removal, the gas is transported in gaseous form through pipeline systems or as liquid natural gas overseas to its destination of consumption [7, 8, 9, 10, 31, 32, 33, 34, 35, 36, 37, 38].

Another growing source of methane rich fuel is bio gas, which can be formed, for instance, via anaerobic digestion of organic matter. In general, raw bio gas is a moist mixture of 40 to 80 % of methane, 20 to 50 % of carbon dioxide, and up to 5 % of other compounds or elements, such as nitrogen, hydrogen sulfide and ammonia. Prior to the injection into natural gas grids, the raw bio gas is upgraded to bio-methane, primarily by carbon dioxide and hydrogen sulfide removal, as well as dehumidification, ultimately enhancing methane contents beyond 90 % [10, 12, 13, 14, 15, 16].

It is projected that renewable hydrogen will play a major role as an energy carrier in the future, due to its similarity and possible interchangeability with current conventional gaseous energy sources. Sustainable hydrogen can, for instance, be produced via electrolysis of water using renewable energy and by pyrolysis or gasification of biomass. Additionally, hydrogen can be further utilized, in the presence of carbon monoxide or carbon dioxide, in the methanation process, ultimately forming synthetic methane [10, 12, 13, 15, 17, 18].

As a result of the possible combinations of natural gas, bio-methane, synthetic methane and even hydrogen of varying qualities from different origins inside highly interconnected gas grids, the natural gas composition at the final point of consumption can vary significantly [7, 8, 9, 10, 11]. Therefore, regulations and standardization have been introduced to define and govern natural gas quality, as outlined for Europe in section 3.2.

Furthermore, this work focuses on high calorific natural gas, abbreviated as H-gas, since group H is regulated in the most recent European standard [11, 39]. More detailed information about the processing, distribution, consumption, and market data of natural gas, bio gas and hydrogen can be obtained in the publications by Ghosh and Prelas [7], Kent [9], van Basshuysen [10], McPhail et al. [12], Demirbas [13, 17], Wellinger et al. [16] and Bhattacharyya [40].

It should be noted that the effects of sulfur containing species in natural gas on SOFC systems, such as catalysts deactivation or enhanced degradation, are beyond the scope of this work. It is assumed that systems equipped with a desulfurization unit reduce sulfur contents below harmful thresholds. The effects of sulfur containing species on SOFCs and research focusing on sulfur tolerant cells are presented by Papurello et al. [41], Nurk et al. [42], Madi et al. [43], Nagel et al. [44], Tan et al. [45], Chen et al. [46], Vincent et al. [47] and Wang et al. [48], respectively.

3.2 Regulatory framework

In the European Union, H-gas quality is standardized to provide the basis for the security of gas supply, due to the simplification of natural gas interchangeability throughout the participating member states. Natural gas quality is defined by domains and limits of physical and chemical properties. The characteristic parameters include the Wobbe-index (w), higher heating value $\left(\tilde{h}_\mathrm{s}\right)$ and relative density (ρ_relative). Additionally, limits of certain species' contents, such as sulfur, oxygen and carbon dioxide, the dew points of hydrocarbons and water, as well as the methane number are specified [11]. The relative density is defined as the quotient of the density of natural gas (ρ_NG) and dry air ($\rho_\mathrm{a,dry}$) at standard conditions. The relative density is used to calculate the Wobbe-index based upon the volumetric higher heating value of natural gas, as shown in equations (3.1) and (3.2) [49][1]. The Wobbe-index is used to classify the interchangeability of gases. It should be noted that the limits of the Wobbe-index and higher heating value can be set individually by the respective standardization organization. Consequently, the boundary values do not have to correlate with equation (3.2).

$$\begin{aligned}\tilde{h}_\mathrm{s} &= \sum_i x_i\,\tilde{h}_{\mathrm{s},i} \\ &= \tilde{h}_{\mathrm{s,CH_4}}\,x_{\mathrm{NG,CH_4}} + \tilde{h}_{\mathrm{s,C_2H_6}}\,x_{\mathrm{NG,C_2H_6}} + \tilde{h}_{\mathrm{s,C_3H_8}}\,x_{\mathrm{NG,C_3H_8}} + \tilde{h}_{\mathrm{s,C_4H_{10}}}\,x_{\mathrm{NG,C_4H_{10}}} + \tilde{h}_{\mathrm{s,H_2}}\,x_{\mathrm{NG,H_2}}\end{aligned} \tag{3.1}$$

$$w = \frac{\tilde{h}_\mathrm{s}}{\sqrt{\rho_\mathrm{relative}}} \qquad \text{with: } \rho_\mathrm{relative} = \frac{\rho_\mathrm{NG}}{\rho_\mathrm{a,dry}} \tag{3.2}$$

In the European Union, every gas transmission network operator is obligated to publish natural gas quality data for the specific transmission area on a regular basis [50]. In general, transmission network operators continuously quantify the natural gas composition in short intervals, using gas chromatography or nondispersive infrared sensors, to prove the agreement with the defined quality domain. Although the Wobbe-index, higher heating value and relative density are calculated based upon the actual gas composition, a publication and characterization of the individual species domains of the gas composition is not compulsory.

Currently, the harmonization of the European gas quality standards of H-Gas is addressed in the standard DIN EN 16726 with a specification for the relative density between 0.555 and 0.700. Nevertheless, a general Wobbe-index domain is not specified based upon the high variety of regulations in the different member states. Further research and studies are currently beeing conducted to provide the basis for the definition of a general Wobbe-index range. Carbon dioxide contents are limited to 2.5 % at entry and interconnection points. However, a higher limit of up to 4.0 % is valid if connected installations are not affected, for instance, in natural gas underground storage facilities. It should be noted, that the carbon dioxide limitation is not compulsory for Hungary, where the carbon dioxide mole fraction is not directly restricted [11].

[1] The calculation of the higher heating value is related to a temperature level of 25 °C, whereas the calculation of the relative density is related to an air temperature of 0 °C [31].

In Figure 3.1[2], the permitted natural gas domains defined by the Wobbe-index, higher heating value and relative density, are shown for Germany, France and Portugal [31, 51, 52]. The permitted relative density domains are adjusted to match the specification of the DIN EN 16726 [11]. As displayed, the permitted domains overlap significantly. However, in comparison, France currently has the strictest regulations, whereas in Portugal, wider ranges of the Wobbe-index and higher heating value are tolerated.

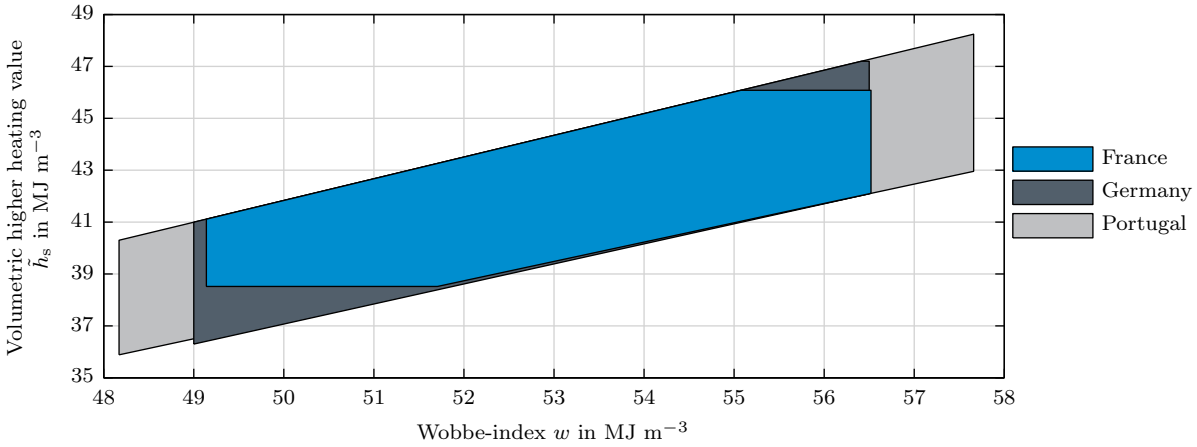

Figure 3.1: Permitted H-gas domains in Germany, France and Portugal[2]

A general limit for the hydrogen addition to the natural gas infrastructure in Europe is currently not specified, since the following issues currently hinder the specification of a general limit: (a) Risk of bacterial growth in underground gas storage; (b) Limitation of maximum hydrogen content of 2 % for steel tanks of natural gas vehicles and gas engines; (c) Maximum hydrogen concentration specification of 1 % for the majority of gas turbines; (d) Incapability of most of the process gas chromatography systems, which are used to prove the compliance with the specified natural gas quality domain, to quantify hydrogen [11].

3.3 Temporally resolved data sets

In this section, measured natural gas data sets from different locations are presented and compared. It should be noted, that the displayed butane contents represent the sum of all higher hydrocarbons containing at least four carbon atoms (C_{4+}).

3.3.1 Saint-Thegonnec - France

In France, a detailed natural gas data set was recorded in 2014 in Saint-Thegonnec using a gas chromatography system with a sampling rate of 30 minutes. The temporally resolved data set is displayed in Figure 3.2[3] [32]. The methane concentrations show high fluctuations with very prominent dips and peaks, especially at the end of September and beginning of December. The annual average of methane is around 91.8 % and the complete fluctuation span between the minimum and maximum concentration is around 7.5 %-points. Ethane has an annual average of around 4.9 % with a high fluctuation span of around 5.3 %-points. The average contents of the remaining species propane, butane, nitrogen and carbon dioxide are each around 1 % or

[2]The corresponding individual limits are listed in Table B.1 in appendix B.

[3]It should be noted, that the data set is incomplete, due to disturbance and maintenance of the equipment. Therefore, only 14096 of the 17856 recorded data points are still feasible for evaluation. For an enhanced visualization, missing data points within a time frame of 24 hours are linear interpolated. However, the interpolated data is not used for further evaluations.

lower. However, excluding butane, the corresponding fluctuations are notably high with around 2 %-points each. As shown, the natural gas data set is highly volatile throughout the entire year, displaying significant changes of the composition.

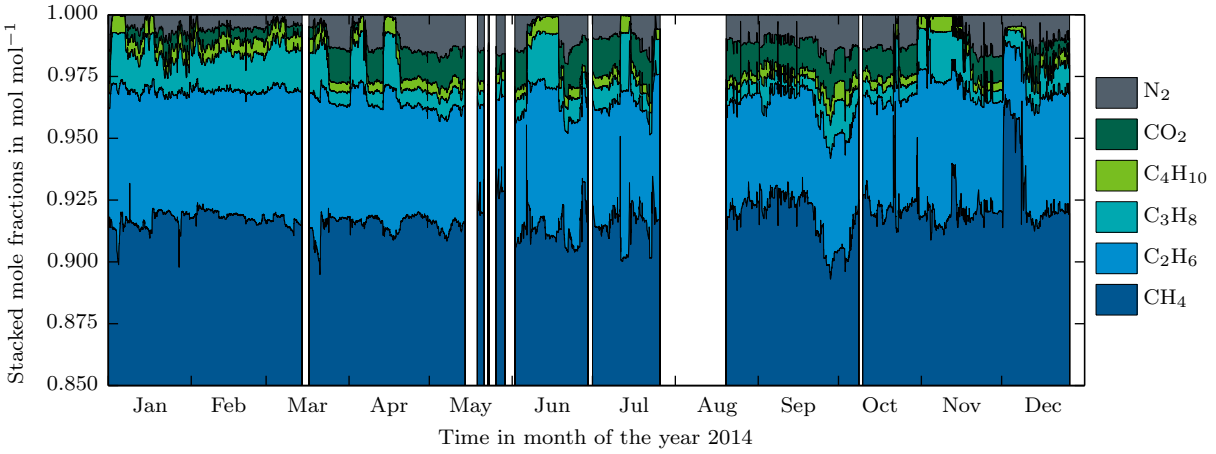

Figure 3.2: Temporally resolved natural gas data set - Saint-Thegonnec 2014[3]

3.3.2 Campo Maior - Portugal

In Portugal, the natural gas quality is continuously analyzed by the transmission network operator in Campo Maior and published as daily average compositions. The temporally resolved data set is shown in Figure 3.3[4] for the time frame between October 2014 to May 2016 [33]. Even though the composition is displayed as a daily average, the composition changes rapidly with very prominent peaks and dips, especially between June and August, 2015. The average methane concentration is around 89.4 % with a complete fluctuation span of around 6.9 %-points between the recorded minimum and maximum. The ethane content has an average of around 7.1 % with an intermediate fluctuation span of roughly 3.9 %-points. Additionally, both carbon dioxide and nitrogen have low average concentrations of around 1 %, however both reach notable fluctuation spans of 1.9 and 3.0 %-points, respectively.

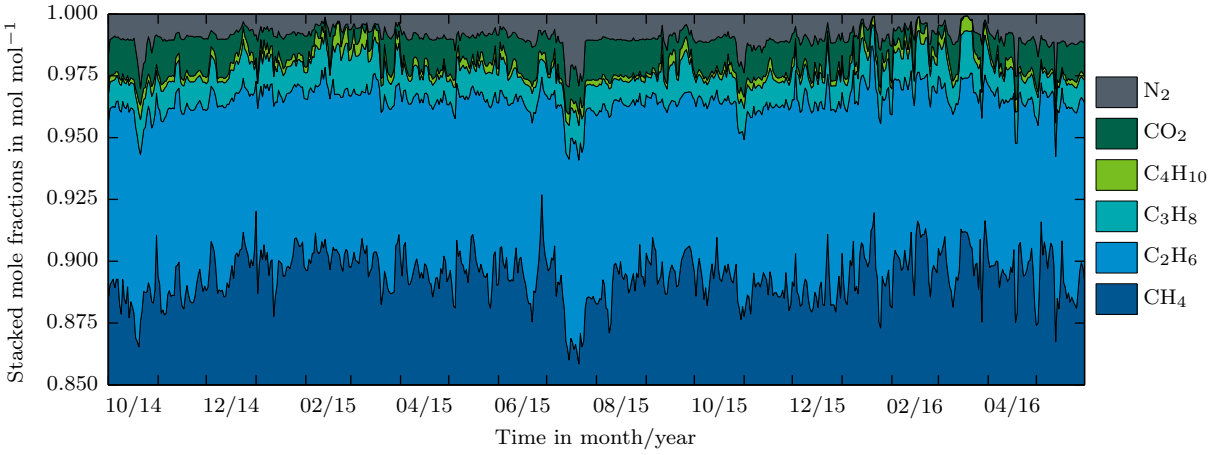

Figure 3.3: Temporally resolved natural gas data set - Campo Maior 2014 - 2016[4]

[4]It should be noted, that 2 of the 609 data points are excluded from the data set, due to a high deviation of the sum of mole fraction to the expected value of 1. For an enhanced visualization, the two excluded data points are linear interpolated. However, the interpolated data points are not used for further evaluations.

3.3.3 Renningen - Germany

In Figure 3.4, the natural gas composition in Renningen is shown for the year 2013 in form of a snapshot analysis of each individual month [34]. Therefore, the temporally resolved data set only consists of twelve data records and the significance is limited. However, the data set still shows remarkable fluctuations in the methane and ethane concentration reaching annual averages of 93.3 and 3.5 %, with minimum to maximum fluctuation spans of around 5.4 and 2.3 %-points, respectively. Additionally, the nitrogen concentration has a notable annual average of 1.5 %, with an intermediate fluctuation span of 1.8 %-points. The annual concentration and fluctuation spans of the remaining species are lower than 1 % and 1 %-point, each.

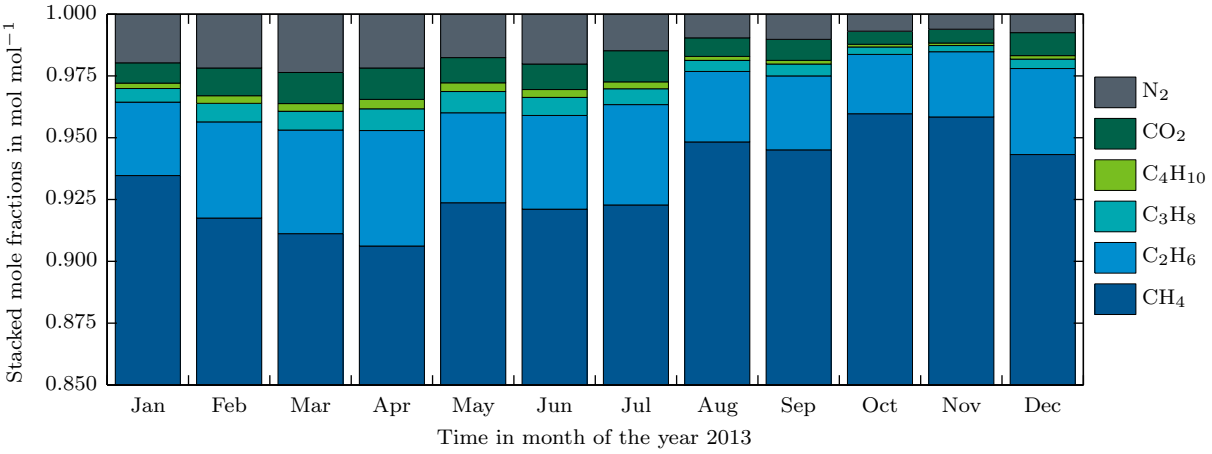

Figure 3.4: Temporally resolved natural gas data set - Renningen 2013

Additionally, the natural gas composition was analyzed throughout the years 2016 and 2017 using an Agilent 7890B gas chromatography system [53]. The results of the analysis are displayed in Figure 3.5 for sampling rates between 30 and 120 minutes among two data points[5]. The gaps in the data set indicate downtime and maintenance of the connected fuel cell system, since natural gas samples are only evaluated if a significant amount of natural gas is consumed at the respective point in time. In each time frame, the distance between two ticks on the x-axis represents 24 hours. It should be noted, that the gas chromatography system setup is not designed to accurately quantify the sum of higher hydrocarbons containing at least four carbon atoms. Therefore, in accordance with the previously analyzed data sets with butane contents of lower than 1 %, higher hydrocarbon contents are neglected during data sampling. Even during small sampling periods of several days, significant fluctuations of the natural gas composition occur. In comparison to the previous data set from 2013, the average methane composition is very similar reaching 93.7 %, whereas the fluctuation span is slightly higher, being equivalent to 5.8 %-points. Additionally, the average ethane content and fluctuation span are noticeable higher, with values of 4.0 % and 3.3 %-points, respectively. The average contents of nitrogen and carbon dioxide are each around 1.0 %, but both show high fluctuation spans of 2.3 and 1.6 %-points, respectively. The high average nitrogen concentration of the year 2013 is not present in a comparable magnitude. However, the large fluctuation span of nitrogen indicates, that a higher average value throughout the year is possible. The average propane content and

[5]The varying sampling times are a result of the mode of operation of the gas analyzing system, including the possibility of the successive analysis of up to four different system sampling points. In particular, those four sampling points are located at the natural gas and reformer inlet, as well as at the reformer and anode outlet, as described in detail in section 4.4.1. Additionally, two recorded valid data samples in June and September are not displayed in the Figure 3.5, since the total consecutive sampling duration was less than 24 hours. However, the data records are used for further evaluations.

fluctuation span closely matches the data from 2013 with values of 0.4 % and 1.1 %-points, respectively.

However, comparing the resolution of the two data sets reveals two inconsistencies, reducing the significance of the conducted detailed comparing analysis. First, the data set from 2013 only consists of a single snapshot analysis of the gas composition for each month of the year. Second, the data sets from the years 2016/2017 have high resolution, but were only conducted for limited periods. Therefore, it has to be concluded, that both data sets show a strong match considering the low resolution of the 2013 data set and the incompleteness of the 2016/2017 data sets. It should be noted, that for the purpose of simplification, the Renningen 2016/2017 data sets are referred to as the Renningen 2016 data set.

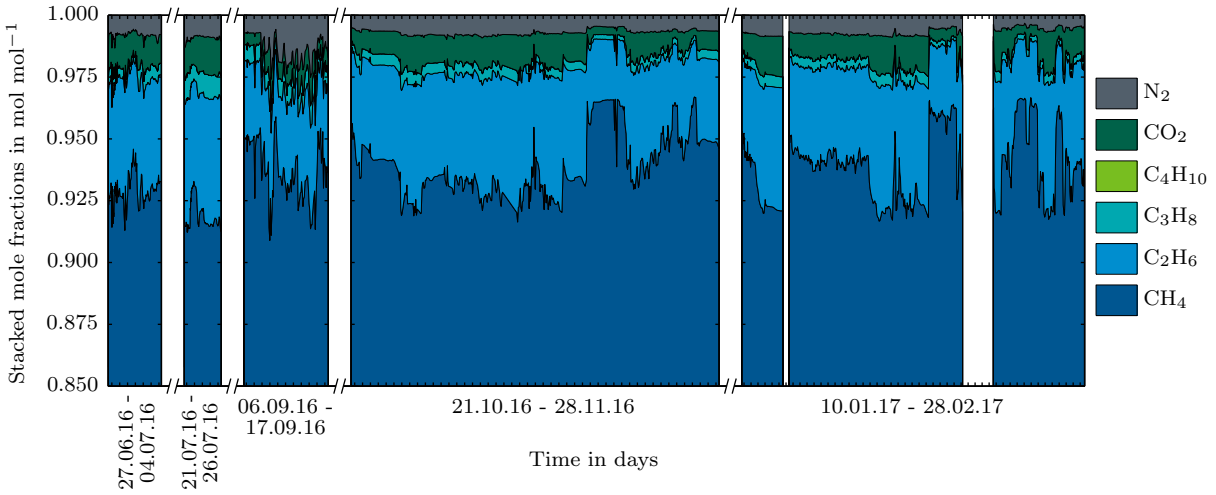

Figure 3.5: Temporally resolved natural gas data set - Renningen 2016 and 2017

3.3.4 Comparison

In addition to the previously displayed data sets, four further temporally resolved European natural gas data sets are added to increase the significance of the comparison. The evaluated natural gas data sets are listed in Table 3.1[6], listing location, start and end date of data recording, resolution of measurement, and number of total recorded and further evaluated data points [32, 33, 34, 35, 36, 37, 38]. It should be noted, that data points are excluded from the data sets if the absolute deviation of the sum of the mole fraction to the expected value of 1 is higher than ± 0.00025. The resulting comparison of the concentration domains of the different locations for each individual natural gas species is displayed in Figure 3.6, highlighting the minimum, maximum and average values of the data set, as well as the 95 % confidence interval [32, 33, 34, 35, 36, 37, 38].

As shown in the first graph in Figure 3.6, the methane mole fraction has high minimum to maximum fluctuation intervals. The only exception is Imatra, which has a very low fluctuation domain due to its special location and the grid topology in Finland. Imatra is the only physical interconnection point of Finland, connecting it to an external transmission network, in particular the Russian grid [54]. Therefore, high and stable concentrations of methane around 96.7 % with a fluctuation span of only 2.3 %-points are present, since natural gas is only delivered from Russia. The other locations are partially subjected to very high methane fluctuation spans between 3.3 and 15.1 %-points, with average contents between 89.2 and 93.7 %. Nevertheless,

[6]It should be noted, that the data sets represent a single point or specific zone in the natural gas grid during a limited or chosen period of time. Therefore, the shown data can not be used for an overall generalization of the situation in an entire country or complete grid area of a transmission network operator.

Table 3.1: Overview of evaluated temporally resolved European natural gas data sets

Location	Country	Measurement period	Resolution	Number of data points	Evaluated data points
Saint-Thegonnec	France	01.2014 - 12.2014	30 minutes	17856	14096
Campo Maior	Portugal	10.2014 - 05.2016	Daily average	609	607
Renningen	Germany	01.2013 - 12.2013	Monthly snapshot	12	12
Renningen	Germany	06.2016 - 02.2017	30 - 120 minutes	1466	1466
Egtved	Denmark	01.2014 - 12.2014	60 minutes	8760	8747
Gent	Belgium	01.2014 - 01.2014	60 minutes	744	744
Imatra	Finland	06.2014 - 05.2016	Daily average	731	686
Unspecified	Hungary	01.2014 - 12.2014	Hourly average	8759	8759

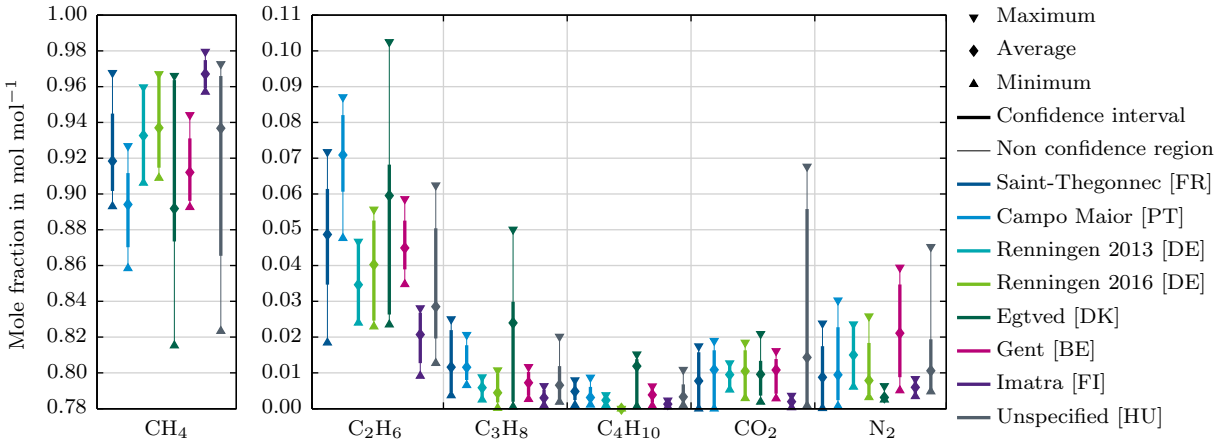

Figure 3.6: Comparison of natural gas compositions for temporally resolved European natural gas data sets including 95 % confidence interval

focusing on the 95 % confidence region, clarifies that methane concentrations below 86.5 % and above 97.5 % are very uncommon.

As displayed in the second graph in Figure 3.6, the ethane concentrations are also highly volatile ranging from a minimum of 0.9 % to a maximum of 10.2 % throughout all data sets. However, the 95 % confidence region shows a slightly reduced range between 1.3 and 8.2 %. Although, the absolute ethane mole fraction is only roughly a tenth of the methane concentration, the fluctuation is still comparable, with average concentration values between 2.1 and 7.1 %. An exceptional high average mole fraction is present in Campo Maior, possibly due to its close proximity to the liquefied natural gas terminal in Sines, Portugal [55].

Except in Egtved, propane contents range from 0.1 to 2.5 %, with low average values between 0.3 and 1.2 %. Additionally, excluding the Hungarian location, the 95 % confidence intervals are only insignificantly lower than the total minimum to maximum range, underlining the high stability of the propane mole fraction. In Egtved, the average, the maximum, and the maximum of the 95 % confidence interval is clearly higher based upon the increased propane contents of natural gas originated from the Danish north sea [31]. This statement is also applicable to the butane contents. Therefore, a similar trend can be identified, showing above average values of butane in Egtved. Excluding the Egtved and the Renningen 2016 data sets, the butane contents are always lower than roughly 1.1 % with very low average values between 0.1 and 0.5 %.

Excluding the Hungarian data set, which has an above average maximum carbon dioxide concentration, the confidence intervals of the carbon dioxide mole fraction range from 0.0 up to 1.6 %. However, the average value of the Hungarian data set matches the magnitude of the other data sets, with values between 0.2 and 1.4 %. The overall low and comparable average contents verify the high density of data points below carbon dioxide concentrations of roughly 1.5 %. Analogous to the methane concentration, Imatra has very low carbon dioxide contents, due to the general small mole fractions of carbon dioxide in natural gas originated from Russia [31].

Lastly, nitrogen contents range from 0.0 up to 4.5 %. The average concentrations alternate between 0.3 and 2.1 %, ultimately outlining the intermediate volatility and significant difference between the evaluated locations. Very low overall nitrogen contents, with small confidence regions, are present in Egtved and Imatra, due to the previously mentioned general composition of natural gas originating either from the Danish north sea or Russia [31]. Omitting the Gent data set, intermediate average contents and confidence interval domains of nitrogen are occurring. In Gent, the average value and the maximum of the confidence interval is above average, possibly due to the high number of interconnection points of the Belgium gas grid to adjacent countries. As a result, natural gas in Belgium is a mixture of natural gas originated from a high variety of different locations, such as the Netherlands, Norwegian and United Kingdom, as well as liquefied natural gas from various locations [56].

In conclusion, methane and ethane show the highest fluctuation domains, whereas the butane and carbon dioxide contents are in general very stable. The comparison outlines, that the natural gas composition in central Europe is highly volatile, including variable magnitudes in various locations. The fluctuation is a result of the high number of interconnections in the European gas grid and the large variety of different supplying origins of natural gas. Additionally, the comparison clarifies, that not a single one of the analyzed natural gas data sets includes any quantifiable amounts of oxygen, carbon monoxide, water vapor or hydrogen. Therefore, as previously stated, natural gas can be considered a mixture of six main species - methane, ethane, propane, sum of higher hydrocarbons containing at least four carbon atoms C_{4+} (represented by butane), carbon dioxide and nitrogen. However, hydrogen is further considered for the sake of the evaluation of possible hydrogen additions to the natural gas grid in the future.

In Figure 3.7, the evaluated natural gas data base is compared to the permitted H-gas domain in Germany, using the volumetric higher heating value and Wobbe-index.

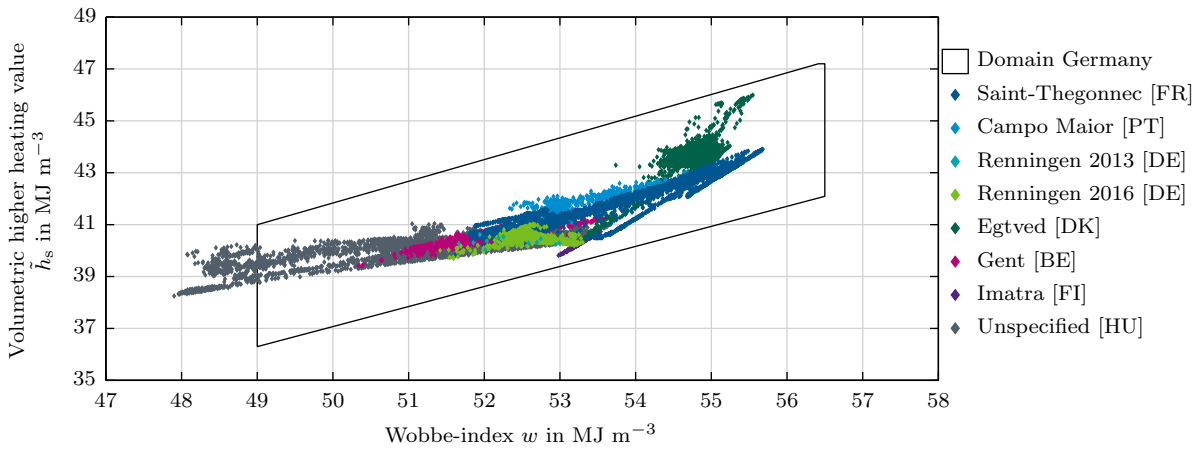

Figure 3.7: Permitted H-gas domain in Germany with evaluated natural gas data

As outlined in Figure 3.7, except parts of the Hungarian data set, the entire collected data base is fulfilling the regulatory framework in Germany, which was previously introduced in section 3.2. The Hungarian data set is partially exceeding the lower boundary of the permitted

domain, based upon the occurring above average carbon dioxide fractions. The high carbon dioxide fractions yield a combination of low higher heating values and large relatively densities, ultimately resulting in low Wobbe-indicies. Figure 3.7 also highlights, that the evaluated data base covers a significant area of the permitted H-gas domain in Germany. Therefore, the data base is considered viable for the derivation of general natural gas constraints, as outlined in section 3.4.3.

3.4 Gas coefficients

3.4.1 Definition

In addition to the six previously mentioned major components of natural gas, hydrogen is also included based upon an evaluation of possible hydrogen feeds to the natural gas grid. For the purpose of simplification, each natural gas composition can be defined with the help of five gas coefficients. The carbon, oxygen, hydrogen (K_{H}) and nitrogen (K_{N}) gas coefficients can be calculated based upon the concentration of each species and the related number of atoms contained by the species. The calculation constraints of the gas coefficients are shown in equations (3.3), (3.4), (3.5) and (3.6), using the number of atoms per molecule, which are listed in Table 3.2. The electron coefficient is defined, as displayed in equation (3.7), using the number of releasable electrons of the complete electrochemical conversion per species, as shown in Table 3.2. In conclusion, each coefficient defines the amount of atoms of a certain species or releasable electrons contained in the respective natural gas mixture. The coefficients are used to exactly classify and cluster different mixtures of natural gas. Therefore, two mixtures with identical gas coefficient will lead to analogous fuel cell system responses, even if the chemical composition of the mixtures is different.

$$K_{\mathrm{C}} = \sum_i x_{\mathrm{NG},i}\, N_{\mathrm{C},i} = x_{\mathrm{NG,CH_4}} + 2\, x_{\mathrm{NG,C_2H_6}} + 3\, x_{\mathrm{NG,C_3H_8}} + 4\, x_{\mathrm{NG,C_4H_{10}}} + x_{\mathrm{NG,CO_2}} \tag{3.3}$$

$$K_{\mathrm{O}} = \sum_i x_{\mathrm{NG},i}\, N_{\mathrm{O},i} = 2\, x_{\mathrm{NG,CO_2}} \tag{3.4}$$

$$K_{\mathrm{H}} = \sum_i x_{\mathrm{NG},i}\, N_{\mathrm{H},i} = 4\, x_{\mathrm{NG,CH_4}} + 6\, x_{\mathrm{NG,C_2H_6}} + 8\, x_{\mathrm{NG,C_3H_8}} + 10\, x_{\mathrm{NG,C_4H_{10}}} + 2\, x_{\mathrm{NG,H_2}} \tag{3.5}$$

$$K_{\mathrm{N}} = \sum_i x_{\mathrm{NG},i}\, N_{\mathrm{N},i} = 2\, x_{\mathrm{NG,N_2}} \tag{3.6}$$

$$K_{\mathrm{e^-}} = \sum_i x_{\mathrm{NG},i}\, N_{\mathrm{e^-},i} = 8\, x_{\mathrm{NG,CH_4}} + 14\, x_{\mathrm{NG,C_2H_6}} + 20\, x_{\mathrm{NG,C_3H_8}} + 26\, x_{\mathrm{NG,C_4H_{10}}} + 2\, x_{\mathrm{NG,H_2}} \tag{3.7}$$

Applying the definition of the gas coefficients to the temporally resolved data base yields a more generic comparison. As displayed in Figure 3.8, in general, the lower the amount of nitrogen and the higher the content of hydrocarbons with more than one carbon atom, the higher the carbon coefficient. Therefore, Saint-Thegonnec, Campo Maior and Imatra data show high average carbon coefficients between 1.08 and 1.14. The previous statement can also be applied

Table 3.2: Number of carbon, oxygen, hydrogen and nitrogen atoms, as well as releasable electrons of different species

Species i	Number of carbon atoms $N_{\mathrm{C},i}$	Number of oxygen atoms $N_{\mathrm{O},i}$	Number of hydrogen atoms $N_{\mathrm{H},i}$	Number of nitrogen atoms $N_{\mathrm{N},i}$	Number of releasable electrons $N_{\mathrm{e}^-,i}$
CH_4	1	0	4	0	8
C_2H_6	2	0	6	0	14
C_3H_8	3	0	8	0	20
C_4H_{10}	4	0	10	0	26
CO_2	1	2	0	0	0
N_2	0	0	0	2	0
H_2	0	0	2	0	2

to the hydrogen coefficient, with the exception that the higher the carbon dioxide contents, the lower the hydrogen coefficient, since carbon dioxide does not contain any hydrogen atoms. The effect has the highest impact on the Hungarian data set, because the carbon dioxide contents are above average. Therefore, the hydrogen coefficient reaches very low values up to only 3.80. However, the average hydrogen coefficients range in a dense domain between 4.00 and 4.24. The oxygen and nitrogen gas coefficients are directly correlated to a single species, either carbon dioxide or nitrogen, and therefore match the concentration domains in Figure 3.6. The electron coefficient has an identical progression to the hydrogen coefficient, because both coefficients are calculated using the same species.

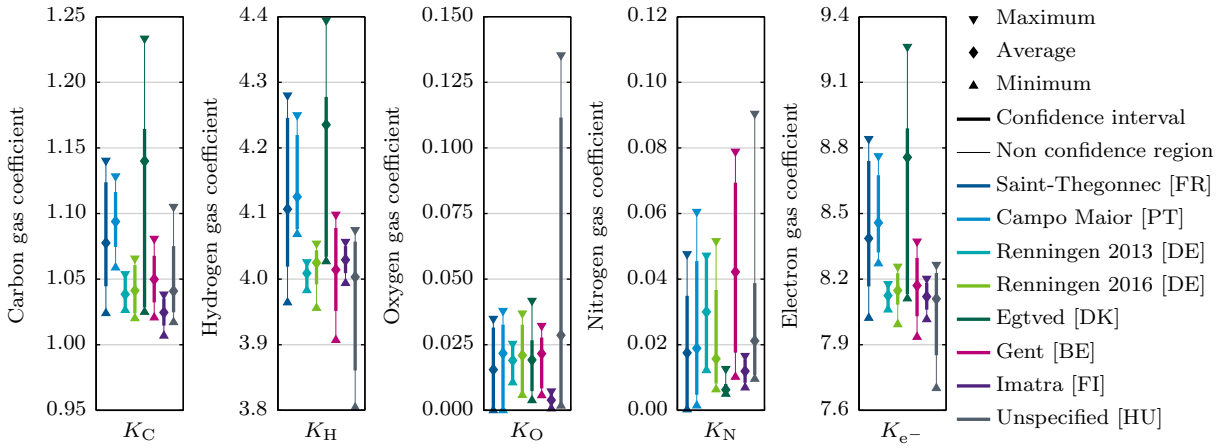

Figure 3.8: Comparison of natural gas coefficients for temporally resolved European natural gas data sets including 95 % confidence interval

In contrast to Figure 3.8, a more broad evaluation, highlighting the concurrency of the data sets, is shown in Figure 3.9. The concurrency of the data sets is included by calculating the individual ratios between the hydrogen, oxygen, nitrogen or electron gas coefficients and the carbon gas coefficients. As displayed in Figure 3.9, the higher the amount of higher hydrocarbons or carbon dioxide, the lower the hydrogen and electron to carbon gas coefficient ratios. Compared to methane, higher hydrocarbons have lower hydrogen atom and electron to carbon atom ratios. Additionally, carbon dioxide contains carbon atoms, but is neither contributing hydrogen atoms nor electrons. The effect is most apparent in the Egtved, Imatra and Hungarian data sets,

having very high or low higher hydrocarbons contents or very high fractions of carbon dioxide, respectively. The oxygen and nitrogen to carbon gas coefficient ratios are both low and follow the previously displayed concentration domains, once again. Focusing on the 95 % confidence interval, the evaluation clarifies, that the hydrogen and electron to carbon coefficient ratio have the widest domains ranging from 3.64 to 3.95 and 7.44 to 7.90. As a result, the high volatility of the natural gas composition is emphasized once more.

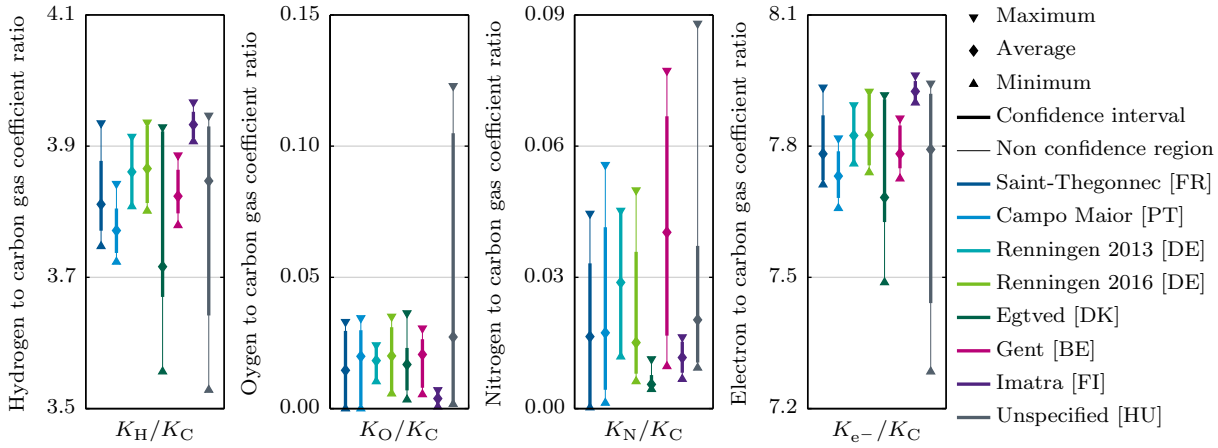

Figure 3.9: Comparison of natural gas coefficient ratios for temporally resolved European natural gas data sets including 95 % confidence interval

3.4.2 Constraints

In this subsection, three major constraints, using the relation between the natural gas composition and the gas coefficients, are introduced. The constraints will be applied for further calculations. It should be noted, that all three constraints are also valid for natural gas mixtures including hydrogen. First, the sum of all mole fractions has to be equal to one. The sum can also be expressed with the help of the gas coefficients, as shown in equation (3.8)[7].

$$\sum_i x_{\mathrm{NG},i} = 1 = \frac{K_\mathrm{H}}{2} - K_\mathrm{C} + K_\mathrm{O} + \frac{K_\mathrm{N}}{2} \tag{3.8}$$

Second, the electron coefficient can be expressed as a function of the hydrogen, carbon and oxygen coefficients based upon a species balance, as illustrated in equation (3.9)[8].

$$K_{\mathrm{e}^-} = K_\mathrm{H} + 4\,K_\mathrm{C} - 2\,K_\mathrm{O} \tag{3.9}$$

Third, both previously derived constraints can be applied to express the molar mass of natural gas (M_NG) as a function of the carbon, oxygen and electron gas coefficients, as well as the molar mass of carbon, hydrogen, oxygen and nitrogen atoms, as outlined in equation (3.10)[9].

$$M_\mathrm{NG} = (M_\mathrm{C} - 4\,M_\mathrm{H} + 6\,M_\mathrm{N})\,K_\mathrm{C} + (M_\mathrm{H} - M_\mathrm{N})\,K_{\mathrm{e}^-} + (M_\mathrm{O} + 2\,M_\mathrm{H} - 4\,M_\mathrm{N})\,K_\mathrm{O} + 2\,M_\mathrm{N} \tag{3.10}$$

[7]The derivation of equation (3.8) is outlined in equation (C.1) in appendix C.1.
[8]The derivation of equation (3.9) is outlined in equation (C.2) in appendix C.2.
[9]The derivation of equation (3.10) is outlined in appendix C.3.

3.4.3 Correlations

3.4.3.1 Higher heating value and electron gas coefficient

Comparing equations (3.1) and (3.7) emphasizes that both computations depend on identical species. Excluding hydrogen, the quotient between the higher heating value or number of releasable electrons of a specific species and methane is an almost constant value for each individual species, as shown in Table (3.3)[10]. Methane is chosen as the reference since it is the major compound of natural gas. As a result, by neglecting possible hydrogen contents in natural gas, a direct correlation between the electron coefficient and higher heating value can be derived, as illustrated in equation (3.11). Even though hydrogen was neglected from the derivation, equation (3.11) can be applied in good approximation for natural gas mixtures, with hydrogen contents lower than 10 %, because the occurring error between calculated and exact value of the electron coefficient is lower than 1 %.

$$\frac{K_{\mathrm{e}^-}}{h_{\mathrm{s}}} = \frac{\sum_i x_{\mathrm{NG},i}\, N_{\mathrm{e}^-,i}}{\sum_i x_i\, h_{\mathrm{s},i}} \rightarrow K_{\mathrm{e}^-} \sim \frac{N_{\mathrm{e}^-,\mathrm{CH_4}}}{h_{\mathrm{s,CH_4}}}\, h_{\mathrm{s}} \sim 8.9831 \cdot 10^{-6}\, \frac{\mathrm{mol}}{\mathrm{J}}\, h_{\mathrm{s}} \tag{3.11}$$

Table 3.3: Quotient between the higher heating value or number of releasable electrons of a specific species and methane

Species i	Higher heating value $h_{\mathrm{s},i}$ in $\mathrm{J\,mol}^{-1}$	Higher heating value ratio $h_{\mathrm{s},i}/h_{\mathrm{s,CH_4}}$	Number of releasable electrons ratio $N_{\mathrm{e}^-,i}/N_{\mathrm{e}^-,\mathrm{CH_4}}$
CH_4	890564.87	1.000	1.000
C_2H_6	1560649.46	1.752	1.750
C_3H_8	2219153.34	2.492	2.500
C_4H_{10}	2877529.38	3.231	3.250
CO_2	0	0	0
N_2	0	0	0
H_2	285828.35	0.321	0.250

Applying equation 3.11 to the entire Saint-Thegonnec data set shows the high accuracy of the approach based upon the low relative deviations between the approximated and exact value of the electron coefficients between -0.0160 and 0.0073 %, respectively. In general, the higher the propane and butane contents, the higher the negative deviation, since the higher heating value ratios are slightly lower than the number of releasable electrons ratios. The positive deviation is a result of the slightly positive deviation of the higher heating value ratio compared to the releasable electron ratio of ethane. Therefore, data sets with high ethane and low propane and butane content, lead to the highest positive deviation from the calculated value of the electron coefficient.

For the purpose of validation, linear regression is applied to a combined natural gas data set, including Saint-Thegonnec, Campo Maior, Renningen 2013, Egtved, Gent, Imatra and the unspecified Hungarian location. As a result, the electron coefficient is expressed as a function of the higher heating value, as shown in Figure 3.10 and equation (3.12). Additionally, the Renningen 2016 data set is used to independently validate the linear regression approach, verifying the applicability.

[10] The higher heating values are calculated based upon the enthalpy of reaction, computed using the thermochemical data base of reaction model USC-Mech II and liquid water for a temperature of 25 °C and 101325 Pa [57]. A description of the USC Mech II is given in section 4.3.1. The number of releasable electrons per species are listed in Table 3.2.

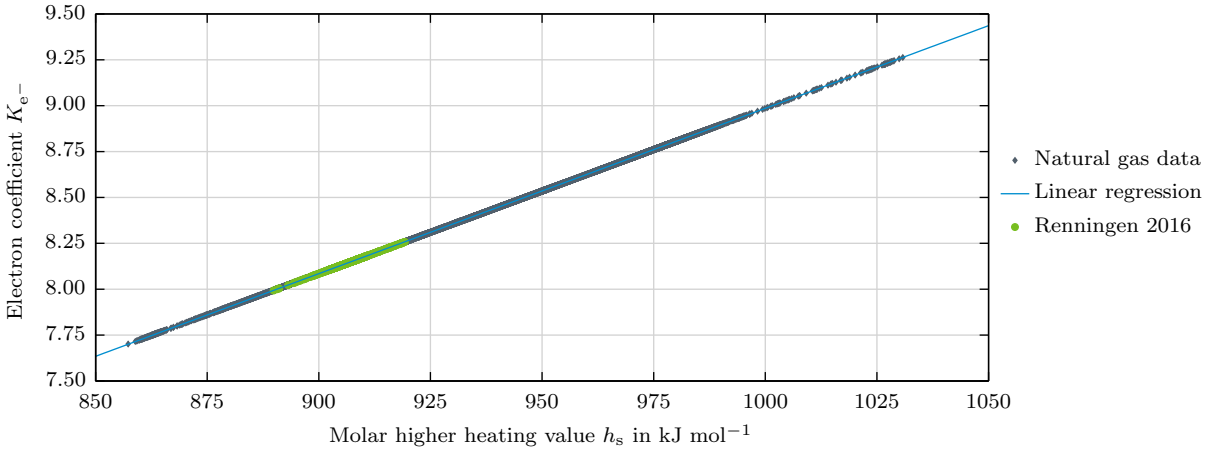

Figure 3.10: Linear regression of molar higher heating value and electron gas coefficient

$$K_{e^-} = 9.0077 \cdot 10^{-6} \frac{\text{mol}}{\text{J}} h_s - 0.02217 \tag{3.12}$$

The evaluation clarifies, that the theoretically deduced equation (3.11) and the empiric derived regression (3.12) are fundamentally matching. Applying the regression equation (3.12) to the entire Saint-Thegonnec data set also shows low relative deviations of -0.0063 up to 0.0208 % between the approximated and calculated values of the electron coefficient, respectively. Therefore, both the derived equation (3.11) and the regression approach (3.12) are feasible for the approximation of the electron coefficient based upon the determination of the higher heating value.

3.4.3.2 Change in molar quantity and electron coefficient

As introduced in equation (3.9), the electron coefficient can be exactly calculated as a function of the hydrogen, carbon and oxygen coefficients. However, as shown for the combined natural gas data set in Figure 3.11, the electron coefficient can be expressed in good approximation using only a relation to the carbon and oxygen coefficients, based upon equation (3.13). Additionally, according to equation (2.15), the relation between the carbon and oxygen coefficients can be replaced with the change in molar quantity coefficient. As illustrated in Figure 3.11 and Table 3.4[11], three different regression approaches are applied to the combined data set to represent the change in molar quantity coefficient as a function of the electron coefficient. As displayed in Table 3.4, all regression approaches achieve coefficients of determination of higher than 0.99, and can therefore be considered applicable. Additionally, the maximum of the negative and positive values of the relative error between the regression data and the calculated value of the change in molar quantity coefficient have only slightly different magnitudes. An exceptional superiority of a single regression approach can not be identified using the relative error. Nevertheless, the quadratic regression approach is chosen for further evaluation, since it achieves high accuracy even at the boundaries of the data set, and enhanced extrapolation capabilities outside of the evaluated data range based upon the intermediate slope. Additionally, the absolute frequency of the error of the quadratic regression approach has the highest count of data points in the deviation interval between -0.5 and 0.5 %, showing the slightly enhanced accuracy. It should be noted, that the Hungarian natural gas data set is causing the high negative error margin of

[11] The corresponding coefficients of the linear, quadratic and power regression approach a_1 - a_8 are shown in appendix D.1.

-1.79 %, based upon the exceptional high carbon dioxide contents. Carbon dioxide is the only electrochemically inactive gas component that contains carbon atoms. Therefore, comparing two natural gas compositions with the same electron coefficient, one with high and one with low carbon dioxide content, clarifies that the one with the higher carbon dioxide content needs to have an increased higher hydrocarbon content to compensate for the lack of electrons. In contrast to methane, higher hydrocarbons have a lower releasable electron to carbon atom ratio. As a result, gas mixtures with higher carbon dioxide fractions can have identical electron coefficients, compared to gases with no or low carbon dioxide content, but at the expense of higher carbon coefficients. The influence can also be seen in equation (3.13), where the carbon dioxide content is eliminated from the calculation but is indirectly influencing the result due to the mole fraction constraint, displayed in equation (3.8). Excluding the Hungarian data set, the negative deviation of the remaining data sets between the approximated and calculated values of the change in molar quantity coefficient is always lower than -1 %. Additionally, as also displayed in Figure 3.11, the $K_{\triangle\mathrm{an}}$ values of the Renningen 2016 data set are used to independently validate the regression approaches, verifying the good applicability.

$$\begin{aligned} K_{\triangle\mathrm{an,LR/QR/PR}} = f(K_{\mathrm{e}^-}) \sim K_{\triangle\mathrm{an}} &= 2\,K_{\mathrm{C}} - K_{\mathrm{O}} \\ &= 2\,(x_{\mathrm{NG,CH_4}} + 2\,x_{\mathrm{NG,C_2H_6}} + 3\,x_{\mathrm{NG,C_3H_8}} + 4\,x_{\mathrm{NG,C_4H_{10}}}) \end{aligned} \tag{3.13}$$

Table 3.4: Coefficient of determination and maximum and minimum of deviation of regression approaches between the electron gas and change in molar quantity coefficients[11]

Regression approach	Linear - LR	Quadratic - QR	Power - PR
Formula: $K_{\triangle\mathrm{an,LR/QR/PR}} =$	$a_1\,K_{\mathrm{e}^-} + a_2$	$a_3\,(K_{\mathrm{e}^-})^2 + a_4\,K_{\mathrm{e}^-} + a_5$	$a_6\,(K_{\mathrm{e}^-})^{a_7} + a_8$
Coefficient of determination	0.9937	0.9952	0.9952
Maximum positive deviation to calculated value of $K_{\triangle\mathrm{an}}$ in %	0.6355	0.8917	0.8843
Maximum negative deviation to calculated value of $K_{\triangle\mathrm{an}}$ in %	-1.9865	-1.7881	-1.7921

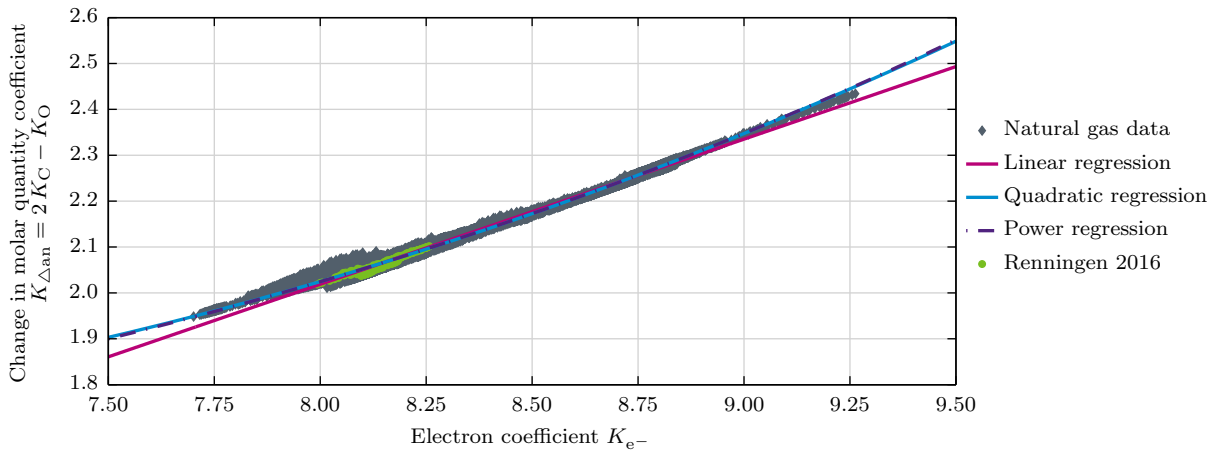

Figure 3.11: Regression between electron gas and change in molar quantity coefficients

In addition to the change in molar quantity coefficient, another reoccurring coefficient for the calculation of SOFC system parameters is a combination of the carbon and oxygen gas

coefficients, as well as the oxygen-to-carbon ratio ($\Phi\, K_\mathrm{C} - K_\mathrm{O}$), as used for the calculation of the recirculation ratio in equation (2.2). For the purpose of the simplification, the combined coefficient ($\Phi\, K_\mathrm{C} - K_\mathrm{O}$) is abbreviated as K_Φ. Multiple linear regression is applied to derive a correlation between the electron coefficient and the oxygen-to-carbon ratio dependent combined gas coefficient K_Φ for different Φ values[12]. The basis for the regression is the combined natural gas data set from all locations. The resulting equation of the multiple linear regression approach, for varying Φ values between 1.5 and 2.5, is shown in equation (3.14)[13]. In Figure 3.12, the calculated K_Φ and the multiple linear regression curves are shown for three different Φ values.

$$K_\Phi = \Phi\, K_\mathrm{C} - K_\mathrm{O} \sim K_{\Phi,\mathrm{MLR}} = f(K_{\mathrm{e}^-}, \Phi) = a_9 + a_{10}\, K_{\mathrm{e}^-} + a_{11}\, \Phi + a_{12}\, \Phi\, K_{\mathrm{e}^-} \tag{3.14}$$

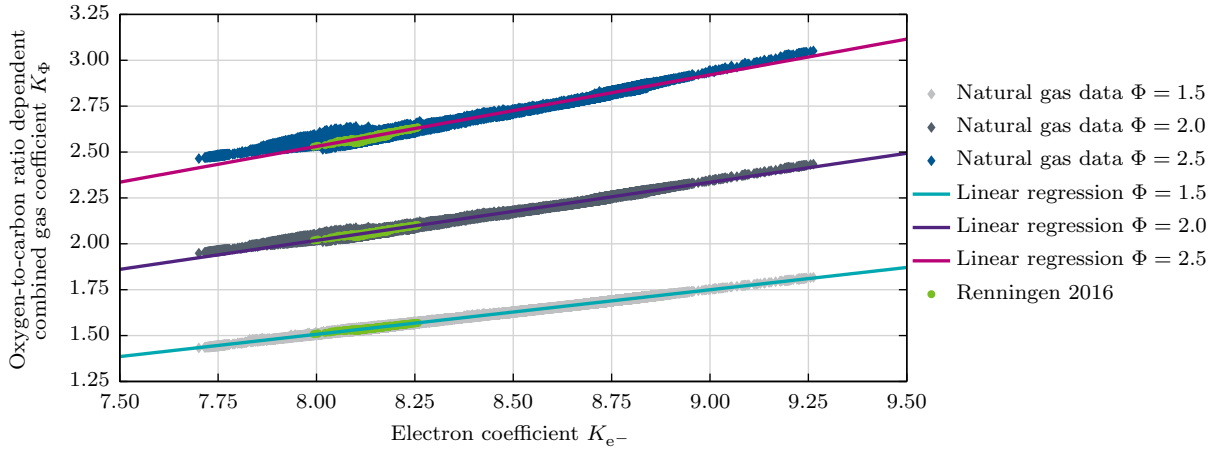

Figure 3.12: Multiple linear regression between electron and oxygen-to-carbon ratio dependent combined gas coefficients

As displayed in Figure 3.12, a strong approximation of the K_Φ is achieved throughout the entire Φ range. However, with an increasing Φ, the deviations between the data base and the regression curves are higher. The increased spread can be explained by using equations (3.7) and (3.8) to express the K_Φ as a function of only the methane, ethane, propane and nitrogen concentrations, as displayed in equation (3.15). As shown, for a fixed electron coefficient and Φ of 1.5, the K_Φ is only dependent on the nitrogen mole fraction. Therefore, the spread of the data base is very low due to the low absolute amounts and fluctuation domains of nitrogen, as previously introduced in Figure 3.6. Except for Φ of 1.5, the spread of the data base is increasing for rising Φ values. The effect is especially visible for electron coefficients around 8, due to the high variety of possible natural gas compositions in this domain. The progression can also be explained with the help of equation (3.15), since methane and ethane contents are highly volatile. Therefore, they have a direct impact on the deviation interval of K_Φ for fixed Φ values.

$$\begin{aligned} K_\Phi = \Phi\, K_\mathrm{C} - K_\mathrm{O} = {} & \frac{K_{\mathrm{e}^-}}{26}\,(3\,\Phi + 2) + \frac{2}{13}\,(3\,x_{\mathrm{NG,CH_4}} + 2\,x_{\mathrm{NG,C_2H_6}} + x_{\mathrm{NG,C_3H_8}})\,(3 - 2\,\Phi) \\ & + \left(1 - x_{\mathrm{NG,N_2}}\right)(\Phi - 2) \end{aligned} \tag{3.15}$$

[12] It should be noted, that K_Φ and $K_{\triangle\mathrm{an}}$ are equal for an oxygen-to-carbon ratio of 2 and the previous chosen quadratic regression approach can be applied for a slightly higher accuracy. The multiple linear regression for an oxygen-to-carbon ratio of 2 results in the previously introduced linear regression shown in Figure 3.11.

[13] The corresponding coefficients of the multiple linear regression approach a_9 - a_{12} are shown in appendix D.2.

Nevertheless, in the entire evaluated Φ range, the relative error between the directly calculated and regression data is always lower than -3 to 1 %, respectively. As a result, the multiple regression approach can be applied for Φ values between 1.5 and 2.5 with sufficient accuracy. Additionally, as also shown in Figure 3.12, K_Φ values of the Renningen 2016 data set are used to independently validate the regression approach, displaying a high match for the entire evaluated Φ range.

Consequently, a relation of all SOFC system parameters to a single natural gas variable, the electron gas coefficient, is achieved. Additionally, by applying the relation between the electron coefficient and the higher heating value, a direct calculation based upon the higher heating value is also possible. Therefore, even for fluctuating natural gas qualities, ideal system behavior can be achieved based upon the determination of a single natural gas coefficient.

3.5 Thermodynamic effects

In this subsection, the effects of varying natural gas qualities on the specific reformer heat flow rate, cell voltage and carbon deposition tendency are evaluated.

The specific reformer heat flow rate in relation to the molar flow rate of natural gas is calculated, as shown in equation (3.16). The equation is based upon an isothermal reformer enthalpy balance applying the system mass and molar balance equations, introduced in subsection 2.2.2.1 and 2.2.2.2. The recirculation rate, the change in molar quantity, as well as the molar masses and molar enthalpy at the reformer inlet and outlet can be computed for a designated natural gas composition, oxygen-to-carbon ratio and fuel utilization factor of the stack using equilibrium states at the reformer and anode outlet for a given pressure and temperature. Additionally, applying equation (2.4) to equation (3.16) yields equation (3.17), which expresses the reformer heat flow rate in relation to the only remaining independent system variables, the electric current and number of cells. As shown in Figure 3.13a, the combined natural gas data set is used to compute the minimum, average and maximum of the specific reformer heat flow rate in relation to the current and number of cells for a given reformer inlet and outlet temperature between 500 and 700 °C, $U_{\mathrm{f,S}}$ between 0.6 and 0.8, as well as a fixed Φ of 2. The molar mass and specific enthalpy at the reformer inlet is calculated based upon the composition at this system point, which is computed using the natural gas and anode outlet concentration. The equilibrium state at the anode outlet is calculated based upon a temperature of 800 °C and a pressure of 101325 Pa. As displayed in Figure 3.13a, focusing on each $U_{\mathrm{f,S}}$, varying natural gas quality only has a moderate impact on the reformer heat flow rate in an ideal system with a constant reformer temperature, demonstrated by the small spread between the minimum and maximum value for any given temperature. An increasing $U_{\mathrm{f,S}}$ yields higher specific heat flow rates for temperatures below 600 °C and lower ones for temperatures above 600 °C, respectively. For a given gas composition, the equilibrium states at the reformer are only dependent on the temperature, pressure and Φ. Therefore, for varying $U_{\mathrm{f,S}}$ values, the resulting equilibrium states are equal, since the determining variables are identical. At low reformer temperatures, the gap between the equilibrium and reformer inlet composition is only nominal for low $U_{\mathrm{f,S}}$. Therefore, specific heat flow rates are low. However, with a rising reformer temperature, the difference between the reformer inlet and equilibrium composition changes drastically. In the range above 600 °C, low $U_{\mathrm{f,S}}$ values yield higher specific heat flow rates based upon the higher total amounts of hydrocarbons at the reformer inlet.

$$\frac{\triangle \dot{H}_{\mathrm{ref}}}{\dot{n}_{\mathrm{NG,in}}} = \frac{(1 + r\, K_{\triangle \mathrm{an}})}{(1 - r)} \left(h_{\mathrm{ref,out}} \frac{M_{\mathrm{ref,in}}}{M_{\mathrm{ref,out}}} - h_{\mathrm{ref,in}} \right) \tag{3.16}$$

$$\frac{\triangle \dot{H}_{\mathrm{ref}}}{I\, N_{\mathrm{Cell}}} = \frac{(1 - r + r\, U_{\mathrm{f,S}})}{U_{\mathrm{f,S}}\, F\, K_{\mathrm{e}^-}} \frac{(1 + r\, K_{\triangle \mathrm{an}})}{(1 - r)} \left(h_{\mathrm{ref,out}} \frac{M_{\mathrm{ref,in}}}{M_{\mathrm{ref,out}}} - h_{\mathrm{ref,in}} \right) \tag{3.17}$$

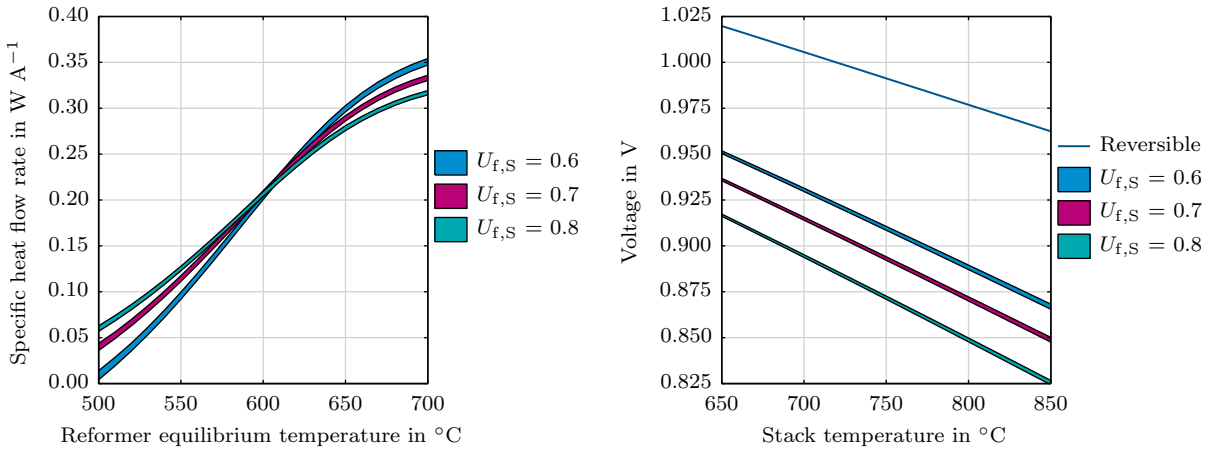

(a) Specific reformer heat flow rate

(b) Ideal reversible and Nernst voltage

Figure 3.13: Thermodynamic effects of varying natural gas quality: Specific reformer heat flow rate, as well as ideal reversible and Nernst voltage

In Figure 3.13b, the ideal reversible open circuit and Nernst voltage are shown for the combined natural gas data set in a temperature range between 650 and 850 °C, for three different $U_{\mathrm{f,S}}$ values. The reversible open circuit voltage is independent of $U_{\mathrm{f,S}}$ and gas composition, since it is calculated using equation (2.35), assuming hydrogen as the only electrochemical active species. The Nernst voltage is calculated based upon equation (2.36), using the anode equilibrium composition at the defined stack temperature and $U_{\mathrm{f,S}}$, as well as the oxygen concentration at the cathode outlet. The cathode outlet oxygen concentration is computed for a fixed air utilization factor, as displayed in equation (3.18)[14]. The Nernst voltage is calculated for the entire combined natural gas data set. The minimum and maximum boundary values are displayed in Figure 3.13b, for each individual combination of stack temperature and $U_{\mathrm{f,S}}$, as well as a designated air utilization factor of 0.25. According to equation (3.18), an air utilization factor of 0.25 is equal to a cathode outlet oxygen concentration of 16.5 % for a cathode inlet composition of 20.9 % oxygen and 79.1 % nitrogen. As shown in Figure 3.13b, increasing $U_{\mathrm{f,S}}$ values yield lower voltages, due to higher water vapor and lower hydrogen fractions at equilibrium state based upon the increased utilization of hydrogen. The influences of the varying natural gas quality on the Nernst voltage are considered proportionally low, showing a minimum to maximum domain between 1.5 and 2.8 mV, as well as 1.2 and 2.4 mV for $U_{\mathrm{f,S}}$ of 0.6 and 0.8, respectively.

$$x_{\mathrm{ca,out,O_2}} = \frac{x_{\mathrm{ca,in,O_2}}\,(1 - U_{\mathrm{a}})}{x_{\mathrm{ca,in,N_2}} + x_{\mathrm{ca,in,O_2}}\,(1 - U_{\mathrm{a}})} \tag{3.18}$$

The risk of carbon formation is increasing in a fuel cell system operated with natural gas due to the higher tendency of decomposition of higher hydrocarbons [8, 20]. However, detailed carbon formation mechanisms and the effects of carbon deposition on a fuel cell system, like catalyst deactivation or plugging of channels and pipes [8, 20], are beyond the scope of this work. The carbon deposition regions for methane and natural gas, highlighting the best and worst

[14] The derivation of equation (3.18) is shown in appendix E.

case of the entire combined data set, in an ideal SOFC system are illustrated in Figure 3.14a[15]. As displayed in Figure 3.14a, the lower the temperature, the higher the required Φ to prevent carbon deposition. In the best case, the combined natural gas data set matches the progression of methane, based upon similar gas properties, for instance, nearly identical hydrogen to carbon ratios. In the outlined temperature range, in the worst case, the combined data set has a significant offset, underlining the increased risk of carbon deposition starting at higher temperatures for a fixed Φ. Additionally, the carbon deposition curves for 500, 600 and 700 °C, as well as the corresponding C-H-O ratios of the combined natural gas data base at the reformer for different Φ values are highlighted in a C-H-O ternary diagram in Figure 3.14b[16]. As shown in Figure 3.14b, for Φ of 2 and an equilibrium temperature of 600 °C the entire data set is outside of the carbon deposition region. The displayed progressions of the carbon depositions curves for the different temperature levels match the trends shown by Sasaki and Teraoka [59] and Lee et al. [60]. As highlighted in gray, by the connector between the two boundary natural gas data points and the bottom right corner of the graph, the C-H-O ternary diagram also outlines that each data point, for varying Φ values, is located on the connector between each individual point of the natural gas data base and pure oxygen. In an SOFC system with AEGR, the only possible sources for oxygen are carbon dioxide contents in natural gas and transferred oxygen from the cathode side. Therefore, the connecting line specifies all possible C-H-O mixtures in the system.

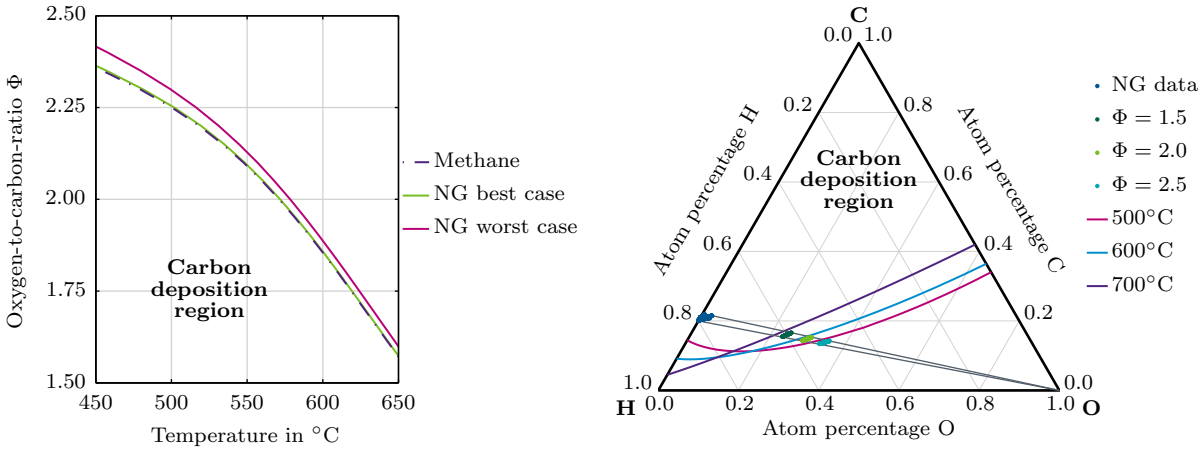

(a) Carbon deposition region for an ideal SOFC system including AEGR for best and worst case of natural gas data and methane

(b) Carbon deposition region in C-H-O ternary diagram for natural gas data with connecting lines of boundary natural gas data and pure oxygen highlighted in gray.

Figure 3.14: Carbon deposition region

Subsequently, the risk of carbon formation is solely evaluated with the help of Figure 3.14a, considering the dependency on Φ and the temperature level. Direct carbon deposition is not taken into account in the modeling approach. Research studying carbon formation and the corresponding effects on fuel cells are frequently addressed, for instance, by Lee et al. [60], Subotić et al. [61], Bae et al. [62], Sumi et al. [63] or Cui et al. [64], respectively.

[15] The boundary curves are calculated for thermodynamic equilibrium states yielding graphite fractions of at least 10^{-6} using Cantera, combining the USC-Mech II and graphite data base [57, 58]. The arbitrary limiting value of 10^{-6} defining the carbon deposition region is determined in accordance with Sasaki and Teraoka [59] and Lee et al. [60].

[16] The carbon, hydrogen and oxygen atom fraction for different oxygen-to-carbon ratios are calculated using the element balance at the reformer inlet, illustrated in subsection 2.2.2.4, subtracting out the inert nitrogen portions by scaling the C, H, O ratios to 100 %,

4 System behavior analysis and control strategy

The following chapter is divided into five parts. As a result of the conducted literature review, focusing on control and operating strategies of SOFCs, the need for further evaluations of the effects of varying natural gas quality on SOFC systems is first addressed. Secondly, the setup and applied control strategy of the evaluated SOFC test rig are outlined. Subsequently, the system modeling methodology and general validation and verification are shown. Furthermore, the experimental results are presented, including a comparison to the simulated outputs. Finally, the chapter is concluded with a sensitivity analysis of the evaluated control strategy in the modeling environment using the Saint-Thegonnec 2014 and Renningen 2016 data sets.

4.1 Literature background

4.1.1 Control and operating strategies of SOFC systems

The following literature review is further structured based upon the related system approach option. Frequently addressed options, in regard to control strategies, are hydrogen fueled or alternative fueled SOFC systems without the need of a reformer unit, SOFC systems with external water supply, systems with CPOX reformer, systems including anode exhaust gas recirculation and hybrid systems, for instance the coupling of a high temperature fuel cell with a gas turbine (GT). It should be noted that the hybrid system section of the review focuses on the control constraints of the fuel cell, whereas the gas turbine parts are generally not outlined in full detail.

4.1.1.1 Hydrogen or alternative fueled SOFCs and SOFC systems

Taher and Mansouri [65] used a dynamic model of an SOFC stack coupled with an inverter to evaluate the performance during small and rapid load changes. Proportional integral (PI) controllers were implemented to control the fuel utilization factor, pressure difference between the anode and cathode inlet and the power output by manipulating the stack current and the flow rates of pure hydrogen and oxygen. The stack temperature was considered an invariant parameter with a fixed designated value. During load changes, the purposed control strategy was able to reset the fuel utilization factor to a designated optimal value, while keeping the pressure difference between the anode and cathode inlet within a safe operating range.

Zhang et al. [66, 67] evaluated the system response during load changes of a hydrogen fueled SOFC system, including balance of plant components, in an experimentally validated system model. The aim of the developed control strategy was to determine optimal operation points by maximizing the electrical efficiency. For a given net power output, the optimal operation point was reached by varying several operating parameters, while satisfying all thermal limitations of the system. The SOFC temperature, stack temperature gradient, the temperature spread of fuel and air at the stack inlet, and the burner temperature were controlled by manipulating the total and bypass air flow rates. Simultaneously, the air utilization factor was maintained within a predefined safety domain. The fuel flow rate was adjusted to match the net power output of the system, while considering the safe operating range of the fuel utilization factor and current. However, for the prevention of fuel starvation and the satisfaction of the temperature constraints, the power adjustment during load changes was performed in two stages. During the switch stage, the power output was quickly adjusted close to the external power requirement. The maintenance stage was used for slow, continuous steady load tracking. As a result, a load following mechanism was developed that prevents fuel starvation and satisfies the temperature limitations, while achieving a reasonable response time without generating tremendous overshoots.

Hajimolana et al. [68] outlined the control of the SOFC stack temperature by manipulating the air inlet temperature, using a heat exchanger bypass, of a tubular SOFC running on ammonia. In comparison to a PI controller, the applied neural network predictive controller (NNPC) achieved less oscillating responses, shorter settling times and reduced thermal stress, during the set point changes of the designated tube temperature. Additionally, the NNPC was able to sufficiently track the set point of the cell temperature during a change in the fuel and air inlet pressures and velocities, as well as in the fuel inlet temperature.

Lee et al. [69] applied model predictive control (MPC) to a sector bounded nonlinear SOFC model to control the stack voltage by manipulating the hydrogen flow rate. The authors outlined that set point tracking of the voltage was sufficiently accomplished by the developed MPC.

Nayeripour and Hoseintabar [70] developed an adaptive control strategy for the purpose of preventing the excess or the starvation of the fuel inside the stack. The SOFC system included a hydrogen fueled SOFC stack and an electrical storage device, which was used during fast transient operation for the purpose of sufficient load tracking. The control strategy included two different modes. During steady state operation, the fuel utilization factor was kept at its optimal value by manipulating the hydrogen fuel feed, while the fuel utilization factor was maintained inside a predefined operating range by controlling the applied current during transient operation. By linking the current to the allowed fuel utilization factor domain and hydrogen fuel feed, a resulting maximum and minimum applicable current was calculated. During a positive current step change, if the current demand exceeded the maximum applicable current of the SOFC, the fuel utilization factor was kept at its maximum, while the remaining power demand was satisfied by the storage device. In a negative load change scenario, in which the current was lower than the minimum applicable current, the fuel utilization factor was kept at its minimum and the excess electrical energy was stored. To reach steady state operation, the fuel utilization factor was returned to the optimal set point value by manipulating the hydrogen feed in correspondence to the applied power demand. The authors stated that by applying the developed control strategy, the size of the storage device and the overall system costs can be reduced. Additionally, compared to other used control approaches in literature, the proposed adaptive control strategy achieved an enhanced transient response and faster load tracking.

Vijay et al. [71] used a zero-dimensional true bond graph model of an SOFC fueled with hydrogen to evaluate the dynamic response of the SOFC during load changes. The implemented control strategy maintained a constant fuel utilization factor and cell temperature by manipulating the flow rates of hydrogen and air. The control strategy was able to satisfy the control objectives even during positive and negative load step changes, with tolerable over- and undershoots in the cell temperature. The authors also proposed that the temperature control can be realized by manipulating the air and fuel inlet temperature levels.

Chaisantikulwat et al. [72] evaluated the performance of an SOFC during step load and inlet gas compositions changes, using low-order models derived from a three-dimensional dynamic model of a single SOFC. The fuel was assumed to be a mixture of hydrogen, water vapor and nitrogen with a fixed molar water vapor content of 3 % and variable hydrogen contents between 10 % and 97 %, whereas the nitrogen content was used for balancing. Additionally, a PI controller was implemented to control the voltage by manipulating the hydrogen concentration during the applied load variations. The authors showed that the voltage can be successfully controlled during rapid load current changes of around 12.5 %.

Yang et al. [73] designed a temperature control strategy for a hydrogen fueled SOFC stack using MPC. The stack temperature was kept at a designated value by manipulating the air flow rate. Furthermore, Yang et al. [74] extended the control strategy using the air and hydrogen flow rate to control the stack temperature, while considering the load current as a disturbance. The authors demonstrated that the proposed MPC achieved a satisfactory effectiveness in keeping the stack temperature at a designated value even during load changes.

Deng et al. [75] developed an adaptive generalized predictive control (GPC) for a dynamic model of a hydrogen fueled SOFC [76]. The proposed strategy controlled the power output of the SOFC by manipulating the electric current. During load tracking, fast and smooth control responses were achieved. Additionally, the authors stated that generalized predictive control strategies are advantageous to realize quick load following capabilities.

4.1.1.2 SOFC systems with catalytic partial oxidation reformer

Tsikonis et al. [77] compared three different approaches to control the stack air inlet temperature of an SOFC system with a CPOX reformer. During load changes, the stack air inlet temperature can be controlled by manipulating either the bypass air flow rate, the total air flow rate or the fuel flow rate, respectively. The authors outlined that all three proposed control options were able to satisfy the control objective during load changes using proportional integral differential (PID) controllers. It should be noted that the authors referred to fueling the SOFC system with natural gas, however no average composition, possible fluctuation domains, system responses or control applications were mentioned.

4.1.1.3 SOFC systems with an external water supply

Georgis et al. [78] designed a control strategy for a methane fueled SOFC system, including a stack, reformer, burner, several heat exchangers and bypass valves. The fuel utilization factor and temperature of the stack was controlled by manipulating the inlet fuel and air flow rates, respectively. Additionally, the reformer temperature was controlled with the help of a bypass, which manipulated the exhaust gas flow through the heat exchanger. Lastly, the temperature at the cathode inlet was controlled by manipulating another inlet air bypass valve. For the application of the control strategy, PI controllers were used. As a result, even during changes of the load current, a smooth and stable closed-loop response was obtained inside the simulation environment.

Wu et al. [79] developed a nonlinear predictive control algorithm to control the stack voltage of a SOFC by manipulating the methane fuel flow rate during load changes. The authors stated that in comparison to a regular constant fuel utilization factor control scheme, the MPC of the stack voltage is more complex. However, the developed strategy assured that the fuel utilization factor was kept inside a safe operating range between 0.7 and 0.9, even during rapid load changes.

Sorce et al. [80] outlined a control strategy for a methane fueled SOFC system, including a stack, reformer and burner. The applied control scheme maintained the fuel utilization factor of the stack and the stack temperature by manipulating the fuel and air flow rates in correspondence to the electrical current. The reformer was kept at a constant temperature level with the help of an electrical heater. The control strategy was not further emphasized by the authors, since the focus of the publication was the evaluation of possible system faults, such as air or fuel leakage. Additionally, the same system setup and control scheme was used by Greco et al. [81] to evaluate the influences of different reformer failures on the temperature gradients in the stack.

Komatsu et al. [82] evaluated the load following behavior of an SOFC system, including a tubular stack and an internal indirect reformer, in a dynamic model. The DC power output, SOFC temperature, fuel utilization factor and steam-to-carbon ratio were controlled by manipulating the electric current, as well as the air, fuel and steam flow rates using a feedback control methodology. During load changes the system response was evaluated comparing the use of proportional (P), PI and PID controllers. The response of the P controller was very smooth but led to a steady state error. The PI and PID controllers partially generated tremendous overshoots during load changes, which can cause severe cell damage due to fuel starvation. However, an adequate setup of the controller parameters can limit the risk of stack damage during load

changes. In brief, the capability of the P controller to ensure safe and efficient load following operation, including set point tracking, was outlined.

Sorrentino et al. [83] evaluated the load following behavior of an SOFC for automotive auxiliary power unit applications using a control-oriented model of a planer SOFC fueled with reformed methane. A PI controller was implemented to control the cell temperature spread by manipulating the air flow rate. During load changes, the PI controller was able to efficiently maintain the temperature spread inside a safe operating range, ultimately reducing the risk of thermal stress.

Li et al. [84] implemented a MPC into an SOFC system model to control the stack output voltage during load changes by manipulating the fuel flow rate. Additionally, the fuel utilization factor was kept within a safe operating range during load tracking. The control methodology was able to efficiently accomplish the control objective, while applying positive and negative step load changes. Additionally, the considered SOFC system included a fuel processing unit and SOFC stack fueled with natural gas. However, as an SOFC input, a pure hydrogen flow rate was considered and no further information about the natural gas composition was given.

Murshed et al. [85] evaluated the load following behavior of a methane fueled SOFC system, including a reformer, SOFC stack, burner and two heat exchangers. The fuel and air were preheated with the help of the burner exhaust gas. Additionally, the reformer was directly supplied with water vapor. A nonlinear MPC strategy was implemented to control the voltage by manipulating the fuel, air and water vapor flow rates, while keeping the stack temperature and fuel utilization factor within a safe operating range. In addition, the effect of a parallel connected capacitor during load changes was evaluated. During a sudden load change, the resulting voltage drop or rise was successfully smoothed by the capacitor. The higher the capacitance, the lower the over- or undershoot of the voltage. However, the settling times of the fuel cell current increased. Therefore, the controller was subjected to a lingering effect and steady state operation was delayed. The authors concluded that the nonlinear MPC was able to achieve a robust system response even during large load changes. However, the implementation of a nonlinear MPC is not straightforward and a detailed and complex model development and maintenance is necessary. Additionally, changes to the plant setup can lead to significant updates to the complex modeling approach. Nonlinear MPC can also lead to high computing times, due to the complexity of the related models.

Zhang et al. [86] designed a nonlinear MPC strategy for a planar SOFC fueled with partial reformed methane. The proposed strategy controlled the power output, fuel utilization factor and cell temperature by manipulating the current, fuel and air flow rates. During load tracking, the implemented nonlinear MPC achieved an efficient and robust satisfaction of the control objectives. However, even though nonlinear MPC achieved promising simulation results, the practical application is difficult. In comparison to other control schemes, the computation time of nonlinear MPC, to continuously solve the nonlinear optimization, is fairly high. In general, iteration with convergence criteria is applied to solve the optimization problem. The computational time of such methodologies are too high for real-time system applications. The authors concluded that the practical implementation of nonlinear MPC strategies are strongly related to the development of enhanced optimization tools.

D'Andrea et al. [87] outlined a control logic for a bio gas fueled SOFC system with external water supply. The system included a reformer, an evaporator and a heat exchanger for the heating of air by using the cathode exhaust gas. Additionally, the reformer, and the anode and cathode inlets were equipped with electrical heaters to reach the designated temperature levels. The stack temperature was controlled in a closed-loop by manipulating the air flow rate. An open-loop control was implemented to set the inlet flow rates of bio gas and water in relation to the applied current density, designated fuel utilization factor of the stack, bio gas composition and steam-to-carbon ratio. By limiting the current ramp rate during a positive load change,

the implemented PID controller was able to effectively control the stack temperature within a designated safe operating domain. It should be noted, that neither an exact composition of the used bio gas, nor fluctuations domains were given by the authors.

Barelli et al. [88] evaluated the performance of a stack temperature control of a methane fueled SOFC during load changes. Methane was assumed to be completely converted to hydrogen and carbon monoxide in an ideal steam reforming reaction, using an external water source. The stack temperature was controlled by manipulating the air flow rate with a PID controller. The fuel flow rate was adjusted to match the designated current for a fixed fuel utilization factor. The authors outlined that the stack temperature can be efficiently controlled in a safe operating domain, even during large load variations.

Mueller et al. [89] designed a control strategy for a methane fueled SOFC system with external water supply. The system included an SOFC stack, a reformer, a burner, an evaporator, an air blower, several heat exchangers and a main fresh air bypass to the cathode inlet. The air was preheated in two stages using the burner exhaust gas. In between both air heating stages, the burner exhaust gas was utilized to supply the reformer with heat. The air flow rate was manipulated to control the stack temperature, whereas the air bypass flow rate was used to maintain a designated cathode inlet temperature. The electric current and fuel flow rate were manipulated to control the electric power and fuel utilization factor. Additionally, a minimum cell voltage limitation was implemented to adjust the electric power demand to a permitted value. It should be noted, that the supplied water was assumed to be adjusted in proportion to the methane flow rate, guaranteeing a designated steam-to-carbon ratio set point, without the implementation of a controller. The proposed control strategy was able to follow rapid load changes efficiently. However, the local depletion of hydrogen in the SOFC, due to the delay of the fuel flow to the anode, was outlined as the major limitation for improving the load tracking.

4.1.1.4 SOFC systems including an anode exhaust gas recirculation

Pohjoranta et al. [90] implemented a generalized predictive control into an SOFC system to control the maximum stack temperature and the temperature spread across the stack. The system model was a linear polynomial input-output model based upon experimental data of a complete natural gas fuel 10 kW planar SOFC system, including anode exhaust gas recirculation [91]. The performance of the GPC, which is a form of a MPC, was compared to a standard PID controller for the purpose of maximum stack temperature control via manipulating the cathode inlet temperature. Additionally, the GPC was utilized for the control of the maximum stack temperature and temperature spread across the stack by manipulating the cathode inlet temperature and the air flow rate. In another case, the fuel flow rate was also implemented as an additional manipulated variable. The control response of the GPC can be slightly enhanced, in comparison to the PID controller, by manipulating multiple input variables. However, according to the authors, the application of the more complex GPC for a simple control case is excessive. It should be noted that the authors refer to an operation of the SOFC system on natural gas, however no average composition or possible fluctuation domains, nor system responses or control applications were mentioned.

Spivey and Edgar [92] developed an advanced control logic for the purpose of SOFC lifetime improvement, due to thermal stress reduction. As a basis for their evaluation, a dynamic model of a tubular cathode supported SOFC system was used. The SOFC system included a stack, reformer and an ejector for anode exhaust gas recirculation. The control strategy comprised two output feedback MPCs. The minimum cell temperature, maximum radial thermal gradient, power output, fuel and air utilization factors, and the steam-to-carbon ratio were the controlled variables. The inlet fuel pressure, cell voltage, inlet fuel temperature, system pressure level and air flow rate were the manipulated variables. Additionally, sinusoidal fuel disturbance tests were carried out in an open-loop environment by changing the methane and carbon dioxide content.

The step size was ±10 %, with nominal methane and carbon dioxide values of 90 and 10 %, respectively. During the concentration shift, the fuel utilization factor reached critical values of higher than 90 %, compared to the nominal value of around 70 %. Regarding close-loop results, the authors stated that their model predictive control strategy was able to satisfy the thermal and operating constraints during load tracking, even if sinusoidal fuel disturbances were applied.

Inui et al. [93] evaluated a temperature control strategy for a methane fueled SOFC, including anode exhaust gas recirculation. The electric current, the air flow rate and the anode and cathode inlet temperatures were manipulated to follow a designated load target and maintain a fixed air utilization factor and cell temperature. As a baseline for the evaluation, the recirculation ratio and fuel utilization factor were assumed to have fixed values. However, a possible control logic for both variables was not addressed. Additionally, it was assumed, that both the anode and cathode inlet temperatures were variable. The authors outlined that the proposed control strategy enhanced the uniformity of the cell temperature distribution. Therefore, thermal stress was reduced and cell durability increased.

Carré [29] developed a control strategy for a natural gas fueled SOFC system with anode exhaust gas recirculation, including start up and nominal operation procedures. The system included a reformer, an SOFC stack, a burner and several heat exchangers and blowers. At nominal operation, an open-loop control was used to manipulate the natural gas and recirculation flow rates to control the fuel utilization factor of the stack and oxygen-to-carbon ratio in the reformer. The stack temperature was kept constant using a closed-loop control by manipulating the air flow rate. The current was an input parameter to calculate the individual set points for the natural gas, air and recirculation flow rates. During the determination of the air flow rate, restrictions due to minimum and maximum limiting values of the air utilization factor, the air-fuel-equivalence ratio for combustion and the temperature of the burner were considered. In a related work, Carré et al. [27] replaced the stack temperature control with an open-loop control of the total air utilization factor of the system, by manipulating the air flow rate. Again, limitations due to minimum and maximum values of the air utilization factor and the air-fuel-equivalence ratio for combustion were considered. Both control approaches were experimentally evaluated and validated in a methane fueled SOFC system test rig. The evaluation proved that both strategies were able to maintain a constant fuel utilization factor and oxygen-to-carbon ratio for varying electric currents. Additionally, in both cases, the stack temperature was kept within safe operating domains. It should be noted, that it is possible to apply both strategies to a natural gas fueled system, due to the connection of the flow rate set point calculations and gas composition. However, the proposed strategies can only be applied if the natural gas composition is known. Furthermore, adjustment, implementation or identification possibilities, coping with unknown and fluctuating natural gas compositions were not addressed by the authors.

Gallet Segarra [28] used the control strategy developed by Carré [29] to evaluate the robustness for varying natural gas composition. In a first step, the deviations between the set points and process values of the fuel utilization factor of the stack and oxygen-to-carbon ratio were calculated for a constant current, air utilization factor and eight high calorific and five low calorific natural compositions. The averages of the different natural gas compositions were used as the reference natural gas compositions to determine the corresponding volume flow rates of natural and recirculated gas, respectively. It was assumed that the blowers could ideally set the designated volume flow rates for each of the 13 natural gas compositions. The resulting steady state deviations of the fuel utilization factor of the stack ranged from 0.52 to 0.74, for a set point value of 0.6. The corresponding oxygen-to-carbon ratios ranged from 1.80 to 2.35, for a set point value of 2.00. Therefore, the author concluded that by simply defining a generic reference composition, the deviations from the set points were too significant to generally guarantee the safe operation and lifetime of an SOFC system, including anode exhaust gas recirculation.

In a second step, six different control methodologies were developed to increase the robustness for varying natural gas quality. All strategies relied on the determination of the mean number of carbon atoms and the estimation of the utilizable electrons per fuel molecule. Consequently, the corresponding set points of the natural gas volume flow rate and recirculation ratio could be calculated for a designated fuel utilization factor of the stack, oxygen-to-carbon ratio, electric current and reference oxygen and carbon dioxide fractions in natural gas. It should be noted, that for the estimation of the utilizable electrons per fuel molecule, a simplified relation to the mean number of carbon atoms per fuel molecule and a designated mole fraction of hydrocarbons in natural gas between 0.8 and 1.0 was used.

The six determination methodologies for the mean number of carbon atoms were based upon the measurement of: (a) the higher heating value of natural gas; (b) the oxygen mole fraction in the exhaust gas of the start up burner and the corresponding supplied volume flow rates of natural gas and air; (c) the exhaust gas temperature of the start up burner and the corresponding supplied volume flow rates of natural gas and air; (d) the oxygen mole fraction in the exhaust gas of the system and the corresponding total supplied volume flow rate of air; (e) the oxygen mole fraction at the cathode outlet and in the exhaust gas of the system; and (f) the carbon dioxide and water vapor fraction in the exhaust gas of the system. For all six options, relations between the measured parameters and the mean number of carbon atoms were derived, using the designated mole fraction of hydrocarbons in natural gas between 0.8 and 1.0. The author discarded options (b) and (c) due to the additional large consumption of natural gas in the start up burner during nominal operation and the estimated high relative error of the determination of the mean number of carbon atoms. The remaining options were evaluated in a simulation environment with ideal sensors and actuators, applying a designated fuel utilization factor of the stack of 0.6 and oxygen-to-carbon ratio of 2. The designated mole fraction of hydrocarbons in natural gas was set to 0.95 for higher and 0.80 for lower calorific natural gas. The authors outlined that options (a), (d) and (e) were able to keep the fuel utilization factor of the stack and oxygen-to-carbon ratio within a safe operating domain. However, option (f) yielded even higher deviations of the fuel utilization factor and oxygen-to-carbon ratio than the previously outlined basic strategy adopted from Carré [29]. The deviations were caused by the high influence of the fixed value of the designated mole fraction of hydrocarbons in natural gas.

Additionally, the author also conducted a propagation of error, including the considered sensors for the options (a), (d), (e) and (f). The evaluation highlighted, that only option (a) always kept the characteristic parameters within a safe domain, since only a single sensor was necessary and the error of the higher heating value determination was considered low. Option (d), (e) and (f) relied on a plurality of sensors, between two and four, which can yield extreme error margins. However, even though option (a) showed superior results in the simulation, only option (d) and (f) were experimentally evaluated by the author. The central component of the used test bench was a burner, which was used to represent an entire SOFC system in form of a complete combustion reactor. The burner was connected to three different mass flow controllers. Two mass flow controllers were used to supply a mixture of methane and nitrogen to reproduce different natural gas compositions, represented by different higher heating values. The third mass flow controller was used to supply air to the burner, ensuring lean combustion conditions. Furthermore, downstream of the burner, the test bench was equipped with an oxygen, a carbon dioxide and a relative humidity sensor.

For options (d) and (f), the detection of the mean amount of carbon atoms per fuel molecule was tested for 29 steady state operation points in the test bench. The 29 different points included variations of the higher heating value, supplied volume flow rate of methane and air-to-fuel-equivalence ratio for combustion of the burner. The author concluded that both methods were applicable for the estimation of the mean amount of carbon atoms per fuel molecule. However, the outlined maximal deviations between the measured and ideal calculated values of

the mean amount of carbon atoms reached values up to 15.6 % and 21.6 % for option (d) and (f), respectively. Additionally, especially for option (f), the fixed mole fraction of hydrocarbons in natural gas and the water content of the inlet air had tremendous effects on the accuracy of the detection. Acceptable accuracy could be achieved if both values were considered variable for the estimation of the mean amount of carbon atoms per fuel molecule.

4.1.1.5 SOFC hybrid systems

Kandepu et al. [94] evaluated the load following behavior of an SOFC-GT hybrid system, including anode exhaust gas recirculation, in a dynamic model. The system was fueled with methane and included a reformer, a burner, a two stage gas turbine, and balance of plant components, such as compressors, heat exchangers and an inverter. A fraction of the anode exhaust gas was recirculated with the help of an ejector. The inlet air was supplied to the system via a compressor, which was directly coupled to the first stage of the turbine. The air was heated with the help of the exhaust gas of the last turbine stage. The fuel utilization factor of the stack and stack temperature were controlled by manipulating the fuel and air inlet flow rates. An air blow off valve at the compressor outlet was used to regulate the air flow rate to the stack. The authors outlined that by implementing two PI controllers, the fuel utilization factor of the stack, as well as the stack temperature, was kept at a constant designated level during load changes.

Martinez et al. [95] developed a dynamic SOFC-GT hybrid system model. The system included a planar SOFC stack with cathode recirculation, a burner and gas turbine, which was directly coupled to the air blower. Prior to reaching the stack, the air was heated in two steps, utilizing the turbine exhaust gas in a heat exchanger and by merging the air with the recirculated fraction of the hot cathode exhaust. Fuel heating and processing units were not included in the approach. Initial conditions were set to represent the temperature and composition of the fuel at the stack inlet. The model was used as a basis for the implementation of a cascaded control logic, which focused on safe operation of the SOFC, prior to satisfying the system power requirements. To reduce thermal stress, the SOFC average temperature and the temperature spread across the stack were controlled by manipulating the air flow rates at the inlet and inside the cathode recirculation loop. Additionally, the fuel utilization factor of the stack was controlled by manipulating the SOFC voltage. The power demand requirements were fulfilled by changing the inlet fuel flow rate. In the applied cascaded control scheme, the temperature requirements and power demand were on the highest and lowest levels, respectively. Proceeding to the next level of the cascade was only allowed if designated set point domains were achieved. During transient operation, the control strategy was able to reach steady state using three different types of fuel, humidified hydrogen, natural gas and diesel steam reformate. The projected system efficiency ranged from 65 to 70 %. It should be noted that the three different fuel types had a designated, fixed composition and fluctuations were not considered.

Jia et al. [96] evaluated an operating strategy for a methane fueled SOFC-GT hybrid system. The SOFC was operated as a baseline power unit, while the gas turbine responded to load variations. During load changes, relations between the input variables, including the air flow rate, air inlet temperature, current density and the fuel flow rate, were used to maintain a constant power and temperature output of the SOFC. The strategy was evaluated using a dynamic modeling approach including an SOFC stack, a gas turbine, a burner, a heat exchanger and an air blower. In the system, the air blower was directly coupled with the turbine shaft. The stack temperature was controlled by manipulating the air flow rate, via the shaft speed. The total power output of the stack was controlled by manipulating the fuel flow rate. Additionally, a shaft speed controller was implemented to prevent excessive air feeds and harmful compressor states, which could lead to a system shutdown. The authors concluded that the developed operating and control strategy was able to respond to immense load changes, while guaranteeing safe and stable operation.

Wu and Zhu [97] developed a multi-loop adaptive, combined PID and MPC strategy for a methane fueled SOFC micro-GT hybrid system. The system included an SOFC stack with anode exhaust gas recirculation, a micro gas turbine, a reformer, heat exchangers, a burner, blowers and further balance of plant components. In the proposed control strategy the power output, turbine inlet temperature, SOFC temperature and fuel utilization factor were controlled by manipulating the electric current, bypass fuel flow rate to the burner, and total fuel and air flow rates. The MPC was used for load tracking. The two different PID controllers were implemented to keep the temperatures of the system in a designated operating range and to reset the fuel utilization factor to the desired value. The author concluded that the proposed control strategy was able to keep the fuel utilization factor, as well as the temperatures of the SOFC and at the turbine inlet, in a safe operating range, while fast, efficient and accurate load tracking was achieved. Additionally, for load tracking, Wu et al. [98] designed a self-tuning PID decoupling controller for the SOFC micro-GT hybrid system. The SOFC and gas turbine output powers were controlled by manipulating the fuel and air flow rates, as well as the SOFC current. Compared to a regular PID controller, the self-tuning PID decoupling controller was able to efficiently track the load.

Ferrari [99] coupled a standard PI controller with a feed-forward technique to prevent thermal stress in the fuel cell, and to reduce the peak values of the cathode to anode pressure difference and the steam-to-carbon ratio, in a SOFC-GT hybrid system. The system was fueled with methane and included anode exhaust gas recirculation, using a single-stage ejector. The fuel utilization factor, stack temperature and power output were controlled by manipulating the fuel, air and bypass air flow rates, as well as the electric current. A battery pack, or grid connection, was used as a buffer, smoothing the operation during load changes and preventing fast oscillation of the controlled variables. Additionally, due to the smoothing, low steam-to-carbon ratios below a value of 2 were prevented. Overall, the proposed control strategy was able to improve the SOFC temperature management by avoiding significant thermal gradients. Furthermore, the anode to cathode pressure difference and the steam-to-carbon ratio were kept in safe operating ranges, while fulfilling load requirements.

Kaneko et al. [100] developed a load following control strategy for an SOFC micro-GT hybrid system. The system was fueled with bio gas and included an SOFC stack, a high and low pressure gas turbine, as well as additional balance of plant components, such as heat exchangers, compressors and a burner. Additionally, a bypass valve was implemented in the exhaust gas stream, for the purpose of bypassing the fuel and air heating units. The fuel was a mixture of bio gas and water vapor, with a fixed water vapor content of 40 % and variable fractions of methane and carbon dioxide between 35 to 40 % and 25 to 20 %, respectively. The authors assumed that the bio gas composition fluctuations were sinusoidal with a 12 hour frequency. For a fixed gas flow rate, the gas composition fluctuation led to a change in energy gas content by 5 %, which resulted in a system power output change of around 13 %. In the proposed control strategy, the cell voltage, power output and fuel cell temperature were controlled by manipulating the cell current, fuel flow rate and exhaust bypass flow rate. The control strategy was able to follow the load, while reacting to gas composition fluctuation, due to the adjustment of the fuel flow rate in correspondence to the designated power output. However, it should be noted, that the authors assumed that the fluctuation in bio gas composition was perfectly predictable or known at every time step of their evaluation.

McLarty et al. [101] developed and evaluated sophisticated control strategies for coal syngas fueled SOFC-GT hybrid systems. In one configuration, the system included an SOFC with cathode exhaust gas recirculation, a burner, a compressor, which is directly coupled to a gas turbine, and heat exchangers for fuel and air heating. Additionally, the system was equipped with two air bypasses. As part of the cathode inlet temperature control, one pathway could bypass the air heat exchanger upstream of the fuel cell. Another pathway connected the compressor outlet

directly with the turbine inlet. The bypass was used in combination with the blower speed to manipulate the total air flow rate, ultimately controlling the cathode outlet temperature. The fuel flow rate and electric current were manipulated to control the power output and fuel utilization factor. Additionally, the cathode inlet temperature was controlled by manipulating the cathode exhaust recirculation flow rate and the bypass air flow rate. The authors demonstrated that the proposed control strategy was able to follow highly dynamic load profiles, while keeping the SOFC conditions within safe, acceptable operating domains.

4.1.2 Conclusions

The summary of the conducted literature review is displayed in Table 4.1, which includes a list of the identified references, focusing on the control and operating strategies of SOFCs. The table contains the evaluated type of unit[1], controller and used fuel. Additionally, the table depicts weather experimental testing was conducted. Lastly, the manipulated and controlled variables[2] are outlined. The following concluding statements are derived based upon the conducted literature review and the summary in Table 4.1:

1. Control and operating strategies of SOFCs or SOFC systems are frequently addressed by a plurality of academic work groups, institutes and companies.

2. The evaluated system approaches cover all types of modifications. Control strategies are developed and evaluated for CPOX, EWS, AEGR and hybrid systems, including the coupling of SOFCs and gas turbines. Additionally, few system approaches include a cathode exhaust gas recirculation loop. Even though systems including an AEGR were the focus of the literature review, the number of identified references are limited.

3. The considered types of fuels range from pure hydrogen to ammonia to common conventional fuels, for instance methane, natural gas, bio gas or coal syngas. A plurality of works and publications use the term natural gas for pure methane. Predominantly, the exact composition or fluctuation domains of natural gas are not addressed.

4. Fluctuations or variability of fuels or components of fuels are only considered by Chaisantikulwat et al. [72], Spivey and Edgar [92], Kaneko et al. [100] and Gallet Segarra [28]. Frequently, natural gas fluctuations are not considered as an unknown disturbance for the control approach.

    a) Chaisantikulwat et al. [72] considered a variable hydrogen content in a hydrogen, nitrogen and water vapor mixture, with a fixed water vapor fraction. However, the evaluated gas mixture is under no circumstances comparable to typical natural gas compositions, since no hydrocarbons were included in the evaluation.
    b) Spivey and Edgar [92] and Kaneko et al. [100] only evaluated the sinusoidal changing of the bio gas composition, which included two variable species, methane and carbon dioxide. However, for the application of the control strategy, the change in composition was assumed to be ideally detected or known.
    c) Gallet Segarra [28] evaluated the effects of variable natural gas quality on SOFC systems, including an AEGR. Additionally, the focus was the evaluation of possibilities to detect characteristic parameters of the natural gas, to adapt a control strategy to be robust against natural gas composition fluctuations. The work considered natural

[1] In Table 4.1, the abbreviation SOFC refers to single cells or stacks, whereas the label system indicates a consideration of balance of plant components.

[2] Parameters, that are controlled inside a designated safety domain, or which are used as limiting values for the control approach are shown in parenthesis.

gas compositions from different origins delivered to Germany. Therefore, the considered compositions partially represent extreme cases, since the temporal resolution at the point of consumption was neglected. Consequently, the outlined extreme fluctuations of the fuel utilization factor of the stack and oxygen-to-carbon ratio are not generally applicable.

5. The general identified main control objectives include:
   a) The adjustment of the flow rate of fuel to match a designated power output, expressed frequently using the electric current, while keeping the fuel utilization factor of the stack constant or inside a safe operating domain.
   b) The change of the water vapor or recirculation gas flow rate to keep the steam- or oxygen-to-carbon ratio at a fixed value or above harmful thresholds.
   c) The manipulation of at least one of the variables, such as the air flow rate, bypass air flow rate and cathode inlet temperature, to control the stack temperature or stack temperature gradients.

6. An open loop control is frequently used to set the flow rate of fuel in correspondence to a designated electric current and fuel utilization factor of the stack. Analogously, the flow rates of water vapor or recirculation gas are set to achieve a designated steam- or oxygen-to-carbon ratio. The open loop approach was used, for instance, by D'Andrea et al. [87], Barelli et al. [88], Carré et al. [27, 29] and Gallet Segarra [28].

7. A closed loop control is usually applied to control the stack temperature or stack temperature gradients by manipulating the total or bypass air flow rates. Additionally, in a plurality of the studies, the fuel flow rate is manipulated in a closed loop to control the stack voltage. The electric current is often altered in a closed loop to achieve a designated power output, while simultaneously adjusting the fuel flow rate.

8. Closed loop controller designs cover a wide range of options from state of the art proportional controllers to advanced adaptive controllers to sophisticated general and model predictive controls. However, Murshed et al. [85] and Pohjoranta et al. [90] claimed, that high processing power and very accurate models with a high level of detail and complexity are necessary for the implementation of MPCs. Additionally, the adaption of MPCs to system and stack degradation mechanisms, as well as possible changes to the system designs are very challenging and often not straightforward, yielding a high degree of maintenance of the control. Consequently, the implementation of sophisticated controls is excluded from further evaluation, since the development and design is beyond the scope of this dissertation.

9. The focus of the majority of publications is the evaluation of the controller behavior during transient load following events, allowing for a dynamic fuel cell operation. Consequently, the plurality of works only outline segments of complete control strategies or individual control constraint tests. Additionally, many modeling approaches only account for sections of complete systems, for instance just the SOFC stack. Excluding hybrid systems, complete system strategies were only developed by Zhang et al. [66, 67], Georgis et al. [78], Sorce et al. [80], Greco et al. [81], Komatsu et al. [82], Murshed et al. [85], D'Andrea et al. [87], Mueller et al. [89], Spivey and Edgar [92] and Carré et al. [27, 29].

10. Experimental testing and validation of implemented strategies in an entire SOFC system were only published by Carré et al. [27, 29]. Gallet Segarra [28] only evaluated two of the developed natural gas quality detection strategies in an experimental setup. The remaining identified publications, at least partially, relied on validated modeling approaches, basing the control development, evaluations and conclusions on verified baselines.

Table 4.1: Literature review - Control and operating strategies of SOFC systems

Source	Unit	Controller	Fuel	Test	Manipulated variables	Controlled variables
Hydrogen or alternative fueled SOFCs						
[65]	SOFC	PI	H_2	No	$\dot{n}_{H_2}$, $\dot{n}_{O_2}$, I	$U_{f,S}$, $\triangle p_{an/ca}$, P_{el}
[66, 67]	System	-	H_2	No	$\dot{n}_{H_2}$, $\dot{n}_{a,in}$, $\dot{n}_{a,bp}$, I	P_{el}, T_S, $\triangle T_S$, $\triangle T_{an/ca,in}$, T_{bu}, $(U_{f,S})$, (U_a)
[68]	SOFC	NNPC	NH_3	No	$T_{ca,in}$	T_S
[69]	SOFC	MPC	H_2	No	$\dot{n}_{H_2}$	E_S
[70]	System	Adapative	H_2	No	$\dot{n}_{H_2}$, I	$U_{f,S}$
[71]	SOFC	PI	H_2	No	$\dot{n}_{H_2}$, $\dot{n}_{a,in}$	T_S, $U_{f,S}$
[72]	SOFC	PI	H_2	No	$x_{H_2,f}$	E_S
[73, 74]	SOFC	MPC	H_2	No	$\dot{n}_{H_2}$, $\dot{n}_{a,in}$	T_S
[75]	SOFC	GPC	H_2	No	I	P_{el}
SOFC systems with catalytic partial oxidation reformer						
[77]	System	PID	NG	No	$\dot{n}_{a,bp}$ / $\dot{n}_{a,in}$ / $\dot{n}_{NG}$	$T_{ca,in}$
SOFC systems with an external water supply						
[78]	System	PI	CH_4	No	$\dot{n}_{CH_4}$, $\dot{n}_{a,ca,in}$, $\dot{n}_{a,bp}$, $\dot{n}_{Exh,ref,bp}$	$U_{f,S}$, T_S, $T_{ca,in}$, T_{ref}
[79]	SOFC+REF	MPC	CH_4	No	$\dot{n}_{CH_4}$	E_S, $(U_{f,S})$
[80, 81]	System	PID	CH_4	No	$\dot{n}_{CH_4}$, $\dot{n}_{a,in}$, I, $P_{el,ref}$	$U_{f,S}$, T_S, T_{ref}
[82]	SOFC+REF	P/PI/PID	CH_4	No	$\dot{n}_{CH_4}$, $\dot{n}_{Steam}$, $\dot{n}_{a,in}$, I	$U_{f,S}$, Υ, T_S, P_{el}
[83]	SOFC	PI	CH_4	No	$\dot{n}_{a,in}$	$\triangle T_S$
[84]	SOFC+REF	MPC	NG	No	$\dot{n}_{NG}$	E_S, $U_{f,S}$
[85]	System	MPC	CH_4	No	$\dot{n}_{CH_4}$, $\dot{n}_{Steam}$, $\dot{n}_{a,in}$	E_S, $(U_{f,S})$, (T_S)
[86]	SOFC	MPC	CH_4	No	$\dot{n}_{CH_4}$, $\dot{n}_{a,in}$, I	$U_{f,S}$, T_S, P_{el}
[87]	System	PID	BG	No	$\dot{n}_{BG}$, $\dot{n}_{Steam}$, $\dot{n}_{a,in}$, I	$U_{f,S}$, Υ, T_S
[88]	SOFC	PID	CH_4	No	$\dot{n}_{CH_4}$, $\dot{n}_{a,in}$, I	$U_{f,S}$, T_S
[89]	System	PI	CH_4	No	$\dot{n}_{CH_4}$, $\dot{n}_{a,in}$, $\dot{n}_{a,bp}$, I	$U_{f,S}$, T_S, $T_{ca,in}$, P_{el}, $(E_{S,min})$
SOFC systems including an anode exhaust gas recirculation						
[90]	System	GPC, PID	NG	No	$T_{ca,in}$, $(\dot{n}_{NG})$, $(\dot{n}_{a,in})$	T_S, $\triangle T_S$
[92]	System	MPC	CH_4	No	$\dot{m}_{a,in}$, E_S, $T_{f,in}$, $p_{f,in}$, p_{sys}	$U_{f,S}$, Υ, U_a, $T_{S,min}$, $\triangle T_{S,radial,max}$, P_{el}
[93]	SOFC	-	CH_4	No	$\dot{n}_{a,in}$, $T_{ca,in}$, $T_{an,in}$, I	U_a, T_S, P_{el}
[29]	System	PI	NG	Yes	$\dot{n}_{NG}$, $\dot{n}_{rec}$, $\dot{n}_{a,in}$	$U_{f,S}$, Φ, T_S, (U_a), (λ), (T_{bu})
[27]	System	-	NG	Yes	$\dot{n}_{NG}$, $\dot{n}_{rec}$, $\dot{n}_{a,in}$	$U_{f,S}$, Φ, U_a, $(U_{a,max})$,(λ)
[28]	System	PI	NG	Yes	$\dot{n}_{NG}$, $\dot{n}_{rec}$, $\dot{n}_{a,in}$	$U_{f,S}$, Φ, T_S, (U_a), (λ), (T_{bu})
SOFC hybrid systems						
[94]	System+GT	PI	CH_4	No	$\dot{n}_{CH_4}$, $\dot{n}_{a,in}$	$U_{f,S}$, T_S
[95]	System+GT	PI	NG/H_2	No	$\dot{n}_f$, $\dot{n}_{a,in}$, $\dot{n}_{a,ca,rec}$, E_S	$U_{f,S}$, T_S, $\triangle T_S$, P_{el}
[96]	System+GT	PI	CH_4	No	$\dot{n}_{CH_4}$, $\dot{n}_{a,in}$	T_S, P_{el}

Source	Unit	Controller	Fuel	Test	Manipulated variables	Controlled variables
[97]	System+GT	PID, MPC	CH_4	No	$\dot{n}_{CH_4}$, $\dot{n}_{CH_4,bp}$, $\dot{n}_{a,in}$, I	$U_{f,S}$, $T_{GT,in}$, T_S, P_{el}
[98]	System+GT	PID	CH_4	No	$\dot{n}_{CH_4}$, $\dot{n}_{a,in}$, I	$P_{el,SOFC}$, $P_{el,GT}$
[99]	System+GT	PI	CH_4	No	$\dot{n}_{CH_4}$, $\dot{n}_{a,in}$, $\dot{n}_{a,bp}$, I	$U_{f,S}$, T_S, P_{el}
[100]	System+GT	PID	BG	No	$\dot{n}_f$, $\dot{n}_{Exh,bp}$, I	E_S, T_S, P_{el}
[101]	System+GT	PI	SG	No	$\dot{n}_f$, $\dot{n}_{a,in}$, $\dot{n}_{a,rec}$, $\dot{n}_{a,bp}$, I	$U_{f,S}$, $T_{ca,in}$, $T_{ca,out}$, P_{el}

As a result of the conducted literature review, this work focuses on the following contents, which are excluded or only to a minor degree addressed in the identified, relevant literature:

1. The use of measured, temporally resolved natural gas data as a basis for the evaluation of the effects of varying natural gas quality on SOFC systems, including an AEGR. Therefore, real natural gas conditions at a specific point of consumption are represented.

2. The development, implementation and long term testing of a complete system control strategy for an SOFC test rig fueled with natural gas from the grid. The strategy fulfills the previous introduced main control objectives, with an open loop control for the anode and a closed loop control for the cathode constraints.

3. The detailed quantification of the naturally occurring fluctuations of the natural gas composition at the chosen SOFC test rig location.

4. The model based validation and verification of the experimentally recorded data samples, where the model is able to reproduce the behavior of the system for the developed control approach.

5. The extension of the model to compare 23 different control approaches, based upon the ideal realization of flow rate set points at variable system locations in accordance to designated reference natural gas compositions.

6. The evaluation of the effect of direct hydrogen addition to the natural gas data base to further assess the robustness of the derived strategies.

7. The application of the derived natural gas data constraints to develop, implement and test a control logic, which can achieve ideal system behavior based solely upon the determination of a single natural gas coefficient.

4.2 Application of control scheme for SOFC system

In the following section, the setup of the evaluated SOFC test rig and the applied control strategy are presented. It should be noted that instead of the previously used molar flow rates, standard volume flow rates can be likewise adopted. The basis for this interchangeability is that all gases are considered ideal and that each volume flow is referenced to the designated standard conditions. In this work, the standard conditions for the calculation of volume flow rates are defined at a temperature and pressure level of 273.15 K and 101325 Pa, respectively. The conversion methodology, connecting the molar and volume flow rate, is outlined in equation (4.1).

$$v_{m,Std} = \frac{R\,T_{Std}}{p_{Std}} \rightarrow \dot{V}_{Std} = \dot{n}\,v_{m,Std} \tag{4.1}$$

4.2.1 SOFC test rig

The piping and instrumentation diagram (P&ID) of the evaluated SOFC test rig, including the control relevant sensor units, is outlined in Figure 4.1 [102, 103, 104, 105]. For a distinct definition of the position in the P&ID, the pipes are numbered consecutively. Analogously, connected sensors and actuators are also labeled using the related pipe number. The displayed sensor elements represent a measurement of the pressure, temperature, rotational speed, volume flow rate and electric current. It should be noted that the volume flow rates of the inlet air (201 / 202) and through the recirculation gas blower (101 / 102) are indirectly measured based upon a characteristic blower map modeling approach. The volume flow rates are determined as a function of the measured pressure difference, rotational speed, pressure and temperature at the blower inlets using the corresponding approximated blower maps and laws of similitude. A brief overview of the applied methodology and the resulting equations are outlined in appendix G. Additionally, the four selected gas sampling locations, at the natural gas inlet, reformer inlet, reformer outlet and anode outlet, are shown in the form of schematic sensor elements. The gas measurement system is explicitly described in section 4.4.1. All displayed heat exchangers (HEX 1 - 4) are designed as counter flow shell and tube heat exchangers. The air, gas and recirculation blowers are side channel compressors. The SOFC module is comprised of 6 individual stacks, including 120 electrolyte support cells, each. The rated nominal power output of the SOFC module at a current of 24 A is approximately 13 kW.

Fresh ambient air is supplied to the air flow path (201) by the air blower. The air is further distributed to four air pathways that are equipped with motor-adjustable electrical valves to control the individual flow rates. Line 203 is the main air path for air heating (in HEX 1), 220 is the main air bypass for the controllability of the cathode inlet temperature, 230 provides cooling air to the anode pathway (in HEX 2) to prevent harmful inlet temperatures at the recirculation gas blower, and 240 supplies air to the start up burner. The air pathways 203, 220 and 230 re-merge upstream of the cathode inlet, providing adequate stack cooling and supplying sufficient oxygen for the electrochemical utilization. At the cathode outlet, the partially depleted air (208) is split into two portions. One portion (209) supplies heat to the steam reformer, which is designed as a parallel flow shell and tube heat exchanger with the air on the shell side. The other fraction (211) bypasses the reformer and re-merges with the colder reformer exhaust air (210).

The system can be fueled either with methane (011) or natural gas (001). Natural gas is desulfurized in a packed bed reactor. A simultaneous feed of methane and natural gas is prevented by mutual interlocking with the help of two on-off solenoid valves. During an operation with methane, the bottled pressure is adjusted with a pressure reducer, whereas during a natural gas feed, the grid pressure has to be increased using a gas blower. The adjustment of the pressure to a designated level is necessary to run the fuel through the system and enhance the controllability of the mass flow controllers (MFC). The fuel is supplied through the controllable MFCs (006 and 008) to the anode pathway (007) or directly to the start up burner (009). During nominal operation, in the anode pathway, fresh fuel (007) is merged with a fraction of the anode exhaust gas (110). The recirculation gas blower supplies the mixture (101) to a first preheating stage (HEX 3), followed by the reformer and then a final preheating stage (HEX 4). The individual tubes of the reformer are filled with noble metal catalyst in bulk. Downstream of HEX 4, the hot and preconditioned fuel (106) is utilized in the anode. The anode exhaust gas (107) is used for the heat transfer in HEX 4 and HEX 3. Ultimately, downstream of HEX3, the anode exhaust (109) is split into the recirculation (110) and burner gas (111).

The burner portion of the anode exhaust (111) is merged with the complete depleted cathode air (212). The mixture is fed to the catalytic burner, which is designed as a catalyst coated monolith. The burner exhaust gas (304) is finally used for air heating in HEX 1, before being discharged to the environment (305).

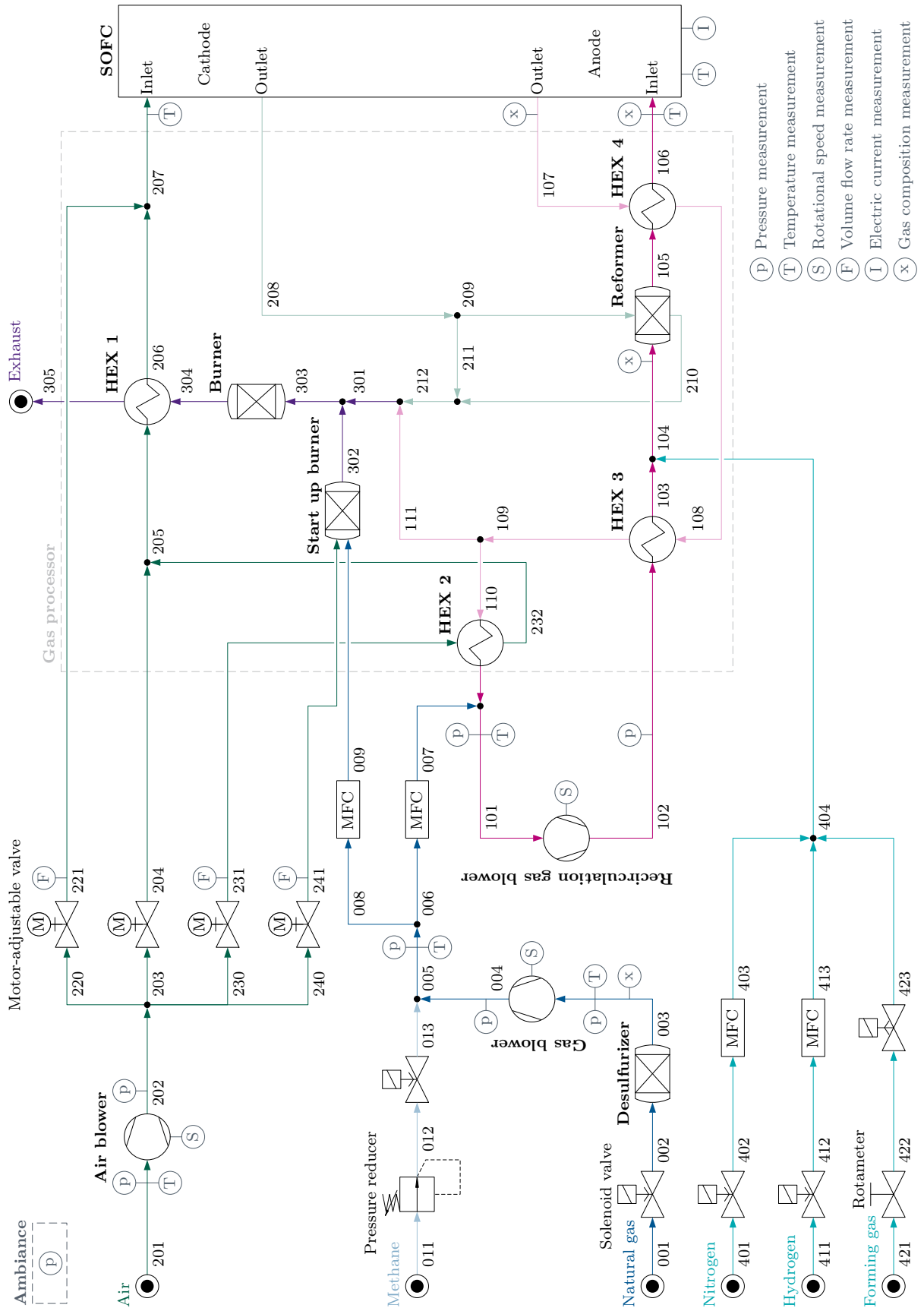

Figure 4.1: Piping and instrumentation diagram of SOFC test rig

During part load operation, the start up burner can be supplied with fuel (009) and air (241) to provide additional heat to the system. Additionally, during system start up, the anode pathway is not supplied with fresh fuel (007), but a mixture of nitrogen (403) and hydrogen (413), subsequently labeled as protection gas. The protection gas is fed to the system, between the HEX 3 and reformer, for anode oxidation protection purposes. The nitrogen to hydrogen ratio is controlled by a 4:1 proportion with the help of two MFCs. The protection gas flow behavior through the anode pathway and air flow through the cathode pathway are analogous to the previously described nominal operation. The exception is the start up burner, which is supplied with air (241) and fuel (009). The start up burner exhaust (302) is combined with the mixture of protection gas and air (301), which is fed to the catalytic burner, where the hydrogen portion is utilized. Therefore, additional heat, for the air heating in HEX 1, is provided. During nominal operation the nitrogen and hydrogen feeds are locked by two on-off solenoid valves.

Additionally, during possible emergency shutdowns of the system, for instance a breakdown of the external power supply, the anode oxidation protection is provided using forming gas (423). This gas is a pressurized bottled mixture of 5 % hydrogen in nitrogen and is supplied to the system with the help of a rotameter and a solenoid valve, which is normally open with zero current.

4.2.2 Overview of applied control strategy in SOFC test rig

The applied control strategy is schematically divided into 13 independent procedures, including six transient, four steady and three emergency operating modes. The different procedures and their connections are shown in Figure 4.2.

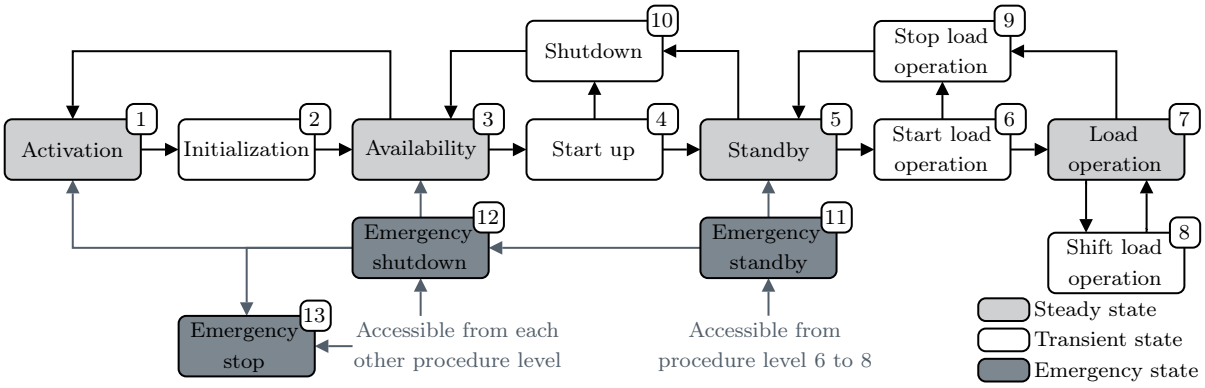

Figure 4.2: Operating procedures of control strategy

It should be noted that beside the main procedures, alarm thresholds are defined, which are divided into four separate levels. The first level displays only a warning message, whereas a permanent exceeding of the second, third or fourth level yields an emergency standby, shutdown or stop, respectively. The following main procedures are defined in the programmable logic controller [106]:

1. Activation, including the supply with electricity and booting of the programmable logic controller.

2. Initialization, including the check of the system components, actuators and sensors.

3. Availability, including the readiness of the system components, actuators and sensors for operation.

4. Start up, including the heat up of the system to reach load operating conditions.

5. Standby, including the maintenance of a hot system state via steady supply of heat using the start up burner.
6. Start load operation, including the first ramp up of the current with a designated rate, using pure bottle hydrogen up to a current of 3 A, prior to the supply of natural gas or methane.
7. Load operation, including nominal and part load with natural gas or methane at a designated electric current.
8. Shift load operation, including the ramp up and ramp down of the electric current.
9. Stop load operation, including the controlled decrease of the electric current with a designated rate.
10. Shutdown, including the controlled cool down of the system.
11. Emergency standby, triggered by minor system failures or second level alarms during load operation (procedures 6 to 9), yields a safe return to the standby.
12. Emergency shutdown, triggered by major system failures or third level alarms, yields a complete safe system shutdown.
13. Emergency stop, triggered by critical or harmful system states or fourth level alarms, yields an instantaneous shutoff by disconnecting the system from any electrical supply.

Subsequently, the control strategy of the SOFC test rig is outlined in detail for the natural gas operation under load operation (Procedure 7). However, with two minor adjustments the methane operation can be analogously realized. The two adjustments are the adaption of the reference gas concentration ($x_{\mathrm{NG,R}}$) to represent pure methane and bypassing the speed control of the natural gas blower ($n_{003,\mathrm{SP}}$). The applied designated set point values for nominal operation are outlined in Table 4.2. Additionally, it should be noted that procedures 4 to 12 can all be realized using the same control logic via bypassing or deactivating controllers and adjusting set point values. However, except for procedure 7, the remaining procedure steps are not the focus of this work since they are affected to a minor degree by varying natural gas quality.

Table 4.2: Set point values for nominal operation

Set point	Label	Unit	Value
Electric current	I_{SP}	A	24
Oxygen-to-carbon ratio	Φ_{SP}	-	2
Fuel utilization factor of the stack	$U_{\mathrm{f,S,SP}}$	%	75
Cathode inlet temperature	$\vartheta_{207,\mathrm{SP}}$	°C	650
Maximum stack temperature	$\vartheta_{\mathrm{S,max,SP}}$	°C	850
Recirculation blower inlet temperature	$\vartheta_{101,\mathrm{SP}}$	°C	150

As shown in Figure 4.3, the control logic of the SOFC test rig can be schematically divided into two major realms, the processing of the set points and process values. Top level set point values are defined in the control console based upon the operating range and further limiting operating requirements of the system components. Those top level set points are either directly transferred or further processed to yield set points for the corresponding actuators of the SOFC system. The further processing comprises a handling of the set points, in an additional calculation step or in a PID controller, to generate appropriate set points.

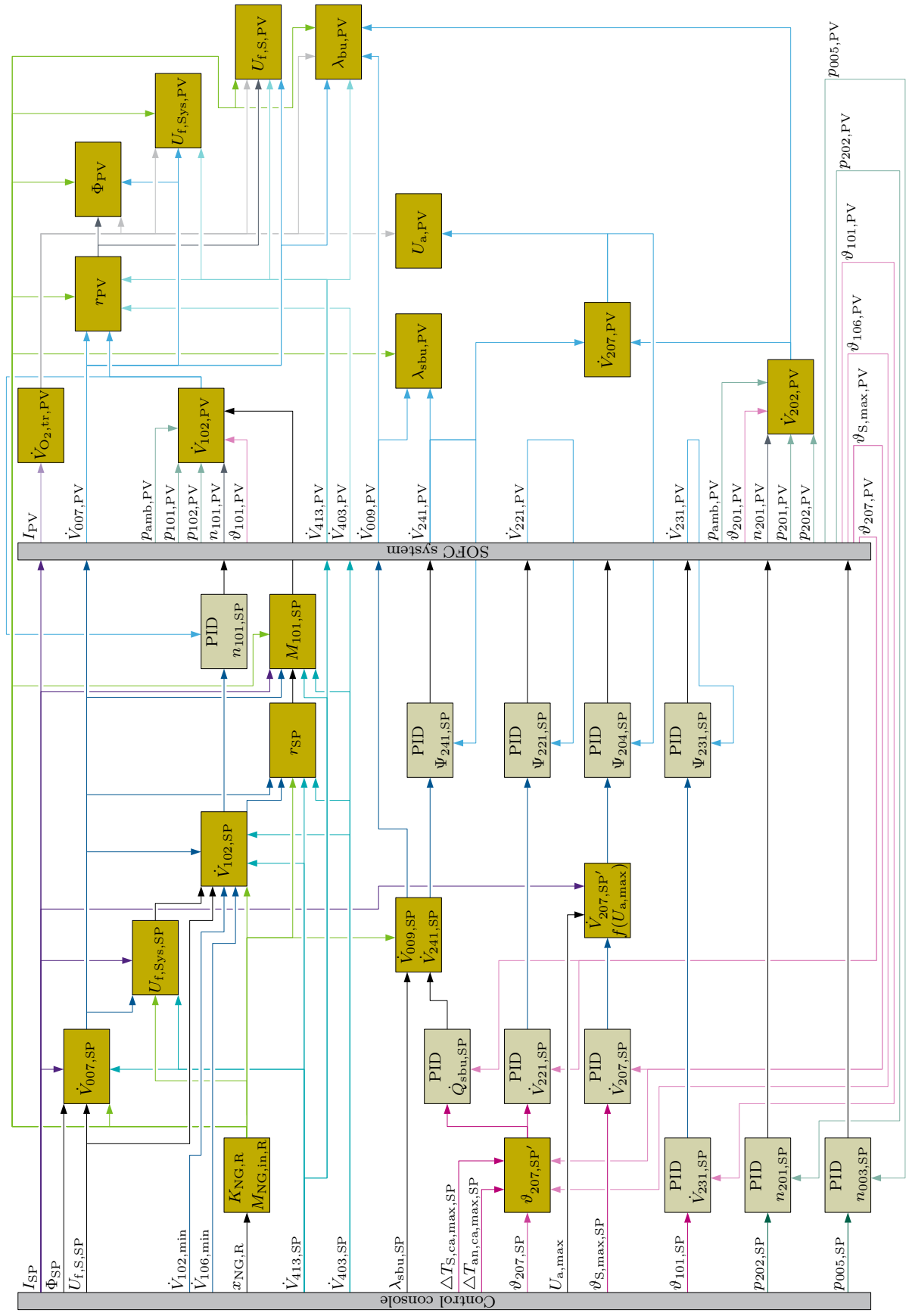

Figure 4.3: Overview of control logic of SOFC test rig

As shown on the top left in Figure 4.3, the electric current set point (I_{SP}) is one of the major leading variables and is directly applied to the inverter. In addition to I_{SP}, the designated oxygen-to-carbon ration (Φ_{SP}), fuel utilization factor of the stack ($U_{\mathrm{f,S,SP}}$) and defined reference natural gas composition ($x_{\mathrm{NG,R}}$), expressed by the corresponding combined natural gas coefficient[3] ($K_{\mathrm{NG,R}}$), are used to calculate the volume flow rate set points of natural gas $\left(\dot{V}_{007,\mathrm{SP}}\right)$ and at the reformer inlet $\left(\dot{V}_{102,\mathrm{SP}}\right)$, as well as the fuel utilization factor of the system ($U_{\mathrm{f,Sys,SP}}$) and recirculation ratio (r_{SP}).[4] Additionally, for the calculation of $\dot{V}_{102,\mathrm{SP}}$, two limiting flow rates have to be considered. The restrictions are the minimum flow rate through the blower $\left(\dot{V}_{102,\mathrm{min}}\right)$, preventing reverse flows, and the limiting anode inlet flow rate $\left(\dot{V}_{106,\mathrm{min}}\right)$, ensuring a uniform distribution of gas inside the stack.[5] Therefore, in transient operation modes, for instance during the beginning of the power ramp up, the applied set points of the fuel utilization factor of the stack and oxygen-to-carbon ratio are not reached due to the restrictions of $\dot{V}_{102,\mathrm{SP}}$.

The set point $\dot{V}_{007,\mathrm{SP}}$ is directly applied to the natural gas MFC, whereas $\dot{V}_{102,\mathrm{SP}}$ is further processed in a PID controller, comparing it to its process value $\left(\dot{V}_{102,\mathrm{PV}}\right)$, ultimately yielding a blower speed set point of the recirculation blower ($n_{101,\mathrm{SP}}$). Furthermore, as outlined on the bottom left in Figure 4.3, to guarantee a sufficient controllability of the natural gas MFC, the pressure at its inlet ($p_{005,\mathrm{SP}}$) is set with the help of a PID controller, which adjusts the rotational speed of the natural gas blower ($n_{003,\mathrm{SP}}$). Additionally, due to the applied indirect determination of the volume flow rate at the recirculation gas blower, using characteristic blower map modeling, the molar mass set point of the gas at the blower inlet[6] ($M_{101,\mathrm{SP}}$) has to be estimated.

For the sake of completeness, the volume flow rate set points of the nitrogen $\left(\dot{V}_{403,\mathrm{SP}}\right)$ and hydrogen $\left(\dot{V}_{413,\mathrm{SP}}\right)$ protection gas and their corresponding connection to the previously introduced set point calculations are shown. However, the hydrogen and nitrogen feeds are only active during transient system states, for instance heat up, shutdown, emergency stop and during the beginning of the power ramp up. Therefore, the influences on the calculation of the different set points and also process values, in form of adjusted equations, are not outlined, since the nominal operation is the focus of this work. Additionally, a complete abandonment of auxiliary bottled gases is desired even during transient operation. A possible option for an auxiliary bottled gas free operation is the humidification of natural gas using a start up evaporator, to generate a hydrogen rich fuel in the reformer without the risk of carbon deposition.

The temperature control of the system comprises of three major set points, the cathode inlet temperature ($\vartheta_{207,\mathrm{SP}}$), the maximum stack temperature ($\vartheta_{\mathrm{S,max,SP}}$) and the inlet temperature of the recirculation gas blower ($\vartheta_{101,\mathrm{SP}}$). The control units are each implemented in the form of cascaded controllers, where the temperature set points and the corresponding process values ($\vartheta_{207,\mathrm{PV}}$, $\vartheta_{\mathrm{S,max,PV}}$ and $\vartheta_{101,\mathrm{PV}}$) are used to generate the volume flow rate set points $\left(\dot{V}_{207,\mathrm{SP}}\right.$, $\dot{V}_{221,\mathrm{SP}}$ and $\left.\dot{V}_{231,\mathrm{SP}}\right)$. The volume flow rate set points are each further processed in a second PID controller using the corresponding volume flow rate process values $\left(\dot{V}_{207,\mathrm{PV}}\right.$, $\dot{V}_{221,\mathrm{PV}}$ and $\left.\dot{V}_{231,\mathrm{PV}}\right)$, ultimately yielding a valve position set point for the motor-adjustable valves ($\Psi_{204,\mathrm{SP}}$, $\Psi_{221,\mathrm{SP}}$ and $\Psi_{231,\mathrm{SP}}$). The pressure at the inlets of the motor-adjustable valves ($p_{202,\mathrm{SP}}$) is set with the help of a PID controller, which adjusts the rotational speed of the air blower ($n_{201,\mathrm{SP}}$) to guarantee an enhanced controllability of the valves. Additionally, for the control of the

[3] The combined natural gas coefficient includes $K_{\lambda,\mathrm{R}}$, $K_{\triangle\mathrm{an,R}}$, $K_{\mathrm{C,R}}$, $K_{\mathrm{O,R}}$ and $K_{\mathrm{e^-,R}}$, calculated based upon equations (2.6), (2.15), (3.3), (3.4) and (3.7).

[4] The calculation of $\dot{V}_{007,\mathrm{SP}}$, $\dot{V}_{102,\mathrm{SP}}$, $U_{\mathrm{f,Sys,SP}}$ and r_{SP} are shown in equations (H.1), (H.4), (H.2) and (H.5) in appendix H.1.

[5] The limits of $\dot{V}_{102,\mathrm{min}}$ and $\dot{V}_{106,\mathrm{min}}$ are defined as 0.6 and 6.0 $\frac{\mathrm{m}^3}{\mathrm{h}}$, respectively.

[6] The calculation of $M_{101,\mathrm{SP}}$ is shown in equation (H.6) in appendix H.1.

maximum stack temperature, the maximal tolerable air utilization factor ($U_{\mathrm{a,max}}$) of 0.25 has to be considered for the scaling of $\dot{V}_{207,\mathrm{SP}}$ to prevent oxygen starvation in the cathode pathway. The limitation of the volume flow rate at the cathode inlet to a minimal tolerable value[7] $\left(\dot{V}_{207,\mathrm{SP}'}\right)$, due to the exceeding of $U_{\mathrm{a,max}}$, can result in reduced stack temperatures. However, during nominal operation, the process value of the air utilization factor ($U_{\mathrm{a,PV}}$) is remarkably lower than $U_{\mathrm{a,max}}$. Therefore, the applied limitation is considered strictly as a safety constraint. The temperature set point of the cathode inlet is further subjected to two limitations, yielding an adjusted cathode inlet temperature set point[8] ($\vartheta_{207,\mathrm{SP}'}$). First, the difference between $\vartheta_{207,\mathrm{SP}}$ and the anode inlet temperature ($\triangle T_{\mathrm{an,ca,max,SP}}$) should not be higher than 175 K. Second, the temperature difference between $\vartheta_{207,\mathrm{SP}}$ and the maximum stack temperature ($\triangle T_{\mathrm{S,ca,max,SP}}$) should not exceed 100 K to prevent severe thermal stress. The two described limitations are particularly relevant during the heat up since the stack and anode flow path are colder than the preheated air. Therefore, the start up burner heat flow rate $\left(\dot{Q}_{\mathrm{sbu,SP}}\right)$ is also linked to $\vartheta_{207,\mathrm{SP}'}$, preventing an excessively steep heat up of the system. Based upon the resulting $\dot{Q}_{\mathrm{sbu,SP}}$, the volume flow rate set points of natural gas $\left(\dot{V}_{009,\mathrm{SP}}\right)$ and air $\left(\dot{V}_{241,\mathrm{SP}}\right)$ to the burner[9] are calculated using a designated air-to-fuel equivalence ratio set point ($\lambda_{\mathrm{sbu,SP}}$). Once more, $\dot{V}_{009,\mathrm{SP}}$ is directly applied to the start up burner MFC, whereas $\dot{V}_{241,\mathrm{SP}}$ and its corresponding process value $\left(\dot{V}_{241,\mathrm{PV}}\right)$ are processed in a second PID controller to generate a valve position set point for the motor-adjustable valve ($\Psi_{241,\mathrm{SP}}$).

The handling of the process values is displayed on the right in Figure 4.3. The process value of the electric current (I_{PV}) is used to calculate the process value of the volume flow rate of transferred oxygen inside the stack $\left(\dot{V}_{\mathrm{O_2,tr,PV}}\right)$. Consecutively, the process values of the natural gas $\left(\dot{V}_{007,\mathrm{PV}}\right)$ and reformer inlet volume flow rate $\left(\dot{V}_{102,\mathrm{PV}}\right)$ are used in connection with $\dot{V}_{\mathrm{O_2,tr,PV}}$ to calculate the process values of the recirculation ratio (r_{PV}), oxygen-to-carbon ratio (Φ_{PV}), fuel utilization factor of the system ($U_{\mathrm{f,Sys,PV}}$) and fuel utilization factor of the stack ($U_{\mathrm{f,S,PV}}$).[10] As previously outlined in section 4.2.1, $\dot{V}_{102,\mathrm{PV}}$ is not directly measured using a flow meter, but determined by a virtual sensor using characteristic blower map modeling. Therefore, $\dot{V}_{102,\mathrm{PV}}$ is calculated as a function of the pressure ($p_{101,\mathrm{PV}}$) and temperature ($\vartheta_{101,\mathrm{PV}}$) at the blower inlet, the pressure at the blower outlet ($p_{102,\mathrm{PV}}$), the ambient pressure ($p_{\mathrm{amb,PV}}$), the rotational speed of the blower ($n_{101,\mathrm{PV}}$), as well as $M_{101,\mathrm{SP}}$. Analogously, the process value of the complete air inlet volume flow rate[11] $\left(\dot{V}_{202,\mathrm{PV}}\right)$ is determined as a function of the pressure ($p_{201,\mathrm{PV}}$) and temperature ($\vartheta_{201,\mathrm{PV}}$) at the blower inlet, the pressure at the blower outlet ($p_{202,\mathrm{PV}}$), the ambient pressure ($p_{\mathrm{amb,PV}}$) and the rotational speed of the blower ($n_{201,\mathrm{PV}}$). In contrast to the recirculation blower, the estimation of the volume flow rate at the air blower is not subjected to the estimation of the molar mass since the composition of air is assumed to be identical to standard air conditions, where the nitrogen and oxygen mole fractions have constant values of 0.791 and 0.209, respectively. The process value of the air-to-fuel equivalence ratio of the burner ($\lambda_{\mathrm{bu,PV}}$) is calculated using $\dot{V}_{007,\mathrm{PV}}$, $\dot{V}_{202,\mathrm{PV}}$, $\dot{V}_{\mathrm{O_2,tr,PV}}$ and the process values of the natural gas flow rate to the start up burner $\left(\dot{V}_{009,\mathrm{PV}}\right)$. Likewise, the process value of the air-to-fuel equivalence ratio of the start up burner ($\lambda_{\mathrm{sbu,PV}}$) can be determined based upon $\dot{V}_{009,\mathrm{PV}}$ and the process values of the air flow rate to the start up burner $\left(\dot{V}_{241,\mathrm{PV}}\right)$. The air utilization factor process value is computed as a function of $\dot{V}_{\mathrm{O_2,tr,PV}}$ and the process value of the cathode inlet

[7] The calculation of $\dot{V}_{207,\mathrm{SP}'}$ is shown in equation (H.7) in appendix H.1.
[8] The calculation of $\vartheta_{207,\mathrm{SP}'}$ is shown in equation (H.8) in appendix H.1.
[9] The calculation of $\dot{V}_{009,\mathrm{SP}}$ and $\dot{V}_{241,\mathrm{SP}}$ are shown in equations (H.9) and(H.10) in appendix H.1.
[10] The calculation of $\dot{V}_{102,\mathrm{PV}}$, $\dot{V}_{\mathrm{O_2,tr,PV}}$, r_{PV}, Φ_{PV}, $U_{\mathrm{f,Sys,PV}}$ and $U_{\mathrm{f,S,PV}}$ are shown in equations (G.6), (H.11), (H.12), (H.13), (H.14) and (H.15) in appendices G and H.2.
[11] The calculation of $\dot{V}_{202,\mathrm{PV}}$ is shown in equation (G.5) in appendix G.

volume flow rate $\left(\dot{V}_{207,\mathrm{PV}}\right)$, which is equal to $\dot{V}_{241,\mathrm{PV}}$ subtracted from $\dot{V}_{202,\mathrm{PV}}$.[12] The volume flow rates to the start up burner are considered for the calculation of $\lambda_{\mathrm{bu,PV}}$ and $\dot{V}_{207,\mathrm{PV}}$ since the start up burner can be active during part load operation, to supply additional heat to the system. Additionally, for safety reasons, even during nominal system operation, the start up burner is always supplied with a minimal air flow rate to prevent a reverse flow of the hot combustible mixture of the anode and cathode exhaust gas.

In brief, the outlined control logic of the SOFC test rig follows an open loop control approach in the fuel pathway with the electric current, oxygen-to-carbon ratio and fuel utilization factor of the stack as the leading system set points. The three leading set points are used to generate the primary actuator set points for the MFC and recirculation blower, in the form of a natural gas mass flow rate and a reformer inlet volume flow rate. The temperature and pressure levels in the system are maintained using a closed loop control approach. It should be noted, that the temperature of the reformer is not actively controlled. However, the reformer can be kept inside a safe operating temperature range of around 600 °C, due to the heating with hot cathode exhaust air and the reformer design as a parallel flow shell and tube heat exchanger. Subsequently, the focus of this dissertation is the evaluation of the effect of changing natural gas quality on the chosen control approach in the fuel pathway. During nominal operation, the control of the temperature and pressure levels is simple and straightforward. Consequently, for the subsequent outlined experimental data, the pressure and temperature control objectives are always sufficiently satisfied and therefore, the results are not outlined in further detail. In the following subsection, the basic constraints of the chosen control approach are used to derive the analytic influence of varying natural gas quality on the characteristic parameters of the fuel pathway.

4.2.2.1 Fuel control strategy during natural gas quality fluctuations - Natural gas mass flow rate CS 1

As outlined in the previous subsection, the volume flow rate set points of natural gas and at the reformer inlet are defined based upon a chosen reference gas composition. The reference gas composition was determined prior to the start of the commissioning of the SOFC test rig, based upon the annual average natural gas composition of the year 2013 at the setup location in Renningen. The annual average gas composition and the corresponding natural gas coefficients are displayed in Table 4.3, using the temporally resolved natural gas data set of Renningen in 2013, which is displayed in Figure 3.4.

Table 4.3: Chosen reference natural gas composition and corresponding gas coefficients for SOFC test rig

Species i	CH_4	C_2H_6	C_3H_8	C_4H_{10}	CO_2	N_2	H_2
Reference mole fraction $x_{\mathrm{NG,R}}$	0.9327	0.0346	0.0059	0.0024	0.0095	0.0150	0.0000
Gas coefficient / Molar mass	$K_{\mathrm{C,R}}$	$K_{\mathrm{O,R}}$	$K_{\mathrm{H,R}}$	$K_{\mathrm{N,R}}$	$K_{\mathrm{e^-,R}}$	$K_{\triangle\mathrm{an,R}}$	$M_{\mathrm{NG,in,R}}$
Value	1.0384	0.0190	4.0089	0.0300	8.1245	2.0578	17.2372

As long as all characteristic gas coefficients of a given supplied natural gas do not deviate from the chosen reference values, the defined set point values of the fuel utilization factor and oxygen-to-carbon ratio can be ideally realized. During a deviation of the current and reference natural gas state, the set points can not be realized since the designated volume flow rate

[12] The calculation of $\lambda_{\mathrm{bu,PV}}$, $\lambda_{\mathrm{sbu,PV}}$, $\dot{V}_{207,\mathrm{PV}}$ and $U_{\mathrm{a,PV}}$ are shown in equations (H.16), (H.17), (H.18) and (H.19) in appendix H.2.

set points do not match the current natural gas state. For an adjustment of the volume flow rate set points, the natural gas compositions or characteristic coefficients need to be steadily determined to match the current state. However, a sensor for the continuous tracking of the natural gas quality was not initially implemented in the SOFC test rig. Therefore, in a first order assumption, it is considered that the MFC keeps the natural gas mass flow rate constant, independent of the change in gas quality. The natural gas mass flow rate is distinctly defined by the applied natural gas volume flow rate set point to the MFC and the molar mass of the chosen reference state ($M_{\mathrm{NG,in,R}}$). Additionally, it is assumed that the designated reference reformer inlet volume flow rate set point is kept constant, even during natural gas quality fluctuations.

Both assumptions can be applied to calculate the deviation of the characteristic system parameters, $U_{\mathrm{f,S}}$, r and Φ , between any fluctuating (F) and the designated reference (R) state. The two basic constraints of a constant natural gas mass flow rate and a constant reformer inlet molar or volume flow rate are shown in equations (4.2) and (4.3).

$$\dot{m}_{\mathrm{NG,in,R}} = \dot{m}_{\mathrm{NG,in,F}} \tag{4.2}$$

$$\dot{n}_{\mathrm{ref,in,R}} = \dot{n}_{\mathrm{ref,in,F}} \tag{4.3}$$

By expressing the mass flow rate constraint as a molar flow rate constraint, using the molar masses of the fluctuating and reference states, and applying the result to the reformer inlet molar flow rate constraint in combination with equation (2.18), the recirculation ratio of the fluctuating state (r_{F}) can be obtained, as outlined in equation (4.4)[13]. The result is only valid for the central assumption that all hydrocarbons are completely converted at the anode outlet, as previously applied for the derivation of the molar system balance in section 2.2.2.2.

$$r_{\mathrm{F}} = \frac{M_{\mathrm{NG,in,F}}\,(1 + r_{\mathrm{R}}\,K_{\triangle\mathrm{an,R}}) - M_{\mathrm{NG,in,R}}\,(1 - r_{\mathrm{R}})}{M_{\mathrm{NG,in,F}}\,(1 + r_{\mathrm{R}}\,K_{\triangle\mathrm{an,R}}) + K_{\triangle\mathrm{an,F}}\,M_{\mathrm{NG,in,R}}\,(1 - r_{\mathrm{R}})} \tag{4.4}$$

The mass flow rate constraint can be used, in combination with equations (2.3) and (2.4), to express the fuel utilization factor of the stack of the fluctuating state ($U_{\mathrm{f,S,F}}$) as a function of the gas coefficients, molar masses and the designated characteristic system parameter of the fluctuating and reference states, as shown in equation (4.5)[14].

$$U_{\mathrm{f,S,F}} = \frac{U_{\mathrm{f,S,R}}\,K_{\mathrm{e^-,R}}\,M_{\mathrm{NG,in,F}}\,(1 - r_{\mathrm{F}})}{K_{\mathrm{e^-,F}}\,M_{\mathrm{NG,in,R}}\,(1 - r_{\mathrm{R}}\,(1 - U_{\mathrm{f,S,R}})) - r_{\mathrm{F}}\,U_{\mathrm{f,S,R}}\,K_{\mathrm{e^-,R}}\,M_{\mathrm{NG,in,F}}} \tag{4.5}$$

As previously outlined in section 2.2.1.4, for two known characteristic system parameters, the third one can be uniquely determined. Therefore, the oxygen-to-carbon ratio of the fluctuating state (Φ_{F}) can be determined based upon the two derived characteristic parameters and the gas coefficients of the fluctuating state, as shown in equation (4.6) using equation (2.2).

$$\Phi_{\mathrm{F}} = \frac{K_{\mathrm{O,F}}}{K_{\mathrm{C,F}}} + \frac{U_{\mathrm{f,S,F}}}{2}\,\frac{K_{\mathrm{e^-,F}}}{K_{\mathrm{C,F}}}\left(\frac{r_{\mathrm{F}}}{1 - r_{\mathrm{F}} + r_{\mathrm{F}}\,U_{\mathrm{f,S,F}}}\right) \tag{4.6}$$

In conclusion, equations (4.4), (4.5) and (4.6) can be used to predict the behavior of the characteristic system parameters for any given natural gas quality fluctuation in correspondence to the chosen natural gas reference composition and designated characteristic parameters. The outlined applied fuel control methodology, with a constant natural gas mass flow rate and

[13] The derivation of the recirculation rate of the fluctuating state is shown in appendix N.2.1.
[14] The derivation of the fuel utilization factor of the fluctuating state is shown in appendix N.1.

constant reformer inlet molar or volume flow rate, is further referred to as the natural gas mass flow rate control scheme 1 (NM_1).

The derived analytic equations are used as the basis for a modeling approach, evaluating the deviation of the resulting system behavior from the assumed reference set points. Additionally, the results are also evaluated and validated using the recorded experimental data of the test rig.

4.2.2.2 Ideal CS

In contrast to the NM_1, the ideal control scheme (IC_0) is defined as the baseline for perfect system behavior and is consecutively used as the desired, optimal comparison case. For the realization of the ideal control scheme, it is assumed that the system is equipped with a perfect natural gas composition detection, allowing for the continuous adjustment of the reference gas composition in accordance with the real natural gas state. Additionally, ideal behavior of all actuators and sensors is assumed, yielding a perfect match for all set points and process values. Therefore, for any given natural gas composition, the ideal control scheme yields an adjustment of the flow rates to perfectly match the set point values, ultimately realizing constant process values of the fuel utilization factor and oxygen-to-carbon ratio.

4.3 Black box system modeling

For the evaluation of the effect of varying natural gas quality on the characteristic parameters of an SOFC system including an AEGR, using a designated control approach for the fuel constraints, a black box system model is developed. The simulated system is a simplified version of the SOFC test rig, focusing on the evaluation of the fuel constraints of the system under steady state load operation. Consequently, it is assumed that the thermal management of the system is robust and functional based upon the straightforward and simple control using the air flow rate. Therefore, the thermal behavior and effects of changing temperature levels are not addressed in the model. The air bypasses are neglected since all split flows of air are, at the latest, merged in front of the cathode inlet. Additionally, the desulfurizer, the start up burner, the heat exchangers, the blowers, as well as the protection and forming gas inlets are not considered. The resulting, simplified system approach is displayed in Figure 4.4.

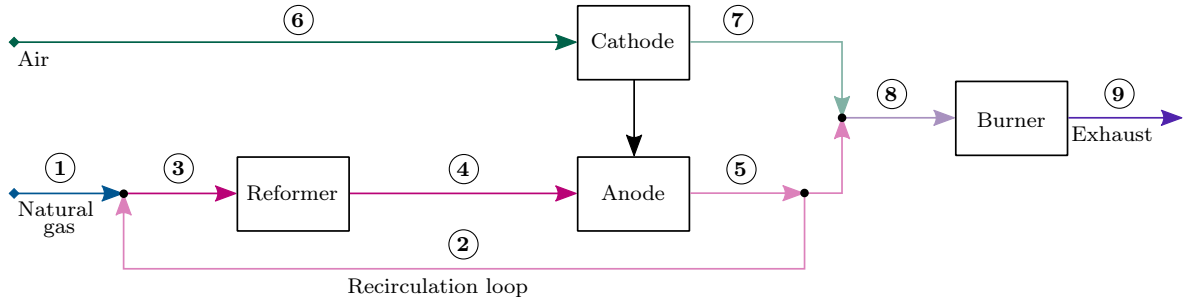

Figure 4.4: Simplified system approach for black box system model including the 9 designated system calculation positions

In brief, the model solves the complete system balance considering, among others, 10 major species: Methane, ethane, propane, butane, carbon dioxide, nitrogen and hydrogen, carbon monoxide, water vapor and oxygen. The outputs include the compositions and flow rates at 9 designated system positions: (1) The natural gas inlet; (2) The recirculation loop; (3) The reformer inlet; (4) The reformer outlet, which is identical to the anode inlet; (5) The anode outlet; (6) The air inlet, which is identical to the cathode inlet; (7) The cathode outlet; (8) The burner inlet; (9) The burner outlet.

The used system structure is identical to the previously introduced simplified system approach, which was used to derive the conservation equations in section 2.2.2. Consequently, the previously derived set of equations can be implemented for the independent verification and expression of general system constraints.

4.3.1 Background and methodology

As outlined in section 4.2.2.1, a set of steady state equations can be derived to evaluate the effect of changing natural gas quality on the characteristic system parameters. Therefore, the necessity of the iterative solving of a system of equations can be bypassed for the calculation of flow rates and gas compositions, since the fuel utilization factor of the stack and recirculation ratio of a fluctuating natural gas state can be uniquely determined. Consequently, the steady state of the complete SOFC system can be simply and straightforwardly computed using appropriate system boundary conditions and physical assumptions. It should be noted that the following description of the calculation methodology can be used to solve the complete system balance for a designated reference natural gas state, as well as the NM_1 and IC_0 for any chosen natural gas data set.

Ideal equilibrium gas compositions can be calculated for given temperature and pressure levels at the reformer and anode outlet based upon the fuel utilization factor, recirculation ratio and gas coefficients of natural gas, in correspondence with the element system balance, outlined in section 2.2.2.4. For a designated electric current, the resulting equilibrium gas compositions are used to calculate the corresponding molar and mass flow rates at the reformer and anode outlet using the fuel utilization factor of the stack and the electron balance equations (2.26) and (2.27)[15], as well as the respective molar masses. Additionally, the molar and mass flow rates of natural gas and air can be computed based upon equations (2.4) and (2.5), for a given current and utilization factor. Excluding the burner outlet, the flow rates and compositions of the recirculation gas, at the reformer inlet, at the cathode inlet, at the cathode outlet and at the burner inlet can be calculated using the molar balance equations, as outlined in section 2.2.2.2. The calculation methodology of the fuel flow path also includes the calculation of the recirculation molar flow rate as a function of the recirculation ratio and anode outlet molar flow rate. Finally, the reformer inlet states can be determined based upon the mixture of fresh natural gas and recirculation gas. In the air flow path, the transfer of oxygen inside of the stack has to be taken into account for the calculation of the cathode outlet conditions, as previously outlined in equation (2.21). By determining the corresponding molar masses, as a function of the composition, the respective mass flow rates can also be computed. Lastly, the burner outlet equilibrium composition can be determined for a given temperature and pressure level using the previously calculated inlet mixture conditions. The flow rate at the outlet is solved using the mass balance equation (2.12) and the corresponding molar mass of the equilibrium state at the burner outlet. As a result, the molar and mass flow rates, as well as the gas compositions can be obtained at all 9 designated system positions, based upon the fuel utilization factor of the stack, recirculation ratio, natural gas composition, air utilization factor and given system boundary conditions.

After the complete calculation, the system mass balance equations, shown in section 2.2.2.1, are used to verify the validity of the calculation. Additionally, for the NM_1, the basic constraint equations (4.2) and (4.3) are used for a further proof of validity of the methodology via a comparison with the reference state results. Therefore, the methodology includes an inherent validation of the mass balance, species conservation and the analytically derived functions for the calculation of the fuel utilization factor and recirculation ratio of the fluctuating state.

[15] It should be noted that the molar flow rate of electrons at the reformer and anode outlet can be expressed as the product of the total molar flow rate and the corresponding electron coefficient at the designated system point.

The described set of steady state equations and methodology are implemented in MATLAB R2011b using the object-oriented software tool Cantera [58] to calculate the equilibrium composition, thermophysical and chemical properties at the respective system positions. The modeling methodology is schematically displayed in Figure 4.5.

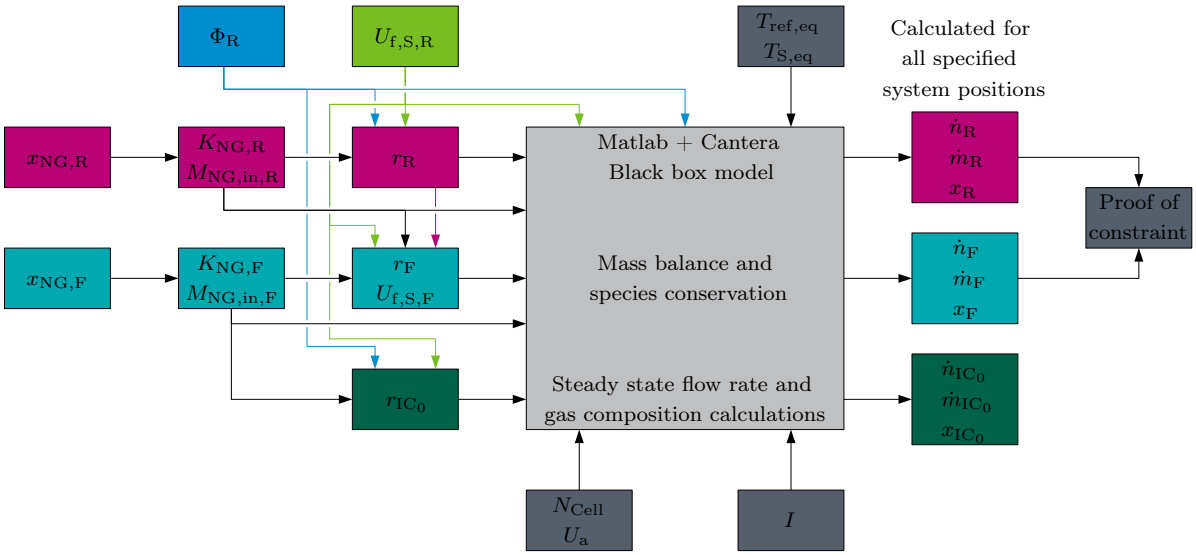

Figure 4.5: Overview of modeling methodology

The depicted approach can be used to calculate the flow rates and compositions at all specified system positions for the reference, fluctuating and ideal states by simply modifying the input values of the fuel utilization factor of the stack and recirculation ratio. The reference and ideal states are determined based upon the set of equations outlined in section 2.2. Therefore, the set points of the fuel utilization factor and oxygen-to-carbon ratio can be ideally realized. The input values of the fluctuating state are calculated in relation to the reference state, as introduced in section 4.2.2.1 for the NM_1. Any of the previously introduced temporally resolved natural gas data sets can be used to represent the fluctuating natural gas state. The reference can be independently defined or computed as a function of the used data set, for instance, as the average of the same or another data set. The designated model input parameters, representing nominal operation, are listed in Table 4.4. The parameters are determined in relation to the stack design and set point values of the control approach, displayed in Table 4.2. The air utilization factor is considered a fixed parameter, since the model focuses on the exact characterization of the fuel flow path and the details of the temperature control of the stack are neglected. The air utilization factor of approximately 0.15 represents an average value during nominal operation at the commissioning of the system. Additionally, it is assumed that the reformer always reaches an equilibrium temperature of 600 °C, due to sufficient heating with the cathode exhaust air. The SOFC module contains 6 individual stacks, where the maximum temperature of the 6 stacks is controlled to 850 °C. Therefore, the average temperature of the 6 stacks is significantly lower than 850 °C. Additionally, the stack temperature is measured directly inside the core of the stacks. Consequently, the anode channel temperatures are even lower than the average stack temperature. In agreement with the experimental results outlined in section 4.3.3, the stack equilibrium temperature is chosen to be 40 K below the maximum control module temperature. The system pressure levels only marginally deviate from standard pressure. For instance, at the natural gas inlet the deviation to standard pressure is lower than 20 mbar, as depicted in Figure 4.13b. Consequently, the pressure influences on the corresponding equilibrium states are neglected at all system positions and the simulations are conducted at standard pressure.

Table 4.4: Fixed model input parameters representing nominal operation

Parameter	Label	Unit	Value	Parameter	Label	Unit	Value
Electric current	I	A	24	Fuel utilization factor of the stack	$U_{\mathrm{f,S,R}}$	%	75
Oxygen-to-carbon ratio	Φ_{R}	-	2	Reformer equilibrium temperature	$\vartheta_{\mathrm{ref,eq}}$	°C	600
Air utilization factor	U_{a}	%	15	Stack equilibrium temperature	$\vartheta_{\mathrm{S,eq}}$	°C	810
Number of cells	N_{Cell}	-	720				

The high-temperature combustion reaction model of H2/CO/C1-C4 compounds (USC-Mech II [57]) is used in the Cantera toolbox for the chemical equilibrium calculations inside the reformer, stack and burner. The USC-Mech II includes 111 species with the corresponding thermodynamic and transport properties, and 784 chemical reactions. The mechanism can be applied to a wide range of equilibrium calculations for the conversion of alkanes up to butane [57]. The considered elements of the mechanism are oxygen, hydrogen, carbon, nitrogen and argon. In comparison to the more commonly used GRI-Mech 3.0 calculation mechanism [107], which is an optimized reaction mechanism for natural gas combustion, including 53 species and 325 reactions, the USC-Mech II lacks the possibility of nitrogen monoxide and ammonia formation but provides a reaction mechanism for conversion of butane. However, Dicks et al. [108] state that ammonia formation is not occurring at atmospheric pressure above temperatures of 450 °C, regardless of the magnitude of the nitrogen content in the fuel stream. Additionally, according to Warnatz et al. [109], surface reactions in catalytic combustion reactors do not generate nitrogen monoxide. Therefore, the formation of nitrogen monoxide and ammonia can be neglected in the operating temperature range of the reformer, stack and catalytic burner between 500 and 1000 °C. In conclusion, the USC-Mech II is preferred since a conversion mechanism for butane is included and a plurality of the previously presented natural gas data sets include butane fractions. The 111 considered species of the USC-Mech II with the number of carbon, oxygen, hydrogen, nitrogen atoms and number of releasable electrons are listed in appendix F. It should be noted that the model outputs of the compositions are reduced to only include 10 major species, since the major species always represent almost 100 % of the mixture. The internal calculation logic considers 111 species and the major species are only read from the internal calculation vector at each of the 9 designated system positions.

In summary, the developed model is able to evaluate the effect of varying natural gas quality on the characteristic parameters of an AEGR SOFC system in relation to a designated control approach for the fuel flow path. Analogous to the control strategy, the modeling methodology uses the three leading set points as major input variables. Additionally, for given equilibrium conditions in the reformer, stack and burner, flow rates and gas compositions can be obtained at all specified system positions for the reference, fluctuating and ideal natural gas system states. The methodology also includes an inherent validation of the mass balance and species conservation.

4.3.2 Evaluation for temporally resolved natural gas data

The temporally resolved natural gas data base, presented in section 3.3, is used as the basis for the evaluation of the capabilities of the model and verification of the chosen methodology. Each individual data point of the natural gas data sets, including Saint-Thegonnec (ST 2014), Campo Maior (CM 2014), Renningen (Rng 2016 / Rng 2013), Egtved (EG 2014), Gent (GE 2014), Imatra (IM 2014) and the unspecified Hungarian location (HU 2014)[16], are used as a simulation

[16] Based upon Figure 3.7, data points of the Hungarian data set, which exceed the permitted natural gas domain in Germany, are excluded from the evaluation.

input, representing the fluctuating natural gas composition. The corresponding reference state is defined using the average composition for each individual data set, representing the best case. As outlined in Figure 4.6, the resulting domains of the fuel utilization factor of the stack and oxygen-to-carbon ratio are displayed for the IC_0 and NM_1 for the nominal operating point values, which are listed in Table 4.4. The IC_0 yields to an ideal realization of the fuel utilization factor and oxygen-to-carbon ratio set points for each individual data set.

Except in Imatra, the application of the NM_1 can result in high deviations of $U_{f,S}$ and Φ from the designated set points, due to natural gas quality fluctuations. The 95 % confidence intervals of $U_{f,S}$ and Φ range from 0.70 to 0.91 and from 1.90 to 2.26, respectively. However, the $U_{f,S}$ and Φ averages match the designated set points, due to the best case definition of the reference natural gas composition, which is defined as the average composition of each individual data set. In Imatra, the natural gas quality is very stable and therefore, the fluctuation domains of the characteristic system parameters are negligible low. The Hungarian data set shows exceptional positive deviations of $U_{f,S}$ and Φ based upon the above average contents of carbon dioxide. By excluding the Hungarian data base, the 95 % confidence intervals of $U_{f,S}$ and Φ are constricted with domains between 0.70 to 0.79 and 1.90 to 2.08, respectively.

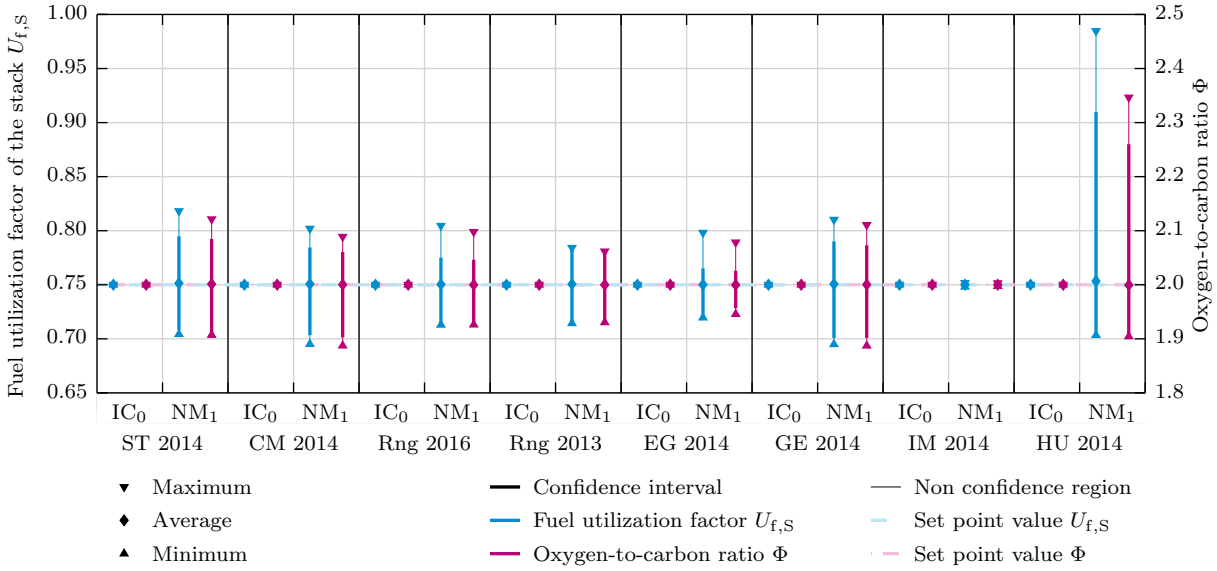

Figure 4.6: Model evaluation - fuel utilization factor and oxygen-to-carbon ratio for IC_0 and NM_1 including 95 % confidence interval

Based upon Figure 3.14a, oxygen-to-carbon ratios below values of around 1.9 can yield to carbon deposition at 600 °C. However, the temperature profile inside the reformer is not necessarily isothermal and prominent dips can occur between the inlet and outlet, due to the endothermic nature of the steam reforming reactions. Consequently, oxygen-to-carbon ratios below values of 2.0 are already considered as a risk for carbon formation, based upon the assumption that temperature dips of up to 20 K can occur inside the reformer unit. As a result, excluding Imatra, the application of the NM_1 yields a risk of carbon deposition for each of the evaluated data sets. Even though high values of Φ decrease the risk of carbon formation, the higher Φ, the higher the dilution of fresh fuel with recirculated gas, ultimately yielding lower Nernst voltages.

Fuel utilization factors above values of around 0.8 increase the risk of irreversible cell damage, due to the partial depletion of fuel inside single cells of the stack. Additionally, as outlined in Figure 2.7b, increasing fuel utilization factors have a strong non linear influence on the Nernst voltage, with extreme gradients for utilization factors above values of 0.8. Low $U_{f,S}$ decrease the risk of irreversible cell damage, but yield lower system efficiency, as shown in Figure 2.3. In

addition, the shift of the thermal balance for both low and high $U_{f,S}$ can result in sharp control ramps or harmful thermal gradients inside system components. For example, low $U_{f,S}$ can result in enhanced stack cooling, due to increased internal reforming, which can lead to high cathode to anode temperature gradients.

In conclusion, both high positive and high negative deviations from the set points of $U_{f,S}$ and Φ are undesirable and increase the risk of enhanced degradation and harmful conditions for system components. However, the predicted deviations of the characteristic parameters in Renningen are barely tolerable based upon the data from the year 2013. Consequently, the NM_1 is used as the basic control approach for experimental testing, due to the simple implementation logic. Nevertheless, the development and implementation of a control scheme that reproduces the performance of the IC_0, and prevents harmful system conditions, is highly desirable. Adapted and advanced control schemes are evaluated in chapter 5.

The verification of the correct implementation of the NM_1 for each individual data set is outlined in Figure 4.7, highlighting the deviation domains of the mass and molar flow rates to the reference state at the natural gas inlet, in the recirculation loop, at the reformer inlet, at the reformer outlet and at the anode outlet.

Figure 4.7: Model evaluation - mass and molar flow rate deviation to reference for IC_0 and NM_1

The respective natural gas mass flow rates and reformer inlet molar flow rates do not deviate from the chosen reference values for the NM_1, validating the correct implementation of the control schemes constraints, previously outlined in section 4.2.2.1. Additionally, the deviations of the mass and molar flow rates to the reference are also displayed for the IC_0. Compared to

the NM_1, the natural gas mass flow rates and the reformer inlet molar flow rates are adjusted to match the designated fuel utilization factor and oxygen-to-carbon ratio set points for each natural gas data point. The higher the maximum $U_{f,S}$ and Φ deviations in the NM_1, the higher the necessary adjustment of the corresponding flow rates at the natural gas and reformer inlets in the IC_0.

4.3.3 Validation with measured system data during methane operation

In this section the validation of the model is outlined based upon a comparison of measured and modeled compositions at the reformer inlet, reformer outlet and anode outlet for the nominal operation of the system fueled with pure methane. Therefore, the composition of the fresh fuel is always known and influences on the system performance, due to varying natural gas compositions, are excluded. It should be noted that this section is a didactic anticipation of section 4.4.1, in which the gas measurement system and the measurement based system balance are outlined in detail. The subsequently described methodology of the comparison of the measured and simulated data, in section 4.4.1.4 and Figure 4.12, can be analogously applied for the methane operation by considering both the measured and reference natural gas composition as pure methane.

A total of 340 individual measured data samples from 11 different methane operating periods are used as the basis for the model validation. The evaluated raw samples each include the reformer inlet, reformer outlet and anode outlet compositions, as well as the reformer and anode outlet average temperatures. The gas chromatography system (GC) discontinuously analyzes the sampled gas with a sampling rate of around 30 minutes. Therefore, the time average of one consecutive set of the composition analysis at the reformer inlet, reformer outlet and anode outlet is taken as the corresponding sampling time. As a result, the average temperatures at the reformer and anode outlet are evaluated with respect to the corresponding GC sampling time, using an hourly average value of temperature records with a sampling rate of 10 seconds. The reformer outlet temperature is measured in the piping directly downstream of the reformer manifold. Therefore, the equilibrium temperature inside the reformer has to be slightly higher than the measured outlet temperature, due to thermal interactions with surrounding components. As a result, a general offset of 1 K is added to the measured temperatures to represent the equilibrium states. Additionally, the temperature at the anode outlet is measured inside the anode exhaust gas manifold of the stack module. Therefore, the measured temperature is already subjected to thermal interactions and heat losses due to the substantial size of the anode exhaust manifold. Consequently, the measured anode exhaust manifold temperature does not sufficiently represent the equilibrium state inside the anode channel. However, the maximum stack temperature is always controlled to be 850 °C. The equilibrium temperature of each individual stack anode channel can not be determined exactly, however has to be between the anode exhaust and maximum stack temperature. The evaluation of the anode outlet and reformer inlet composition measurements, in comparison to the calculated system states, has shown that the equilibrium state of the entire stack module can be represented sufficiently by adding an offset of 10 K to the measured anode exhaust gas manifold temperature.

In Table I.1[17] in appendix I, the characteristic measured system data of the 11 different methane operating periods are listed. The data samples were all recorded during nominal load operation at an electric current of 24 A and atmospheric system pressure. The average measured temperature inside the anode exhaust gas manifold varies between 793 and 805 °C. The average reformer outlet temperature ranges from 573 to 590 °C. The fuel utilization factors of the stack and oxygen-to-carbon ratios vary from 0.68 to 0.77 and 2.04 to 2.29, respectively. In

[17] The fuel utilization factor of the stack and oxygen-to-carbon ratio are computed based upon the gas composition quantification at the reformer inlet, reformer outlet and anode outlet, as derived in section 4.4.1

comparison to the listed corresponding set points of the fuel utilization factor of the stack and oxygen-to-carbon ratio, high offsets are apparent for the oxygen-to-carbon ratios. The measured oxygen-to-carbon ratios always show a positive deviation from the specified set point, reaching deviations of up to approximately 10 %. The deviations are resulting from an arbitrary safety scaling factor, which was used during the commission of the system. The safety scaling factor causes an increase of the recirculation flow rate above the given set point without adjusting the specified oxygen-to-carbon ratio set point. Therefore, the risk of carbon deposition is reduced, due to higher water vapor contents at the reformer. Excluding the data sample between the 15th and 17th of February in 2017, the safety scaling factor was always reset to its original value to ensure identical conditions, since the methane operating periods were used as the reference to evaluate long term effects, such as system and stack degradation. At the end of February, the safety scaling factor was deactivated, resulting in a closer match of the oxygen-to-carbon ratio set points and measured process values.

As shown in Figure 4.5, any specified oxygen-to-carbon ratio and fuel utilization factor of the stack can be used to calculate the ideal state of the system for given equilibrium temperatures and electric currents. Therefore, the 340 individual measured data samples can each be used to compute the corresponding ideal system states at the 9 specified system positions for a pure methane feed. For the purpose of model validation, the measured compositions are compared to the ideal calculated compositions at the reformer inlet, reformer outlet and anode outlet for each individual measured data sample. As outlined in Figure 4.8, a strong agreement between the measured and calculated mole fractions is achieved at the reformer inlet, reformer outlet and anode outlet, due to 95 % of the corresponding absolute deviations ranging between approximately -0.004 and +0.006.

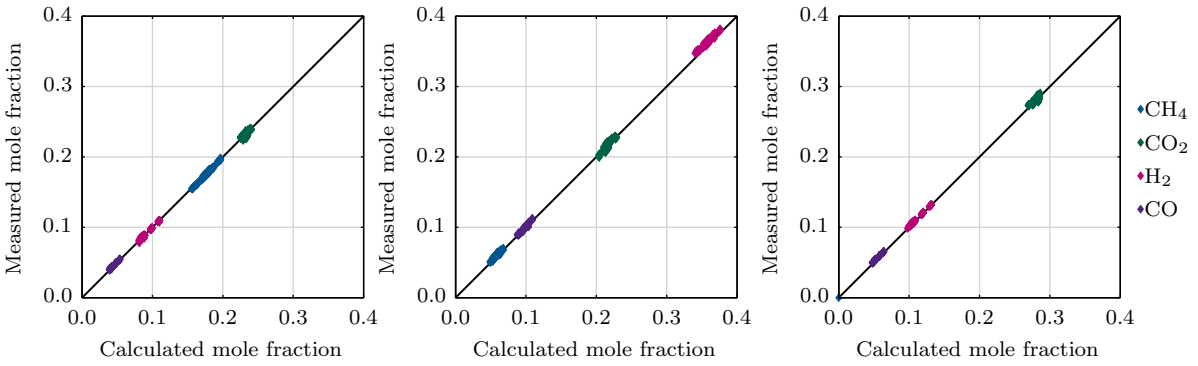

(a) Reformer inlet (b) Reformer outlet (c) Anode outlet

Figure 4.8: Model validation - Comparison of calculated and measured gas composition

The reformer inlet composition is a mixture of fresh methane and recirculated anode exhaust gas. Therefore, an agreement of the measured and simulated compositions also implies a concurrence of the real and calculated flow rates. Consequently, the developed modeling approach is able to accurately reproduce real system conditions, including gas compositions and flow rates. The implemented slight temperature offsets at the reformer and anode outlet of 1 and 10 K have shown to sufficiently adjust the measured temperature levels to closely represent equilibrium states. Additionally, the strong agreement between the measured and calculated mole fractions validates that the deliberate neglect of the pressure influence on the equilibrium state is not obstructing the evaluation significance. Lastly, as shown in Figure 4.8c, the measured and calculated mole fractions of methane at the anode outlet are both always lower than 0.005 %. Consequently, the previously used assumption that hydrocarbons are completely converted at the anode outlet is verified.

4.3.4 Propagation of error

As outlined in section 4.2.2.1, for the derivation of the control scheme constraints, it was assumed that the actuators can ideally realize the designated set points. However, in reality, the flow rates at the natural gas and reformer inlets, as well as the electric current, might deviate from the designated set points, due to measurement errors. Consequently, Gaussian propagation of error calculations are conducted to estimate the impact of the deviation from the designated set points on the fuel utilization factor and oxygen-to-carbon ratio. It should be noted that the effects of deviations from the designated set points are occurring in addition to the outlined impact of fluctuating natural gas quality. For the Gaussian propagation of error calculation, the fuel utilization factor and oxygen-to-carbon ratio have to be expressed as functions of the three corresponding actuator set points, the electric current, natural gas mass flow rate and reformer inlet molar flow rate.

By applying equations (2.4), (2.14), (2.18) and (2.19) to equation (2.2), the recirculation ratio can be expressed as a function of the reformer inlet molar flow rate and natural gas mass flow rate. In combination with equation (2.3), the derived function of the recirculation ratio can be applied to equation (2.4), yielding equation (4.7), which expresses the fuel utilization factor of the stack as a function of the three actuator set points.

$$U_{\mathrm{f,S,PoE}} = \frac{I\, N_{\mathrm{Cell}} \left(\frac{\dot{m}_{\mathrm{NG,in}}}{M_{\mathrm{NG,in}}}\right) (1 + K_{\triangle \mathrm{an}})}{\left(\frac{\dot{m}_{\mathrm{NG,in}}}{M_{\mathrm{NG,in}}}\right) F\, K_{\mathrm{e}^-} \left(\dot{n}_{\mathrm{ref,in}} + \left(\frac{\dot{m}_{\mathrm{NG,in}}}{M_{\mathrm{NG,in}}}\right) K_{\triangle \mathrm{an}}\right) - I\, N_{\mathrm{Cell}} \left(\dot{n}_{\mathrm{ref,in}} - \left(\frac{\dot{m}_{\mathrm{NG,in}}}{M_{\mathrm{NG,in}}}\right)\right)} \tag{4.7}$$

Additionally, equations (2.3), (2.4) and (4.7) can also be used to express the oxygen-to-carbon ratio as a function of the three actuator set points.

$$\Phi_{\mathrm{PoE}} = \frac{I\, N_{\mathrm{Cell}} \left(\dot{n}_{\mathrm{ref,in}} - \left(\frac{\dot{m}_{\mathrm{NG,in}}}{M_{\mathrm{NG,in}}}\right)\right)}{2\, K_{\mathrm{C}}\, F \left(\frac{\dot{m}_{\mathrm{NG,in}}}{M_{\mathrm{NG,in}}}\right) \left(\dot{n}_{\mathrm{ref,in}} + \left(\frac{\dot{m}_{\mathrm{NG,in}}}{M_{\mathrm{NG,in}}}\right) K_{\triangle \mathrm{an}}\right)} + \frac{K_{\mathrm{O}}}{K_{\mathrm{C}}} \tag{4.8}$$

Gaussian propagation of error is applied to compute the standard uncertainty (u) of $U_{\mathrm{f,S}}$ and Φ by partially differentiating equations (4.7) and (4.8) with respect to the three actuator set points, as outlined for $U_{\mathrm{f,S}}$ in equation (4.9). The uncertainties (s) of the electric current, natural gas mass flow rate and reformer inlet molar flow rate are assumed to be 0.5 %, 1.5 % and 5 % of the corresponding set point value, respectively [110, 111]. Equation (4.9) and an analogous equation for Φ can be used in connection with the modeling outputs for any given natural gas data set to calculate the corresponding error domains of $U_{\mathrm{f,S}}$ and Φ, as a result of the uncertainties of the set point realization.

$$u_{U_{\mathrm{f,S,PoE}}} = \sqrt{\left(\frac{\delta U_{\mathrm{f,S,PoE}}}{\delta \dot{m}_{\mathrm{NG,in}}}\, s_{\dot{m}_{\mathrm{NG,in}}}\right)^2 + \left(\frac{\delta U_{\mathrm{f,S,PoE}}}{\delta \dot{n}_{\mathrm{ref,in}}}\, s_{\dot{n}_{\mathrm{ref,in}}}\right)^2 + \left(\frac{\delta U_{\mathrm{f,S,PoE}}}{\delta I}\, s_I\right)^2} \tag{4.9}$$

The progression and resulting error domains of $U_{\mathrm{f,S}}$ and Φ of the NM_1 for the temporally resolved Saint-Thegonnec natural gas data set are outlined in Figure 4.9. In the worst case, in Saint-Thegonnec, $U_{\mathrm{f,S}}$ and Φ are ranging from 0.68 to 0.85 and 1.84 to 2.19, respectively.

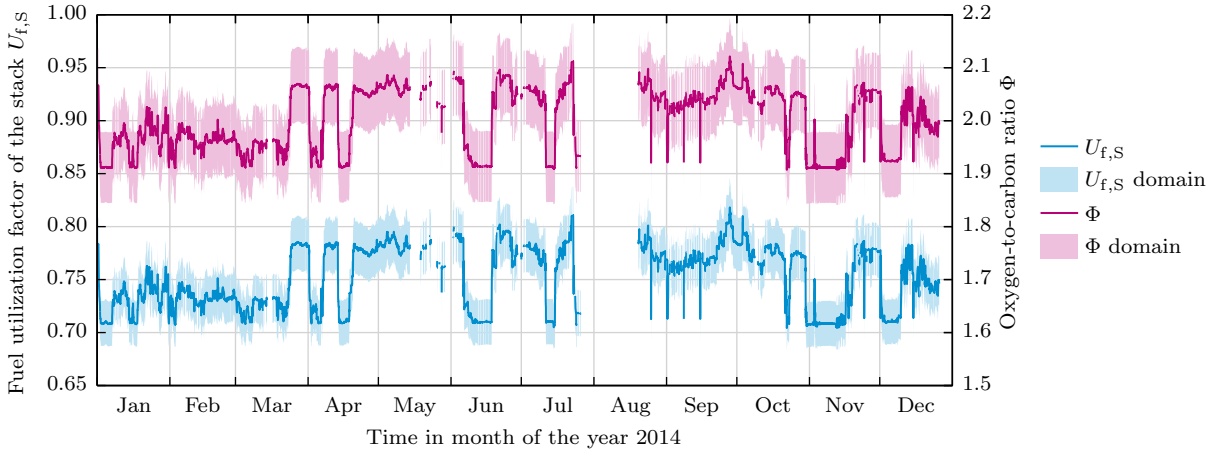

Figure 4.9: Model propagation of error - fuel utilization factor and oxygen-to-carbon ratio progression for Saint-Thegonnec data set with NM_1 including error domains

In addition, the worst case domains of $U_{f,S}$ and Φ of the IC_0 and NM_1 are displayed for the entire temporally resolved natural gas data base in Figure 4.10[18], including the 95 % confidence interval. In comparison to Figure 4.6, the consideration of the deviation from the designated set points significantly increases the limits of $U_{f,S}$ and Φ. The domain of the 95 % confidence intervals of $U_{f,S}$ and Φ of the NM_1 are extended to range from 0.68 to 0.91 and from 1.84 to 2.26, respectively. By excluding the Hungarian data base, the domains of the 95 % confidence intervals of $U_{f,S}$ and Φ are reduced to vary between 0.69 to 0.81 and 1.85 to 2.14, respectively. In contrast to Figure 4.6, the consideration of the deviation from the designated set points also impacts the IC_0, yielding fluctuation intervals of $U_{f,S}$ and Φ between 0.73 to 0.77 and 1.93 to 2.07, respectively. Still, the best case definition of the reference natural gas composition yields a perfect match between the designated set points and the average values of $U_{f,S}$ and Φ.

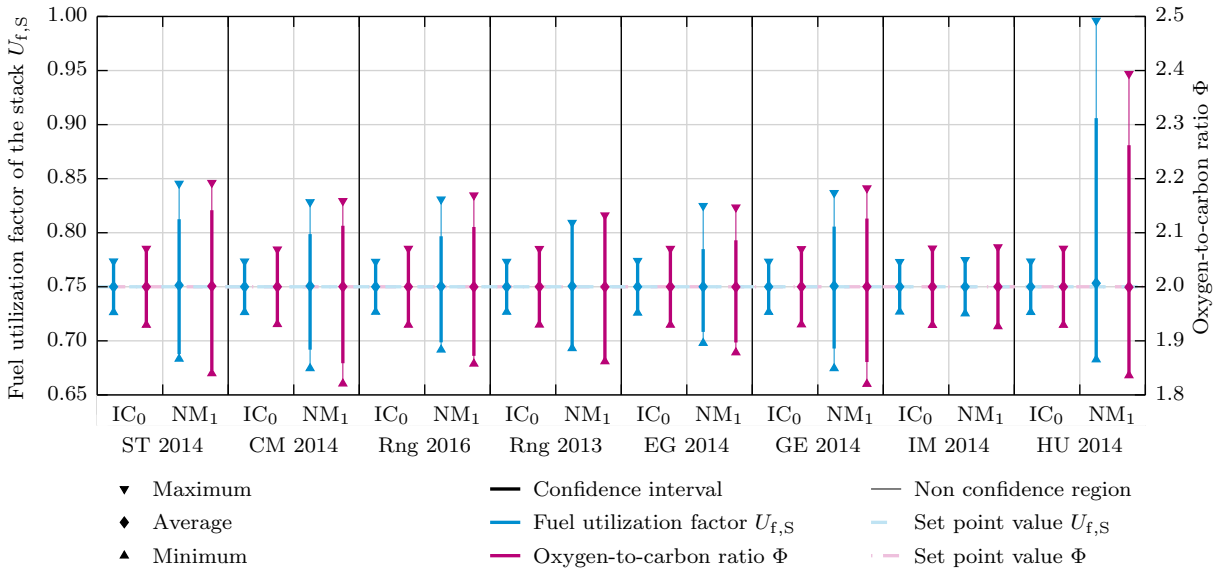

Figure 4.10: Model propagation of error - fuel utilization factor and oxygen-to-carbon ratio for IC_0 and NM_1 including 95 % confidence interval[18]

[18] It should be noted that six data points are excluded from the NM_1 of the Hungarian data set since, considering the error domains, the physical fuel utilization factor limit of 1 is exceeded.

The results of the propagation of error, underline that the application of the NM_1 can yield to undesirably high set point deviations of $U_{f,S}$ and Φ, which can cause enhanced degradation and harmful conditions for system components. Additionally, for the IC_0, the consideration of the deviation from the designated set points yields to intermediate fluctuations of $U_{f,S}$ and Φ. Consequently, the development and testing of advanced control schemes, which are outlined in chapter 5, are necessary. By including the worst case error domains, the predicted deviations of the characteristic parameters in Renningen are exceeding the barely tolerable thresholds based upon the data from the year 2013, including $U_{f,S}$ higher than 0.8 and Φ below 1.9. However, in section 4.4, the NM_1 is still used as the basic control approach for the experiments to validate the derived constraints and modeling approach.

4.4 SOFC test rig results

The objective of this section is to simultaneous analyze and compare the measured data with a parallel representation of the system states, using the outlined modeling approach for the previously described control strategy. Therefore, this section is divided into three parts: (a) The description of the gas measurement system and the processing methodology of the measured data; (b) The outline of the mass flow controller behavior and derived scaling during natural gas operation; (c) The comparison of the measured and simulated data during the entire testing period. It should be noted that the section has a non sequential structure. A portion of the measured system data used to evaluate the MFC behavior is presented in section 4.4.2, whereas the complete analysis of the results is outlined in section 4.4.3. The structure was deliberately chosen to establish a baseline to understand the evaluation of the results.

To generate a significant data base, the application of the NM_1 to the SOFC test rig was tested between October 2016 and February 2017 in 12 individual periods, including a variation of I_{SP} and $U_{f,S,SP}$. As outlined in section 4.3.2, Φ values below 2 are already considered as a carbon formation risk. Additionally, an increase of Φ can result in lower net system efficiency, due to higher auxiliary recirculation blower power demands and reduced Nernst voltages from increasing water vapor fractions at the stack inlet. Consequently, the set point of Φ is not varied throughout the entire testing period. The corresponding time frames, sample sizes and set points of the leading system variables for the individual testing periods are listed in Table J.1 in appendix J. One sample includes the condensed GC data points at a single aggregated time step, as described in section 4.4.1.4. Additionally, as shown in section 4.4.2, the data samples from 2016 were used to derive a scaling methodology for the MFC, which was used in 2017 to emulate an enhanced MFC calibration. The utilization of the MFC scaling and the application of the arbitrary safety scaling factor of the recirculation flow rate are also presented in Table J.1. The average of the Renningen 2013 data set was used as the reference natural gas composition throughout the entire testing period.

4.4.1 Gas measurement system

For a detailed system evaluation and model validation, the SOFC test rig is equipped with an Agilent 7890B gas chromatography system [53]. The GC is connected to four SOFC system sampling positions via heated pipes, which prevent condensation. As schematically shown in Figure 4.1, the four sampling positions are located upstream of the natural gas inlet, upstream of the reformer inlet, between the reformer outlet and anode inlet and downstream of the anode outlet. The GC discontinuously analyzes the gas with a sampling rate of approximately 30 minutes and the four different positions are continuously rotated. Therefore, one complete measurement cycle of all four positions lasts approximately two hours. While the current gas sample is analyzed, the sampling loops of the GC are purged with gases from the adjacent

position, to optimize the sampling routine. However, the consumption of gas, due to the GC analysis, does not affect the SOFC system, since the volume flow rates of the purged gas are lower than one-tenth of a percent of the corresponding total flow rates in the test rig.

The GC is calibrated with bottled standard gas mixtures used to quantify eight species, using two-point calibrations, respectively. The quantifiable species are methane, ethane, propane, carbon monoxide, carbon dioxide, hydrogen, oxygen and nitrogen. The determination of the sum of higher hydrocarbons containing at least four carbon atoms is not implemented, due to the high complexity of the calibration of all possible species. Additionally, as shown in section 3.3.4, the amount of the sum of higher hydrocarbons is usually lower than 1 % in natural gas. The C_{4+} concentration is distinctly lower than 1 % at all other evaluated system positions, since fresh natural gas is mixed with recirculated gas and higher hydrocarbons are completely converted inside the reformer. As a result, it is assumed, that the detection error resulting from the deliberate neglect of the sum of higher hydrocarbons is tolerably low. The water vapor content is also not directly quantified, since a calibration with a reproducible water vapor standard is very challenging and costly. Therefore, the water vapor content is indirectly estimated at the reformer inlet, reformer outlet and anode outlet as the difference of the sum of the detected species from 100 %, whereas natural gas is considered completely dry. The calculation mechanism of the water vapor fraction is outlined in equation (4.10). For the sake of simplification, the corresponding subscripts for the reformer inlet, reformer outlet or anode outlet are not displayed in equation (4.10). Additionally, it should be noted, that the used calculation methodology for the water vapor fraction naturally includes the scaling of the sum of mole fractions to 100 %.

$$x_{\mathrm{GC,H_2O}} = 1 - x_{\mathrm{GC,CH_4}} - x_{\mathrm{GC,C_2H_6}} - x_{\mathrm{GC,C_3H_8}} - x_{\mathrm{GC,CO}} - x_{\mathrm{GC,CO_2}} - x_{\mathrm{GC,H_2}} - x_{\mathrm{GC,O_2}} - x_{\mathrm{GC,N_2}} \quad (4.10)$$

For the natural gas quantification, the sum of the mole fractions can marginally exceed or fall below a value of 100 %, due to the quantification uncertainty margins of each individual species, which are around 1 % of the measured value. Therefore, the quantified species are equally scaled, considering the total deviation of the sum of the mole fractions to 100 %, as outlined in equation (4.11). As a result, the sum of the scaled mole fractions exactly matches a value of 100 %. It should be noted that the shown scaling methodology partially obliterates the recorded data base and occurring error margins. However, scaling of the recorded data is necessary for comparison with other natural gas data sets and for the use of the data as an accurate, valid model input.

$$x_{\mathrm{NG,GC,scaled},i} = \frac{1}{\sum_i x_{\mathrm{NG,GC,raw},i}} x_{\mathrm{NG,GC,raw},i} \quad (4.11)$$

For a more detailed and continuous evaluation of the natural gas quality, the natural gas inlet pipe is also connected to a multi gas analyzer, type INCA1051 [112]. The gas analyzer uses nondispersive infrared sensors (NDIR) to determine the methane ($x_{\mathrm{NG,NDIR,CH_4}}$) and higher hydrocarbon content, represented with the help of ethane equivalents $\left(x_{\mathrm{NG,NDIR,(C_2H_6)_{eqv}}}\right)$. Additionally, the internal calculation logic of the unit estimates the relative density of the analyzed natural gas. The sampling rate of the sensor is in the magnitude of 15 seconds. Every 6 hours, the multi gas analyzer is calibrated with bottled methane and ambient air in a completely automated procedure. Therefore, the 0 and 100 % points of methane are continuously readjusted. In contrast to the gas chromatography system, the analyzed gas is not altered in the multi gas analyzer and can consequently be transferred back to the natural gas inlet pipe. Even though the system is equipped with an online natural gas quality quantification sensor, the measured responses are only used for the validation and verification of the system data in the first step. However, as shown in section 4.4.2, the online measurement is used for the accurate realization

of the natural gas mass flow set point by emulating an enhanced MFC calibration logic. In a second step, the measured signal is used as the basis for an enhanced control scheme, which adjusts the flow rates in correspondence to the detected natural gas quality, ultimately aiming to match the ideal control scheme. The methodology, as well as the simulated and experimental results of the advanced control scheme are outlined in chapter 5.

4.4.1.1 Indirect measurement of fuel utilization factor

The fuel utilization factor of the stack is one of the central characteristic parameters of an SOFC system and a leading variable of the control strategy. However, $U_{\mathrm{f,S}}$ can not be directly measured since it is the ratio between the utilized and supplied flow rate of electrons, as introduced in equation (2.26). Nevertheless, $U_{\mathrm{f,S}}$ can be calculated solely from the anode inlet and outlet compositions. Consequently, $U_{\mathrm{f,S}}$ can be indirectly measured using the quantification results of the gas chromatography system. For this purpose, equation (2.26) can be rewritten by applying equation (2.27) and further altered via equations (2.25), (3.7), (2.14), (2.15) and (2.19), ultimately yielding a sole dependence on the anode inlet and outlet compositions. The result is outlined in equation (4.12)[19], which can be further simplified by assuming that methane, hydrogen and carbon monoxide are the only remaining electrochemical active species at the reformer outlet and that methane is completely converted at the anode outlet. Additionally, methane is considered the only remaining species, resulting in a change in molar quantity in the anode channels, as previously depicted in Table 2.4.

$$\begin{aligned} U_{\mathrm{f,S,Msd}} &= 1 - \frac{\left(1 + \sum_i x_{\mathrm{an,in},i}\, \triangle \dot{n}_{\mathrm{an},i}\right) \sum_i x_{\mathrm{an,out},i}\, N_{\mathrm{e^-},i}}{\sum_i x_{\mathrm{an,in},i}\, N_{\mathrm{e^-},i}} \\ &= 1 - \frac{\left(1 + 2\, x_{\mathrm{an,in,GC,CH_4}}\right)\left(x_{\mathrm{an,out,GC,H_2}} + x_{\mathrm{an,out,GC,CO}}\right)}{4\, x_{\mathrm{an,in,GC,CH_4}} + x_{\mathrm{an,in,GC,H_2}} + x_{\mathrm{an,in,GC,CO}}} \end{aligned} \tag{4.12}$$

For the evaluation of the indirectly measured fuel utilization factor of the stack, the time difference of around 30 minutes between the measurement of the anode inlet and outlet has to be taken into account. Consequently, the indirectly estimated value has to be considered slightly vague, since the natural gas composition and therefore system conditions can vary during the gas sampling duration. Nonetheless, it is assumed that for steady state conditions, two consecutive measurements of the anode inlet and outlet can be used to represent the trend of the fuel utilization factor of the stack.

4.4.1.2 Indirect measurement of oxygen-to-carbon ratio

Analogous to the fuel utilization factor, the oxygen-to-carbon ratio in the reformer is also a central characteristic parameter of the SOFC system and leading variable of the control strategy, which can not be directly measured. However, the amount of oxygen and carbon atoms present at the reformer inlet and outlet can be calculated based upon the quantification results from the gas chromatography system. The analysis at the reformer inlet is chosen to determine the oxygen-to-carbon ratio, since the gas quantification at the reformer outlet is already included in the calculation of the fuel utilization factor of the stack. As a result, a decoupling of the estimation of both characteristic values is achieved, which is beneficial when a quantification error or a failure of the measurement system occurs. Equation (2.1) can be rewritten by applying forms of equations (3.3) and (3.4), as well as considering the relevant oxygen and carbon containing species, as outlined in equation (4.13).

[19] The derivation of equation (4.12) is shown in appendix K.

$$\begin{aligned}\Phi_{\mathrm{Msd}} &= \frac{\dot{n}_{\mathrm{O,ref,in}}}{\dot{n}_{\mathrm{C,ref,in}}} = \frac{\dot{n}_{\mathrm{ref,in}} \sum_i x_{\mathrm{ref,in},i}\, N_{\mathrm{O},i}}{\dot{n}_{\mathrm{ref,in}} \sum_i x_{\mathrm{ref,in},i}\, N_{\mathrm{C},i}} \\ &= \frac{2\, x_{\mathrm{ref,in,GC,CO_2}} + x_{\mathrm{ref,in,GC,CO}} + x_{\mathrm{ref,in,GC,H_2O}}}{x_{\mathrm{ref,in,GC,CH_4}} + 2\, x_{\mathrm{ref,in,GC,C_2H_6}} + 3\, x_{\mathrm{ref,in,GC,C_3H_8}} + x_{\mathrm{ref,in,GC,CO_2}} + x_{\mathrm{ref,in,GC,CO}}}\end{aligned} \tag{4.13}$$

4.4.1.3 Indirect measurement of gas coefficients, molar mass and specific heat capacity of natural gas

The gas coefficients can be determined based upon the natural gas composition quantification from the gas chromatography system, using the individual definition of each gas coefficient. The general equation for each gas coefficient is shown in equation (4.14), which is based upon equations (3.3) to (3.7), using the corresponding number of atoms or electrons listed in Table 3.2. Additionally, the outputs of the methane concentrations and ethane equivalents of the nondispersive infrared sensors can be used to determine the hydrogen and electron coefficients, as outlined in equations (4.15) and (4.16). The remaining natural gas coefficients can not be distinctly estimated using the NDIR, since carbon dioxide and nitrogen fractions are not directly quantified. Carbon dioxide has to be considered for both the carbon and oxygen coefficients, whereas nitrogen is directly linked to the nitrogen coefficient.

$$K_{\Lambda,\mathrm{GC}} = \sum_i x_{\mathrm{NG,GC},i}\, N_{\Lambda,i} \qquad \text{with } \Lambda \in \left\{\mathrm{C};\ \mathrm{O};\ \mathrm{H};\ \mathrm{N};\ \mathrm{e^-}\right\} \tag{4.14}$$

$$K_{\mathrm{H,NDIR}} = N_{\mathrm{H,CH_4}}\, x_{\mathrm{NG,NDIR,CH_4}} + N_{\mathrm{H,C_2H_6}}\, x_{\mathrm{NG,NDIR,(C_2H_6)_{eqv}}} \tag{4.15}$$

$$K_{\mathrm{e^-,NDIR}} = N_{\mathrm{e^-,CH_4}}\, x_{\mathrm{NG,NDIR,CH_4}} + N_{\mathrm{e^-,C_2H_6}}\, x_{\mathrm{NG,NDIR,(C_2H_6)_{eqv}}} \tag{4.16}$$

The molar mass can also be calculated based upon the measured gas composition from the GC as outlined in equation (4.17), using the molar masses of each individual species listed in Table 4.5. Additionally, by applying the ideal gas law to equation (3.2), the molar mass of natural gas can be computed using the relative density signal of the multi gas analyzers, as outlined in equation (4.18)[20].

$$M_{\mathrm{NG,in,GC}} = \sum_i x_{\mathrm{NG,GC},i}\, M_i \tag{4.17}$$

$$M_{\mathrm{NG,in,NDIR}} = \rho_{\mathrm{a,dry}}\, \rho_{\mathrm{relative,NDIR}}\, \frac{R\, T_{\mathrm{Std}}}{p_{\mathrm{Std}}} \tag{4.18}$$

Table 4.5: Molar mass of individual species

Species i	CH_4	C_2H_6	C_3H_8	C_4H_{10}	CO_2	N_2	H_2	CO	H_2O	O_2
Molar mass in $\mathrm{g\,mol^{-1}}$	16.04	30.07	44.10	58.12	44.01	28.01	2.02	28.01	18.02	32.00

[20] In the standard DIN EN ISO 6976, the standard density of dry air is defined as 1.292923 $\mathrm{kg\,m^{-3}}$ [49].

The molar heat capacity is calculated as a function of temperature and gas composition using the equation and coefficients defined by McBride et al. [113] for a pressure level of 100 kPA, as outlined in equation (4.19)[21]. For the measurement taken by the nondispersive infrared sensor unit, the natural gas composition is assumed to be a pure mixture of methane and ethane, where the ethane content is identical to the fraction of ethane equivalents.

$$c_{\mathrm{p,mol,NG,GC/NDIR}}(T) = R \sum_i x_{\mathrm{NG,GC/NDIR},i} \left(y_{1,i} + y_{2,i}\, T + y_{3,i}\, T^2 + y_{4,i}\, T^3 + y_{5,i}\, T^4\right) \tag{4.19}$$

Additionally, for both gas quantification systems, the specific heat capacity can be computed based upon the respective molar heat capacity and molar mass, as outlined in equation (4.20), using equations (4.19), (4.17) and (4.18).

$$c_{\mathrm{p,NG,GC/NDIR}}(T) = \frac{c_{\mathrm{p,mol,NG,GC/NDIR}}(T)}{M_{\mathrm{NG,in,GC/NDIR}}} \tag{4.20}$$

To compare the gas chromatography system and nondispersive infrared sensor unit results, the ethane equivalents $\left(x_{\mathrm{NG,GC,(C_2H_6)_{eqv}}}\right)$ are also calculated from the GC quantification. The calculation methodology is outlined in equation (4.21), converting propane to ethane equivalents using the ratio of the respective number of releasable electrons. It should be noted that the GC was installed before the commissioning of the SOFC test rig, whereas the multi gas analyzer was added in October 2016. Consequently, data for the comparison of both quantification systems is only available between October 2016 and March 2017. The comparison of the quantified amounts of methane and ethane equivalents are outlined in Figures 4.11a and 4.11b. Even though the sampling rate of the GC is significantly lower than that of the multi gas analyzer, both quantification methods yield results in high general agreement. The occurring offsets are within the respective quantification error margins of around 1 %. Additionally, the agreement between both quantification systems is also represented by the matching of the estimated electron gas coefficient, as outlined in Figure 4.11c.

$$x_{\mathrm{NG,GC,(C_2H_6)_{eqv}}} = x_{\mathrm{NG,GC,C_2H_6}} + \frac{N_{\mathrm{e^-,C_3H_8}}}{N_{\mathrm{e^-,C_2H_6}}}\, x_{\mathrm{NG,GC,C_3H_8}} \tag{4.21}$$

The two different molar mass computation methodologies for the gas quantification systems also display a strong agreement, as depicted in Figure 4.11d. Lastly, as shown in Figure 4.11e, the calculated specific heat capacities also match, even though the NDIR only uses two species for the computation. However, the higher the mismatch in the molar mass, the lower the agreement of the specific heat capacity. Consequently, the match of the molar heat capacities is very high and the deviations are caused by the direct dependency on the molar mass, which is outlined in equation (4.20).

In summary, the comparison outlines a very high agreement between the gas chromatography system and the nondispersive infrared sensor unit, for both the direct natural gas quantification and the respective calculation of characteristic gas properties. The occurring offsets are within the expected error margins of around 1 %. The strong match of the experimental results also verifies and validates the appropriate application, setup and calibration of both gas measurement systems. Therefore, both systems can be used for the long term analysis of natural gas. Consecutively, the GC is used for the steady tracking of the characteristic parameters of the entire SOFC test rig, due to its capability of accurately quantifying gas samples at the reformer inlet, reformer outlet and anode outlet. The fast sampling time of the NDIR establishes the basis for the quick response of the SOFC system to changing natural gas quality and the development of adjusted control schemes.

[21] The coefficients $y_{1,i}$ to $y_{5,i}$, used in equation (4.19), are listed in Table L.1 in appendix L.

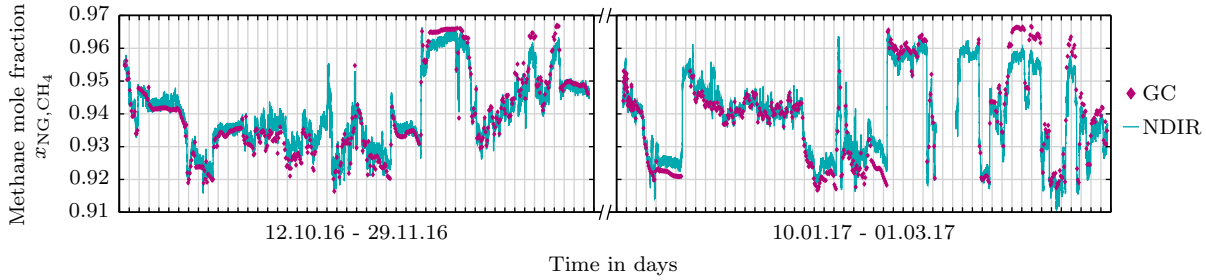

(a) Mole fraction of methane

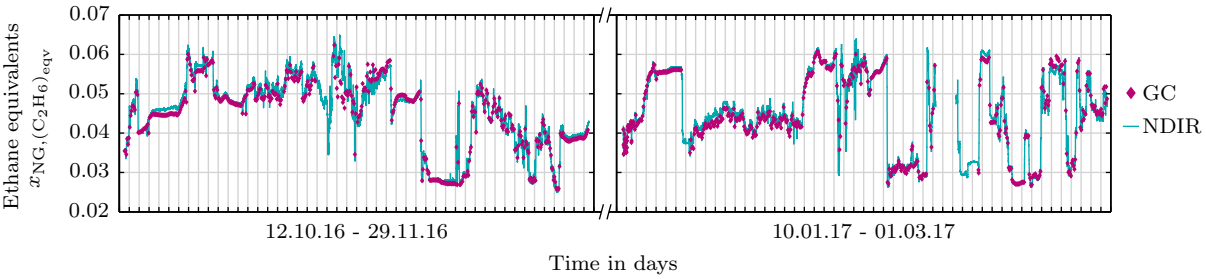

(b) Mole fraction of ethane equivalents

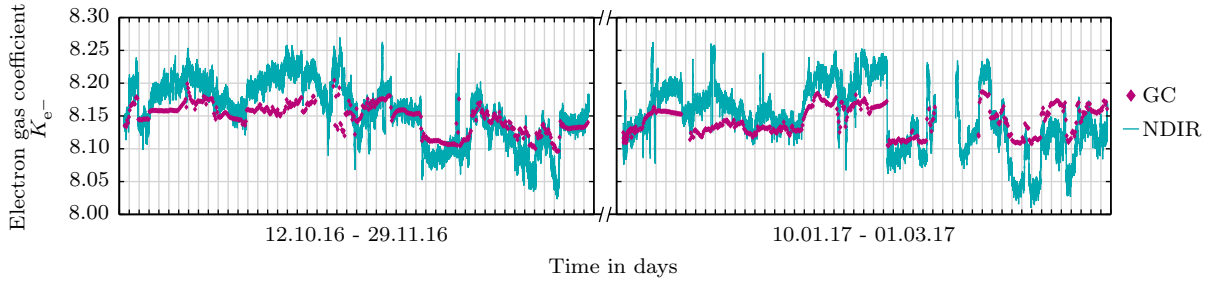

(c) Electron gas coefficient

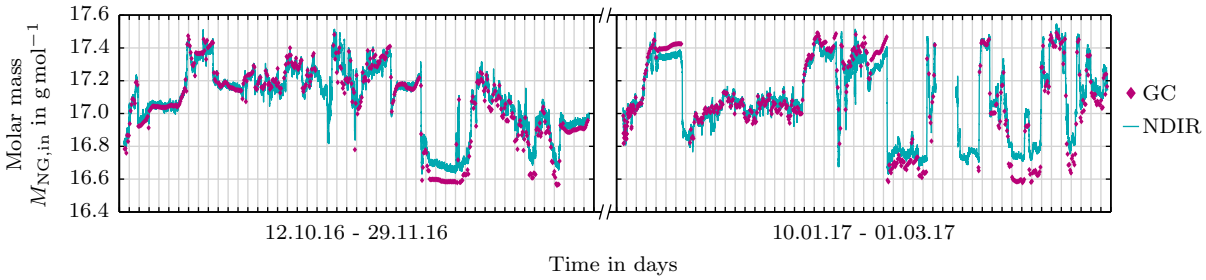

(d) Molar mass

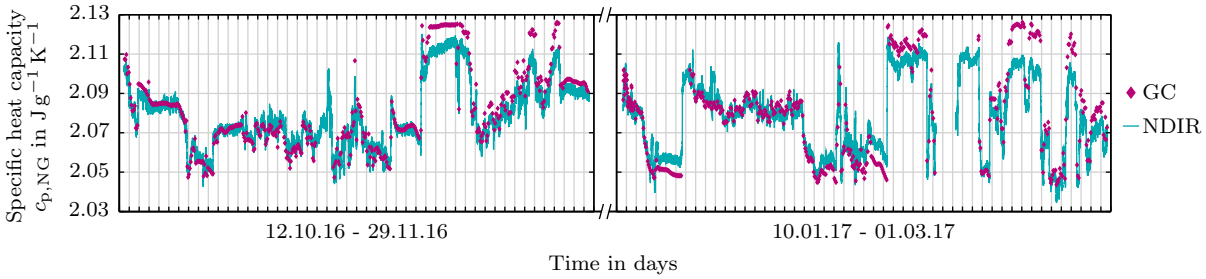

(e) Specific heat capacity for a temperature of 273.15 K

Figure 4.11: Comparison between natural gas quantification systems

4.4.1.4 Measurement based system balance and propagation of error

As previously outlined, consecutive quantification at the four designated system positions with the GC lasts approximately two hours, due to the automated rotation of the positions and the individual sampling time of roughly 30 minutes. Therefore, a change in the natural gas quality within the quantification time frame of two hours might affect the system operating conditions, ultimately influencing the compositions at the designated system positions. Nevertheless, since only a single GC was available, simultaneous analyses of all four positions at the exact same time were impossible. Consequently, it is assumed that four consecutive GC samples can be used to accurately represent the system behavior within the time frame of two hours. As a result, four consecutive quantification samples at the natural gas inlet, reformer inlet, reformer outlet and anode outlet are grouped together. The four grouped samples, at the four different system positions, are referred to as the condensed GC data points. For the corresponding point in time, the time average of the four quantification samples is used. The point in time is denoted as the aggregated time step. Consequently, four consecutive quantification samples are treated as if the condensed GC data points were recorded at a simultaneous aggregated time step.

The condensed GC data points can be utilized to completely characterize the SOFC system, following the set of governing system equations as outlined in section 2.2. As displayed in Figure 4.12, the quantified compositions at the four system positions are used to compute the fuel utilization factor of the stack, oxygen-to-carbon ratio and gas coefficients for the corresponding aggregated time step, using equations (4.12), (4.13) and (4.14). Consecutively, the system molar and mass flow rate balances can be solved from the set of equations presented in section 2.2. The calculated flow rates are representative of the state of the system at the aggregated time step. Analogous to Figure 4.5, it should be noted that $U_{\mathrm{f,S,Msd}}$ and Φ_{Msd} are also used as inputs in the ideal control scheme to compute the corresponding ideal system balance for the purpose of the verification of the analytical system constraints. For the sake of simplicity, the connection of the measured characteristic parameters to the ideal control scheme is not shown in Figure 4.12.

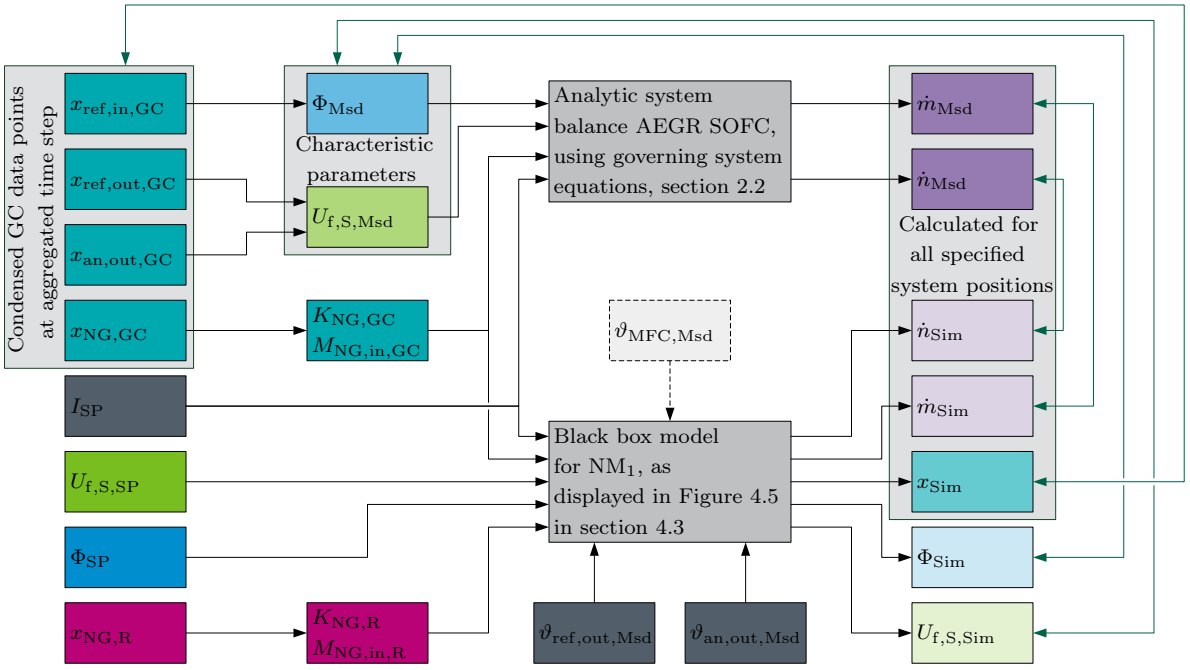

Figure 4.12: Schematic view of measurement based analytic system balance and comparison to modeling results

As also shown in Figure 4.12, analogous to Figure 4.5, the quantified natural gas composition can be used as an input in the modeling approach to calculate the system behavior for the NM_1, using the designated natural gas reference composition and defined set points of $U_{f,S}$, Φ and I. In comparison to Figure 4.5, the inputs $x_{NG,GC}$, $U_{f,S,SP}$, Φ_{SP}, I_{SP}, $\vartheta_{ref,out,Msd}$ and $\vartheta_{an,out,Msd}$ are used as the corresponding black box model inputs for $x_{NG,F}$, $U_{f,S,R}$, Φ_R , I, $T_{ref,eq}$ and $T_{S,eq}$, whereas N_{Cell} and U_a are considered invariant. The outputs $\dot{n}_{Sim}$, $\dot{m}_{Sim}$ and x_{Sim} are equal to the black box model outputs $\dot{n}_F$, $\dot{m}_F$ and x_F of the NM_1. Additionally, the corresponding compositions at the reformer inlet, reformer outlet and anode outlet can be computed with the black box model, using the measured temperatures at the reformer and anode outlet. To represent a temperature value for the aggregated time step, an hourly average temperature at the reformer and anode outlet is used, utilizing temperature records with a sampling rate of 10 seconds equally spread around the aggregated time step. As previously outlined in section 4.3.3, to compensate the mismatch between the position of the temperature measurement and the equilibrium states in the channels, generalized offsets of 1 K and 10 K are added to the measured temperatures at the reformer outlet and anode outlet, respectively. Consequently, the measured and simulated $U_{f,S}$ and Φ, as well as the analytically determined and modeled flow rates and compositions at the specified system positions can be used to compare the measured and simulated states of the system at each aggregated time step. Additionally, trends and progressions of the characteristic parameters can be comprehended in more detail. For the purpose of simplification, the relation of each component of the analytic system balance to the condensed GC data points is abbreviated with the help of a general function symbol $f(x_{\Lambda,GC})$.

Gaussian propagation of error is used to calculate the standard uncertainty for the indirectly estimated characteristic parameters, gas coefficients, molar masses, and all related molar and mass flow rates of the condensed GC data points at each aggregated time step. The propagation of error is solely based upon the measured compositions and deviation of the species quantification from the gas chromatography system. The electric current and number of cells are the only remaining independent variables, but both are considered fixed and invariant. In contrast to section 4.3.4, the electric current uncertainty is excluded, since this error propagation strictly focuses on the GC quantification uncertainties. For the error calculation, each equation is solely expressed using the measured gas compositions. As generally outlined in equation (4.22), the partial derivatives are used to calculate the standard uncertainty based upon the individual quantification uncertainties. For each individual detected species, the quantification error of the GC is 1 % of the measured concentration.

$$u_{PoE} = \sqrt{\sum_i \left(\frac{\delta f(x_{\Lambda,GC})}{\delta x_{\Lambda,GC,i}} \, s_{x_{\Lambda,i}} \right)^2} \quad \text{with } \Lambda \in \{(NG);\, (ref, in);\, (an, in);\, (an, out)\} \tag{4.22}$$

4.4.2 Mass flow controller behavior for varying natural gas composition

As outlined in section 4.2.2.1, it was assumed that the mass flow controller should keep the natural gas mass flow rate constant even if the inlet composition slightly varies. However, even with extreme error margins, the comparison of the measurement based system balance and black box model results clarifies that the used assumption was inaccurate, as subsequently shown in Figure 4.15c. Prior to the commission of the SOFC system, the natural gas MFC was calibrated with pure methane by the manufacturer. However, methane does not sufficiently represent typical natural gas properties, due to the lower contents of methane and the increased contents of higher hydrocarbons in natural gas. The mass flow rate set point of the MFC is defined with the help of the designated reference natural gas composition in form of a normalized volume flow rate. Consequently, due to the calibration with pure methane, the calculation logic of the MFC interprets this normalized volume flow rate as a methane set point and controls

the corresponding methane mass flow rate, which is illustrated in equation (4.23). It should be noted, that the MFC neither keeps the mass, volume or heat flow rate constant during natural gas quality fluctuations.

$$\dot{m}_{\mathrm{CH_4,in,SP}} = \frac{\dot{V}_{\mathrm{007,SP}}}{v_{\mathrm{m,Std}}} M_{\mathrm{CH_4}} \tag{4.23}$$

Nevertheless, as outlined in Figure 4.13a, the ratio between the measurement based calculated natural gas mass flow rate and the specified methane mass flow rate set point of the MFC can be expressed as a function of the ratio of the specific heat capacities of methane and natural gas at the measured average MFC inlet temperature, which is displayed in Figure 4.13b. As a basis for the evaluation, 285 condensed GC data points were used to solve the analytical system balance and calculate the specific heat capacity of natural gas, using equation (4.20), for each aggregated time step. The corresponding temperatures and pressures at the MFC inlet are evaluated as an hourly average value of data points recorded with a sampling time of 10 seconds, equally distributed around the aggregated time step. For the computation of the specific heat capacity, the pressure dependency is neglected since the deviations to standard pressure are very low, as shown in Figure 4.13b[22]. The relation between the specific heat capacity of methane and natural gas for the measured temperature and the mass flow rate ratio can be expressed using a linear correlation, achieving high accuracy with a coefficient of determination of approximately 0.98. The corresponding linear regression function is outlined in equation (4.24).

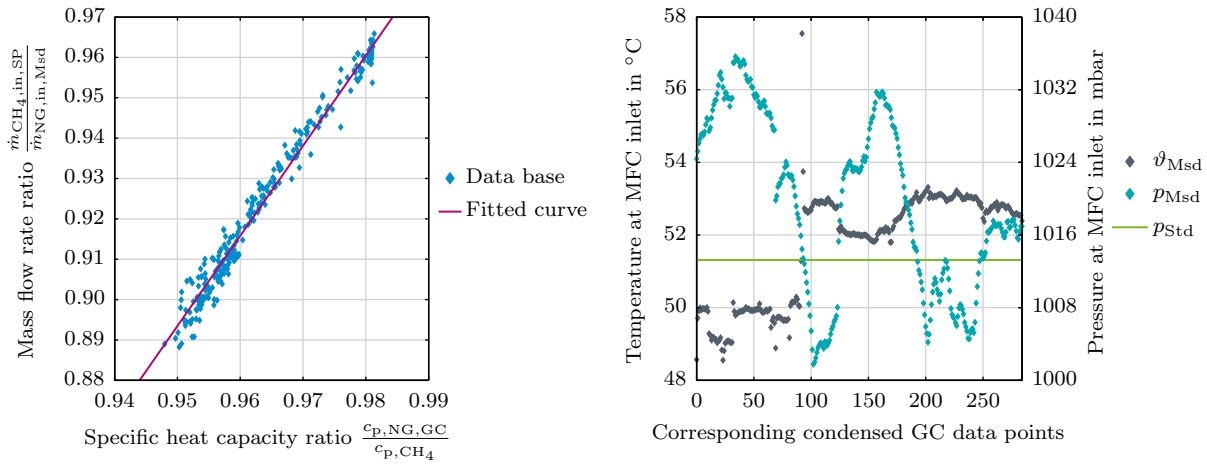

(a) Correlation between specific heat capacity and mass flow rate ratio

(b) Hourly average of temperature and absolute pressure

Figure 4.13: Mass flow controller - Correlation between specific heat capacity and mass flow rate ratio, as well as temperature and pressure data

$$\frac{\dot{m}_{\mathrm{CH_4,in,SP}}}{\dot{m}_{\mathrm{NG,in,calc}}} = f\left(\frac{c_{\mathrm{p,NG,calc}}(\vartheta_{\mathrm{MFC,Msd}})}{c_{\mathrm{p,CH_4}}(\vartheta_{\mathrm{MFC,Msd}})}\right) = 2.23\left(\frac{c_{\mathrm{p,NG,calc}}(\vartheta_{\mathrm{MFC,Msd}})}{c_{\mathrm{p,CH_4}}(\vartheta_{\mathrm{MFC,Msd}})}\right) - 1.22 \tag{4.24}$$

The derived linear regression between the specific heat capacities and mass flow rate ratios can be utilized to calculate the resulting natural gas mass flow rate for a given $\dot{m}_{\mathrm{CH_4,in,SP}}$, or

[22] According to Lemmon et al. [114], the pressure dependent change of the molar heat capacity of the major species of natural gas for low pressure differences is negligible. For a given temperature of 320 K and pressure levels of 101325±5000 Pa the change of the molar heat capacity of all majors natural gas species is low, showing deviations to standard pressure conditions of around ±0.01% for methane, ±0.03% for ethane, ±0.04% for propane, ±0.08% for butane, ±0.03% for carbon dioxide and ±0.01% for nitrogen, respectively [114].

can be used to determine $\dot{m}_{\mathrm{CH_4,in,SP}}$ for a designated natural gas mass flow rate, as shown in equation (4.25), respectively. The latter can be used to ensure that a designated set point for a natural gas mass flow rate is correctly applied to the MFC if the specific heat capacity of natural gas for the current state can be detected. The derived linear relation provides the basis for the implementation of the advanced control scheme, since an accurate application and utilization of the designated natural gas mass flow rate set point is necessary to react to changing natural gas quality. As previously outlined in section 4.4.1, the multi gas analyzer allows for the continuous determination of the specific heat capacity of natural gas. Consequently, the calculated signal can be used to scale the methane mass flow rate set point of the MFC in accordance to the derived regression function, ultimately realizing a designated flow rate of natural gas. For the purpose of validation, the SOFC test rig is also operated with the $\mathrm{NM_1}$, including a set point scaling of the MFC, utilizing the signal of the multi gas analyzer. As a result, an enhanced calibration of the MFC, representing natural gas properties, is emulated in the test rig. It should be noted that a system equipped with a multi gas analyzer can be beneficially operated with an advanced control scheme, providing significant enhanced robustness against fluctuating natural gas quality, as outlined in chapter 5. Nevertheless, the collection of data with an accurate application of the basic control scheme constraint of the $\mathrm{NM_1}$ is necessary for the verification and validation of the derived analytical functions and the used modeling approach.

$$\dot{m}_{\mathrm{NG,in,calc}} = \frac{\dot{m}_{\mathrm{CH_4,in,SP}}}{f\left(\frac{c_{\mathrm{p,NG,calc}}(T_{\mathrm{MFC,Msd}})}{c_{\mathrm{p,CH_4}}(T_{\mathrm{MFC,Msd}})}\right)} \iff \dot{m}_{\mathrm{CH_4,in,SP}} = \dot{m}_{\mathrm{NG,in,calc}}\, f\left(\frac{c_{\mathrm{p,NG,calc}}(T_{\mathrm{MFC,Msd}})}{c_{\mathrm{p,CH_4}}(T_{\mathrm{MFC,Msd}})}\right) \tag{4.25}$$

Additionally, equation (4.25) can be applied to interpret the collected data in the modeling approach by manipulating the basic constraints of the $\mathrm{NM_1}$ to represent non constant flow rates. Consequently, a scaled version of the $\mathrm{NM_1}$ can be computed using an adjusted natural gas mass flow rate constraint, as outlined in equation (4.26) based upon equations (4.2) and (4.25). As a result, the influence of the MFC behavior on the natural gas flow rate can be estimated using the scaling coefficient (S_{MFC}). Additionally, as introduced in section 4.3.3, the arbitrary safety scaling factor of the recirculation flow rate (S_{rec}) has to be considered for the adjustment of the flow rate constraint at the reformer inlet, as depicted in equation (4.27) based upon equation (4.3).

$$\dot{m}_{\mathrm{NG,in,F}} = \frac{\dot{m}_{\mathrm{CH_4,in,SP}}}{f\left(\frac{c_{\mathrm{p,NG,calc}}(T_{\mathrm{MFC,Msd}})}{c_{\mathrm{p,CH_4}}(T_{\mathrm{MFC,Msd}})}\right)} = \frac{\dot{m}_{\mathrm{CH_4,in,SP}}\, \dot{m}_{\mathrm{NG,in,R}}}{f\left(\frac{c_{\mathrm{p,NG,calc}}(T_{\mathrm{MFC,Msd}})}{c_{\mathrm{p,CH_4}}(T_{\mathrm{MFC,Msd}})}\right) \dot{m}_{\mathrm{NG,in,R}}} = S_{\mathrm{MFC}}\, \dot{m}_{\mathrm{NG,in,R}} \tag{4.26}$$

$$\dot{n}_{\mathrm{ref,in,F}} = S_{\mathrm{rec}}\, \dot{n}_{\mathrm{ref,in,R}} \tag{4.27}$$

Therefore, analogous to section 4.2.2.1 and appendices N.1 and N.2.1, a scaled recirculation ratio and fuel utilization factor of the stack of the fluctuating state can be derived. The scaled expressions for $r_{\mathrm{F,scaled}}$ and $U_{\mathrm{f,S,F,scaled}}$ are outlined in equations (4.28) and (4.29). Both equations can be applied to compute the modeling approach's scaled outputs by using the measured MFC inlet temperature as an additional input to calculate the specific heat capacity of natural gas at the aggregated time step. Consequently, a comparison between the measured data, the simulated data using ideal flow rate constraints and the scaled simulated data is possible. The integration of the measured MFC inlet temperature to the comparison methodology between measured and simulated data at the aggregated time step is schematically shown in Figure 4.12.

$$r_{\mathrm{F,scaled}} = \frac{S_{\mathrm{rec}}\, M_{\mathrm{NG,in,F}}\,(1 + r_{\mathrm{R}}\, K_{\triangle\mathrm{an,R}}) - S_{\mathrm{MFC}}\, M_{\mathrm{NG,in,R}}\,(1 - r_{\mathrm{R}})}{S_{\mathrm{rec}}\, M_{\mathrm{NG,in,F}}\,(1 + r_{\mathrm{R}}\, K_{\triangle\mathrm{an,R}}) + S_{\mathrm{MFC}}\, K_{\triangle\mathrm{an,F}}\, M_{\mathrm{NG,in,R}}\,(1 - r_{\mathrm{R}})} \tag{4.28}$$

$$U_{\mathrm{f,S,F,scaled}} = \frac{U_{\mathrm{f,S,R}}\, K_{\mathrm{e^-,R}}\, M_{\mathrm{NG,in,F}}\,(1 - r_{\mathrm{F}})}{S_{\mathrm{MFC}}\, K_{\mathrm{e^-,F}}\, M_{\mathrm{NG,in,R}}\,(1 - r_{\mathrm{R}}\,(1 - U_{\mathrm{f,S,R}})) - r_{\mathrm{F}}\, U_{\mathrm{f,S,R}}\, K_{\mathrm{e^-,R}}\, M_{\mathrm{NG,in,F}}} \tag{4.29}$$

4.4.3 Results of natural gas operation

For the purpose of enhanced visualization, consecutive data points of each individual sampling period are connected, even though the data is based upon discontinuous GC samples. Additionally, the conducted propagation of error computes an uncertainty for each individual measurement based calculated parameter at each aggregated time step. However, in the following Figures 4.14 and 4.15, the error bars are only outlined for every 20th aggregated time step to prevent confusing overlaps.

4.4.3.1 Natural gas properties

As outlined in section 4.2.2.1, for a designated $U_{\mathrm{f,S}}$, the effect of fluctuating natural gas quality in the NM_1 can be expressed using the electron gas coefficients, change in molar quantity coefficients and molar masses for any fluctuating and defined reference natural gas state. According to equation (2.15), the change in molar quantity coefficient can be expressed using the carbon and oxygen gas coefficients. Consequently, to emphasize the occurring natural gas quality fluctuations during the testing period, the comparison of the measured and reference values of the carbon, oxygen and electron gas coefficients, as well as the molar masses are depicted in Figure 4.14. The corresponding reference values, as well as the averages, minima and maxima of the measured data base of K_{C}, K_{O}, $K_{\mathrm{e^-}}$ and $M_{\mathrm{NG,in}}$ are listed in Table J.3 in appendix J. Additionally, the respective deviations between the averages, minima and maxima of the measured data base and the reference values are included. As previously mentioned, the reference natural gas composition was defined as the average of the Renningen 2013 data set. Therefore, the natural gas properties of the reference state remain unchanged through the entire testing period.

As outlined in Figure 4.14a, the carbon coefficients only moderately deviate from the reference value, having deviations from -1.6 to 1.8 %. The displayed uncertainties are high, due to the direct relation of the carbon coefficient to the two major species in natural gas, which are methane and ethane.

The oxygen coefficients highly differ from the reference value, showing deviations between -69.4 and 89.9 %, as depicted in Figure 4.14b. The uncertainties are very low, since the computation methodology only includes carbon dioxide.

As shown in Figure 4.14c, the electron coefficients slightly deviate from the reference values with deviations from -0.4 to 1.0 %. Analogous to the carbon coefficients, the computed uncertainties are high, based upon the direct relation of the electron coefficient to the two major species in natural gas.

Surprisingly, the carbon, oxygen and electron coefficients have very similar progressions during the outlined sampling period. Consequently, an increasing carbon dioxide content almost always leads to a rise in the amount of higher hydrocarbons, simultaneously increasing K_{C}, K_{O} and $K_{\mathrm{e^-}}$. The effect occurs vice versa for decreasing amounts of carbon dioxide. However, the match of the progressions was already indicated in Figure 3.11, where the entire Renningen 2016 data set shows a very good match to the regression function between the electron coefficient and change in molar quantity coefficient.

The molar masses temporarily have high deviations from the reference value, including deviations between -3.9 and 1.5 %, as shown in Figure 4.14d. The uncertainties of the molar mass calculations are high, since all measured species are used for the computation.

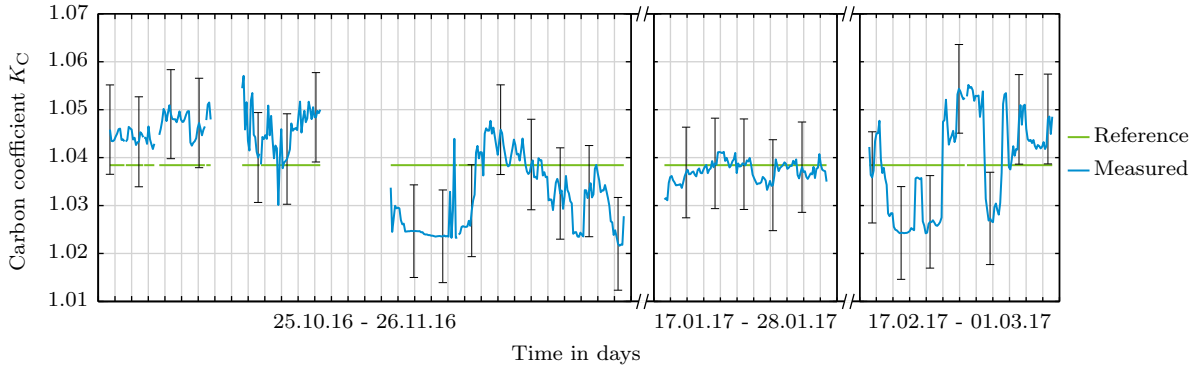

(a) Carbon gas coefficient

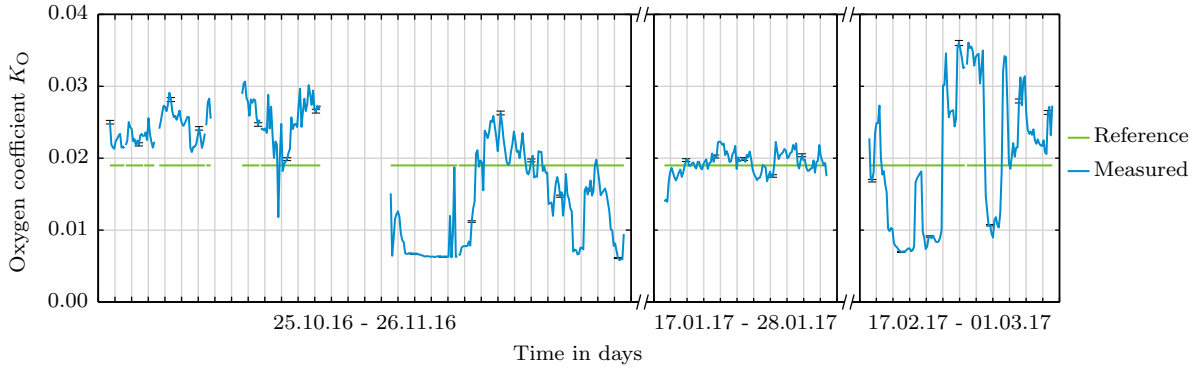

(b) Oxygen gas coefficient

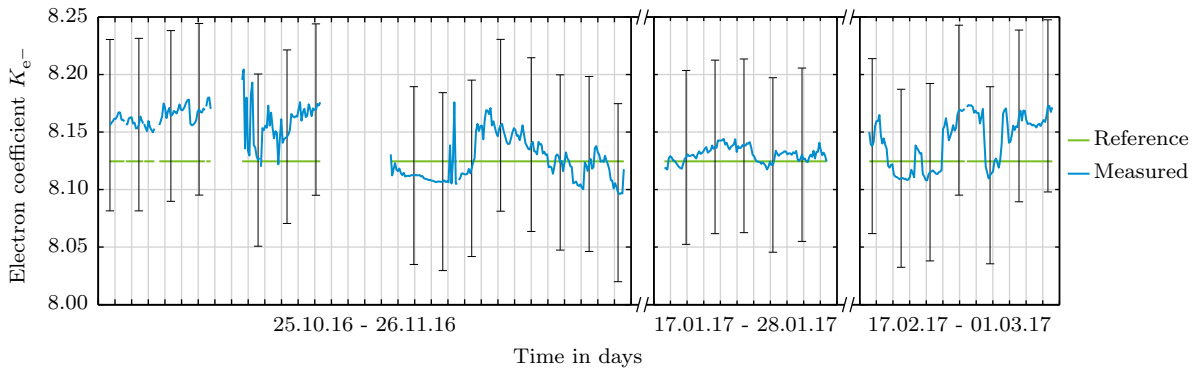

(c) Electron gas coefficient

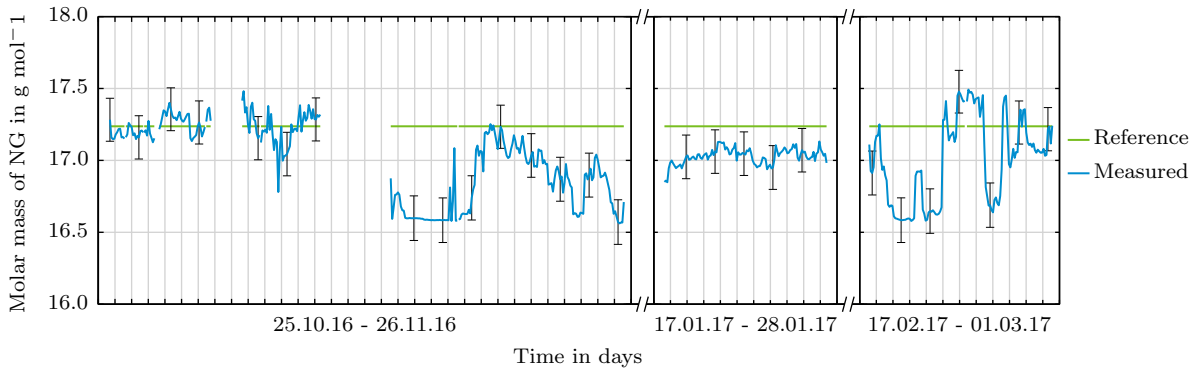

(d) Molar mass

Figure 4.14: Experimental results of NM_1 - Comparison between reference and measured natural gas states

In summary, compared to the chosen reference state, the natural gas quality noticeably fluctuates during the testing period. Consequently, the evaluated time frame provides a significant baseline for the assessment of the fluctuating natural gas quality effect on an AEGR SOFC system operated with the NM_1. However, the K_C, K_O, K_{e^-} and $M_{NG,in}$ averages nearly match the reference values, with the highest deviation in the molar mass of -1.3 %. Therefore, the Renningen 2013 data set average is an almost ideal reference composition for the NM_1 testing period, based upon the agreement of the averages of the measured data set and reference values.

4.4.3.2 Characteristic parameters and flow rates

The fluctuating natural gas quality effects on $U_{f,S}$ and Φ during the NM_1 testing period are depicted in Figures 4.15a and 4.15b. Additionally, the agreement of the measurement based values and the basic constraints of the NM_1 are displayed in Figures 4.15c and 4.15d. As shown in equations (4.2) and (4.3), the two basic constraints of the NM_1 are a constant natural gas mass flow rate and a constant reformer inlet molar or volume flow rate for any fluctuating and designated reference state. As previously introduced, the corresponding time frames, samples sizes and leading system set points in the individual testing periods are listed in Table J.1 in appendix J. Each subplot of Figure 4.15 outlines four individual progressions:

1. Set point - the set points of the characteristic parameters $\left(U_{f,S,SP} \text{ and } \Phi_{SP}\right)$ or the corresponding actuator set points $\left(\dot{m}_{NG,in,SP} \text{ and } \dot{V}_{ref,in,SP}\right)$.

2. Measured - the indirectly measured characteristic parameters $\left(U_{f,S,Msd} \text{ and } \Phi_{Msd}\right)$ or measurement based analytically calculated values $\left(\dot{m}_{NG,in,Msd} \text{ and } \dot{V}_{ref,in,Msd}\right)$.

3. Simulated - the simulated values $\left(U_{f,S,NM_1}, \Phi_{NM_1}, \dot{m}_{NG,in,NM_1} \text{ and } \dot{V}_{ref,in,NM_1}\right)$ based upon the NM_1 equations, as outlined in section 4.2.2.1.

4. Scaled Sim - the scaled simulated outputs $\left(U_{f,S,NM_1,scaled},\ \Phi_{NM_1,scaled},\ \dot{m}_{NG,in,NM_1,scaled} \text{ and } \dot{V}_{ref,in,NM_1,scaled}\right)$ based upon the adjusted NM_1 equations, as outlined in section 4.4.2.

The description of the results is divided into two portions, 2016 and 2017, since in 2017 the derived MFC scaling was incorporated in the control logic of the SOFC test rig. Consequently, the 2016 portion includes the NM_1 samples from the 25th of October to the 26th of November, as well as the scaled simulated outputs. The 2017 portion includes the NM_1 samples from the 17th of January to the 1st of March.

As shown in Figures 4.15a and 4.15b, in 2016, the measured values of $U_{f,S}$ and Φ cannot be reproduced with the simulated outputs, since the progressions have extreme offsets and completely different trends. The deviations are a result of the disagreement between the measurement based analytically calculated values and the two basic constraints of the NM_1. As outlined in Figures 4.15c and 4.15d, neither the natural gas mass flow rate nor the reformer inlet volume flow rate are kept constant by the actuators in the SOFC test rig, whereas the simulation of the NM_1 is in perfect agreement with the two designated actuator set points. The measurement based natural gas mass flow rate fluctuates around the specified set point value, due to the previously outlined MFC behavior during natural gas operation. The designated reformer inlet volume flow rate set point is always exceeded by the corresponding measurement based value, due to the applied constant safety scaling factor of the recirculation flow rate. As a result, for the majority of the aggregated time steps, the measured $U_{f,S}$ is lower than the simulated value, whereas the measured Φ exceeds the estimated value. Additionally, none of the outlined deviations in Figure 4.15 can be explained by the measurement uncertainties, since the displayed error bars do not

close the distinct gaps between the measured and simulated values. However, all measurement based values can be accurately reproduced with the scaled simulation outputs, even though the reformer inlet volume flow rate is only scaled with constant values for each individual time frame. The measured values and scaled simulated outputs of $U_{f,S}$ are in high agreement, based upon the accurate reproduction of the MFC behavior using the derived MFC scaling methodology, which was previously described in section 4.4.2. Consequently, as outlined in Figure 4.15c, the natural gas mass flow rate can be almost ideally predicted by the scaled modeling approach. For the majority of the aggregated time steps, the progression of the measured and scaled simulated values of Φ match, as outlined in Figure 4.15b. Nevertheless, compared to the fuel utilization factor, the disagreement of the Φ progressions are still more apparent, based upon the scaling of the reformer inlet flow rate with constant values for each individual time frame. The remaining offsets between the measured and scaled simulated data can be partially explained with the displayed error bars, which often bridge the gaps between both data sets. Nonetheless, for several aggregated time steps, the gaps between the measured and scaled simulated trends of $U_{f,S}$ and Φ are still exceeding the displayed error margins. Additional offsets may be caused by natural gas quality fluctuations, which occur during the two hour sampling period of one consecutive quantification at the four designated system positions of the GC. Consequently, the condensed GC data points at the aggregated time step, which are the basis of the evaluation, may already include an intrinsic error, since a simultaneous analysis of all four positions at the exact same time was impossible. However, the intrinsic error is very small and the agreement between the measured and scaled simulated mass and volume flow rates verifies the derived MFC scaling approach.

In 2017, MFC scaling was implemented into the control logic of the SOFC test rig using the multi gas analyzer for a continuous determination of the specific heat capacity of natural gas. Additionally, the arbitrary safety scaling factor of the recirculation flow rate was removed, ultimately yielding a realization of the two basic constraints of the NM_1. As displayed in Figure 4.15c and 4.15d, the natural gas mass flow rate and reformer inlet volume flow rate were kept close to the set points at a nearly constant level for a long period of time, even though comparable natural gas quality fluctuations to the year 2016 occurred, as outlined in Figure 4.14. Consequently, for the majority of the aggregated time steps, the trends of the measured values of $U_{f,S}$ and Φ can be reproduced with the NM_1 simulation without any scaling. The offsets between the measured and simulated data can be partially explained with the displayed error bars, which frequently bridge the gaps between both trends. Nevertheless, additional deviations are apparent which were not included in the calculation of the uncertainties. First, the realizations of the mass and volume flow rate set points by the actuators are not ideal, as indicated by the slight offsets to the designated set points in Figures 4.15c and 4.15d. Second, the previously mentioned intrinsic error also effects the 2017 data records. Third, the simulated data was calculated based solely upon the natural gas quantification of the GC, whereas the online MFC scaling was implemented using the multi gas analyzer. Consequently, the applied MFC scaling coefficient may not completely match the corresponding simulated states, since the determined specific heat capacities from the multi gas analyzer and GC have a slight deviation, as outlined in Figure 4.11e. For the 2016 portion, the effect of an ideally matching MFC scaling coefficient to the natural gas state, quantified with the GC, was already outlined for the scaled simulation results. Instead of the multi gas analyzer outputs, the GC data was used to compute the MFC scaling coefficient for the scaled simulation. However, in comparison to 2016, the implementation of the MFC scaling and removal of the arbitrary safety scaling factor of the recirculation flow rate in 2017 allows for the interpretation of the measured data and trends, using the NM_1 simulation results without scaling. The basic constraint of the NM_1 are realized by the actuators with adequate accuracy.

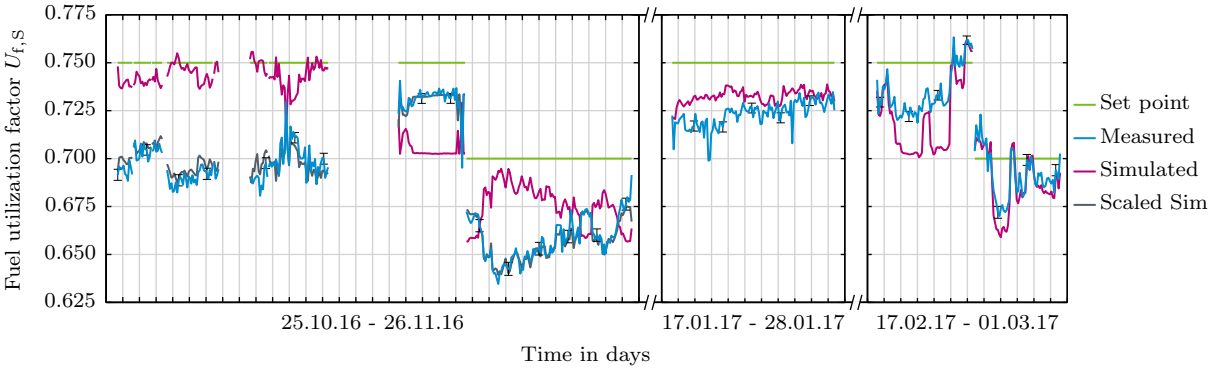

(a) Fuel utilization factor of the stack

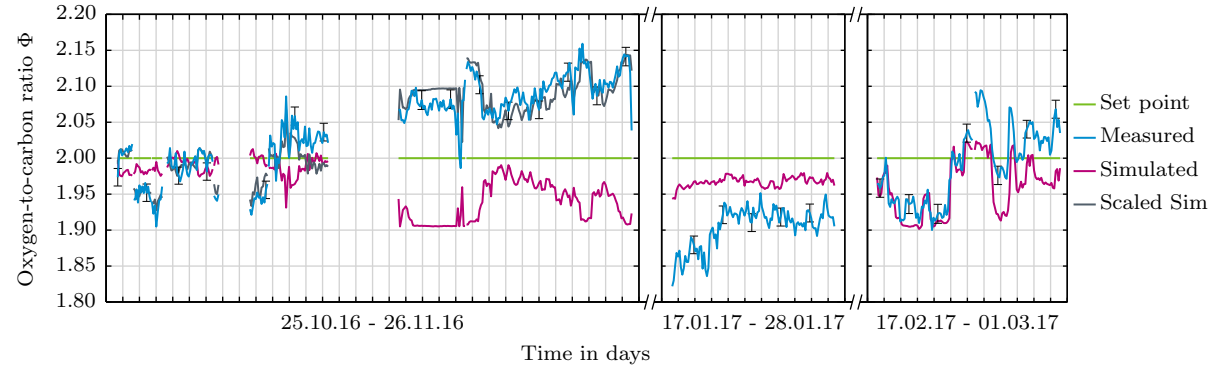

(b) Oxygen-to-carbon ratio

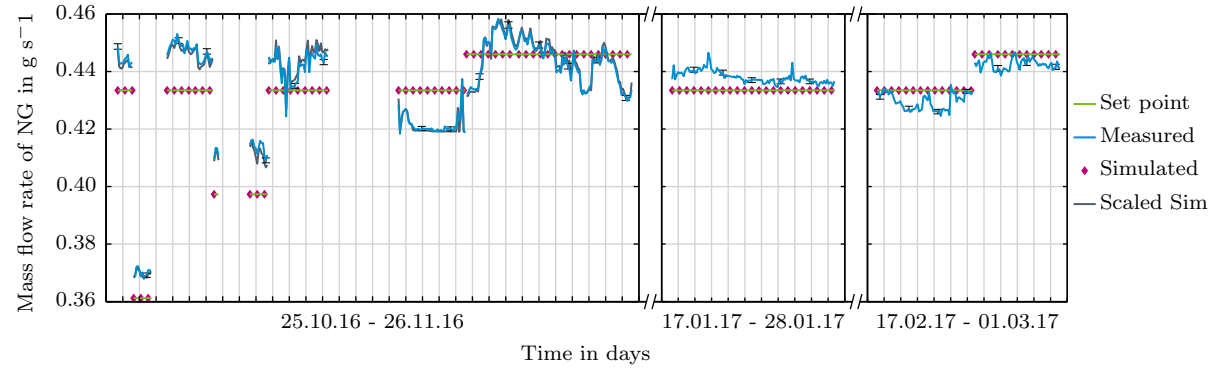

(c) Mass flow rate of natural gas

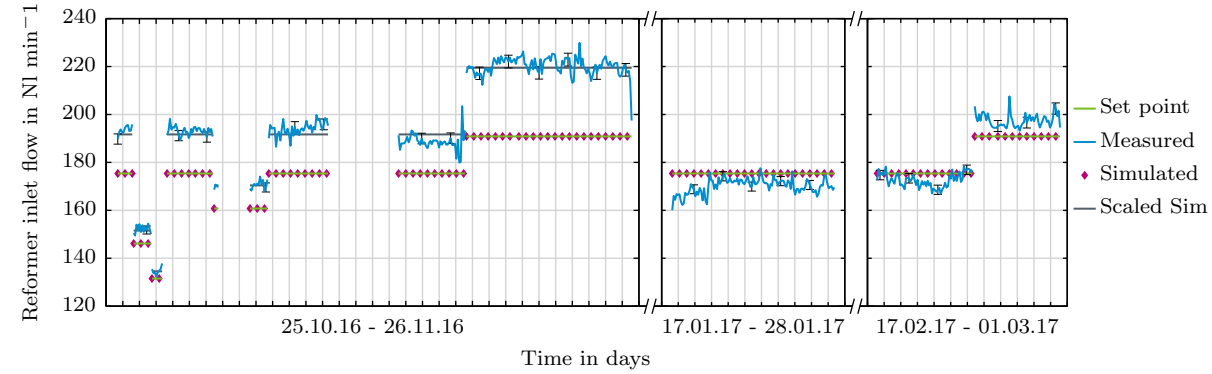

(d) Volume flow rate at reformer inlet

Figure 4.15: Experimental results of NM_1 - Comparison of set point values, simulated outputs and measurement based calculated values with active MFC scaling in 2017

In summary, the accurate realization of the designated flow rate set points by the actuators provides the basis for the interpretation of the measured data and trends using the NM_1 simulation results. The derived MFC scaling logic was successfully tested and implemented, ultimately yielding an accurate implementation of the NM_1. Additionally, the validation of the MFC scaling, including the accurate realization of the mass flow rate set point at the MFC, provides the basis for the development of advanced control approaches. Consequently, the mass flow rate at the MFC can be accurately controlled to any designated set point. This ultimately enables the adaptability to fluctuating natural gas quality by linking the determination of the mass flow rate set point to a natural gas quality indicator. Therefore, as subsequently outlined in section 5.5, the system responses during natural gas operation can nearly match the ideal outputs of the IC_0. Furthermore, the high agreement of the measured and simulated results validates the modeling approach for natural gas operation and verifies the analytically derived constraints of the NM_1, introduced previously in section 4.2.2.1. Additionally, the high accuracy and validity of the volume flow rate determination at the reformer inlet, as a function of the measured pressure difference, rotational speed, pressure and temperature at the blower inlets using the corresponding approximated blower maps and laws of similitude, are outlined by the precise realization of the set point in 2017, as shown in Figure 4.15d.

As shown in Figure 4.15a and Table J.2, for $U_{f,S,SP}$ of 0.70 and 0.75, the total occurring measured spreads of $U_{f,S}$ are 0.63 to 0.72 and 0.68 to 0.76, respectively. Consequently, the risk of irreversible cell damage, due to the partial depletion of fuel inside single cells of the stack, is very low. In addition, as a result of the robust control of the stack temperature using the air flow rate, the thermal balance of the stack is only slightly affected by the deviation of $U_{f,S}$, based upon the small anode exhaust gas manifold temperature spreads between 797 and 807 °C. Nevertheless, low $U_{f,S}$ yield reduced gross efficiency, as depicted in Figure 4.18. Additionally, as outlined in Figure 4.15b and Table J.2, Φ deviates between 1.82 and 2.16. Therefore, during the NM_1 testing period, the risk of carbon deposition was temporarily very high. Especially between the 27th and 28th of October 2016, the risk of carbon formation was excessive, due to the low minimal values of the oxygen-to-carbon ratio and reformer outlet temperature of 1.9 and 568 °C, respectively.

In 2017, the characteristic parameter spreads are reduced based upon the implementation of the MFC scaling and the safety scaling factor removal. For $U_{f,S,SP}$ of 0.70 and 0.75, the intervals of $U_{f,S}$ are constricted to 0.67 to 0.72 and 0.70 to 0.76, respectively. Additionally, the Φ spread is reduced to 1.82 to 2.09. In addition, the corresponding temperature levels at the reformer and anode outlet range between 589 to 599 °C and 797 to 804 °C, respectively. As a result, the gross efficiency is increased, but the risk of carbon deposition is still temporarily very high, due to the low Φ minima.

In comparison to Figure 4.10, for $U_{f,S,SP}$ of 0.75 in the 2017 data portion, the outlined deviation interval of $U_{f,S}$ covers a wide range of the corresponding 95 % confidence interval of the complete Renningen 2016 data set with boundary values of 0.70 and 0.80. However, the minimal measured Φ of 1.82 exceeds the lower boundary value of 1.87 of the corresponding 95 % confidence interval. The deviation of the minimal and lower boundary Φ values may be caused by three major circumstances: (a) The use of the average from the Renningen 2013 data set as the reference gas composition yields a downward shift of the entire Φ domain, as outlined in Figure 4.21 in section 4.5.2; (b) The uncertainties of the realization of the electric current, natural gas mass flow rate and reformer inlet molar flow rate set points may exceed the assumed magnitudes; (c) The determination of Φ with the GC may be subjected to system settling effects between the 17th and 21st of January 2017, since Φ values lower than 1.9 only occurred during this time frame and the system was restarted after a short downtime. Nevertheless, the outlined measured values of $U_{f,S}$ and Φ are still in sufficient agreement with the corresponding calculated 95 % confidence intervals.

4.4.3.3 Mole fractions at reformer inlet, reformer outlet and anode outlet

As introduced in section 4.4.1.4, equilibrium mole fractions can be computed for the IC_0, using the indirectly measured characteristic parameters as modeling inputs. Consequently, the measured and calculated equilibrium mole fractions are compared at the reformer inlet, reformer outlet and anode outlet, as outlined in Figure 4.16. In contrast to the previously displayed comparison of the measured and calculated mole fractions during methane operation in section 4.3.3, the agreement is slightly lower. The deviations from the ideal matching lines are higher, since the natural gas composition may fluctuate during consecutive GC analyses, ultimately causing an intrinsic error. Nevertheless, the overall agreement between the measured and calculated equilibrium mole fractions with the IC_0 during natural gas operation are strong, due to 95 % of the corresponding absolute deviations ranging between approximately -0.006 and +0.007.

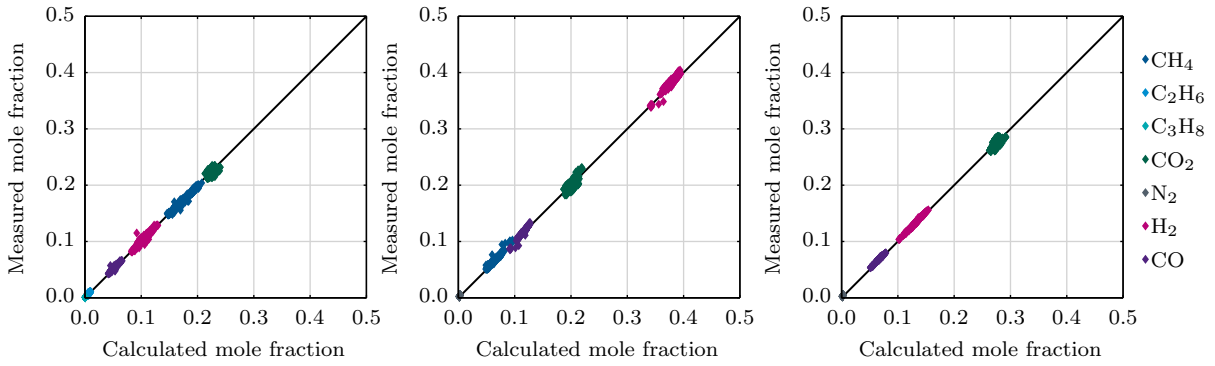

(a) Reformer inlet (b) Reformer outlet (c) Anode outlet

Figure 4.16: Experimental results of NM_1 - Comparison of measured and calculated equilibrium gas composition with IC_0

Additionally, the equilibrium mole fractions can also be calculated for the NM_1 based upon the natural gas quantification and set points of the characteristic parameters, as introduced in section 4.4.1.4. The comparison of the measured and calculated equilibrium mole fractions with the NM_1 at the three evaluated system positions are depicted in Figure 4.17. It should be noted that for the 2016 data samples, the scaled simulated composition outputs are displayed.

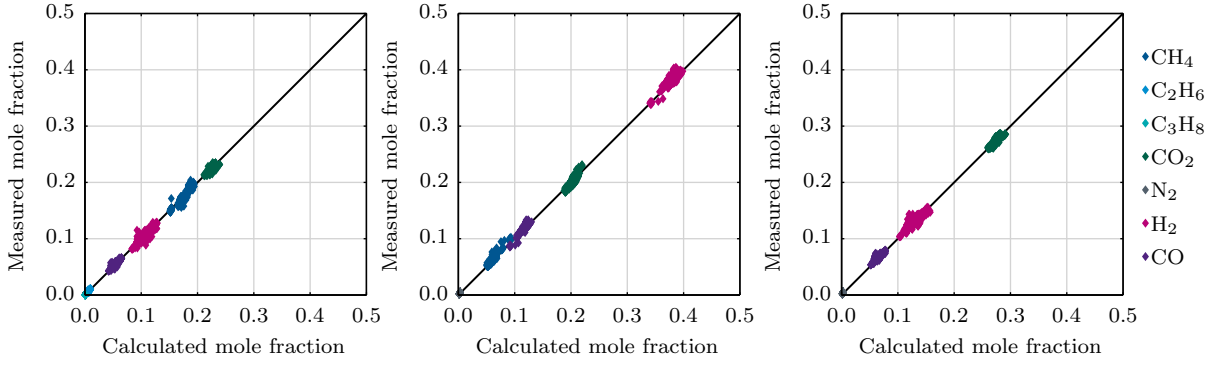

(a) Reformer inlet (b) Reformer outlet (c) Anode outlet

Figure 4.17: Experimental results of NM_1 - Comparison of measured and calculated equilibrium gas composition with NM_1

The agreement between the calculated equilibrium mole fractions with the NM_1 and the measured data is still strong, due to 95 % of the corresponding absolute deviations ranging between approximately -0.006 and +0.009. Compared to the IC_0 results, the deviations to the ideal matching lines are higher, due to intrinsic error and slight mismatch between the measured and simulated characteristic parameters, previously displayed in Figures 4.15a and 4.15b. However, both comparisons of the measured and calculated mole fractions outline that higher hydrocarbons are completely converted at the reformer outlet and that methane is not present in quantifiable amounts at the anode outlet. In summary, the strong agreement between the measured and calculated mole fractions validates the modeling approach and the correct implementation of the IC_0 and NM_1 for natural gas operation.

4.4.3.4 Electrical efficiency

For the application of the control scheme, a reference natural gas composition needs to be defined. Therefore, without access to a natural gas quantification system, the gross electrical efficiency can only be calculated in relation to the reference natural gas composition, yielding an imaginary reference efficiency value. However, fluctuating natural gas quality also affects the efficiency, due to corresponding changes of the characteristic parameters and natural gas properties, ultimately yielding another system state with potentially different voltage levels for a fixed electric current. Additionally, even for identical system states, the voltage and thus, the electrical efficiency are subjected to steady degradation effects, ultimately decreasing the values over time. Consequently, a degradation independent parameter was derived to compare the imaginary reference efficiency value to the measured natural gas state. The ratio between the measured gross electrical efficiency and the imaginary reference efficiency can be expressed independently of the voltage, since the measured voltage is a result of the corresponding system state. The ratio can be used to asses whether the efficiency at a single aggregated time step is higher or lower compared to the corresponding expected reference value. The ratio is calculated based upon the application of equation (2.41), and assuming a constant voltage level for the reference and measured state, as shown in equation (4.30).

$$\frac{\eta_{\text{Gross,Msd}}}{\eta_{\text{Gross,R}}} = \frac{\frac{E_{\text{Cell,Msd}}\, U_{\text{f,Sys,Msd}}\, F\, K_{\text{e}^-,\text{Msd}}}{h_{\text{i,NG,Msd}}}}{\frac{E_{\text{Cell,Msd}}\, U_{\text{f,Sys,R}}\, F\, K_{\text{e}^-,\text{R}}}{h_{\text{i,NG,R}}}} = \frac{U_{\text{f,Sys,Msd}}\, K_{\text{e}^-,\text{Msd}}\, h_{\text{i,NG,R}}}{U_{\text{f,Sys,R}}\, K_{\text{e}^-,\text{R}}\, h_{\text{i,NG,Msd}}} \tag{4.30}$$

As outlined in Figure 4.18, for the majority of the aggregated time steps in the NM_1 testing period, the measured gross efficiency is lower than the corresponding expected reference value, showing differences up to 4.4 %.

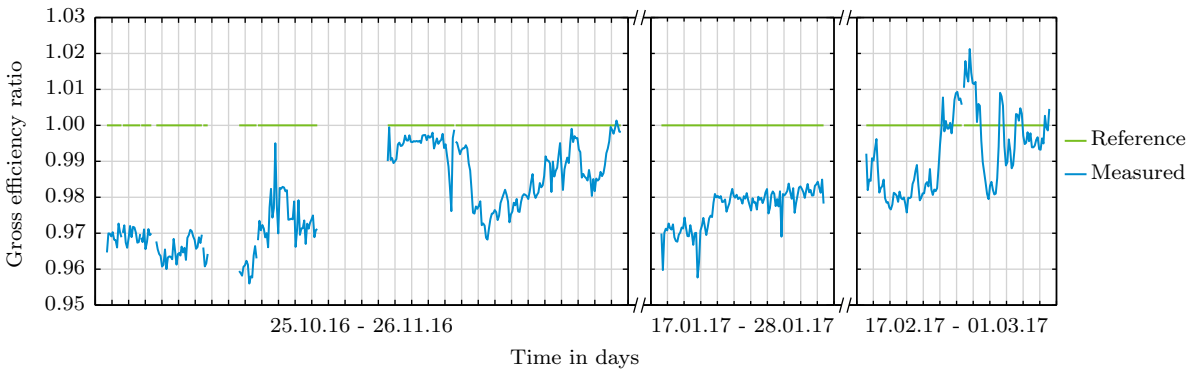

Figure 4.18: Experimental results of NM_1 - Comparison of expected and measured electrical efficiency

The 2016 data portion displays high negative offsets, as a result of the strong negative deviation between the measured and designated set point values of $U_{f,S}$, as outlined in Figure 4.15a. The deviations of $U_{f,S}$ are based upon the excessive supply of natural gas, as displayed in Figure 4.15c. Occasionally, in the 2016 data portion, the measured and expected efficiencies have comparable values, since low $U_{f,S}$ are overcompensated by excessive Φ, ultimately yielding intermediate $U_{f,Sys}$. Both $U_{f,S}$ and Φ are small in the January 2017 data, causing low $U_{f,Sys}$ and therefore, reduced gross efficiency. In the February 2017 data, the effects of fluctuating natural gas quality are moderate, ultimately yielding gross efficiency values that fluctuate about the reference values by approximately $\pm 2\,\%$.

4.4.3.5 Conclusions

The evaluation of the experimental results of the SOFC test rig operated with natural gas using the NM_1 highlights the following major conclusions:

1. The NM_1 was successfully implemented and the measured states were reproduced with the modeling approach. However, scaling the mass flow controller set point was necessary to realize the basic constraint of the NM_1 with a fixed natural gas mass flow rate, due to the calibration of the MFC to pure methane.

2. The derived scaling logic of the MFC set points, as a function of the measured specific heat capacity, was successfully implemented. The scaling allows for the accurate realization of any given natural gas mass flow rate set point, ultimately providing the basis for the implementation of an advanced control scheme, which manipulates the natural gas mass flow rate as a function of the detected natural gas quality.

3. The modeling approach was further validated for natural gas operation, based upon the strong agreement between the calculated and measured compositions at the reformer inlet, reformer outlet and anode outlet for both the NM_1 and IC_0.

4. The implemented characteristic blower map modeling approach was verified based upon the accurate realization of the reformer inlet volume flow rate set point in 2017.

5. The occurring intrinsic error, due to possible natural gas fluctuations during a single consecutive GC quantification interval, does not obstruct the reproduction of the system states using the simulation. The intrinsic error can be eliminated with simultaneous analyses at all four system sampling positions, using four individual GCs.

6. The deviations to the designated set points of the fuel utilization factor during the testing period were tolerable. Whereas, the low oxygen-to-carbon ratios temporarily lead to very high risks of carbon deposition.

7. The fluctuations of the natural gas quality during the testing period did not exceed the expected range. The measured deviation domains are similar to the previously outlined 95 % confidence intervals of the characteristic parameters from the Renningen 2013 and Renningen 2016 data sets, displayed in Figure 4.10.

8. The measured gross efficiency was frequently lower than the expected reference values, primarily because the measured fuel utilization factors of the stack have a highly negative deviation to the designated set points.

In the following section, the effect of fluctuating natural gas quality on the NM_1 system responses are evaluated in more detail by conducting a sensitivity analysis in the modeling environment.

4.5 Sensitivity analysis for natural gas mass flow rate CS I

The focus of this section is the evaluation of the applicability of the NM_1 by conducting a sensitivity analysis, focusing primarily on the leading set point variables of the control strategy. The sensitivity for the NM_1 is evaluated by varying: (a) the set point of the fuel utilization factor of the stack; (b) the set point of the oxygen-to-carbon ratio; (c) the set point of the electric current; (d) the natural gas reference composition; and (e) the arbitrary hydrogen addition to the natural gas data base. As the basis of the evaluation, the natural gas data sets of Saint-Thegonnec 2014 and Renningen 2016 are used, providing a baseline of roughly 15500 measured natural gas compositions. It should be noted that only a single parameter is varied, while all other inputs are kept at the designated nominal values, which are listed in Table 4.2.

4.5.1 Variation of leading set points

4.5.1.1 Fuel utilization factor of the stack

The variation of $U_{f,S,SP}$ between 0.6 and 0.8 is depicted in Figure 4.19. In both the Saint-Thegonnec 2014 and Renningen 2016 data sets, an increasing $U_{f,S,SP}$ yields larger fuel utilization factor domains and confidence intervals. Consequently, the impact of fluctuating natural gas quality on $U_{f,S}$ is higher with a higher designated set point. For instance, in the Saint-Thegonnec 2014 data set, the 95 % confidence interval of $U_{f,S}$ has a spread of 0.066 for a set point of 0.6, but for a set point of 0.8 the domain increases to 0.094. Additionally, an increasing $U_{f,S,SP}$ also slightly enlarges the oxygen-to-carbon ratio domains. However, the effect is only nominal, since for $U_{f,S,SP}$ of 0.6 and 0.8, the spreads of the 95 % confidence intervals of Φ are only 0.168 and 0.175, respectively. Nevertheless, as previously outlined in Figure 2.3, lower absolute values of $U_{f,S}$ yield reduced gross electrical efficiency. As a result, lower $U_{f,S,SP}$ represent a trade-off between reduced efficiency and increased robustness against fluctuating natural gas quality.

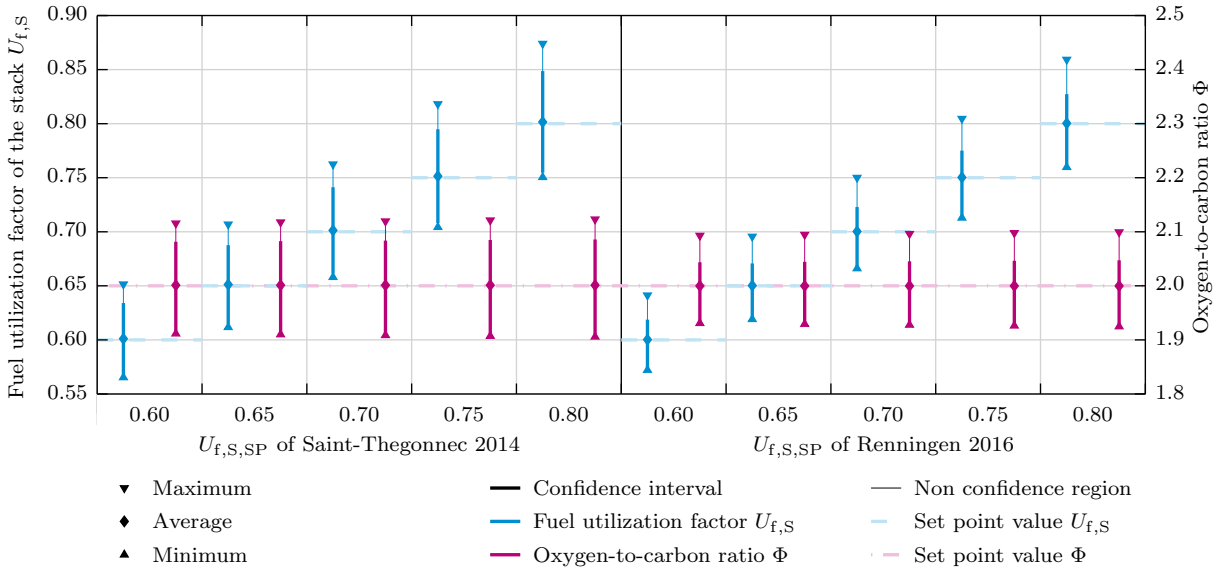

Figure 4.19: Sensitivity analysis for NM_1 - Variation of fuel utilization factor of the stack set point for Saint-Thegonnec 2014 and Renningen 2016 data set

4.5.1.2 Oxygen-to-carbon ratio

Figure 4.20 displays the variation of Φ_{SP} between 1.9 and 2.3 for the Saint-Thegonnec 2014 and Renningen 2016 data set. In both data sets, the lower Φ_{SP}, the lower the spreads of the 95 %

confidence intervals of Φ. However, the impact is considered very small, since the spreads of the 95 % confidence intervals of Φ are only 0.169 and 0.186 for Φ_{SP} of 1.9 and 2.3 in the Saint-Thegonnec data set, respectively. Nevertheless, the spreads of the 95 % confidence interval of $U_{f,S}$ are enlarged significantly by higher Φ_{SP}. In the Saint-Thegonnec data set, the spread of the 95 % confidence interval of $U_{f,S}$ is increasing from 0.082 to 0.104 for Φ_{SP} of 1.9 and 2.3, respectively. As a result, the minimization of Φ to values barely above harmful carbon deposition thresholds is desirable, since the fluctuating domains of both $U_{f,S}$ and Φ are reduced. Additionally, lower values of Φ can result in increased net system efficiency, due to a reduction in the auxiliary recirculation blower power demand and enhanced Nernst voltages, based upon smaller water vapor fractions at the stack inlet.

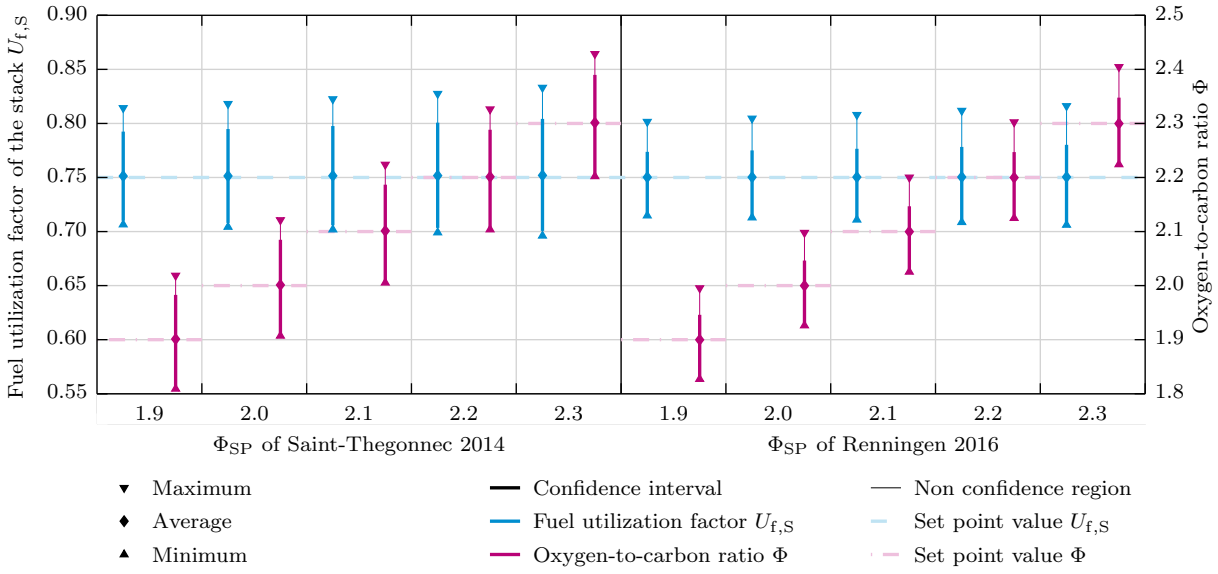

Figure 4.20: Sensitivity analysis for NM_1 - Variation of oxygen-to-carbon ratio set point for Saint-Thegonnec 2014 and Renningen 2016 data set

4.5.1.3 Electric current

As previously outlined in section 4.3.1, the electric current is simply used as an input parameter to compute flow rates in the modeling approach. Additionally, as shown in section 4.2.2.1, the electric current was completely eliminated in the derivation of the constraints of the NM_1. As a result, both domains of $U_{f,S}$ and Φ are completely unaffected by a variation of I_{SP}, as outlined in Figure M.1 in appendix M. Nevertheless, it should be noted that in reality, the change of I_{SP} is tremendously influencing the thermal balance of the SOFC system and the flow rates of air and fuel. Consequently, the risk for carbon deposition might increase for lower I_{SP}, since the 95 % confidence intervals of Φ remain unchanged but the designated reformer equilibrium temperature might not be reached. Additionally, lower absolute flow rates at the stack inlet increase the risk of fuel starvation inside single cells of the stack for an unchanged 95 % confidence interval of $U_{f,S}$, due to an enhanced effect of possible unequal fuel distributions. Lastly, decreased flow rates might lead to increased sensor and actuator uncertainties, based upon possible higher error margins at non nominal operation.

4.5.2 Variation of reference natural gas composition

The influence of different reference natural gas compositions on the fluctuation domains of $U_{f,S}$ and Φ in the Saint-Thegonnec 2014 and Renningen 2016 data sets are shown in Figure 4.21. The best case definition for the reference natural gas composition, as the average composition

of the respective data set, is outlined for both data sets as the ideal comparison baseline. The comparison cases are displayed in the first and last segment in Figure 4.21, highlighting the match of the $U_{f,S}$ and Φ averages to the designated set points.

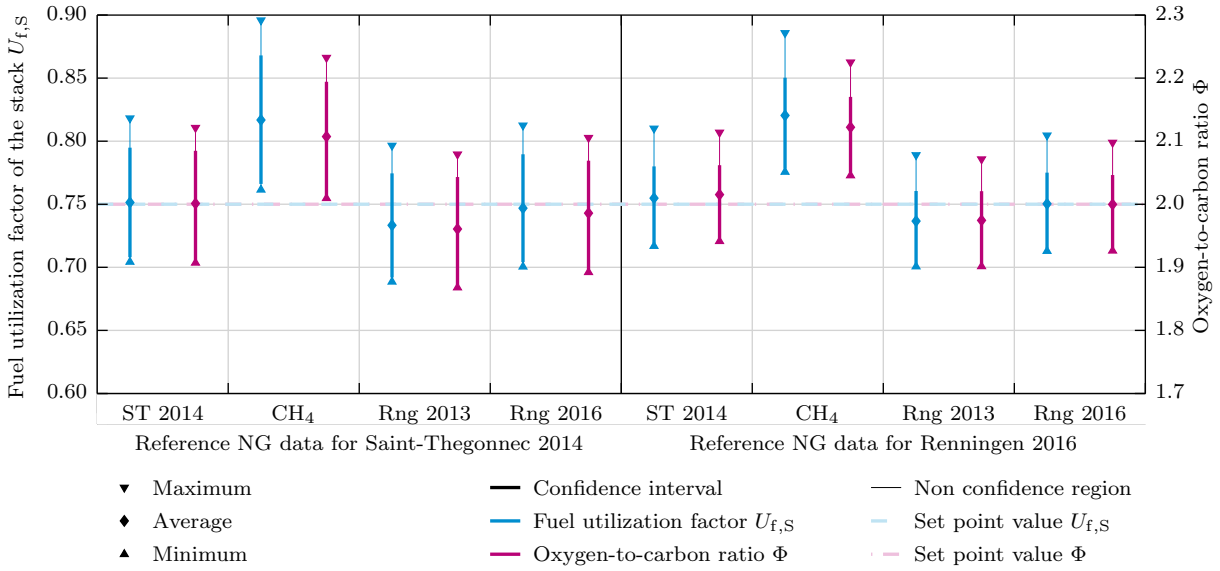

Figure 4.21: Sensitivity analysis for NM_1 - Variation of the reference natural gas composition for Saint-Thegonnec 2014 and Renningen 2016 data set

As outlined in the set of equations in section 4.2.2.1, the influence of a changing reference composition on the NM_1 is a multi-variable effect, which can not entirely be expressed by simple ratios between the properties of the reference and fluctuating state. However, as shown in equation (4.31), a slight rearrangement of equation (4.5) highlights the major hypothetical influence on the fuel utilization factor of the fluctuating state, which is the molar mass to electron coefficient ratio (K_M) of the fluctuating and reference states. For the reference state, the ratio is occurring as the reciprocal value. The data outlined in Figure 4.21 and Table 4.6 clarifies that the major effect on $U_{f,S}$ can be described with K_M for the fluctuating and designated reference state. Consequently, if $K_{M,R}$ is less than the average of $K_{M,F}$, then the domain of $U_{f,S}$ shifts upwards. Additionally, the higher the difference between $K_{M,R}$ and $K_{M,F}$, the higher the enlargement of the minimum to maximum domains of $U_{f,S}$ and Φ. However, for $K_{M,R}$ greater than the average of $K_{M,F}$, the effects occur vice versa, resulting in downward shifts and constrictions of both domains.

$$U_{f,S,F} = \frac{U_{f,S,R}\,\frac{K_{e^-,R}\,M_{NG,in,F}}{M_{NG,in,R}\,K_{e^-,F}}\,(1-r_F)}{(1-r_R\,(1-U_{f,S,R}))-r_F\,U_{f,S,R}\,\frac{K_{e^-,R}\,M_{NG,in,F}}{M_{NG,in,R}\,K_{e^-,F}}} = \frac{U_{f,S,R}\,\frac{K_{M,F}}{K_{M,R}}\,(1-r_F)}{(1-r_R+r_R\,U_{f,S,R})-r_F\,U_{f,S,R}\,\frac{K_{M,F}}{K_{M,R}}} \quad (4.31)$$

Table 4.6: Molar mass to electron coefficient ratios of different reference natural gases

Mean composition of natural gas data set as reference state	ST 2014	CH_4	Rng 2013	Rng 2016
Molar mass to electron coefficient ratio $\left(K_M = \frac{M_{NG,in}}{K_{e^-}}\right)$ in $g\,mol^{-1}$	2.096	2.005	2.122	2.101

As depicted in Figure 4.21, a shift of the reference composition to pure methane has tremendous effects on the fluctuation domains of $U_{f,S}$ and Φ. For both natural gas data sets, the

reference methane case yields remarkable upward shifts in the domains and distinct enlargements in the spreads of the 95 % confidence intervals. As outlined in Table 4.6, the molar mass to electron coefficient ratio of methane is significantly lower than that of both natural gas data set averages. As a result, based upon equation (2.4), the defined reference methane mass flow rate of fresh gas is far too low to represent stable natural gas conditions. In summary, the use of pure methane as the reference gas composition in the NM_1 yields extreme deviations from the designated set points, based upon the high disparity between the properties of pure methane and natural gas. Consequently, very harmful system states during natural gas operation are highly probable, due to the excessively high values of $U_{f,S}$. It should be noted that the increase of Φ is a direct result of the high values of $U_{f,S}$, since a higher amount of water vapor is present in the anode exhaust gas.

The average of the Renningen 2013 data set has a very high molar mass to electron coefficient ratio, as shown in Table 4.6. Therefore, the application of the Renningen 2013 data as the reference composition yields to small downward shifts of the domains of $U_{f,S}$ and Φ in both the Saint-Thegonnec 2014 and Renningen 2016 data sets, as displayed in Figure 4.21. The downward shifts and constrictions in the $U_{f,S}$ and Φ domains in the Saint-Thegonnec 2014 data set are slightly higher, since the molar mass to electron coefficient ratio is the lowest. In summary, the average of the Renningen 2013 data set is a very conservative reference in regard to $U_{f,S}$, based upon the large molar mass to electron coefficient ratio and the corresponding large reference natural gas mass flow rate. However, the Φ domains also shift towards lower values, due to lower $U_{f,S}$. Consequently, the risk of carbon deposition is enhanced, while the risk for fuel starvation is reduced.

Additionally, as displayed in Figure 4.21, the implementation influence of the Renningen 2016 data set average as the reference composition for the NM_1 in the Saint-Thegonnec 2014 data set is only minor, due to the small deviation between the molar mass to electron coefficient ratios. Consequently, the domains of $U_{f,S}$ and Φ shift slightly downwards with constrictions of both domains. The influences occur vice versa in identical magnitudes for the application of the Saint-Thegonnec 2014 data set average as the reference in the Renningen 2016 data.

In summary, the definition of an appropriate reference natural gas composition for the designated location of operation is of utmost importance for the implementation of the NM_1. A definition for the reference composition with a too low molar mass to electron coefficient ratio can yield excessive $U_{f,S}$, ultimately enhancing the risk of fuel starvation and cell degradation. The choice of a too conservation reference composition with a too high molar mass to electron coefficient ratio can increase the risk of carbon deposition, due to reduced oxygen-to-carbon ratios. For $K_{M,R}$ less than the average of $K_{M,F}$, the effect of changing natural gas quality on the fluctuation domains of $U_{f,S}$ and Φ is enlarged by high deviations between the designated reference composition and the best case definition of the reference state.

However, the definition of an appropriate reference composition is very challenging, since knowledge of the natural gas quality fluctuations at the designated location of operation is necessary. Nevertheless, the comparison of the Saint-Thegonnec 2014, Renningen 2016 and Renningen 2013 data sets indicate that the averages of any of the three data sets are applicable as an appropriate reference for the application of the NM_1 at both locations. In general, reference compositions can be estimated without the need of expensive equipment. For instance, by (a) the analysis of a single natural gas measurement at the designated location prior to the commissioning of the system; (b) the request of an average composition from the responsible transmission network operator; or (c) the collection or acquisition from temporally resolved natural gas data of a location as close as possible to the designated location of operation. It should be noted that option (a) can be steadily improved by extending the data base, due to the continuous analysis of natural gas samples in defined intervals.

4.5.3 Hydrogen addition

The effects of hydrogen addition to the Saint-Thegonnec 2014 and Renningen 2016 data sets on the fluctuation domains of $U_{f,S}$ and Φ are displayed in Figure 4.22. As a basis for the evaluation, the reference state is fixed, using the average of the temporally resolved data set without any hydrogen addition. The hydrogen is added as a hypothetical designated mole fraction to the respective data set, yielding a proportional reduction of the remaining species. For instance, a mixture of 95.0 % CH_4 and 5.0 % CO_2 subjected to a 10.0 % substitution with H_2 results in a composition of 85.5 % CH_4, 4.5 % CO_2 and 10.0 % H_2.

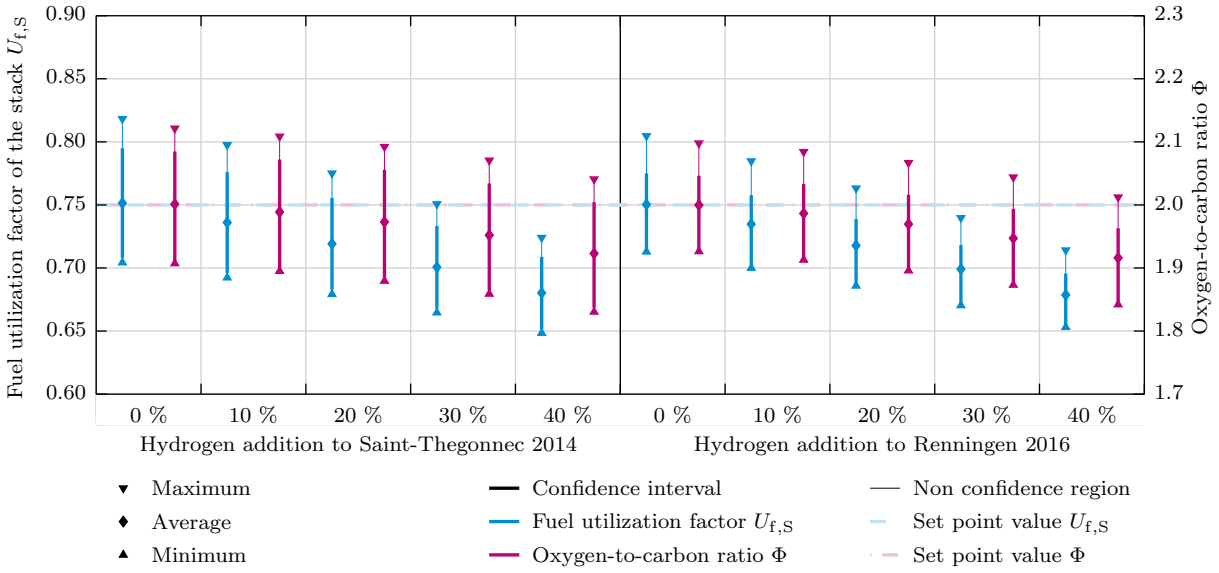

Figure 4.22: Sensitivity analysis for NM_1 - Variation of hydrogen addition with fixed reference natural gas composition for Saint-Thegonnec 2014 and Renningen 2016 data set

As outlined in Figure 4.22, increasing hydrogen content yields a downward shift and constriction in the $U_{f,S}$ and Φ domains for both natural gas data sets, respectively. As listed in Table 4.7, the molar mass to electron coefficient ratio is decreasing with rising hydrogen fractions.

Table 4.7: Molar mass to electron coefficient ratios for hydrogen addition to Saint-Thegonnec 2014 and Renningen 2016 data sets

Molar mass to electron coefficient ratio $\left(K_M = \frac{M_{NG,in}}{K_{e^-}}\right)$ in g mol^{-1} for mean composition of natural gas data					
Hydrogen addition in %	0	10	20	30	40
Saint-Thegonnec 2014	2.096	2.068	2.035	1.995	1.947
Renningen 2016	2.101	2.072	2.038	1.997	1.947

Therefore, $K_{M,R}$ is always greater than the average of $K_{M,F}$, since the average of the temporally resolved data set without any hydrogen addition is used as the reference. The depicted effects match the previous conclusions, derived for the variation of the reference natural gas composition in section 4.5.2. However, the influence on the shift of the Φ domain is less marked, due to the reduced amount of carbon atoms in the natural gas mixture for an increase in hydrogen fraction. Consequently, the effects of a 10 % H_2 addition to the Saint-Thegonnec 2014 or Renningen 2016 data sets are comparable to the application of the Renningen 2013 data as the reference composition. As a result, for an appropriate reference natural gas composition, the

NM_1 has a high robustness towards an addition of H_2, up to a total mole fraction of approximately 10 %. Beyond H_2 fractions of 10 %, the risk of carbon deposition is enhanced, due to the shift of the Φ domain towards lower values.

The influences of hydrogen addition on the $U_{f,S}$ and Φ domains can be completely compensated by an adjustment in the reference natural gas composition, as illustrated in Figure 4.23. In each individual segment of the graph, the respective natural gas data set average with the designated amount of added hydrogen is used as the ideal reference. Consequently, as previously outlined in section 4.3.2, the $U_{f,S}$ and Φ averages perfectly match the designated set point values of 0.75 and 2.00, respectively. Additionally, an increasing addition of H_2 leads to enhanced homogenization of the natural gas data set, ultimately reducing the fluctuation domain of $U_{f,S}$.

However, the adjustment of the reference is only possible if the hydrogen content is fixed and the resulting average natural gas data set composition is known. As a result, the previously discussed challenges of an appropriate reference composition definition are enhanced by possible hydrogen fractions in natural gas, since another degree of freedom has to be considered. Additionally, the differences in the chemical and physical properties of H_2 and CH_4 are strong. Consequently, increasing fractions of H_2 drastically change the properties of the natural gas mixture, such as the molar mass and electron coefficient.

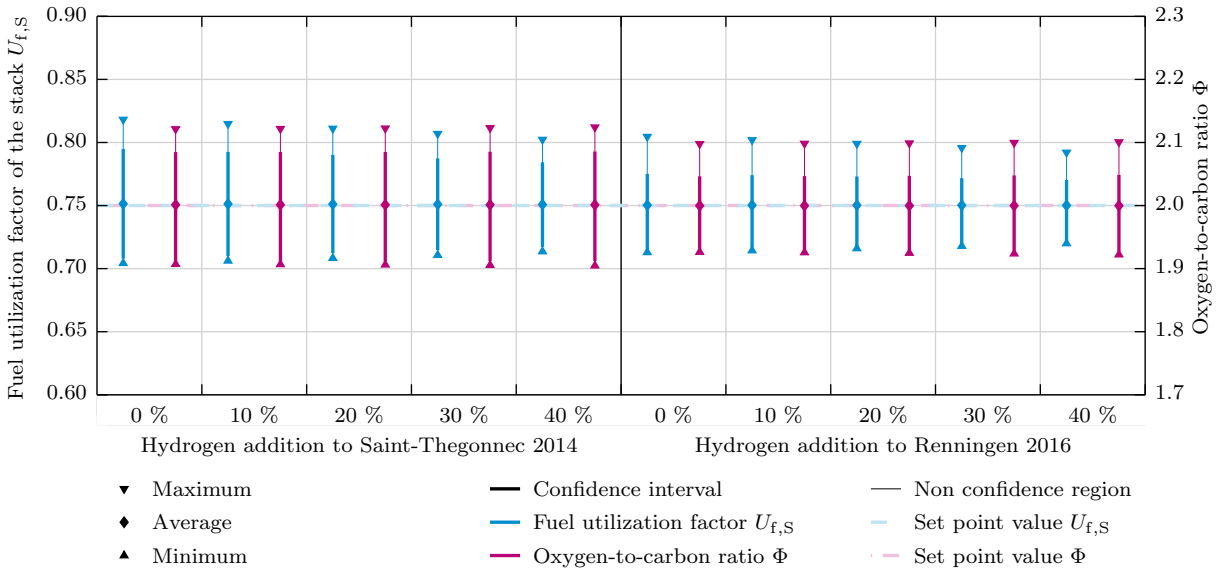

Figure 4.23: Sensitivity analysis for NM_1 - Variation of hydrogen addition with adjustment of reference natural gas composition for Saint-Thegonnec 2014 and Renningen 2016 data set

4.5.4 Conclusions

The conducted sensitivity analysis of the NM_1 leads to the following major conclusions:

1. Low set point values of $U_{f,S}$ result in constrictions in the $U_{f,S}$ and Φ domains at the cost of lower system efficiency. The constriction in the $U_{f,S}$ domain is significant, whereas the reduction in the Φ interval is only nominal. Consequently, the choice of $U_{f,S,SP}$ is subjected to a trade-off between higher system efficiency and lower robustness towards fluctuating natural gas quality.

2. Reduced Φ set point values result in distinct constrictions in the $U_{f,S}$ and Φ domains. Consequently, the definition of Φ_{SP} precisely at the edge of harmful carbon deposition thresholds is very desirable. As a result, the robustness towards fluctuating natural gas

quality can be increased. Additionally, the net system efficiency may be higher, due to a reduction in the auxiliary recirculation blower power demand and increased Nernst voltages, based upon smaller water vapor fractions at the stack inlet.

3. The set point of the electric current has no direct effect on the $U_{f,S}$ and Φ domains. However, indirect effects of amplifying or reducing nature towards the robustness against fluctuating natural gas quality can be connected with the I_{SP} variation. Indirect effects can include changes in the thermal balance of the system or influences on the behavior of sensors and actuators, which are not evaluated in the modeling approach.

4. The choice of an appropriate reference natural gas composition is of utmost importance for the application of the NM_1, due to the tremendous effect on the robustness towards fluctuating natural gas quality. However, the reference composition definition is a very challenging task, since knowledge about the natural gas composition at the location of operation in the recent past or a continuous tracking of the natural gas quality is necessary. In general, the closer the molar mass to electron coefficient ratio of the reference is to the average of the fluctuating natural gas states, the lower the deviations of the $U_{f,S}$ and Φ averages are to the designated set point values.

5. The NM_1 has a high robustness towards the addition of H_2, up to a total mole fraction of approximately 10 %, without the adjustment of the reference composition to consider H_2 as a possible species in natural gas. The effects of the addition of H_2 are comparable to the influence of a non ideal reference natural gas composition definition.

In the following chapter, the NM_1 is compared with 23 different control approaches inside the modeling environment. Additionally, based upon the derived natural gas data constraints, an advanced control logic is developed and experimentally evaluated in the SOFC test rig.

5 Evaluation of modified control strategies

In the following chapter, additional control strategies are outlined and evaluated. In the first step, analogous to the previously introduced NM_1, further control schemes are derived via the combination of at least two possible mass or volume flow rate control element positions in the AEGR SOFC system. The varied system control element positions are at the natural gas inlet, reformer inlet, reformer outlet, anode outlet and inside the recirculation loop. In the second step, an advanced control methodology, coupled to the natural gas quality detection, is derived. The methodology only uses a single natural gas quality indicator, the electron gas coefficient, to steadily determine the adjusted flow rate set points, using the natural gas correlations outlined in section 3.4.3. The advanced control scheme is referred to as the natural gas electron coefficient control scheme (NC_0). In the third step, the simulated results of all the derived control schemes are compared and further evaluated via a sensitivity analysis. Additionally, the technical feasibility of the derived control schemes is evaluated. In the final step, the NC_0 is implemented and experimentally tested in the SOFC test rig.

5.1 Modified control scheme options

Analogous to the previously presented NM_1, additional system control strategies can be defined by changing the related pair of controlled flow rate set points. Therefore, by considering the mass and volume flow rates at the natural gas inlet, inside the recirculation loop, at the reformer inlet, at the reformer outlet and at the stack outlet controllable, a combination of two set points can be used to characterize a control scheme. It should be noted that the recirculation ratio is also considered controllable, with the help of at least two sensors at the anode outlet and inside the recirculation loop, using equation (2.2). All possible evaluated positions are shown in a simplified system layout in Figure 5.1, using schematic mass and volume flow rate control elements. In theory, a constant mass flow rate at a specific system position can be realized with a mass flow controller or a mass flow meter (MFM). It should be noted that to accurately control the mass flow rate, a MFC needs a sufficiently high pressure level, whereas a MFM is subject to a simultaneous control of the rotational speed of the blowers. Constant volume flow rates can be achieved by measuring the flow rates using a sensor unit, for instance flow meters, and simultaneously controlling the rotational speed of the blowers. Additionally, the outlined volume flow rate detection methodology, using the characteristic blower map modeling, can be implemented for the control of volume flow rates. All described flow rate control options are represented by the simplified mass and volume flow rate control elements in Figure 5.1.

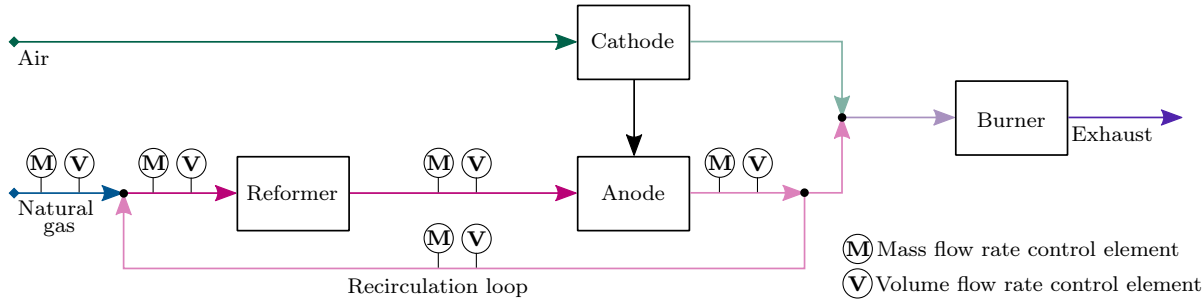

Figure 5.1: Overview of possible control element positions in simplified schematic SOFC system

In theory, the mutual combination of two leading flow rate control variables yield a total of 100 possibilities, neglecting the simultaneous control of the mass and volume flow rates at the

same system position. However, as outlined in Table 5.1, only 23 of the total 100 possibilities can be uniquely realized. A vast number of positions is redundant, due to the distinct relations in the mass and molar balance, as introduced previously in sections 2.2.2.1 and 2.2.2.2. Additionally, several combinations yield non feasible approaches, as outlined in the corresponding table footnotes. For the distinction between the different possibilities, each control scheme is uniquely labeled, based upon an arbitrary definition of the leading control element position with a hierarchical assignment order and a consecutive number. Therefore, control schemes are labeled by the control element position and type, mass (M) or volume (V) flow rate detection, of the highest hierarchical level that is part of the control scheme. The highest level is the reformer outlet volume flow rate (RV), since it is the only position without a distinct analytic solution, as introduced in section 2.2.2.2. The second level is the natural gas inlet (N), followed by the anode outlet (A) and the reformer inlet (R_i). The resulting labels, defining all possibilities, are the reformer outlet volume flow rate (RV), the natural gas mass (NM) and volume flow rate (NV), the anode outlet mass (AM) and volume flow rate (AV), as well as the reformer inlet volume flow rate (R_iV) control schemes. It should be noted that the NV_1 is the strategy derived and evaluated by Carré et al. [27, 29] and Gallet Segarra [28].

Table 5.1: List of possible control scheme options

	$\dot{n}_{NG,in}$	$\dot{m}_{NG,in}$	$\dot{n}_{rec}$	$\dot{m}_{rec}$	$\dot{n}_{ref,in}$	$\dot{m}_{ref,in}$	$\dot{n}_{ref,out}$	$\dot{m}_{ref,out}$	$\dot{n}_{an,out}$	$\dot{m}_{an,out}$	r
$\dot{n}_{NG,in}$	-	-	NV_1	NV_3	NV_1	NV_5	RV_3	NV_5	NV_4	NV_5	NV_2
$\dot{m}_{NG,in}$	-	-	NM_2	NM_3	NM_1	NM_3	RV_2	NM_3	NM_4	NM_3	NM_3
$\dot{n}_{rec}$	NV_1	NM_2	-	-	NV_1	AM_2	-[1]	AM_2	AV_2	AM_2	AV_2
$\dot{m}_{rec}$	NV_3	NM_3	-	-	R_iV_1	NM_3	RV_6	NM_3	AV_3	NM_3	NM_3
$\dot{n}_{ref,in}$	NV_1	NM_1	NV_1	R_iV_1	-	-	-[2]	AM_1	AV_1	AM_1	R_iV_2
$\dot{m}_{ref,in}$	NV_5	NM_3	AM_2	NM_3	-	-	RV_4	-[3]	AV_4	-[4]	NM_3
$\dot{n}_{ref,out}$	RV_3	RV_2	-[1]	RV_6	-[2]	RV_4	-	-	RV_5	RV_4	RV_1
$\dot{m}_{ref,out}$	NV_5	NM_3	AM_2	NM_3	AM_1	-[3]	-	-	AV_4	-[4]	NM_3
$\dot{n}_{an,out}$	NV_4	NM_4	AV_2	AV_3	AV_1	AV_4	RV_5	AV_4	-	-	AV_2
$\dot{m}_{an,out}$	NV_5	NM_3	AM_2	NM_3	AM_1	-[4]	RV_4	-[4]	-	-	NM_3
r	NV_2	NM_3	AV_2	NM_3	R_iV_2	NM_3	RV_1	NM_3	AV_2	NM_3	-

Analogous to the previously presented NM_1, for each distinct group of control scheme options, which are clustered under an identical label, a steady state equation for the fuel utilization factor of the stack of the fluctuating state can be derived using the basic leading constraint of each control scheme between the reference and fluctuating state, respectively. Again, the basic constraint is defined based upon the hierarchical assignment order of the control element positions. The corresponding basic constraint of the six different control scheme clusters, the related steady state equation of the fuel utilization factor of the fluctuating state and the corresponding reference to the derivation in the appendix are outlined in Table 5.2.

[1] Implementation yields extreme deviations from the fuel utilization of the stack and oxygen-to-carbon ratio set points and the option is therefore not further evaluated.

[2] The steady state solutions of $U_{f,S}$ and r are outside of the possible physical range ($U_{f,S,F} > 1$ and $U_{f,S,F} < 0$, $r_F > 1$ and $r_F < 0$). Therefore, the option is excluded from further evaluation.

[3] The implementation is impossible, since the mass flow rates at the reformer inlet and outlet are always identical. Therefore, the control of both mass flow rates is redundant.

[4] The implementation is impossible, since the mass flow rates at the reformer inlet or outlet and anode outlet are directly related via the constant mass flow rate of transferred oxygen. Therefore, the control of both mass flow rates is redundant.

Table 5.2: Basic constraint and steady state fuel utilization factor equation of the fluctuating state for different control schemes

CS	Basic constraint and fuel utilization factor equation	Appendix
NM	$\dot{m}_{\mathrm{NG,in,F}} = \dot{m}_{\mathrm{NG,in,R}}$ $U_{\mathrm{f,S,F}} = \frac{U_{\mathrm{f,S,R}}\, K_{\mathrm{e^-,R}}\, M_{\mathrm{NG,in,F}}\, (1-r_{\mathrm{F}})}{K_{\mathrm{e^-,F}}\, M_{\mathrm{NG,in,R}}\, \left(1-r_{\mathrm{R}}\, \left(1-U_{\mathrm{f,S,R}}\right)\right)-r_{\mathrm{F}}\, U_{\mathrm{f,S,R}}\, K_{\mathrm{e^-,R}}\, M_{\mathrm{NG,in,F}}}$	N.1
NV	$\dot{n}_{\mathrm{NG,in,F}} = \dot{n}_{\mathrm{NG,in,R}}$ $U_{\mathrm{f,S,F}} = \frac{U_{\mathrm{f,S,R}}\, K_{\mathrm{e^-,R}}\, (1-r_{\mathrm{F}})}{K_{\mathrm{e^-,F}}\, \left(1-r_{\mathrm{R}}\, \left(1-U_{\mathrm{f,S,R}}\right)\right)-r_{\mathrm{F}}\, U_{\mathrm{f,S,R}}\, K_{\mathrm{e^-,R}}}$	O.1
$\mathrm{R_i V}$	$\dot{n}_{\mathrm{ref,in,F}} = \dot{n}_{\mathrm{ref,in,R}}$ $U_{\mathrm{f,S,F}} = \frac{U_{\mathrm{f,S,R}}\, K_{\mathrm{e^-,R}}\, (1-r_{\mathrm{R}})\, (1-r_{\mathrm{F}})\, \left(1+r_{\mathrm{F}}\, K_{\triangle \mathrm{an,F}}\right)}{K_{\mathrm{e^-,F}}\, (1-r_{\mathrm{F}})\, \left(1-r_{\mathrm{R}}\, \left(1-U_{\mathrm{f,S,R}}\right)\right)\, \left(1+r_{\mathrm{R}}\, K_{\triangle \mathrm{an,R}}\right)-r_{\mathrm{F}}\, U_{\mathrm{f,S,R}}\, K_{\mathrm{e^-,R}}\, (1-r_{\mathrm{R}})\, \left(1+r_{\mathrm{F}}\, K_{\triangle \mathrm{an,F}}\right)}$	P.1
RV	$\dot{n}_{\mathrm{ref,out,F}} = \dot{n}_{\mathrm{ref,out,R}}$ $U_{\mathrm{f,S,F}} = U_{\mathrm{f,S,R}}\, \frac{K_{\mathrm{e^-,ref,out,R}}}{K_{\mathrm{e^-,ref,out,F}}}$	Q.1
AM	$\dot{m}_{\mathrm{an,out,F}} = \dot{m}_{\mathrm{an,out,R}}$ $U_{\mathrm{f,S,F}} = \frac{4\, U_{\mathrm{f,S,R}}\, K_{\mathrm{e^-,R}}\, M_{\mathrm{NG,in,F}}\, (1-r_{\mathrm{R}})\, (1-r_{\mathrm{F}})}{4\, K_{\mathrm{e^-,F}}\, M_{\mathrm{NG,in,R}}\, \left(1-r_{\mathrm{F}}-r_{\mathrm{R}}\, (1-r_{\mathrm{F}})\, \left(1-U_{\mathrm{f,S,R}}\right)\right)+U_{\mathrm{f,S,R}}\, K_{\mathrm{e^-,R}}\, \left(K_{\mathrm{e^-,F}}\, M_{\mathrm{O_2}}\, (r_{\mathrm{R}}-r_{\mathrm{F}})-4\, r_{\mathrm{F}}\, M_{\mathrm{NG,in,F}}\, (1-r_{\mathrm{R}})\right)}$	R.1
AV	$\dot{n}_{\mathrm{an,out,F}} = \dot{n}_{\mathrm{an,out,R}}$ $U_{\mathrm{f,S,F}} = \frac{U_{\mathrm{f,S,R}}\, K_{\mathrm{e^-,R}}\, (1-r_{\mathrm{R}})\, (1-r_{\mathrm{F}})\, \left(1+K_{\triangle \mathrm{an,F}}\right)}{K_{\mathrm{e^-,F}}\, (1-r_{\mathrm{F}})\, \left(1-r_{\mathrm{R}}\, \left(1-U_{\mathrm{f,S,R}}\right)\right)\, \left(1+K_{\triangle \mathrm{an,R}}\right)-r_{\mathrm{F}}\, U_{\mathrm{f,S,R}}\, K_{\mathrm{e^-,R}}\, (1-r_{\mathrm{R}})\, \left(1+K_{\triangle \mathrm{an,F}}\right)}$	S.1

Furthermore, an additional constraint is defined by the secondary control element position with the lower hierarchical order. The respective basic and additional constraints, as well as the resulting equation of the recirculation ratio and the reference to the derivation in the appendix of each control scheme option are outlined in Table 5.3. Additionally, in accordance to Table 5.1, all possible combinations of constraints that yield identical results are grouped under the appropriate control scheme option. Excluding the reformer outlet volume flow rate, for all control schemes, an analytic steady state equation for the recirculation ratio of the fluctuating state can be derived from the mass and molar balance. Control schemes subjected to a constant reformer outlet volume flow rate have to be solved iteratively, since the flow rate is dependent on the equilibrium state, which is a function of the changing characteristic variables. The resulting oxygen-to-carbon ratio of the fluctuating state can be uniquely determined for all control schemes using the fuel utilization factor and recirculation ratio of the fluctuating state, as previously outlined for the $\mathrm{NM_1}$ in equation (4.6).

Except for the RV control schemes, all control scheme options can be simulated in the same manner as the $\mathrm{NM_1}$ modeling methodology outlined in Figure 4.5, by simply implementing the respective equations of r_{F} and $U_{\mathrm{f,S,F}}$. Additionally, for the reformer outlet volume flow rate control scheme computations, the model methodology is individually adjusted to include an iterative solving logic for r_{F} and $U_{\mathrm{f,S,F}}$. The iterative solving logic is limited to the necessary part of the system balance, ultimately optimizing computation times. The iterative loops are terminated if the deviation between the current and previous computation values of $U_{\mathrm{f,S,F}}$ is smaller than 10^{-12}. Consequently, the methodology still includes an inherent validation of the basic and additional constraints, mass balance and species conservation for all control scheme options, due to the implementation in the previously introduced modeling environment in section 4.3.1.

Table 5.3: Basic and additional control scheme constraints, and equations for the recirculation ratio calculation of fluctuating state

CS	Basic constraint	Additional constraint	Recirculation ratio r	Appendix
NM_1	$\dot{m}_{NG,in,F} = \dot{m}_{NG,in,R}$	$\dot{n}_{ref,in,F} = \dot{n}_{ref,in,R}$	$r_F = \frac{M_{NG,in,F}\left(1+r_R\,K_{\triangle an,R}\right)-M_{NG,in,R}\,(1-r_R)}{M_{NG,in,F}\left(1+r_R\,K_{\triangle an,R}\right)+K_{\triangle an,F}\,M_{NG,in,R}\,(1-r_R)}$	N.2.1
NM_2	$\dot{m}_{NG,in,F} = \dot{m}_{NG,in,R}$	$\dot{n}_{rec,F} = \dot{n}_{rec,R}$	$r_F = \frac{r_R\,M_{NG,in,F}\left(1+K_{\triangle an,R}\right)}{r_R\,M_{NG,in,F}\left(1+K_{\triangle an,R}\right)+M_{NG,in,R}\,(1-r_R)\left(1+K_{\triangle an,F}\right)}$	N.2.2
NM_3	$\dot{m}_{NG,in,F} = \dot{m}_{NG,in,R}$	$\dot{m}_{rec,F} = \dot{m}_{rec,R}$ $\dot{m}_{ref,in,F} = \dot{m}_{ref,in,R}$ $\dot{m}_{ref,out,F} = \dot{m}_{ref,out,R}$ $\dot{m}_{an,out,F} = \dot{m}_{an,out,R}$ $r_F = r_R$	$r_F = r_R$	N.2.3
	$\dot{m}_{rec,F} = \dot{m}_{rec,R}$	$\dot{m}_{ref,in,F} = \dot{m}_{ref,in,R}$ $\dot{m}_{ref,out,F} = \dot{m}_{ref,out,R}$ $\dot{m}_{an,out,F} = \dot{m}_{an,out,R}$ $r_F = r_R$		
	$\dot{m}_{ref,in,F} = \dot{m}_{ref,in,R}$	$r_F = r_R$		
	$\dot{m}_{ref,out,F} = \dot{m}_{ref,out,R}$	$r_F = r_R$		
	$\dot{m}_{an,out,F} = \dot{m}_{an,out,R}$	$r_F = r_R$		
NM_4	$\dot{m}_{NG,in,F} = \dot{m}_{NG,in,R}$	$\dot{n}_{an,out,F} = \dot{n}_{an,out,R}$	$r_F = 1 - \frac{M_{NG,in,R}\,(1-r_R)\left(1+K_{\triangle an,F}\right)}{M_{NG,in,F}\left(1+K_{\triangle an,R}\right)}$	N.2.4
NV_1	$\dot{n}_{NG,in,F} = \dot{n}_{NG,in,R}$	$\dot{n}_{rec,F} = \dot{n}_{rec,R}$ $\dot{n}_{ref,in,F} = \dot{n}_{ref,in,R}$	$r_F = \frac{r_R\left(1+K_{\triangle an,R}\right)}{1+K_{\triangle an,F}+r_R\left(K_{\triangle an,R}-K_{\triangle an,F}\right)}$	O.2.1
	$\dot{n}_{rec,F} = \dot{n}_{rec,R}$	$\dot{n}_{ref,in,F} = \dot{n}_{ref,in,R}$		
NV_2	$\dot{n}_{NG,in,F} = \dot{n}_{NG,in,R}$	$r_F = r_R$	$r_F = r_R$	-
NV_3	$\dot{n}_{NG,in,F} = \dot{n}_{NG,in,R}$	$\dot{m}_{rec,F} = \dot{m}_{rec,R}$	$r_F = \frac{r_R\left(4\,M_{NG,in,R}\left(1-r_R\left(1-U_{f,S,R}\right)\right)+U_{f,S,R}\,K_{e^-,R}\,M_{O_2}\right)}{U_{f,S,R}\,K_{e^-,R}\,M_{O_2}+4\left(1-r_R\left(1-U_{f,S,R}\right)\right)\left(M_{NG,in,F}+r_R\left(M_{NG,in,R}-M_{NG,in,F}\right)\right)}$	O.2.2
NV_4	$\dot{n}_{NG,in,F} = \dot{n}_{NG,in,R}$	$\dot{n}_{an,out,F} = \dot{n}_{an,out,R}$	$r_F = 1 - \frac{(1-r_R)\left(1+K_{\triangle an,F}\right)}{\left(1+K_{\triangle an,R}\right)}$	O.2.3

CS	Basic constraint	Additional constraint	Recirculation ratio r	Appendix
NV_5	$\dot{n}_{NG,in,F} = \dot{n}_{NG,in,R}$	$\dot{m}_{ref,in,F} = \dot{m}_{ref,in,R}$ $\dot{m}_{ref,out,F} = \dot{m}_{ref,out,R}$ $\dot{m}_{an,out,F} = \dot{m}_{an,out,R}$	$r_F = \frac{4\left(1-r_R\left(1-U_{f,S,R}\right)\right)\left(M_{NG,in,R}+M_{NG,in,F}\left(r_R-1\right)\right)+r_R\,U_{f,S,R}\,K_{e^-,R}\,M_{O_2}}{U_{f,S,R}\,K_{e^-,R}\,M_{O_2}+4\,M_{NG,in,R}\left(1-r_R\left(1-U_{f,S,R}\right)\right)}$	O.2.4
R_iV_1	$\dot{n}_{ref,in,F} = \dot{n}_{ref,in,R}$	$\dot{m}_{rec,F} = \dot{m}_{rec,R}$	$r_F = \frac{-\beta_{R_iV_1}-\sqrt{\left(\beta_{R_iV_1}\right)^2-4\,\alpha_{R_iV_1}\,\gamma_{R_iV_1}}}{2\,\alpha_{R_iV_1}}$	P.2
R_iV_2	$\dot{n}_{ref,in,F} = \dot{n}_{ref,in,R}$	$r_F = r_R$	$r_F = r_R$	-
RV_1	$\dot{n}_{ref,out,F} = \dot{n}_{ref,out,R}$	$r_F = r_R$	Iterative solving with $r_F = r_R$	Q.2.1
RV_2	$\dot{n}_{ref,out,F} = \dot{n}_{ref,out,R}$	$\dot{m}_{NG,in,F} = \dot{m}_{NG,in,R}$	Iterative solving with $r_F = \frac{\dot{n}_{ref,out,F}\,M_{ref,out,F}-\dot{m}_{NG,in,R}}{\dot{n}_{ref,out,F}\,M_{ref,out,F}+\dot{m}_{O_2,tr,R}}$	Q.2.2
RV_3	$\dot{n}_{ref,out,F} = \dot{n}_{ref,out,R}$	$\dot{n}_{NG,in,F} = \dot{n}_{NG,in,R}$	Iterative solving with $r_F = \frac{\dot{n}_{ref,out,F}\,M_{ref,out,F}-\dot{n}_{NG,in,R}\,M_{NG,in,F}}{\dot{n}_{ref,out,F}\,M_{ref,out,F}+\dot{m}_{O_2,tr,R}}$	Q.2.3
RV_4	$\dot{n}_{ref,out,F} = \dot{n}_{ref,out,R}$	$\dot{m}_{an,out,F} = \dot{m}_{an,out,R}$ $\dot{m}_{ref,in,F} = \dot{m}_{ref,in,R}$	Iterative solving with $r_F = \frac{\dot{m}_{an,out,R}-\dot{m}_{O_2,tr,R}-\dot{m}_{NG,in,F}}{\dot{m}_{an,out,R}}$	Q.2.4
RV_5	$\dot{n}_{ref,out,F} = \dot{n}_{ref,out,R}$	$\dot{n}_{an,out,F} = \dot{n}_{an,out,R}$	Iterative solving with $r_F = \frac{\dot{n}_{ref,out,F}\,M_{ref,out,F}-\dot{m}_{NG,in,F}}{\dot{n}_{an,out,R}\,M_{an,out,F}}$	Q.2.5
RV_6	$\dot{n}_{ref,out,F} = \dot{n}_{ref,out,R}$	$\dot{m}_{rec,F} = \dot{m}_{rec,R}$	Iterative solving with $r_F = \frac{\dot{m}_{rec,R}}{\dot{n}_{ref,out,F}\,M_{ref,out,F}+\dot{m}_{O_2,tr,R}}$	Q.2.6
AM_1	$\dot{m}_{an,out,F} = \dot{m}_{an,out,R}$ $\dot{m}_{ref,out,F} = \dot{m}_{ref,out,R}$	$\dot{n}_{ref,in,F} = \dot{n}_{ref,in,R}$ $\dot{n}_{ref,in,F} = \dot{n}_{ref,in,R}$	$r_F = \frac{-\beta_{AM_1}+\sqrt{\left(\beta_{AM_1}\right)^2-4\,\alpha_{AM_1}\,\gamma_{AM_1}}}{2\,\alpha_{AM_1}}$	R.2.1
AM_2	$\dot{m}_{an,out,F} = \dot{m}_{an,out,R}$ $\dot{n}_{rec,F} = \dot{n}_{rec,R}$	$\dot{n}_{rec,F} = \dot{n}_{rec,R}$ $\dot{m}_{ref,in,F} = \dot{m}_{ref,in,R}$ $\dot{m}_{ref,out,F} = \dot{m}_{ref,out,R}$	$r_F = \frac{-\beta_{AM_2}+\sqrt{\left(\beta_{AM_2}\right)^2-4\,\alpha_{AM_2}\,\gamma_{AM_2}}}{2\,\alpha_{AM_2}}$	R.2.2
AV_1	$\dot{n}_{an,out,F} = \dot{n}_{an,out,R}$	$\dot{n}_{ref,in,F} = \dot{n}_{ref,in,R}$	$r_F = \frac{\left(1+r_R\,K_{\triangle an,R}\right)\left(1+K_{\triangle an,F}\right)-K_{\triangle an,R}-1}{K_{\triangle an,F}\left(1+K_{\triangle an,R}\right)}$	S.2.1
AV_2	$\dot{n}_{an,out,F} = \dot{n}_{an,out,R}$ $\dot{n}_{rec,F} = \dot{n}_{rec,R}$	$\dot{n}_{rec,F} = \dot{n}_{rec,R}$ $r_F = r_R$ $r_F = r_R$	$r_F = r_R$	S.2.2
AV_3	$\dot{n}_{an,out,F} = \dot{n}_{an,out,R}$	$\dot{m}_{rec,F} = \dot{m}_{rec,R}$	$r_F = \frac{-\beta_{AV_3}-\sqrt{\left(\beta_{AV_3}\right)^2-4\,\alpha_{AV_3}\,\gamma_{AV_3}}}{2\,\alpha_{AV_3}}$	S.2.3
AV_4	$\dot{n}_{an,out,F} = \dot{n}_{an,out,R}$	$\dot{m}_{ref,in,F} = \dot{m}_{ref,in,R}$ $\dot{m}_{ref,out,F} = \dot{m}_{ref,out,R}$	$r_F = \frac{r_R\,U_{f,S,R}\,K_{e^-,R}\,M_{O_2}\left(1+K_{\triangle an,F}\right)+4\left(1-r_R\left(1-U_{f,S,R}\right)\right)\left(M_{NG,in,R}\left(1+K_{\triangle an,F}\right)-M_{NG,in,F}\left(1+K_{\triangle an,R}\right)\right)}{U_{f,S,R}\,K_{e^-,R}\,M_{O_2}\left(1+K_{\triangle an,F}\right)+4\left(1-r_R\left(1-U_{f,S,R}\right)\right)\left(M_{NG,in,R}\left(1+K_{\triangle an,F}\right)-M_{NG,in,F}\left(1+K_{\triangle an,R}\right)\right)}$	S.2.4

5.2 Natural gas electron coefficient control scheme

This section outlines an additional control strategy, solely relying on the quantification of the electron gas coefficient ($K_{e^-,Msd}$), labeled the natural gas electron coefficient CS. For the detection of the electron coefficient, two different techniques were previously introduced in section 4.4.1. In contrast to the other presented control schemes, the NC_0 is not dependent on any constraints, defined with the help of the reference gas composition. Therefore, in theory, the resulting recirculation ratio and fuel utilization factor of the stack can be calculated based upon the detected gas coefficient and derived gas coefficient correlation, as previously introduced in section 3.4.3. Consequently, flow rate set points can be adjusted to match the fluctuating natural gas state and the behavior of the IC_0 can be approximately reproduced.

However, even for an ideal detection of the electron gas coefficient, the resulting recirculation ratio and fuel utilization factor slightly deviate from the designated ideal set points values, due to the application of the regression based estimation of $K_{\triangle an}$ and K_{Φ}. Analogous to the previously introduced control schemes, the theoretical resulting recirculation ratio and fuel utilization factor can be calculated as a function of the estimated and real natural gas coefficients, as well as the fuel utilization factor of the stack set point. The resulting recirculation ratio and fuel utilization factor of the fluctuating state are outlined in equations (5.1) and (5.2)[5], where $K_{\triangle an,QR}$ and $K_{\Phi,MLR}$ are calculated, as introduced in Table 3.4 and equation (3.14). It should be noted that for a designated oxygen-to-carbon ratio set point of exactly 2, $K_{\Phi,MLR}$ can be replaced with $K_{\triangle an,QR}$, ultimately improving the accuracy slightly. The NC_0 is implemented in the modeling methodology by removing the relation to the reference state and adjusting the r_F and $U_{f,S,F}$ computation equations.

$$r_F = \frac{(1 + K_{\triangle an,QR})}{(1 + K_{\triangle an,QR}) + U_{f,S,SP}\left(\frac{K_{e^-,Msd}}{2\,K_{\Phi,MLR}} - 1\right)(1 + K_{\triangle an})} \tag{5.1}$$

$$U_{f,S,F} = \frac{(1 - r_F)\left(U_{f,S,SP}\,K_{e^-,Msd} + 2\,K_{\Phi,MLR}\,(1 - U_{f,S,SP})\right)}{K_{e^-,Msd} - r_F\left(U_{f,S,SP}\,K_{e^-,Msd} + 2\,K_{\Phi,MLR}\,(1 - U_{f,S,SP})\right)} \tag{5.2}$$

Additionally, the derived equations are valid for a control logic that adjusts the natural gas flow rate and either the recirculation or reformer inlet flow rate, based upon the detected electron gas coefficient. The control scheme can also be implemented using a recirculation ratio or anode outlet flow rate control in correspondence with a natural gas flow rate adjustment. However, all three possible application options yield nearly identical results, with deviations in the resulting fuel utilization factor of less than 0.5%. The differences between the three application options are also briefly shown in appendix T. In conclusion, the evaluation focuses on the control of the natural gas and reformer inlet flow rates, due to the simplicity of applying the option into the SOFC test rig setup without any adjustments.

5.3 Performance of control strategies

As previously described, all 25 derived control schemes were implemented in the same modeling environment, which is outlined in section 4.3. Consequently, analogous to section 4.3.2, the temporally resolved natural gas data base can be used to evaluate the effect of fluctuating natural gas quality on each individual control scheme. Nevertheless, as outlined in sections 5.3.1 and 5.3.2, only the Renningen 2016 and Saint-Thegonnec 2014 data sets are used for the comparison of the different control strategies at nominal operation, providing a baseline of approximately

[5]The derivation of r_F and $U_{f,S,F}$ of the fluctuating state are shown in appendix T.

15500 measured natural gas compositions. The model input parameters representing nominal operation are listed in Table 4.4. The corresponding reference state is defined using the average composition for each individual natural gas data set, which represents the best case. Additionally, analogous to section 4.5, the influence of a change in reference natural gas composition and a hydrogen addition of 4 % is evaluated via a sensitivity analysis for the Renningen 2016 data set. The outlined evaluations and parameter variations are limited in order to highlight the major effects of fluctuating natural gas quality on all derived control schemes more effectively.

5.3.1 Renningen 2016 data set

The validation of the correct implementation of each individual control scheme in the modeling environment is displayed in Figure 5.2, outlining the relative deviations of the mass and molar flow rates at the five relevant SOFC system positions, as well as the recirculation ratios between the computed and reference states. The recirculation ratio is included to verify the constant recirculation ratio constraint between the reference and fluctuating natural gas states of the NM_3, NV_2, R_iV_2, RV_1 and AV_2. Consequently, Figure 5.2 highlights the perfect match between the defined basic and additional constraints of the reference and fluctuating natural gas states for each individual control scheme, as previously defined in Table 5.3. As a result, the derived equations for $U_{f,S,F}$ and r_F, as well as the implementation logic in the modeling environment are validated for each individual control scheme option, due to the accurate match of the basic and additional constraints. However, as outlined in Figure 5.2, the relative deviations of the mass and molar flow rates at the five relevant SOFC system positions between the computed and reference states frequently exceed values of approximately $\pm 4\,\%$ and $\pm 3\,\%$, respectively. The resulting deviation domains and 95 % confidence intervals of $U_{f,S}$ and Φ are outlined for each individual control scheme option in Figure 5.3. Analogous to the defined control scheme labels, Figures 5.2 and 5.3 are conceptually divided in 8 individual sections, where each portion includes clustered control scheme options. The first section outlines the IC_0, which is used as the ideal comparison case. The second and third sections depict the NM and NV control schemes. Followed by the R_iV and RV control schemes, shown in the fourth and fifth sections. Additionally, the sixth and seventh sections include the AM and AV control schemes. Finally, the eighth section outlines the NC_0.

In contrast to NM_1 in section 4.3.4, the extension of the $U_{f,S}$ and Φ domains, due to the corresponding control element uncertainties, are not considered. The equitable and accurate determination of the error margins at each individual control element position is extremely challenging without access to detailed experimental data. Therefore, the propagation of error for each individual control scheme is excluded from this work, ultimately allowing for an unbiased evaluation and comparison of the control schemes in the modeling environment. It should be noted that the generalized comparison statements are based upon the $U_{f,S}$ and Φ confidence intervals of the individual control scheme clusters. However, the total robustness towards fluctuating natural gas quality is evaluated in relation to the resulting $U_{f,S,F}$ maximum and Φ_F minimum of each individual control scheme option. As introduced in section 4.3.2, the upper and lower boundary values of $U_{f,S,F}$ and Φ_F are especially crucial, since system components can be harmed and degradation risks are enhanced.

As outlined in Figure 5.3, the NM control schemes' $U_{f,S}$ confidence intervals are similar, due to the supply of a constant natural gas mass flow rate. Additionally, the Φ confidence intervals also have identical magnitudes. The only small exception is the NM_3, which covers a slightly smaller Φ domain. However, the NM_3 implementation is more challenging than the NM_1, since the corresponding possible flow rate control positions are less applicable. The feasibility of the different flow rate control element positions, the implementation challenges and the generic comparison of all evaluated control scheme options are discussed in more detail in section 5.3.4.

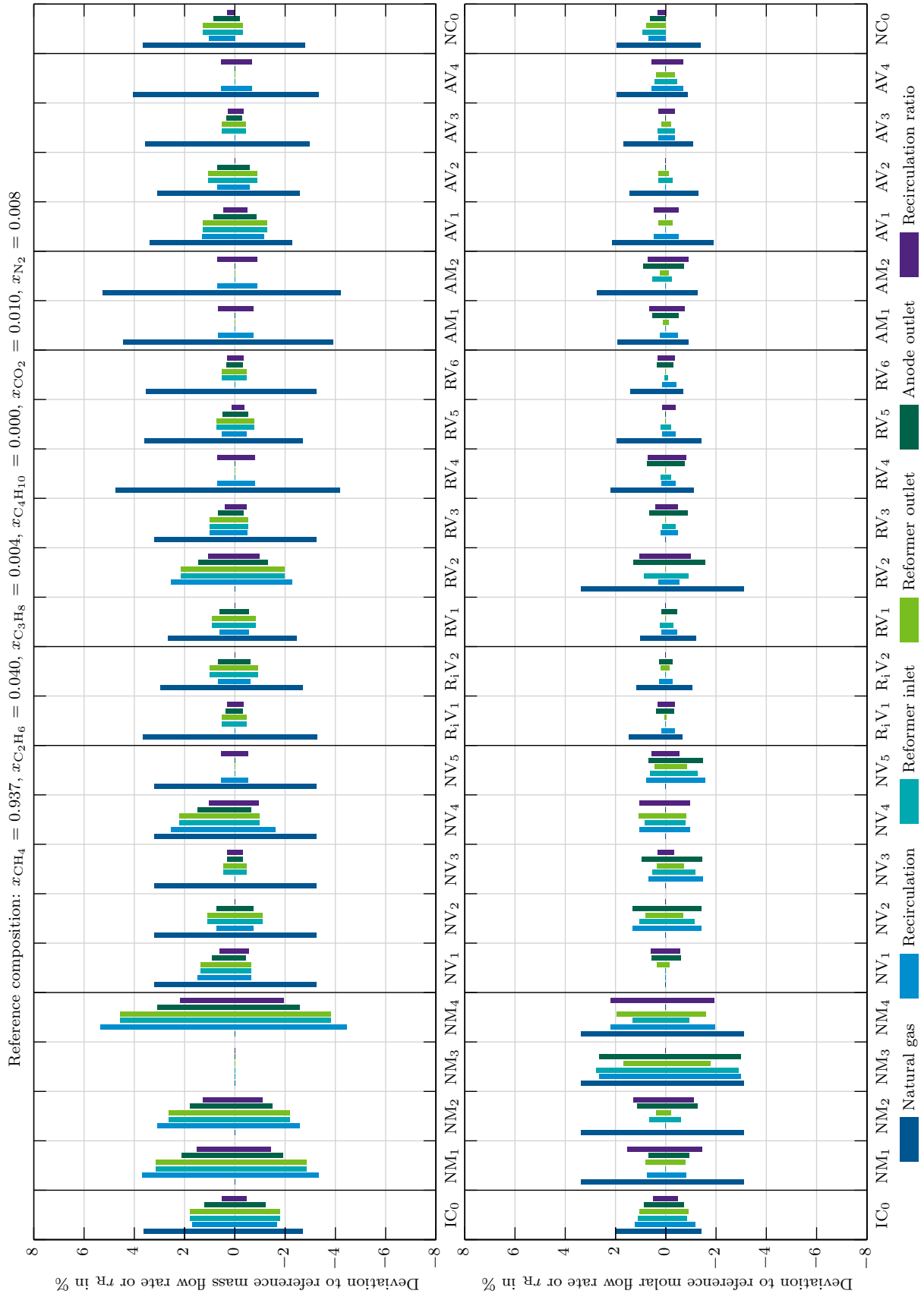

Figure 5.2: Comparison of control schemes for Renningen 2016 natural gas data set - Mass flow rate, molar flow rate and recirculation ratio deviation to reference

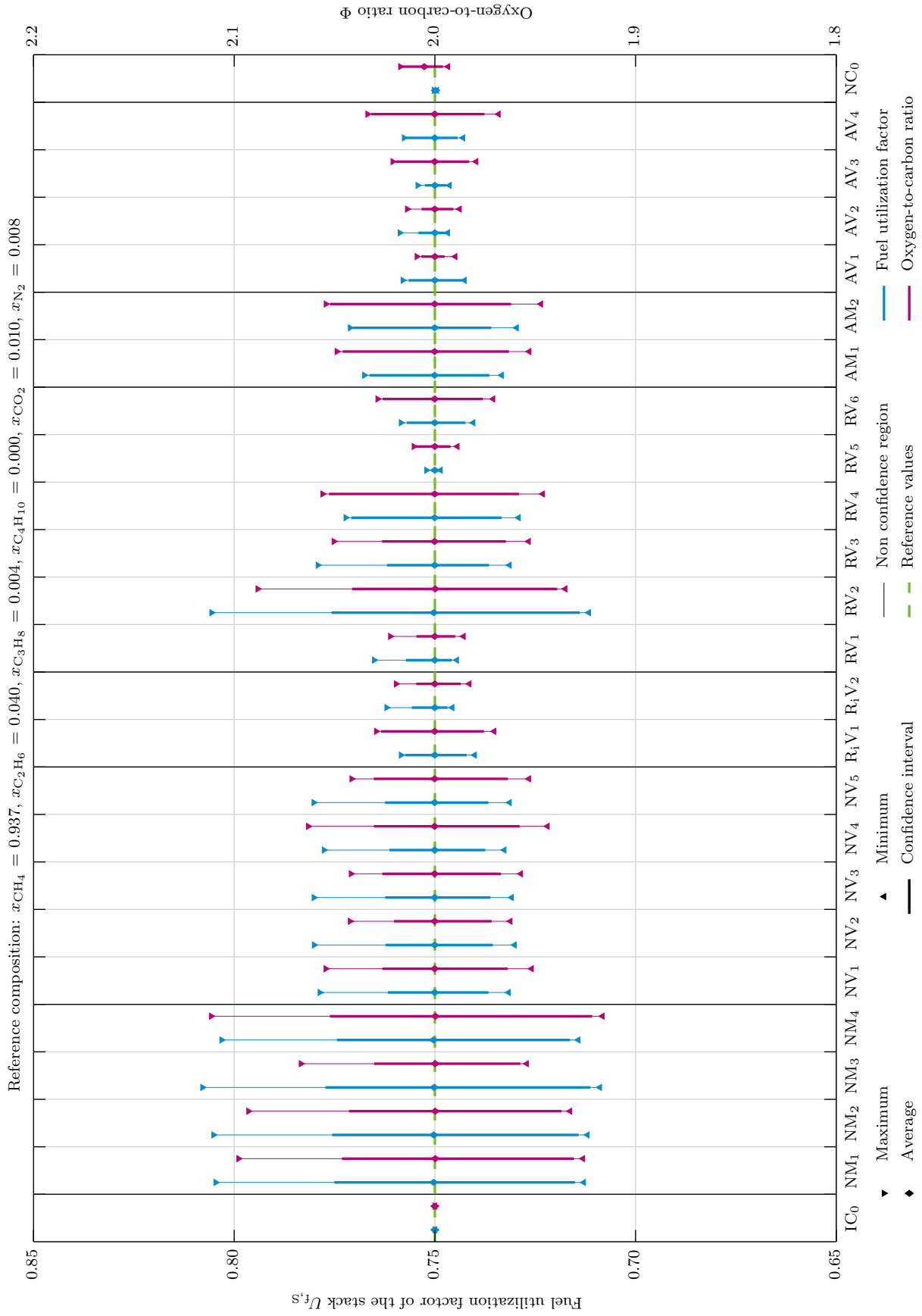

Figure 5.3: Comparison of control schemes for Renningen 2016 natural gas data set - Fuel utilization factor of the stack and oxygen-to-carbon ratio

The $U_{f,S}$ and Φ confidence intervals of the NM control schemes range from approximately 0.7113 to 0.7773 and 1.922 to 2.052, respectively. Additionally, the absolute $U_{f,S}$ and Φ deviation domains are significantly larger than the confidence intervals. Therefore, the robustness of the NM control schemes towards natural gas quality fluctuations is very low in the Renningen 2016 data. In comparison to the NM_1, the remaining NM control schemes do not yield significant improvements in the robustness against fluctuating natural gas quality and implementation feasibility.

Analogous to the NM control schemes, the NV control schemes' $U_{f,S}$ confidence intervals are also similar, due to the supply of a constant natural gas volume flow rate. Additionally, the differences between the Φ confidence intervals are very small. Nevertheless, compared to the NM control schemes, the $U_{f,S}$ and Φ confidence intervals of the NV control schemes are significantly smaller, ranging from approximately 0.7356 to 0.7624 and 1.958 to 2.030, respectively. The absolute $U_{f,S}$ and Φ deviation domains are only moderately larger than the confidence intervals. Consequently, the NV control schemes are fairly robust towards natural gas quality fluctuations in the Renningen 2016 data and significant improvements are achieved compared to the NM_1. However, except of the NV_1, the implementation of the NV control schemes is considered more challenging than the NM_1, as outlined in section 5.3.4.

The implementation of the R_iV control schemes yield small $U_{f,S}$ and Φ confidence intervals, ranging from approximately 0.7421 to 0.7575 and 1.976 to 2.027, respectively. Additionally, in comparison to the NM and NV control schemes, the absolute $U_{f,S}$ and Φ deviation domains are also significantly constricted. Consequently, the R_iV control schemes are very robust towards fluctuating natural gas quality and the absolute deviations are very low. The improvements are significant compared to the NM_1. Nevertheless, the implementation of the R_iV control schemes is considered more challenging than the NM_1.

In contrast to the previously discussed options, the RV control schemes partially have very divergent $U_{f,S}$ and Φ confidence intervals and a general evaluation statement can not be derived. This is due to the hierarchical labeling of the control schemes with the reformer outlet on the highest level, as introduced in section 5.1. Consequently, the RV control schemes include options where the dominant influencing system position is not consistent with the hierarchical labeling. As a result, based upon the defined constraints listed in Table 5.3, the RV_2 and NM control schemes have similar $U_{f,S}$ and Φ domains, due to the constant natural gas mass flow rate constraint. The RV_3 and NV control schemes have matching $U_{f,S}$ and Φ domains, due to the constant natural gas molar flow rate constraint. The RV_4 follows the trends of the AM control schemes, because all options depend on the constant anode outlet mass flow rate constraint. Lastly, the RV_5 domains correspond to the AV control schemes intervals, due to the constant anode outlet molar flow rate constraint. Consequently, the two remaining independent control schemes are the RV_1 and RV_6, which yield very small $U_{f,S}$ and Φ confidence intervals with ranges of approximately 0.7424 to 0.7572 and 1.976 to 2.026, respectively. The outlined intervals are similar to the R_iV domains. In particular, the RV_1 and R_iV_2, as well as the RV_6 and R_iV_1 have almost matching trends, due to the constant recirculation ratio constraint and the constant recirculated mass flow rate constraint, respectively. Consequently, the effects of natural gas quality fluctuations on each individual RV control scheme are more consistent with the NM, NV, R_iV, AM and AV control schemes, respectively. Nevertheless, the hierarchical order was deliberately chosen, since all RV control schemes rely on a volume flow rate control element at the reformer outlet and an analytic balance solution can not be derived. The implementation of the RV control schemes is extremely challenging, since the reformer outlet has a high temperature and the gas composition depends on the current equilibrium state of the reformer unit. Excluding the RV_2, the RV control schemes are significantly more robust than the NM_1 towards natural gas quality fluctuations in the Renningen 2016 data.

The AM control schemes have intermediate $U_{f,S}$ and Φ confidence intervals in the Renningen 2016 data between approximately 0.7360 to 0.7704 and 1.962 to 2.052, respectively. Additionally, the deviations between the confidence intervals and absolute fluctuation domains of $U_{f,S}$ and Φ are small. Consequently, the AM control schemes are fairly robust towards natural gas quality fluctuations in the Renningen 2016 data and significant improvements are achieved compared to the NM_1. Nevertheless, the implementation of the AM control schemes is considered more challenging than the NM_1.

The application of the AV control schemes yields low $U_{f,S}$ and Φ confidence intervals in the Renningen 2016 data, ranging from approximately 0.7431 to 0.7571 and 1.975 to 2.032, respectively. Additionally, the AV control schemes are very robust towards natural gas quality fluctuations in the Renningen 2016 data, due to the nominal deviations between the confidence intervals and absolute fluctuation domains. The improvements compared to the NM_1 are very significant. However, the AV control scheme implementation is considered more demanding than the NM_1.

The NC_0 can partially reproduce the IC_0 outputs, based upon the detection of a single natural gas quality indicator. The deviation of $U_{f,S}$ from the designated set point is negligibly small, due to the assumed ideal detection of K_{e-}. However, Φ has a very small deviation interval, based upon the implemented empirical gas coefficient correlation. Nevertheless, the $U_{f,S}$ and Φ confidence intervals in the Renningen 2016 data are very small, ranging approximately between 0.7495 to 0.7501 and 1.996 to 2.017, respectively. Additionally, the deviation between the confidence intervals and absolute fluctuation domains are only nominal. Consequently, the NC_0 is very robust towards natural gas quality fluctuations and the improvements compared to the NM_1 are very significant. The implementation of the NC_0 is considered slightly more challenging than the NM_1, since the installation of a natural gas quality sensor and the adaption of the control logic are necessary. The sensitivities of the NC_0 towards varying $U_{f,S}$ and Φ set points are further evaluated in section 5.4.

The comparison and ranking of each individual control scheme in the Renningen 2016 data is further discussed in section 5.3.4, where further rating criteria are introduced. Foreshadowing, the R_iV_2, RV_5, AV_1, AV_2, AV_3 and NC_0 achieve the highest robustness towards natural gas quality fluctuations, including the most significant improvements compared to the NM_1.

5.3.2 Saint-Thegonnec 2014 data set

In contrast to the Renningen 2016 data, the Saint-Thegonnec 2014 data set is subjected to higher natural gas quality fluctuations, due to wider domains of the natural gas coefficients, as previously outlined in section 3.4. As a result, the robustness of the derived control scheme options are evaluated under more challenging conditions. The verification of the correct implementations of each individual control scheme in the modeling environment, based upon the defined basic and additional constraint agreements, are outlined in Figure 5.4. Compared to the Renningen 2016 data, the relative deviations of the mass and molar flow rates at the five relevant SOFC system positions between the computed and reference states are significantly higher, frequently exceeding values of approximately $\pm 6\,\%$, respectively. The corresponding deviation domains and 95 % confidence intervals of $U_{f,S}$ and Φ are outlined for each individual control scheme option in Figure 5.5 for the Saint-Thegonnec 2014 data set. It should be noted that this section focuses on the evaluation of the Saint-Thegonnec 2014 data results, whereas a comparison to the Renningen 2016 data is outlined in section 5.3.4. The implementation challenges of each individual control scheme compared to the NM_1 were already discussed in section 5.3.1 and therefore, are not repeated in the following evaluation.

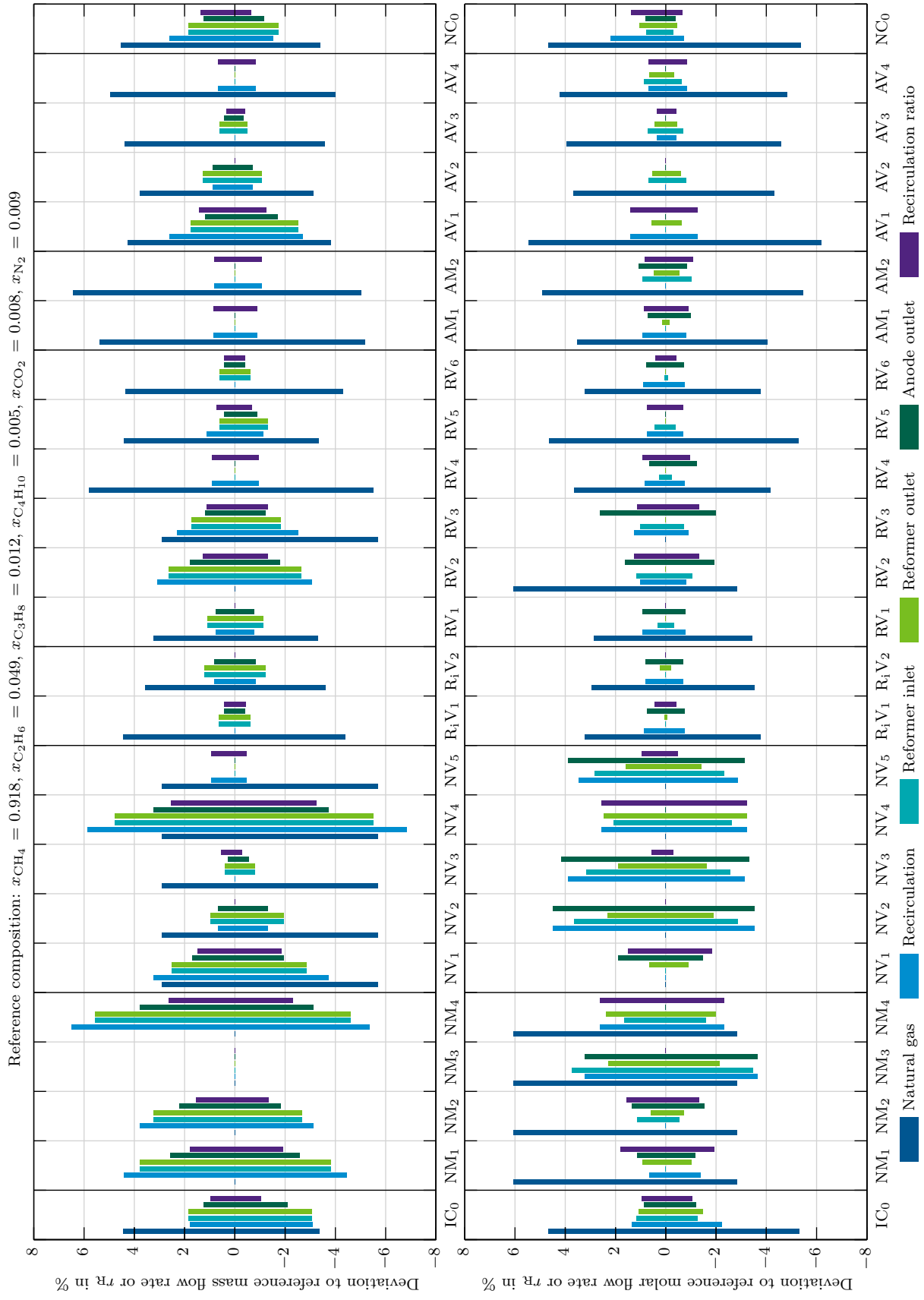

Figure 5.4: Comparison of control schemes for Saint-Thegonnec 2014 natural gas data set - Mass flow rate, molar flow rate and recirculation ratio deviation to reference

The $U_{f,S}$ and Φ confidence intervals of all NM control schemes have identical magnitudes, covering domains from approximately 0.7049 to 0.7975 and 1.897 to 2.097, respectively. Additionally, the absolute $U_{f,S}$ and Φ deviation domains are significantly larger than the confidence intervals. Consequently, the NM control schemes' robustness towards fluctuating natural gas quality is extremely low in the Saint-Thegonnec 2014 data. Compared to the NM_1, the implementation of any remaining NM control scheme does not result in significant improvements. The only minor exception is the NM_3, which has a nominally lower Φ domain, based upon the constant recirculation ratio constraint.

Analogous to the NM control schemes, the NV control schemes' $U_{f,S}$ and Φ confidence intervals are similar. However, the Φ intervals of the NV_2, NV_3 and NV_5 are slightly smaller compared to that of the NV_1 and NV_4. In general, the NV control schemes' $U_{f,S}$ and Φ confidence intervals range from approximately 0.6904 to 0.7923 and 1.857 to 2.095, respectively. Additionally, the absolute $U_{f,S}$ and Φ deviation domains are significantly larger than the confidence intervals. Therefore, in the Saint-Thegonnec 2014 data, the robustness of NV control schemes towards fluctuating natural gas quality is extremely low. As a result, the implementation of the NV control schemes does not yield an improvement compared to the NM_1.

The R_iV control schemes have intermediate $U_{f,S}$ and Φ confidence intervals approximately between 0.7292 to 0.7644 and 1.957 to 2.031, respectively. Additionally, the deviations between the confidence intervals and absolute fluctuation domains of $U_{f,S}$ and Φ are small. Consequently, the R_iV control schemes are fairly robust towards natural gas quality fluctuations in the Saint-Thegonnec 2014 data and therefore, are considered a significant improvement compared to the NM_1.

Analogous to the Renningen 2016 data, the RV control schemes have very divergent $U_{f,S}$ and Φ confidence intervals in the Saint-Thegonnec 2014 data. As previously discussed, the influence of fluctuating natural gas quality on each individual RV control scheme is consistent with the corresponding NM, NV, R_iV, AM and AV control schemes, respectively. The evaluation and confidence intervals follow the corresponding control scheme cluster. However, excluding the RV_2 and RV_3, the RV control schemes have a significantly higher robustness towards natural gas quality fluctuations than the NM_1. The RV_5 has an especially superior robustness, yielding $U_{f,S}$ and Φ confidence intervals between 0.7487 to 0.7512 and 1.993 to 2.010, respectively.

The AM control schemes have intermediate $U_{f,S}$ and Φ confidence intervals approximately between 0.7331 to 0.7698 and 1.961 to 2.050, respectively. However, the deviations between the confidence intervals and absolute fluctuation domains of $U_{f,S}$ and Φ are also intermediate. Consequently, the AM control schemes are fairly robust towards fluctuating natural gas quality and therefore, are considered a significant improvement compared to the NM_1.

The AV control schemes yield low $U_{f,S}$ and Φ confidence intervals, ranging from approximately 0.7384 to 0.7592 and 1.969 to 2.032, respectively. The robustness of the AV control schemes towards natural gas quality fluctuations is very high in the Saint-Thegonnec 2014 data, due to small deviations between the confidence intervals and absolute fluctuation domains. As a result, the improvements compared to the NM_1 are very significant.

Analogous to the Renningen 2016 data, the NC_0 can partially reproduce the IC_0 outputs, yielding very small $U_{f,S}$ and Φ confidence intervals approximately between 0.7497 to 0.7503 and 1.989 to 2.009, respectively. Additionally, the deviation between the confidence intervals and absolute fluctuation domains are only nominal. Consequently, the NC_0 achieves a very high robustness towards natural gas quality fluctuations and very significant improvements compared to the NM_1.

The results of the evaluation are further discussed and compared to the Renningen 2016 data in section 5.3.4. In the Saint-Thegonnec 2014 data, the RV_5 and NC_0 achieve the highest robustness towards fluctuating natural gas quality and demonstrate the most significant improvements compared to the NM_1.

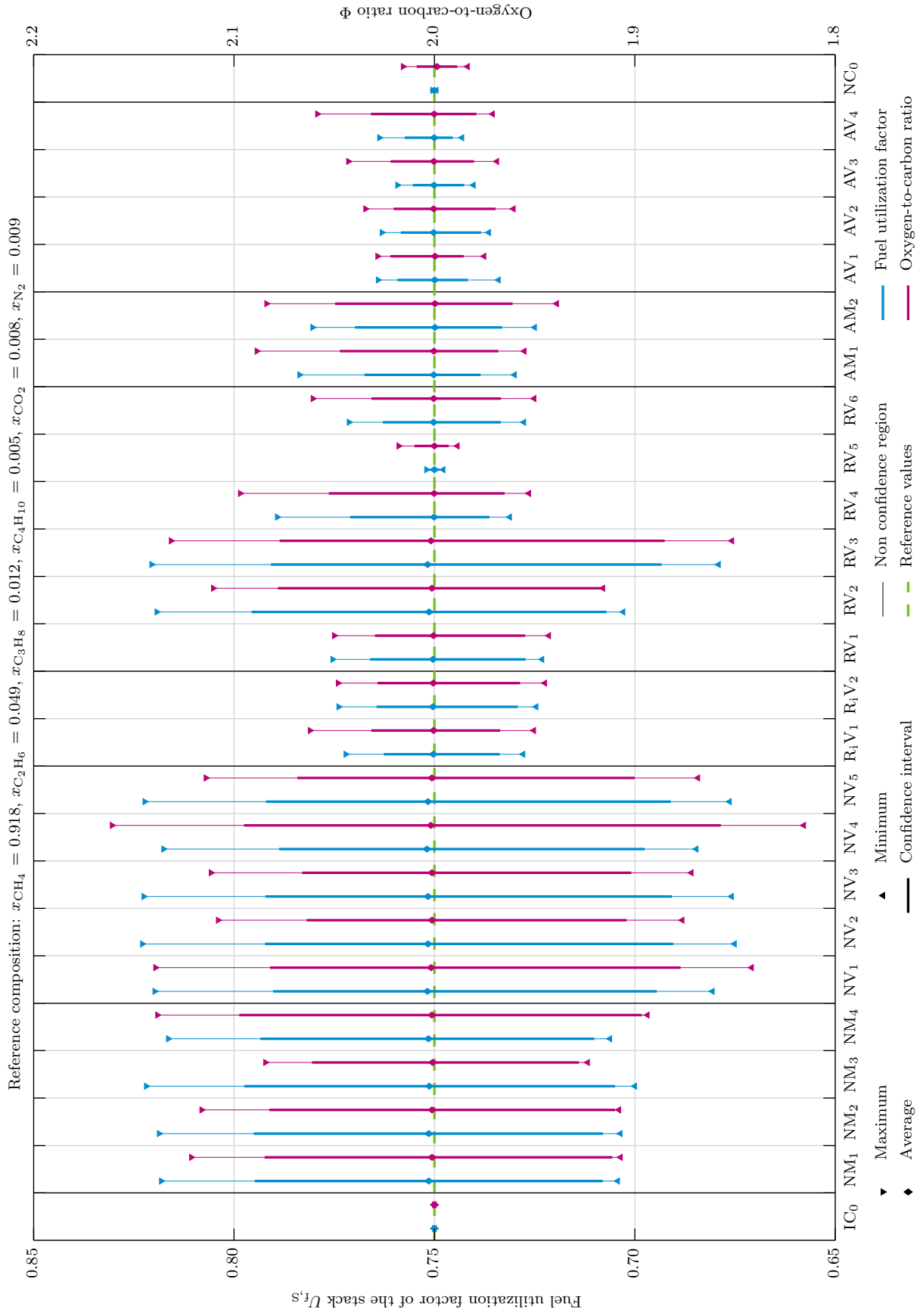

Figure 5.5: Comparison of control schemes for Saint-Thegonnec 2014 natural gas data set - Fuel utilization factor of the stack and oxygen-to-carbon ratio

5.3.3 Sensitivity analysis for Renningen 2016 data set

5.3.3.1 Variation of reference natural gas composition

Analogous to section 4.5.2, the influences on the $U_{f,S}$ and Φ fluctuation domains in the Renningen 2016 data for the implementation of the Renningen 2013 data set average, as the reference natural gas composition, are shown in Figure 5.6. The focus of the sensitivity analysis is the quantitative comparison to the NM_1. A comprehensive analysis would include the determination of the major influencing coefficient or coefficients on $U_{f,S,F}$ and Φ_F for each individual control scheme option, as well as the definition of significant reference natural gas compositions for several qualitative comparison cases. The complexity and scope of the comprehensive analysis for the NM_1 was previously conducted in section 4.5.2. Consequently, a detailed evaluation of the effects of changing reference natural gas compositions on each individual control scheme option is beyond the scope of this work. Therefore, only the Renningen 2013 data set average is chosen for the quantitative comparison, since it was used as the reference composition in the SOFC test rig control logic. As a result, Figure 5.6 outlines the modeled system responses corresponding to the SOFC test rig under nominal operation, for each individual control scheme option. It should be noted that the influence of the implementation of the Renningen 2013 data set average as the reference natural gas composition on the Renningen 2016 data is simply abbreviated as the influence of the Renningen 2013 reference.

The IC_0 and NC_0 are completely unaffected by a change in reference natural gas quality, since both options do not rely on the reference. Consequently, the NC_0 can be safely implemented without any prior knowledge of the gas quality fluctuations at any designated location of operation. Additionally, the challenges of an appropriate reference composition definition are eliminated. As a result, the improvements compared to the NM_1 are very significant.

The influences of the Renningen 2013 reference on the NM control schemes have similar trends and magnitudes, yielding small downward shifts of the $U_{f,S}$ and Φ domains. Compared to the $U_{f,S}$ and Φ domain averages displayed in Figure 5.3, the downward shifts of the $U_{f,S}$ and Φ averages are approximately -1.4 %-points and -0.025, respectively. However, in comparison to the remaining control scheme options, excluding the RV_2, the Renningen 2013 reference has the highest impact on the NM control schemes. As a result, the boundary shifting values of the NM control schemes are subsequently used to define rating intervals, ultimately allowing for a quantitative comparison of all control scheme options, as presented in section 5.3.4.

The NV control schemes are only minorly affected by implementing the Renningen 2013 reference. Compared to the $U_{f,S}$ and Φ domain averages shown in Figure 5.3, the $U_{f,S}$ and Φ averages shift slightly downwards with deviations of approximately -0.4 %-points and -0.003, respectively. In comparison to the NM_1, the NV control schemes are significantly less impacted by the Renningen 2013 reference.

The influences of the Renningen 2013 reference on the R_iV control schemes are very small. The resulting R_iV control schemes' maximum $U_{f,S}$ and Φ averages shifts are approximately -0.3 %-points and +0.004, respectively. Compared to the NM_1, the effect of the Renningen 2013 reference on the R_iV control schemes is negligibly small.

Analogous to the previous evaluations, the RV control schemes have very divergent responses to the Renningen 2013 reference. As previously discussed, the influences on the RV control schemes are consistent with the corresponding NM, NV, R_iV, AM and AV control schemes. Consequently, excluding the RV_2, the RV control schemes are significantly less affected by the Renningen 2013 reference than the NM_1.

The impacts of the Renningen 2013 reference on the AM control schemes are low, yielding upward shifts of the $U_{f,S}$ and Φ domain averages by approximately +0.4 %-points and +0.012, respectively. In comparison to the NM_1, the AM control schemes are significantly less affected by the Renningen 2013 reference.

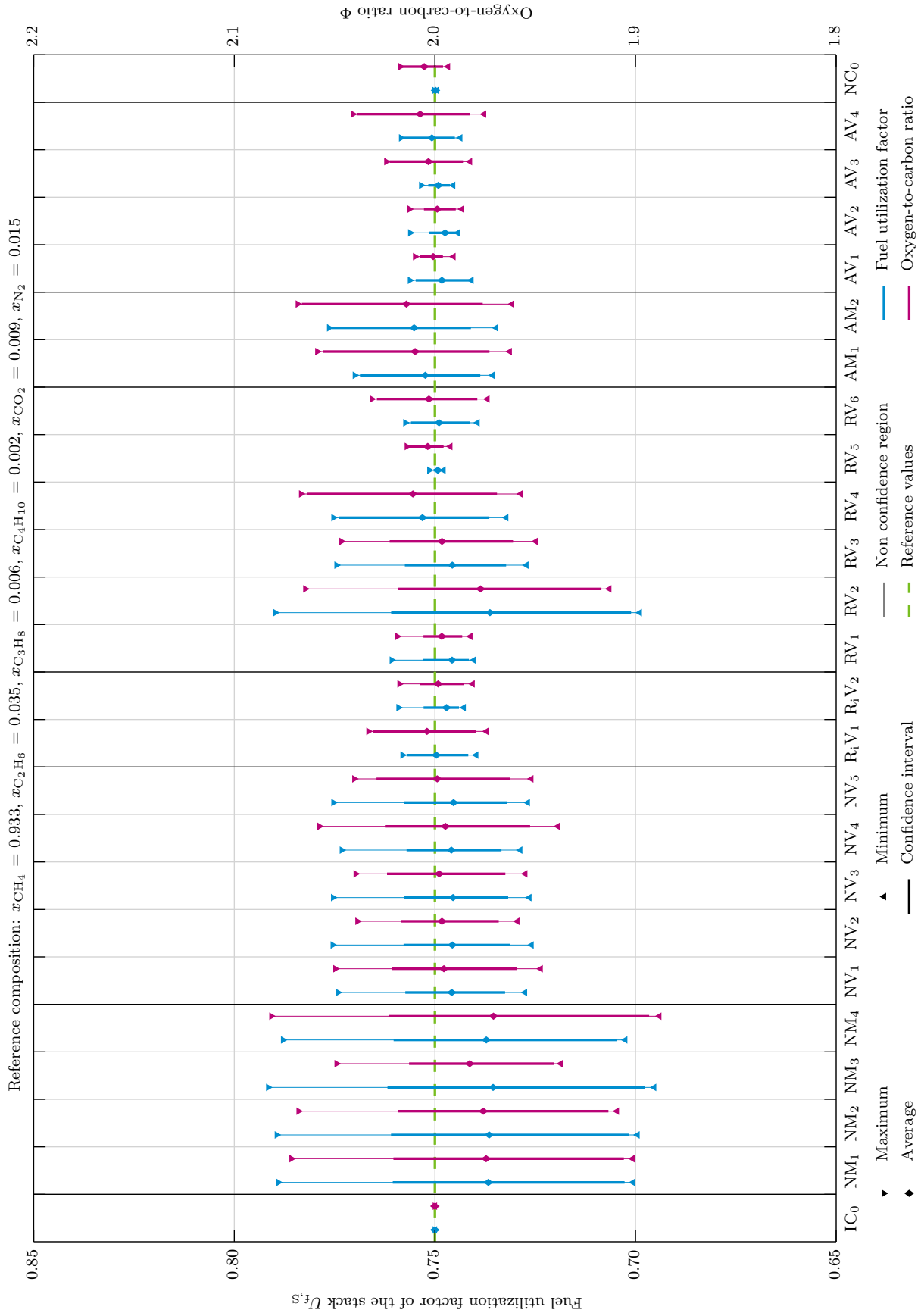

Figure 5.6: Comparison of control schemes for natural gas data Renningen 2016 - Fuel utilization factor of the stack and oxygen-to-carbon ratio for reference natural gas composition Renningen 2013

The AV control schemes are only marginally impacted by the Renningen 2013 reference. The corresponding maximum $U_{f,S}$ and Φ averages shifts are approximately -0.3 %-points and +0.007, respectively. Compared to the NM_1, the effect of the Renningen 2013 reference on the AV control schemes is negligible small.

In summary, the absolute impacts of the Renningen 2013 reference on each individual control scheme options are low. However, a comparison with the NM_1 outlines that several control scheme options are significantly more tolerable to the Renningen 2013 reference, resulting in very small to negligible deviations of the $U_{f,S}$ and Φ domain averages. The robustness towards the Renningen 2013 reference is used in section 5.3.4 as a rating criteria to further compare all control scheme options, based upon generalized grading ratios. Foreshadowing, the most robust control scheme options towards the Renningen 2013 reference are the R_iV_1, R_iV_2, RV_5, RV_6, AM_1 and all AV control schemes.

5.3.3.2 Hydrogen addition

Analogous to section 4.5.2, the influences of a 4 % hydrogen addition on the $U_{f,S}$ and Φ fluctuation domains in the Renningen 2016 data set are outlined in Figure 5.7. The chosen hydrogen addition value of 4 % is only one tenth of the previously used maximum sensitivity range of the NM_1. Several control scheme options are significantly less robust towards hydrogen addition and the axis scaling is kept consistent with the other outlined graphs in this chapter. Additionally, as depicted in Figure U.1 in appendix U, an addition of 4 % hydrogen to the Renningen 2016 data set already marginally exceeds the permitted H-gas domain in Germany. Therefore, 4 % hydrogen addition is considered an approximated boundary value.

Analogous to the NM_1, the NM control schemes are very robust towards hydrogen addition. The $U_{f,S}$ domain averages shift slightly downwards by approximately -0.7 %-points. The Φ domain averages move by -0.005 to +0.010, respectively. Consequently, all the NM control schemes are comparably robust towards hydrogen addition.

The NV control schemes are strongly influenced by small amounts of hydrogen addition, due to the low number of releasable electrons per volume of hydrogen. The upward shifts of the $U_{f,S}$ and Φ domain averages are significant, reaching deviations of approximately +4.7 %-points and +0.1, respectively. Consequently, the robustness of the NV control schemes towards hydrogen addition is extremely low and therefore, display no improvements compared to the NM_1.

The impacts of hydrogen addition on the R_iV control schemes are intermediate to high. The $U_{f,S}$ and Φ domain averages of both the R_iV_1 and R_iV_2 shift upwards by approximately +1.8 %-points and +0.05, as well as +1.3 %-points and +0.04, respectively. Therefore, the R_iV_2 is slightly more robust towards hydrogen addition than the R_iV_1. However, compared to the NM_1, both R_iV control schemes are less robust and demonstrate no improvements.

Analogous to the previous evaluations, hydrogen addition yields extremely divergent responses from the RV control schemes. As previously discussed, the outputs of the individual RV control schemes are consistent with the corresponding NM, NV, R_iV, AM and AV control schemes, respectively. Consequently, excluding the RV_2 and RV_5, the robustness towards hydrogen addition of the RV control schemes is significantly lower compared to the NM_1. The RV_5 has an enhanced robustness towards hydrogen addition, yielding very low $U_{f,S}$ and Φ domain average shifts of +0.1 %-points and +0.01, respectively.

The AM control schemes are strongly influenced by hydrogen addition. The $U_{f,S}$ and Φ domain averages of both the AM_1 and AM_2 shift upwards by approximately +2.3 %-points and +0.06, as well as +1.3 %-points and +0.04, respectively. Consequently, the AM_2 is more robust towards hydrogen addition than the AM_1. Nevertheless, in comparison to the NM_1, both AM control schemes have a lower robustness towards hydrogen addition and therefore, demonstrate no improvements.

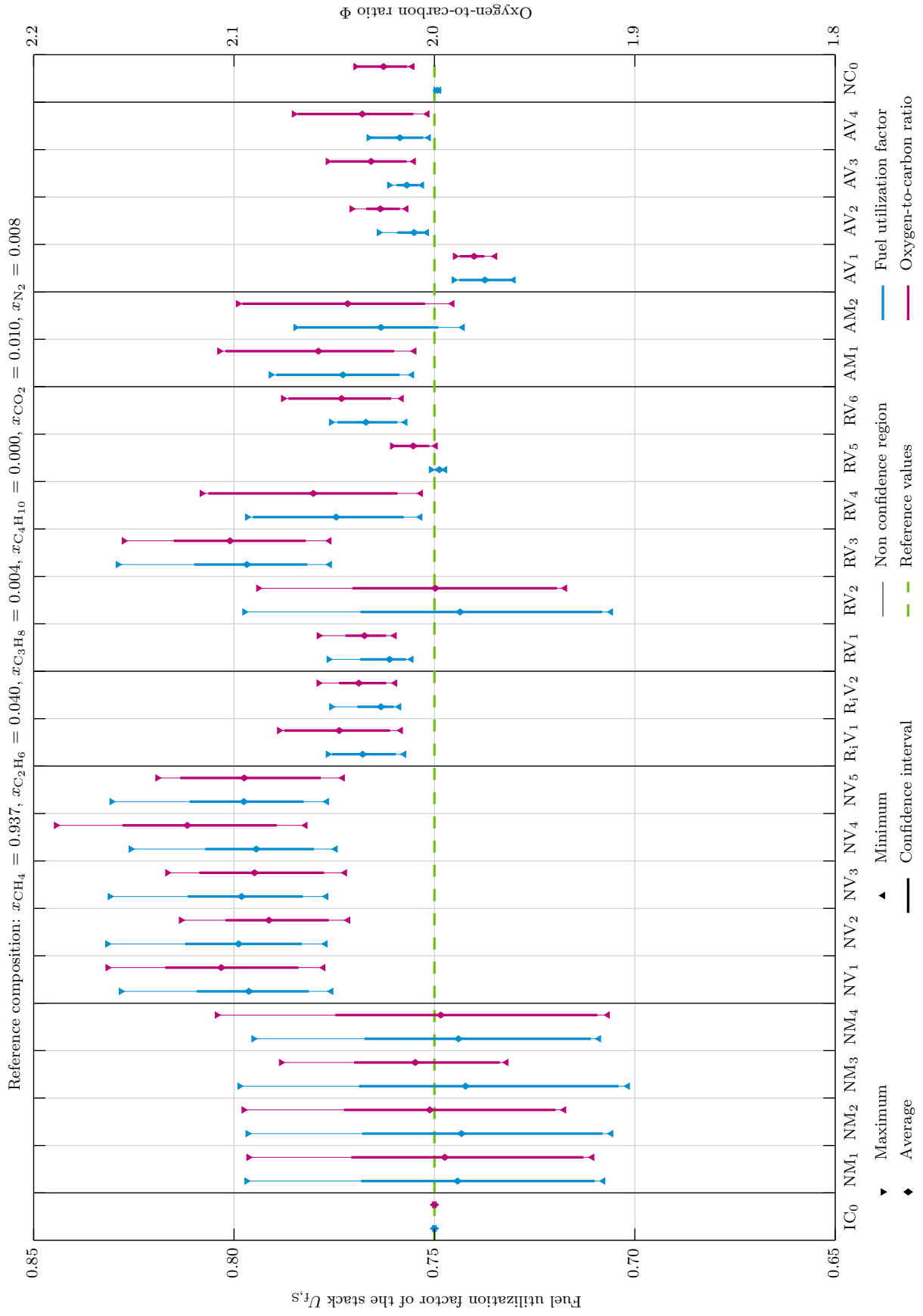

Figure 5.7: Comparison of control schemes for natural gas data Renningen 2016 - Fuel utilization factor of the stack, oxygen-to-carbon ratio and recirculation ratio for 4 % hydrogen addition

The influences of hydrogen addition on the AV control schemes are low to intermediate. Surprisingly, the $U_{f,S}$ and Φ domain averages of the AV_1 shift downwards, whereas the domain averages of the remaining AV control schemes drift upwards. The shifts of the $U_{f,S}$ and Φ domain averages of the AV_1 are approximately -1.3 %-points and -0.02, respectively. The $U_{f,S}$ and Φ domain averages of the other AV control schemes deviate by approximately +0.7 %-points and +0.03, respectively. Consequently, the AV_1 is slightly less robust towards hydrogen addition than the remaining AV control schemes. However, excluding the AV_1, the AV control schemes and NM_1 are comparably robust towards hydrogen addition.

The $U_{f,S}$ domain average of the NC_0 is only negligibly impacted by hydrogen addition, due to the assumed ideal detection of K_{e^-}. The $U_{f,S}$ domain average shifts downward in magnitude by less than -0.1 %-points. However, the Φ domain average is influenced more, shifting upwards by approximately +0.02. The Φ domain shift is a result of the implemented empirical natural gas coefficient correlation. As outlined in section 3.4.3, the correlation was derived using the natural gas data base, which does not contain any hydrogen. However, the derived regression can, in good approximation, be used for natural gas mixtures containing low hydrogen contents. As a result, the NC_0 is extremely robust towards hydrogen addition and the deviations of the $U_{f,S}$ and Φ domain averages are comparable to that of the NM_1. The sensitivity of the NC_0 towards hydrogen additions up to 40 % is further evaluated in section 5.4.

In summary, the influences of a 4 % hydrogen addition on the $U_{f,S}$ and Φ fluctuation domains in the Renningen 2016 data are extremely significant for some of the control scheme options. The NV control schemes have very low robustness towards small hydrogen additions, yielding excessively high $U_{f,S}$ values above 0.8. Additionally, the RV_3, RV_4 and AM_1 are also strongly affected by small hydrogen additions. In comparison to the NM_1, only the RV_2, RV_5, AV_2, AV_3, AV_4 and NC_0 are similarly robust towards hydrogen addition. The robustness towards hydrogen addition is also used as a rating criteria in the following section to further compare all control scheme options.

5.3.4 Comparison

In this section, all derived control scheme options are compared based upon the previously conducted analyses and two further defined criteria. In total, six criteria are evaluated, including: (a) the $U_{f,S}$ robustness; (b) the Φ robustness; (c) the robustness towards the non ideal reference natural gas composition definition; (d) robustness towards hydrogen addition; (e) the implementation feasibility; and (f) the projected cost. The six criteria are described throughout this section in more detail. It should be noted that criteria (e) and (f) are denoted as soft criteria, since in contrast to the other criteria, the rating is not based upon defined numerical intervals. For evaluation purposes, the deviation intervals and sensitivities, as well as the soft criteria of each individual control scheme are rated on an arbitrary integer scale. The rating boundary values are one and five, where the former and latter represent the worst and best ratings, respectively. The rating details for each individual criteria are listed in appendix V, including an assignment of clear text labels to each individual integer and a justification of the chosen ratings for the implementation feasibility and projected cost. The assignment of a defined integer for each of the six criteria allows for the arithmetic averaging of different ratings, ultimately yielding overall ratings for each individual control scheme option.

The first evaluated overall average rating is the combination of the criteria (a) and (b), which is labeled plain natural gas quality robustness or plain NG robustness for short. Criteria (a) and (b) are the most significant criteria, since both the Renningen 2016 and Saint-Thegonnec 2014 data sets were used for the comparison of the different control strategies at nominal operation, providing a baseline of roughly 15500 measured natural gas compositions. The plain NG robustness criteria, (a) and (b), are specified as follows:

- Criteria (a) - $U_{f,S}$ robustness: The maximum positive $U_{f,S}$ deviation between each individual control scheme and the corresponding reference value. As previously discussed in section 4.3.2, $U_{f,S}$ values above 0.8 are considered intolerable. Consequently, the individual ratings are defined in relation to the highest positive $U_{f,S}$ deviations in the Renningen 2016 and Saint-Thegonnec 2014 data sets, as outlined in Figures 5.3 and 5.5. The details of the $U_{f,S}$ deviation rating intervals are listed in Table V.1 in appendix V.

- Criteria (b) - Φ robustness: The maximum negative Φ deviation between each individual control scheme and the corresponding reference value. As previously introduced in section 4.3.2, Φ values below 1.9 are considered critical. Therefore, the individual ratings are determined in relation to the highest negative Φ deviations in the Renningen 2016 and Saint-Thegonnec 2014 data sets, as outlined in Figures 5.3 and 5.5. The details of the Φ deviation rating intervals are listed in Table V.1 in appendix V.

The $U_{f,S}$ and Φ deviation intervals of each individual control scheme in the Renningen 2016 and Saint-Thegonnec 2014 data sets were already discussed in sections 5.3.1 and 5.3.2, respectively. The corresponding $U_{f,S}$ robustness, Φ robustness and overall average plain NG robustness ratings of the Renningen 2016 and Saint-Thegonnec 2014 data sets are outlined in Figure 5.8.

Except for the IC_0, RV_5 and NC_0, at least one of the $U_{f,S}$ or Φ robustness is rated at least one category worse in the Saint-Thegonnec 2014 data compared to the Renningen 2016 data. The differences in the ratings are most apparent in the NV control schemes and the RV_3, where those control scheme options have the worst robustness ratings in both categories in the Saint-Thegonnec 2014 data set. The Renningen 2016 data set includes approximately 12500 data points less than the Saint-Thegonnec 2014 data set. Therefore, the Renningen 2016 data set is less significant. Additionally, the occurring natural gas quality fluctuations are more prominent in Saint-Thegonnec. Consequently, the imposed challenges on the control schemes, especially on the natural gas volume flow rate based control schemes, are orders of magnitudes higher in the Saint-Thegonnec 2014 data set. As a result, the $U_{f,S}$ and Φ domains are wider and the general ratings are lower. Nevertheless, as outlined in the bottom section of Figure 5.8, nine control scheme options achieve an average rating of four or higher for both data sets. The IC_0 has a flawless score, due to the ideal detection of the gas quality and the corresponding perfect adjustment of the flow rates. The RV_5 and NC_0 also achieve flawless scores for both data sets, highlighting extremely high robustness towards changing gas quality for both control scheme options. The AV_1 and AV_3 have ratings of at least 4.5, followed by the R_iV_1, RV_6, AV_2 and AV_4 with average ratings of at least 4 for both data sets, emphasizing high robustness. The NM_1 is one of the worst overall rated control scheme option, achieving scores of 2.0 and 1.5 in the Renningen 2016 and Saint-Thegonnec 2014 data sets, respectively. The low plain NG robustness rating of the NM_1 further emphasizes the need for implementation and testing of a more robust control scheme option.

However, for the choice of a suitable control scheme option, the four other rating criteria, (c) to (f), are subsequently considered. It should be noted that for further evaluations, the plain NG robustness rating is calculated using the lowest $U_{f,S}$ and Φ robustness ratings of both the Renningen 2016 and Saint-Thegonnec 2014 data sets. As a result, the total overall plain NG robustness rating follows the grades of the Saint-Thegonnec 2014 data set, since it generally has lower individual ratings. The only exception is the RV_4 Φ robustness, which is lower in the Renningen 2016 data set. Consequently, the subsequently outlined plain NG robustness ratings are identical to the evaluations of the Saint-Thegonnec 2014 data sets, except for the RV_4 rating, which is 2.5 instead of 3.0. The lowest $U_{f,S}$ and Φ robustness ratings of both the Renningen 2016 and Saint-Thegonnec 2014 data sets and the corresponding overall average plain NG robustness ratings are displayed in the two bottom graphs in Figure 5.9, respectively.

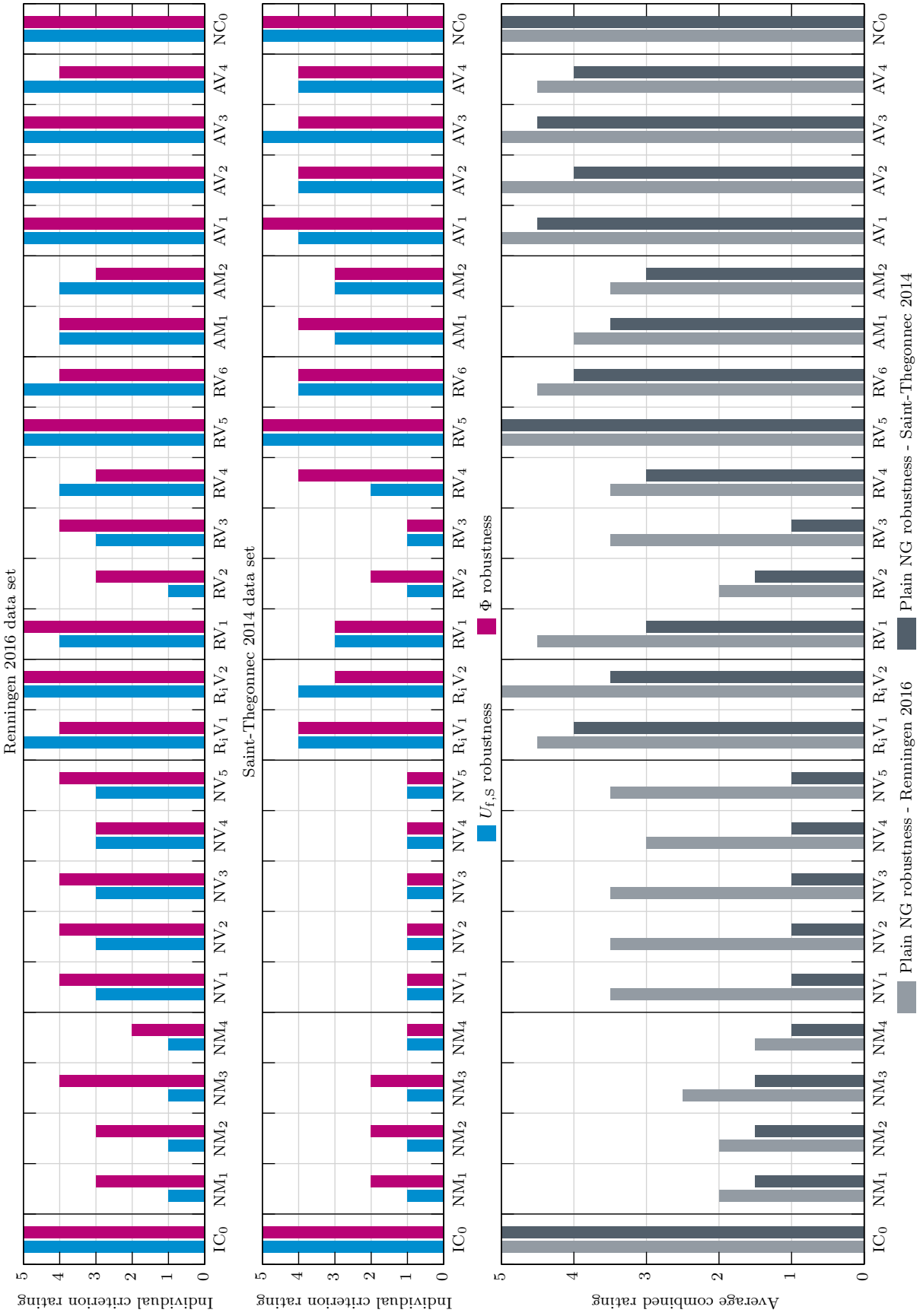

Figure 5.8: Comparison of plain natural gas quality robustness of control schemes for the Renningen 2016 and Saint-Thegonnec 2014 data sets

The second evaluated overall average rating is the combination of the criteria (a) to (d), which is labeled extended natural gas quality robustness or extended NG robustness for short. Criteria (c) and (d) are less significant than criteria (a) and (b), since only the Renningen 2016 data set was used for the sensitivity analyses of the different control strategies. Additionally, only a single variation of the reference natural gas composition and hydrogen addition were conducted. Therefore, the plain and extended robustness ratings are purposely separated to respect the divergent significance of both ratings. The additional extended NG robustness criteria, (c) and (d), are specified as follows:

- Criteria (c) - robustness towards the non ideal reference natural gas composition definition, abbreviated $x_{\mathrm{NG,R}}$ robustness: The shift of the $U_{\mathrm{f,S}}$ and Φ averages, resulting from the non ideal definition of the reference composition. The higher the negative or positive shifts in comparison to the ideal definition of the reference composition, the lower the $x_{\mathrm{NG,R}}$ robustness. The individual ratings are defined in relation to the highest of the $U_{\mathrm{f,S}}$ or Φ average shifts in the Renningen 2016 data set, as outlined in Figure 5.6. The rating details are listed in Table V.2 in appendix V.

- Criteria (d) - robustness towards hydrogen addition, abbreviated H_2 robustness: The shift of the $U_{\mathrm{f,S}}$ and Φ averages resulting from hydrogen addition to the natural gas data set. The higher the negative or positive shifts in comparison to the data set without hydrogen addition, the lower the H_2 robustness. The individual ratings are determined in relation to the highest of the $U_{\mathrm{f,S}}$ or Φ average shifts in the Renningen 2016 data set, including the 4 % hydrogen addition, as outlined in Figure 5.7. The details of the rating intervals are listed in appendix V.3 in appendix V.

The $U_{\mathrm{f,S}}$ and Φ average shifts of each individual control scheme in the Renningen 2016 sets, due to a change of the reference natural gas composition and hydrogen addition, were already discussed in sections 5.3.3.1 and 5.3.3.2, respectively. The corresponding $x_{\mathrm{NG,R}}$ robustness, H_2 robustness and overall average extended NG robustness ratings are outlined in the upper middle and bottom graphs in Figure 5.9. Unsurprisingly, the IC_0 achieves a flawless score in the overall average extended NG robustness rating, since neither a change in the reference natural gas composition nor an addition of hydrogen affects the IC_0. Additionally, the RV_5 and NC_0 keep their superior performance, reaching perfect scores in the extended NG robustness rating. Both control schemes are only minorly influenced by the addition of hydrogen. The RV_5 has an extremely high $x_{\mathrm{NG,R}}$ robustness, whereas the NC_0 is completely unaffected by a change in reference natural gas quality. The AV_3 is the only CS reaching a rating of at least 4.5. In comparison to the plain NG ratings, the AV_1 is slightly downgraded to the category with extended NG robustness ratings of at least 4. This category also includes the AV_2 and AV_4. Consequently, the high average ratings emphasize the high robustness of all the AV control schemes. The R_iV_1 and RV_6 no longer achieve ratings above 4, due to low tolerances towards hydrogen addition. In general, the differences to the plain NG robustness ratings are low to intermediate, showing a maximum increase of +1.0 for the NM_4, due to the high H_2 robustness. However, the NM_4 still achieves a poor extended NG robustness rating of 2.0. The only two control scheme options that achieve a plain NG robustness rating of at least 4, and benefit from the inclusion of criteria (c) and (d), are the AV_2 and AV_4. Nevertheless, the extended NG robustness ratings are only 0.25 higher than that of the plain NG robustness ratings. As a result, by including the extended NG robustness criteria (c) and (d) into the plain NG robustness rating, the average ratings only marginally change. The NM_1 continues to be one of the lowest overall rated control scheme option, reaching an extended NG robustness rating of just 2.25. Consequently, the demand for the implementation and testing of more robust control options, for instance the RV_5 or NC_0, is underlined once more by the evaluation of the extended NG robustness ratings.

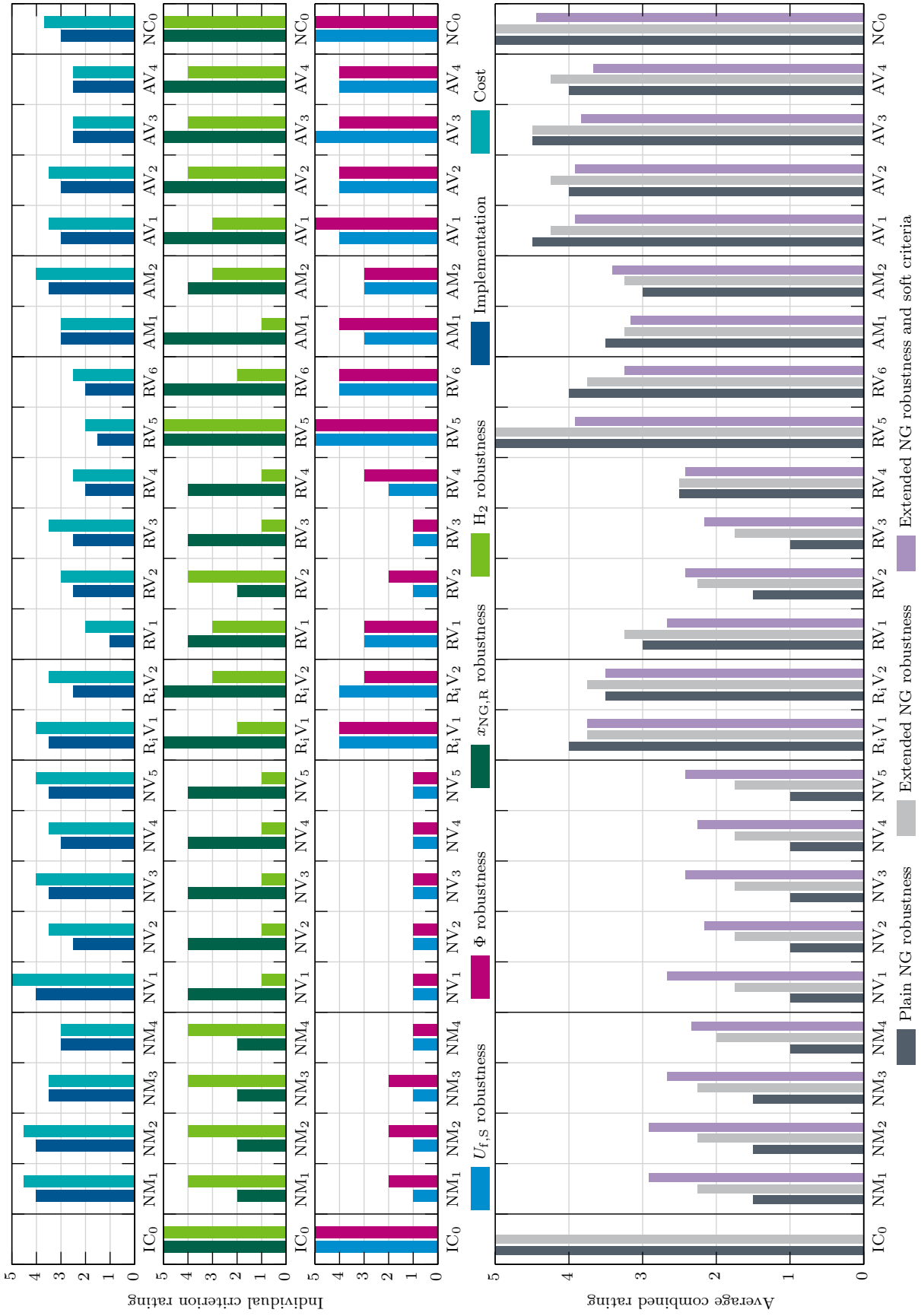

Figure 5.9: Generic comparison of control scheme options

The third evaluated overall average rating is the combination of criteria (a) to (f), which is labeled extended NG robustness and soft criteria. Criteria (e) and (f) are the least significant criteria, since the implementation feasibility and projected cost of each individual control scheme option are only determined based upon a quantitative assessment. Consequently, criteria (e) and (f) are considered soft criteria and the extended NG robustness and soft criteria rating is used for viability distinctions between the individual control scheme options. The soft criteria, (e) and (f), are specified as follows:

- Criteria (e) - implementation feasibility, abbreviated implementation: The application difficulty of the individual control scheme in relation to the necessary control elements, as previously introduced in section 5.1. The implementation feasibility includes the availability and simplicity of the corresponding flow rate detection, the predictability of the gas composition at the related control element position, as well as the control logic complexity. The rating criteria and justification for each individual control element position are listed in Tables V.4 and V.5 in appendix V. The individual implementation feasibility ratings for each control scheme option are calculated as the average of the corresponding control element ratings. In correspondence to Tables 5.1 and 5.3, for control scheme options that can be implemented with multiple control element position combinations, the highest scoring setup is evaluated. It should be noted that the evaluation of the NC_0 also accounts for the necessary natural gas quality detection setup, which is considered very hard to implement.

- Criteria (f) - projected cost, abbreviated cost: The assumed total expenses to implement the necessary hardware related to the control scheme option. For each individual control element position, several implementation possibilities exist. For instance, the natural gas volume flow rate can be controlled by detecting the volume flow rate with a sensor or from the developed characteristic compressor map modeling. The rating criteria and justification for each individual control element position are listed Tables V.4 and V.6 in appendix V. The individual projected cost ratings for each control scheme option are calculated as the average of the corresponding control element ratings. In correspondence to Tables 5.1 and 5.3, for control scheme options that can be implemented with multiple control element position combinations, the highest scoring setup is evaluated. It should be noted that the evaluation of the NC_0 also includes the cost of the necessary natural gas quality detection setup, which is considered very expensive.

The implementation feasibility and projected cost ratings of each individual control scheme option are outlined in the top graph in Figure 5.9. The IC_0 is not rated for both the implementation feasibility and projected cost categories, since sensor units that continuously and perfectly detect the gas quality, as well as control units that ideally realize flow rates, are only hypothetical solutions.

The individual control element position implementation ratings can be clustered in four groups. First, volume and mass flow rate detection at the natural gas inlet and volume flow rate determination at the reformer inlet and inside the recirculation loop are the most feasible solutions. Second, mass flow rate control at the reformer inlet and inside the recirculation loop are considered intermediately feasible. Third, anode outlet mass and volume flow rate control are hard to implement. Lastly, volume and mass flow rate control at the reformer outlet, as well as recirculation ratio control are considered the hardest implementation options. It should be noted that no control element position was classified to be very easily implementable, since an adjustment to the average natural gas composition is always necessary for an accurate control of any flow rate. As a result, no control scheme option achieves a perfect implementation feasibility rating. Implementation ratings of 4 are achieved by the NM_1, NM_2 and NV_1, since those control scheme options only rely on control elements from the first cluster. The NV_2, R_iV_2, AV_3, AV_4 and all RV control scheme options achieve poor implementation scores, since they include at

least one control element from the fourth cluster or only elements from the second and third cluster. The worst rated control scheme option is the RV_1, since it relies on two control elements from the fourth cluster. For the evaluation of the NC_0, the CS is implemented, as introduced in section 5.2, with a mass or volume natural gas flow rate control and a volume flow rate control at the reformer inlet or inside the recirculation loop. Consequently, analogous to the NM_1, NM_2 and NV_1, the NC_0 should achieve an implementation rating of 4. However, when factoring in the necessary sensor unit for the detection of the electron gas coefficient and the adjustment of the control logic, the implementation rating of the NC_0 is lowered to an intermediate value of 3. The implementation feasibility rating of the NC_0 is only marginally higher than the average of all evaluated control scheme options.

The determination of the projected cost ratings is based upon two major assumptions. First, controlling the volume flow rate is cheaper than controlling the mass flow rate at any designated system position. Second, at higher temperature levels, more sophisticated methods have to be applied to provide accurate control element functionality. Furthermore, technology options are limited, which results in increasing costs. As a result, control scheme options that only rely on control elements at the natural gas inlet, reformer inlet and inside the recirculation loop achieve the highest projected cost ratings, due to low to intermediate temperature levels. The NV_1 can be implemented using only the developed characteristic compressor map modeling at two system positions. Consequently, the NV_1 reaches a perfect score, since compressors are inherently available and the installation of additional sensors is unnecessary. The NM_1, NM_2, NV_3, NV_5, R_iV_1 and AM_2 achieve projected cost ratings of at least 4, due to the necessity of only one mass flow rate control element at low or intermediate temperatures. The worst rated control scheme options are RV_1 and RV_5, with scores of 2, due to the necessary combination of two high temperature control element positions. Analogous to the NV_1, the NC_0 should achieve a projected cost rating of 5, since it can be implemented with the same control elements. However, analogous to the implementation feasibility, the projected cost rating of the NC_0 is reduced to a value of approximately 3.7, by factoring in very high costs for the electron gas coefficient detection sensor unit. Nevertheless, the projected cost rating of the NC_0 is still slightly above the average of all evaluated control scheme options.

The influences of the soft criteria on the extended NG robustness ratings for each individual control scheme are outlined in the bottom graph in Figure 5.9. The NM and NV control schemes, as well as the RV_2, RV_3 and AM_2 benefit from the inclusion of the soft criteria. The benefit is the most apparent for the NV_1, reaching an extended NG robustness and soft criteria rating of around 2.7, which is approximately 0.9 higher than the corresponding extended NG robustness rating. Nevertheless, the total scores of all NM and NV control schemes are still lower than 2.9, outlining the necessity for an improved control scheme. The R_iV_2, RV_1, RV_4, RV_5, RV_6, AM_1, NC_0 and all AV control schemes achieve reduced ratings. The rating of the RV_5 is influenced the most, reaching an extended NG robustness and soft criteria rating of around 3.9, which is approximately 1.1 lower than the corresponding extended NG robustness rating. Consequently, the RV_5, R_iV_1, R_iV_2, and all AV control scheme ratings are comparable, achieving good scores approximately between 3.5 and 3.9. The NC_0 is the only control scheme option maintaining an extended NG robustness and soft criteria rating above 4, outlining an overall superior performance with an independence from the reference natural gas composition definition and an intermediate application viability.

As a result, the NC_0 is the second designated control scheme option, which is implemented and tested in the SOFC test rig. In a first step, analogous to the NM_1 in section 4.5, the NC_0 is further evaluated via a sensitivity analysis, in section 5.4. In a second step, the NC_0 is implemented into the SOFC test rig control logic and experimentally evaluated. The necessary adjustments to the control logic and the experimental results are outlined in sections 5.5.1 and 5.5.2.

5.4 Sensitivity analysis for natural gas electron coefficient CS

Analogous to section 4.5, the applicability of the NC_0 is further evaluated via a sensitivity analysis, varying the set points of the fuel utilization factor of the stack and oxygen-to-carbon ratio. Additionally, the influences of hydrogen addition to the natural gas data base are evaluated on a wider scale up to 40 %, as an extension of the results outlined in Figure 5.7. The Renningen 2016 data set is used as the basis for the evaluation. It should be noted that only a single parameter is varied, while all other inputs are kept at the designated nominal values, which are listed in Table 4.2. In contrast to the NM_1 in section 4.5.2, the sensitivity towards the variable reference natural gas composition is excluded, since the NC_0 does not rely on a relation to the reference natural gas composition, as outlined in section 5.3.3.1.

Figure 5.10 displays a variation of $U_{f,S,SP}$ and Φ_{SP} between 0.6 to 0.8 and 1.9 to 2.3, respectively. The performance of the NC_0 is nearly unaffected by the variation of the set points. The NC_0 closely matches any designated $U_{f,S,SP}$, due to the assumed ideal detection of K_{e^-}. As previously mentioned, the Φ domain averages do not ideally match the corresponding Φ_{SP}, due to the regression based estimation of $K_{\triangle an}$ and K_Φ. However, the resulting offsets and spreads of the Φ domains are very small and the interval magnitudes are only slightly affected by varying Φ_{SP}. For increasing Φ_{SP}, the Φ domains are only marginally extended, since the 95 % confidence interval spreads are only 0.016 and 0.023 for Φ_{SP} of 1.9 and 2.3, respectively. The reason for the marginal increase in the Φ domains is the accuracy of the regression based estimation of K_Φ, which decreases slightly for increasing Φ values, as outlined in Figure 3.12.

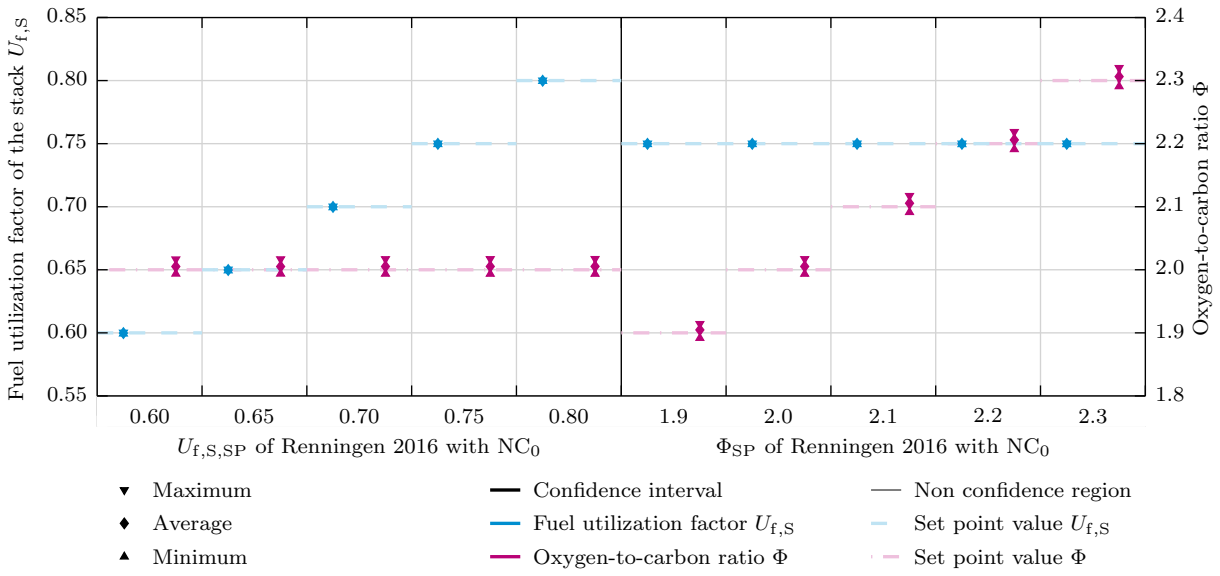

Figure 5.10: Sensitivity analysis for NC_0 - Variation of fuel utilization factor of the stack and oxygen-to-carbon ratio set points for the Renningen 2016 data set

Figure 5.11 depicts the effects of hydrogen additions up to 40 % for two different NC_0 implementation cases. In the left segment of the graph, the NC_0 is implemented as introduced in section 5.2, using the quadratic regression approach to determine $K_{\triangle an}$ and K_Φ for the designated Φ_{SP} of 2. For increasing hydrogen contents, the quadratic regression estimation accuracy of $K_{\triangle an}$ and K_Φ diminishes. The corresponding K_{e^-} of the hydrogen natural gas mixture are considerably smaller than the data base used to empirically determine the regression function, as previously outlined in Figure 3.11. For instance, a 40 % hydrogen addition to the Renningen 2016 data set yields K_{e^-} values of approximately 5.7, which are significantly lower than the smallest K_{e^-} values in the entire natural gas data base, with a value of approximately 7.7. Con-

sequently, the quadratic regression overestimates $K_{\triangle an}$ and K_{Φ} for increasing hydrogen contents. The mismatches between the real value of $K_{\triangle an}$ and the corresponding quadratic regression approach estimated values for the Renningen 2016 data set with hydrogen additions up to 40 % are outlined in Figure 5.12. Additionally, analogous to Figure 3.11, the linear regression approach and the entire natural gas data base results are depicted. As previously mentioned, it should be noted that $K_{\triangle an}$ and K_{Φ} are identical for Φ_{SP} of 2. As a result of the mismatch for increasing hydrogen contents, the recirculation ratio and oxygen-to-carbon ratio increase, whereas the fuel utilization factor decreases, due to the overestimated reformer inlet volume flow rate set point. However, the $U_{f,S}$ domain spreads are unaffected by increasing hydrogen contents, due to the assumed ideal detection of K_{e^-}. In contrast, the Φ domain spreads are significantly enlarged by increasing hydrogen contents, since the offsets between the real and estimated values of $K_{\triangle an}$ are higher.

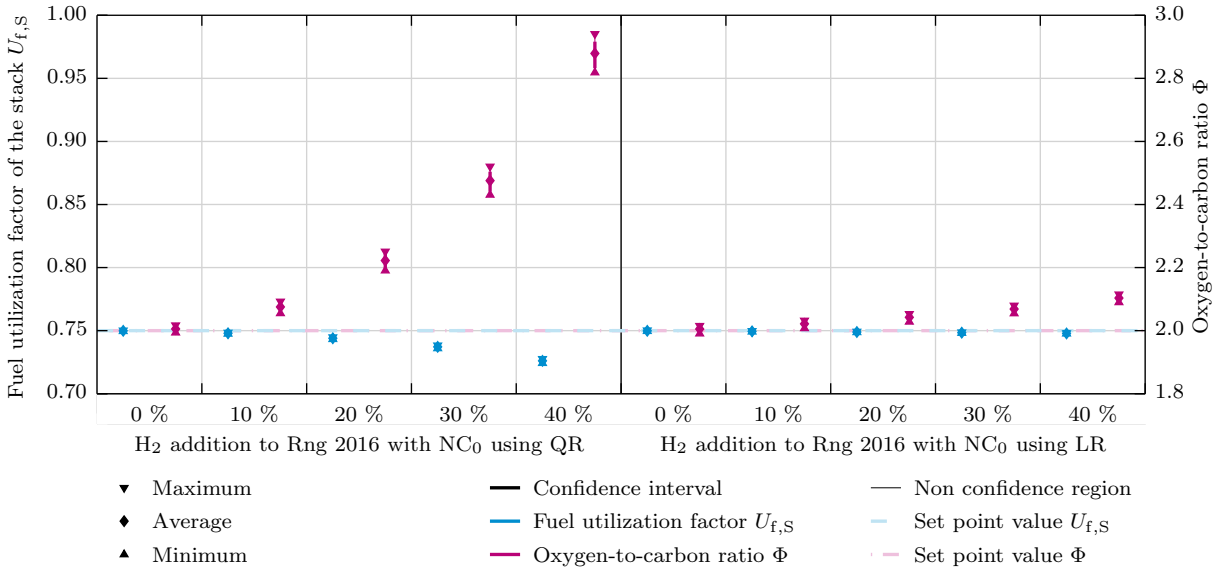

Figure 5.11: Sensitivity analysis for NC_0 - Variation of hydrogen addition for the Renningen 2016 data set

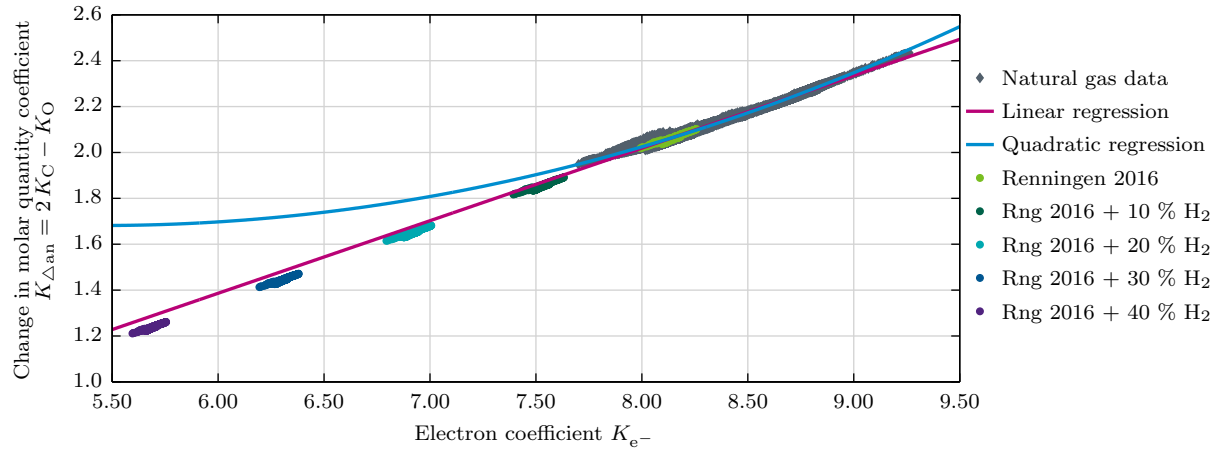

Figure 5.12: Applicability of regression between electron gas and change in molar quantity coefficient for the Renningen 2016 data set with hydrogen addition up to 40 %

In summary, the influence of hydrogen addition on the NC_0 Φ domains with a quadratic regression estimation of $K_{\triangle an}$ and K_Φ is high, whereas the influence on the $U_{f,S}$ domains is only marginal. However, the Φ domains steadily shift upwards and the $U_{f,S}$ domains shift slightly downwards for increasing hydrogen contents. Consequently, the implementation of the NC_0 still prevents values higher than approximately 0.75 and lower than approximately 2.0 for $U_{f,S}$ and Φ, respectively. Therefore, the risk of reaching harmful system operating conditions is limited. Nevertheless, combining decreasing $U_{f,S}$ values with rising Φ values can result in lower system efficiencies, due to increased dilution of fresh fuel and higher auxiliary blower power demands. Compared to the sensitivity results of the NM_1 discussed in section 4.5.3, the negative shift of the $U_{f,S}$ domain is significantly smaller, whereas the Φ domain is moving in the opposite direction at a distinctly higher amplitude. As a result, compared to the NM_1, the implementation of the NC_0 with a quadratic regression estimation of $K_{\triangle an}$ and K_Φ is more robust towards hydrogen additions up to total mole fractions of approximately 20 % H_2. The Φ domains are shifting away from the carbon deposition region and the $U_{f,S}$ intervals are significantly smaller for the NC_0. Nevertheless, the NC_0 responses using a quadratic regression estimation of $K_{\triangle an}$ and K_Φ still reach undesirable operating points for high hydrogen additions.

In a following step, the behavior of the NC_0 with a linear approximation of $K_{\triangle an}$ and K_Φ is evaluated for hydrogen additions up to 40 %. As outlined in Figure 5.12, increasing hydrogen fractions impose new challenges for the estimation of $K_{\triangle an}$ and K_Φ, yielding a linear shift of the Renningen 2016 data sets towards lower K_{e^-} and $K_{\triangle an}$ values. The boundary case is pure hydrogen with K_{e^-} and $K_{\triangle an}$ values of 2.0 and 0.0, respectively. Therefore, compared to the quadratic regression, the linear regression between K_{e^-} and $K_{\triangle an}$ has a distinctly higher correlation to the Renningen 2016 data with hydrogen addition. Consequently, as outlined in the right segment of Figure 5.11, even for high hydrogen fractions, the deviations of $U_{f,S}$ and Φ to the designated set point values are low. The Φ domains still steadily shift upwards for increasing hydrogen contents, due to the increasing mismatch between the real value of $K_{\triangle an}$ and the corresponding linear regression approach estimated values. However, the offset of 40 % hydrogen addition in the linear regression case is comparable to the mismatch of 10 % hydrogen addition in the quadratic regression approach.

As a result, by a slight adjustment of the NC_0 implementation logic, the robustness towards hydrogen additions can be significantly increased. Even for hydrogen additions of 40 %, the NC_0, with a linear approximation of $K_{\triangle an}$ and K_Φ, shows exceptional results with small $U_{f,S}$ and Φ deviations. The linear regression approach should be favored over the quadratic regression approach for regions or locations where significant hydrogen fractions are present in natural gas. As outlined in section 3.3.4, quantifiable amounts of hydrogen are not present in any natural gas data set. Therefore, for the experimental implementation of the NC_0 in the SOFC test rig control logic, the quadratic regression approach is used. As discussed in section 3.4.3.2, the quadratic regression approach has a slightly enhanced accuracy and is therefore, favored for natural gas mixtures without hydrogen contents. Nevertheless, as previously mentioned in section 5.3.3.2, it should be noted that a 4 % hydrogen addition to the Renningen 2016 data set exceeds the currently permitted H-gas domain in Germany, as depicted in Figure U.1 in appendix U. Consequently, the quadratic regression approach is sufficiently applicable.

In summary, the NC_0 displays exceptional simulation results, accurately realizing a wide range of designated $U_{f,S,SP}$ and Φ_{SP}, as well as being extremely robust towards large hydrogen additions. Additionally, the NC_0 does not rely on the definition of a reference composition and can therefore, be implemented at any designated location without any prior knowledge of the natural gas quality. In the following section, the implementation into the SOFC test rig control logic and the experimental results of the NC_0 are outlined.

5.5 Experimental evaluation of natural gas electron coefficient CS

5.5.1 Adjustments of control logic

The NC_0 is implemented in the SOFC test rig control logic, which was introduced in section 4.2.1, by replacing the connection to the defined reference natural gas composition with the measured signals of the multi gas analyzer. Consequently, the set point determinations and process value computations remain nearly unchanged. However, some minor adjustments have to be implemented. First, the outputs of the methane concentrations and ethane equivalents of the nondispersive infrared sensors are used to calculate the electron coefficient, as outlined in equation (4.16) in section 4.4.1.3. Second, $K_{\triangle an,QR,NDIR}$ and $K_{\Phi,MLR,NDIR}$ are computed as a function of the determined $K_{e^-,NDIR}$ and designated Φ_{SP}, based upon Table 3.4 and equation (3.14). As a result, the terms ($2\,K_{C,R} - K_{O,R} = K_{\triangle an,R}$) and ($\Phi_{SP}\,K_{C,R} - K_{O,R} = K_{\Phi,R}$) are replaced in all set point and process value computations with $K_{\triangle an,QR,NDIR}$ and $K_{\Phi,MLR,NDIR}$. Third, as outlined in equation (4.18), the molar mass of natural gas can be calculated using the relative density signal of the multi gas analyzer and $M_{NG,in,R}$ can be substituted. Lastly, the multi gas analyzer outputs can be applied to calculate $h_{i,NG,NDIR}$ and $K_{\lambda,NG,NDIR}$ analogous to equations (3.1) and (2.6). The only exception or inconsistency is the Φ_{PV} calculation, since the exact values of K_C and K_O are necessary and both can not be determined with the multi gas analyzer, as discussed in section 4.4.1.3. For the sake of completeness, an arbitrary reference value for K_O is set and the determined $K_{\triangle an,QR,NDIR}$ value is used to estimate K_C, as outlined in equation (5.3). The chosen K_O value is equal to $K_{O,R}$, which was defined in Table 4.3. However, Φ_{PV} is only used for representative purposes and the computation inconsistency does not influence the definition of the set point values. Analogous to the NM_1 testing in 2017, the derived MFC scaling logic remains active. The multi gas analyzer is used for continuous determination of the specific natural gas heat capacity to accurately set the natural gas mass flow rate using equation (4.25).

$$K_{C,estimated} \sim \frac{K_{\triangle an,QR,NDIR} + K_{O,R}}{2} \tag{5.3}$$

5.5.2 Experimental results

The performance of the NC_0 was tested in the SOFC test rig in January and February 2017 during three separate periods, where $U_{f,S,SP}$ was varied in the last testing cycle. Analogous to the NM_1 testing, Φ_{SP} was not varied, since lower values than the designated set point of 2 are already considered risks for carbon formation. The corresponding time frames, sample sizes and set points of the leading system variables for the individual testing periods are listed in Table W.1 in appendix W. Once again, one sample includes the condensed GC data points at a single aggregated time step, which were used to compute the measurement based analytic system balance, as previously introduced in section 4.4.1.4. It should be noted that the safety scaling factor of the recirculation flow rate was deactivated and the MFC scaling was active throughout the entire NC_0 testing period.

The recorded data was evaluated using an extension of the previously outlined methodology in section 4.4.1.4, ultimately allowing for a comparison of the measured and simulated system states for the NC_0. The only extensions were the parallel integration of the NC_0 equations in the black box modeling approach and the recording of the multi gas analyzer outputs. As a result, the simulated outputs of the NM_1 and NC_0 were compared at each aggregated time step. Additionally, the NC_0 simulated results were compared with the corresponding measurement based analytic system balance. Lastly, the match between the outputs of the GC and multi gas analyzer were displayed for the testing period. Analogous to the NM_1 evaluation, Gaussian

propagation of error was applied to calculate the standard uncertainty for the indirectly estimated characteristic parameters, gas coefficients, molar masses, and all related molar and mass flow rates of the condensed GC data points at each aggregated time step.

For the purpose of enhanced visualization, consecutive data points from each individual sampling period are connected, even though the data is based upon discontinuous GC and NDIR samples. Additionally, the conducted propagation of error presents an uncertainty for each individual measurement based calculated parameter at each aggregated time step. However, the error bars in Figures 5.13 and 5.14 are only outlined for every 10th aggregated time step to prevent confusing overlaps.

5.5.2.1 Natural gas properties

Analogous to the NM_1 evaluation, to outline the occurring natural gas quality fluctuations during the testing period, the measured and reference values of the carbon, oxygen and electron gas coefficients, as well as the molar masses are compared in Figure 5.13. Additionally, for K_{e^-} and $M_{NG,in}$, the corresponding outputs of the multi gas analyzer are shown beside the GC results. It should be noted that the reference values are displayed as a baseline, ultimately allowing for a comparison with the natural gas quality fluctuations during the NM_1 testing period. The related reference values, as well as the averages, minima and maxima of the GC measured data base of K_C, K_O, K_{e^-} and $M_{NG,in}$ are listed in Table W.3 in appendix W. Additionally, Table W.3 includes the corresponding deviations between the averages, minima and maxima of the measured data base and the reference values.

As outlined in Figure 5.13, K_C, K_O, K_{e^-} and $M_{NG,in}$ significantly fluctuate during the NC_0 testing period. The uncertainties of K_C, K_{e^-} and $M_{NG,in}$ are high, due to the direct relation of the calculation to the two major species in natural gas. The K_O uncertainty is very low, since the computation only includes carbon dioxide. The corresponding deviations between K_C, K_O, K_{e^-} or $M_{NG,in}$ and the designated reference values are between -1.5 and 1.6 %, -65.2 and 72.7 %, -0.2 and 0.7 %, as well as -3.8 and 1.5 %, respectively. Consequently, even though the NC_0 testing period was significantly shorter than the NM_1 evaluation cycle, the natural gas quality fluctuations during both periods are comparable. As a result, the evaluated time frame provides a significant baseline for the assessment of the fluctuating natural gas quality effects on an AEGR SOFC system operated with the NC_0. Analogous to the NM_1 evaluation cycle, K_C, K_O and K_{e^-} have nearly identical progressions during the evaluated time frame. Consequently, as already discussed in section 4.4.3.1, rising carbon dioxide amounts almost always lead to an increase of higher hydrocarbon contents, simultaneously elevating K_C, K_O and K_{e^-}. For decreasing carbon dioxide contents, the trend occurs vice versa. As a result, the change in molar quantity coefficient and K_{e^-} have a nearly linear relation, as previously indicated in Figure 3.11. As outlined in Figures 5.13c and 5.13d, the determined K_{e^-} and $M_{NG,in}$ via the GC and the NDIR sensors are in good agreement, as previously depicted for a longer time frame in Figures 4.11c and 4.11d. The outlined offsets are within the respective GC quantification error margins of around 1 %.

5.5.2.2 Characteristic parameters and flow rates

The measured and simulated system responses of $U_{f,S}$ and Φ during the NC_0 testing period are depicted in Figures 5.14a and 5.14b. Additionally, the corresponding mass and volume flow rates at the natural gas and reformer inlet are outlined in Figures 5.14c and 5.14d, respectively. Moreover, the corresponding simulated values of the NM_1 are shown for comparison. As previously introduced, the corresponding set points of the leading system variables in the individual testing periods are listed in Table W.1 in appendix W. Each subplot of Figure 5.14 outlines four individual progressions:

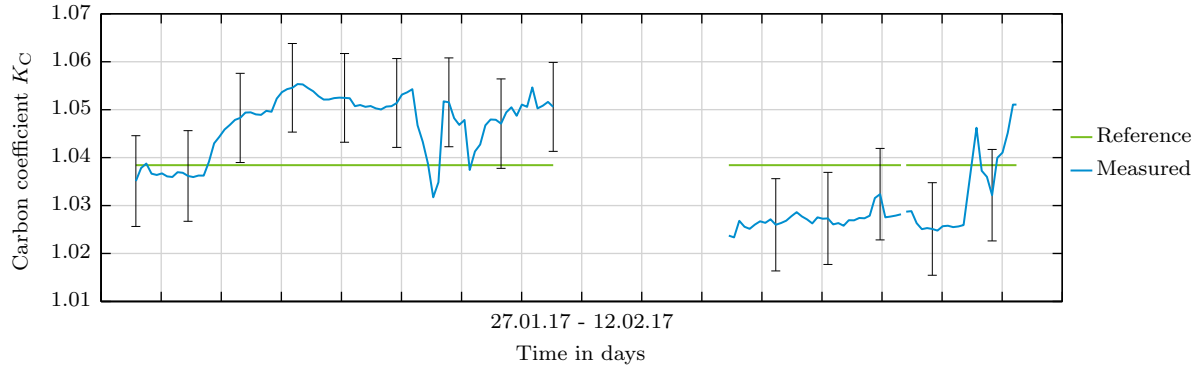

(a) Carbon gas coefficient

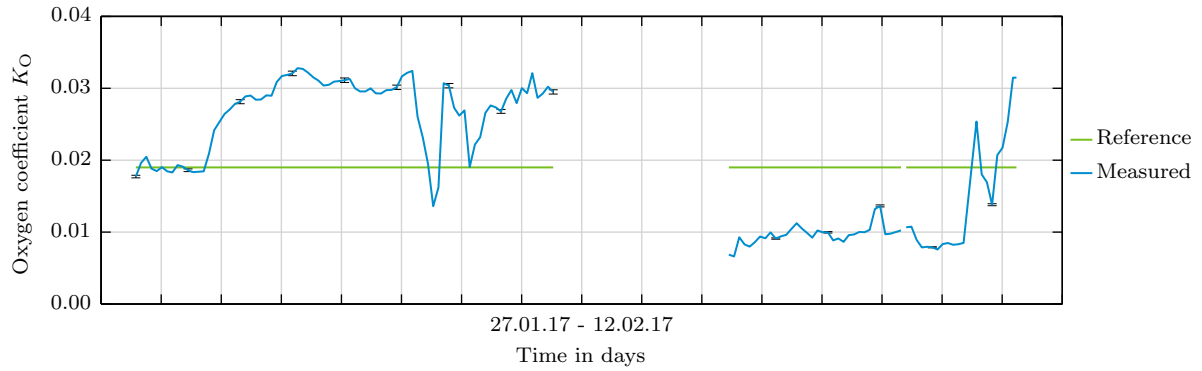

(b) Oxygen gas coefficient

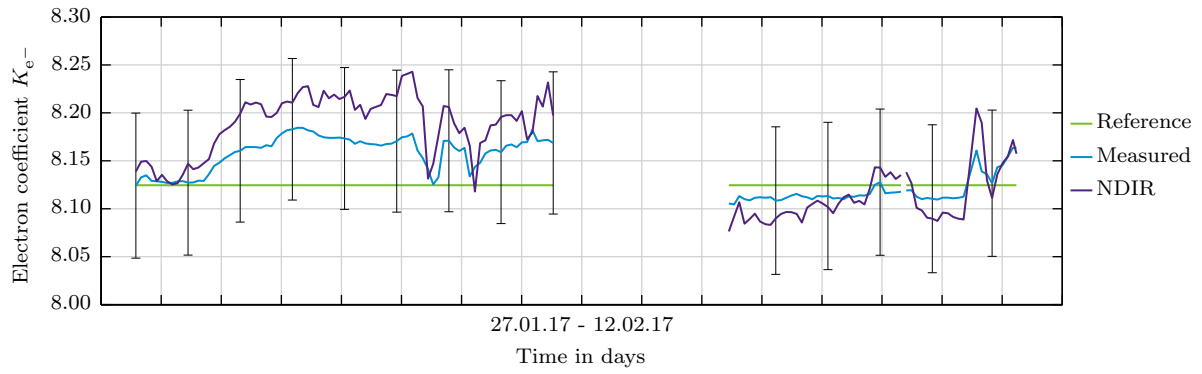

(c) Electron gas coefficient

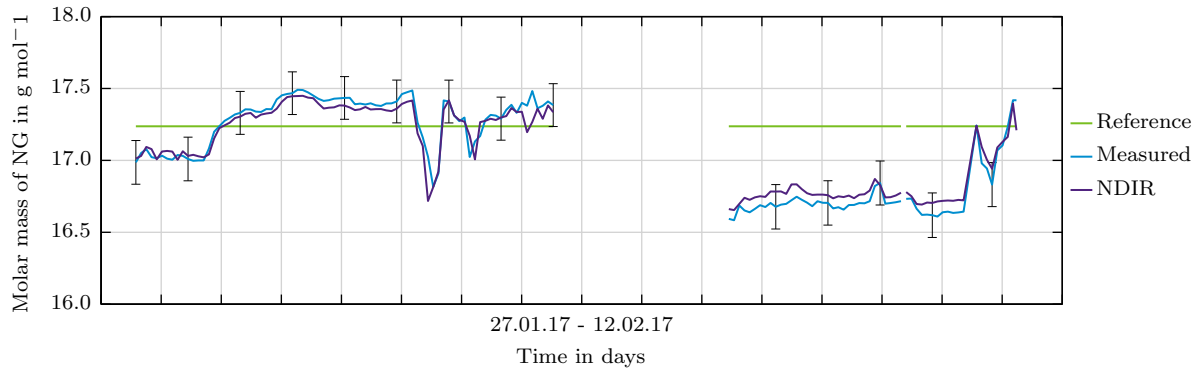

(d) Molar mass

Figure 5.13: Experimental results of NC_0 - Comparison between reference and measured natural gas states

1. Set point - the set points of the characteristic parameters $\left(U_{\mathrm{f,S,SP}}\right.$ and $\left.\Phi_{\mathrm{SP}}\right)$ or the corresponding actuator set points $\left(\dot{m}_{\mathrm{NG,in,SP}}\right.$ and $\left.\dot{V}_{\mathrm{ref,in,SP}}\right)$.

2. Measured - the indirectly measured characteristic parameters $\left(U_{\mathrm{f,S,Msd}}\right.$ and $\left.\Phi_{\mathrm{Msd}}\right)$ or measurement based analytically calculated values $\left(\dot{m}_{\mathrm{NG,in,Msd}}\right.$ and $\left.\dot{V}_{\mathrm{ref,in,Msd}}\right)$.

3. $\mathrm{NC_0}$ Sim - the simulated values $\left(U_{\mathrm{f,S,NC_0}}\right.$, $\Phi_{\mathrm{NC_0}}$, $\dot{m}_{\mathrm{NG,in,NC_0}}$ and $\left.\dot{V}_{\mathrm{ref,in,NC_0}}\right)$ based upon the $\mathrm{NC_0}$ equations, as outlined in section 5.2.

4. $\mathrm{NM_1}$ Sim - the simulated values $\left(U_{\mathrm{f,S,NM_1}}\right.$, $\Phi_{\mathrm{NM_1}}$, $\dot{m}_{\mathrm{NG,in,NM_1}}$ and $\left.\dot{V}_{\mathrm{ref,in,NM_1}}\right)$ based upon the $\mathrm{NM_1}$ equations, as outlined in section 4.2.2.1.

As depicted in Figure 5.14a, the measured $U_{\mathrm{f,S}}$ are in good agreement with the corresponding set points and simulated values. Additionally, the measured $U_{\mathrm{f,S}}$ display stable progressions for both tested $U_{\mathrm{f,S,SP}}$ values of 0.75 and 0.70, respectively. The small occurring offsets between $U_{\mathrm{f,S,Msd}}$ and $U_{\mathrm{f,S,SP}}$, which are not bridged by the displayed error bars, are the result of three major influences. First, the small deviations between the determined $K_{\mathrm{e^-}}$ with the GC and NDIR sensors, shown in Figure 5.13c, can ultimately result in a slightly insufficient natural gas supply. The over- or underestimation of $K_{\mathrm{e^-}}$ via the NDIR sensors yields natural gas mass flow rate set points that differ slightly from the simulated set points, as outlined in Figure 5.14c. Second, the actuators can not ideally realize both the mass and volume flow rate set points at the natural gas and reformer inlets, as outlined in Figures 5.14c and 5.14d. Third, two different gas measurement systems were used as a basis for the evaluation. The multi gas analyzer was used to determine the necessary outputs to operate the SOFC test rig with the $\mathrm{NC_0}$, whereas the GC measurements were applied to compute the analytic system balance and characteristic parameters. To generate a single condensed GC data point, several measurements have been combined, ultimately resulting in the previously described intrinsic error in section 4.4.3. Additionally, the GC and multi gas analyzer have completely different sampling rates. As a result, the outlined agreement between the $U_{\mathrm{f,S,Msd}}$ and $U_{\mathrm{f,S,SP}}$ is considered exceptionally high. In comparison to the corresponding outlined simulated $\mathrm{NM_1}$ $U_{\mathrm{f,S}}$ progression, the advantage of the $\mathrm{NC_0}$ implementation is very prominent. The $\mathrm{NC_0}$ constantly reaches $U_{\mathrm{f,S}}$ that are close to the defined $U_{\mathrm{f,S,SP}}$, emphasizing the ability to accurately respond to fluctuating natural gas quality. In the testing periods with $U_{\mathrm{f,S,SP}}$ of 0.75, $U_{\mathrm{f,S,Msd}}$ only deviates between 0.754 and 0.763, whereas the corresponding simulated $\mathrm{NM_1}$ $U_{\mathrm{f,S}}$ values cover a domain between 0.703 and 0.761.

The measured Φ are also in good agreement with the corresponding set points and simulated values. The outlined offsets can be mostly explained with the displayed error bars, bridging the gaps between Φ_{SP} and Φ_{Msd}. The only minor exception is the testing period with $U_{\mathrm{f,S,SP}}$ of 0.70 in February, where the offsets between Φ_{SP} and Φ_{Msd} are significantly higher. The slightly increased Φ_{Msd} values are a result of the excessive volume flow rates at the reformer inlet. The inaccuracies of the volume flow rate determination with the characteristic compressor map modeling increase for higher absolute flow rates. Consequently, the recirculation ratio is slightly too high. As a result, Φ increases, while $U_{\mathrm{f,S}}$ slightly deceases, due to higher fractions of hydrogen, carbon monoxide, carbon dioxide and water vapor at the reformer inlet. However, in comparison to the corresponding outlined simulated $\mathrm{NM_1}$ Φ progressions, the $\mathrm{NC_0}$ results are significantly superior. The oxygen-to-carbon ratio of the $\mathrm{NC_0}$ has a stable progression with values hovering around the designated set point. In the testing periods with $U_{\mathrm{f,S,SP}}$ of 0.75, the Φ_{Msd} only covers a domain between 1.97 and 2.03, whereas the corresponding simulated $\mathrm{NM_1}$ Φ deviates between 1.91 and 2.02. Consequently, the risk of carbon formation is significantly decreased by the $\mathrm{NC_0}$ implementation, since excessively low values of Φ are prevented.

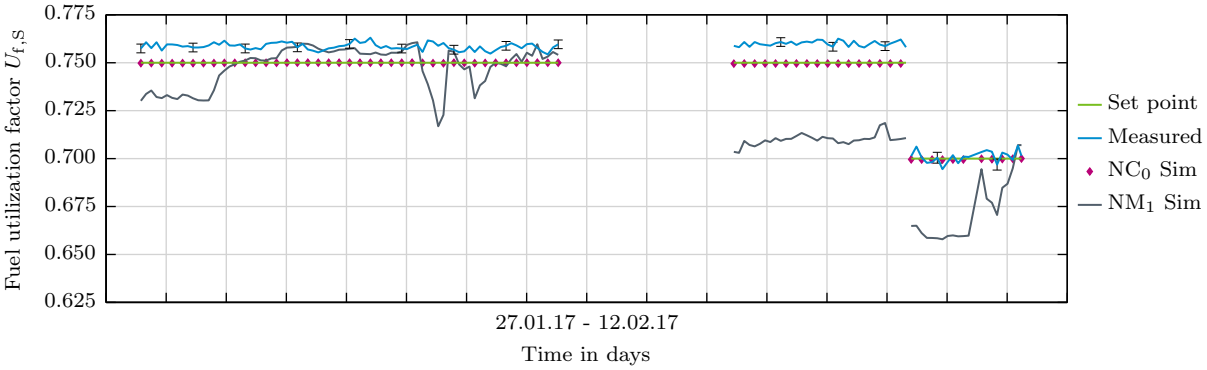

(a) Fuel utilization factor of the stack

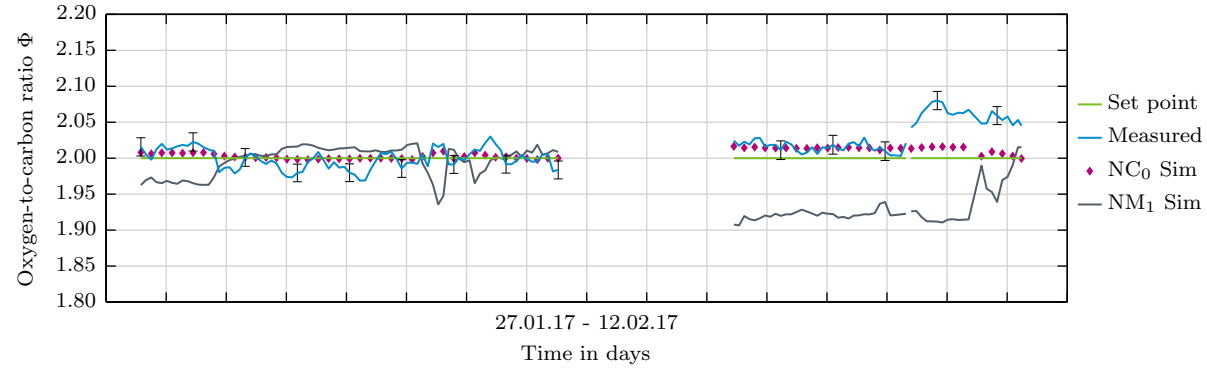

(b) Oxygen-to-carbon ratio

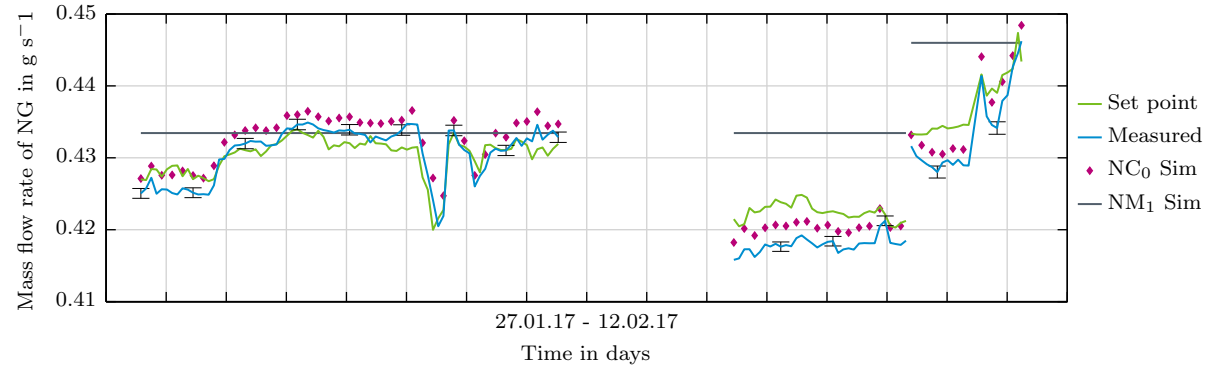

(c) Mass flow rate of natural gas

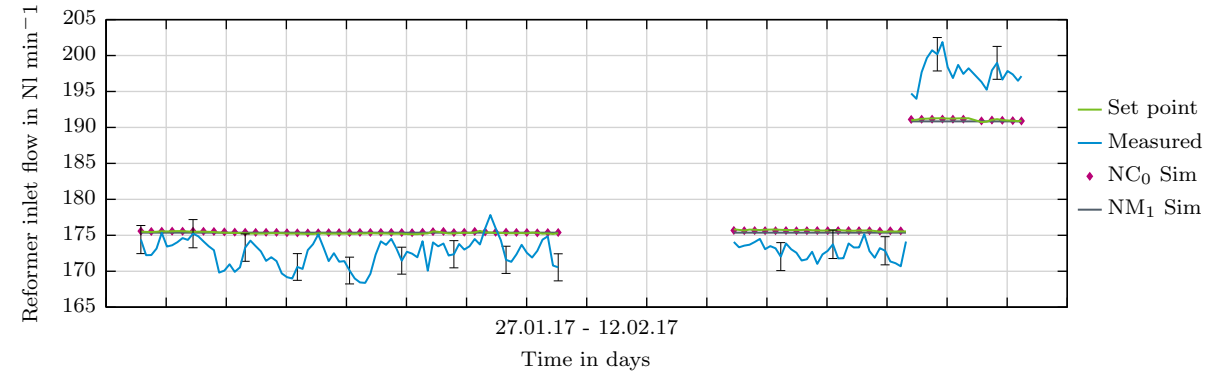

(d) Volume flow rate at reformer inlet

Figure 5.14: Experimental results of NC$_0$ - Comparison of set point values, simulated outputs and measurement based calculated values

As displayed in Figures 5.14c and 5.14d, the main difference between the NC_0 and NM_1 is the adjustment of the mass flow rate set point of natural gas, which has a tremendous effect on the related characteristic system parameters and performance of the system. The volume flow rates at the reformer inlet only marginally differ from the defined reference values, since the K_{e^-} and $K_{\triangle an}$ averages during the NC_0 testing period are similar to the reference values. The measured mass and volume flow rates are in overall good agreement with the corresponding set points and simulated values, verifying the correct implementation of the NC_0 into the control logic and validating the derived analytical set of equations in section 5.2.

5.5.2.3 Mole fractions at reformer inlet, reformer outlet and anode outlet

Analogous to section 4.4.3.3, the comparison of the measured and calculated NC_0 equilibrium mole fractions at the reformer inlet, reformer outlet and anode outlet are outlined in Figure 5.15. The agreement between the calculated equilibrium mole fractions and the measured data are strong, due to 95 % of the corresponding absolute deviations ranging between approximately -0.004 and +0.007. Consequently, the simulation methodology, derived analytical set of equations and correct implementation into the control logic are further validated for the NC_0.

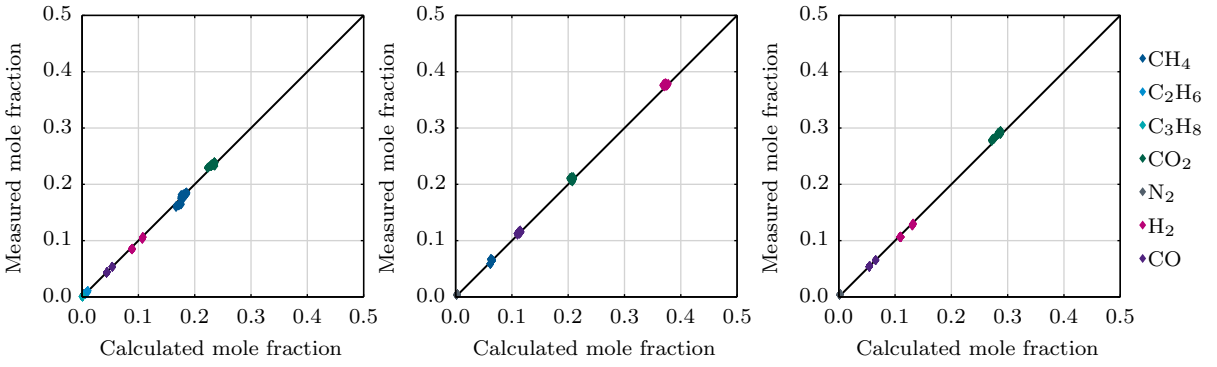

(a) Reformer inlet (b) Reformer outlet (c) Anode outlet

Figure 5.15: Experimental results of NC_0 - Comparison of measured and calculated equilibrium gas composition with NC_0

5.5.2.4 Conclusions

The experimental evaluation of the SOFC test rig data operated with natural gas using the NC_0 highlights the following major conclusions:

1. The NC_0 was successfully implemented into the control logic and the measured states were reproduced with the modeling approach.
2. The previously derived MFC set point scaling logic was further validated, due to the accurate realization of the natural gas mass flow rate set points.
3. The strong agreement between the calculated and measured compositions at the reformer inlet, reformer outlet and anode outlet validates the NC_0 modeling approach.
4. The occurring intrinsic error does not obstruct the reproduction of the system states using the simulation.
5. The measured deviations of $U_{f,S}$ and Φ from the designated set points are low, ultimately reducing the risk of irreversible stack damage and carbon deposition. The advantages of the NC_0 are very prominent compared to the NM_1.

6 Conclusion and outlook

In summary, this dissertation outlined the effects of fluctuating natural gas quality on anode exhaust gas recirculation (AEGR) solid oxide fuel cell (SOFC) systems by implementing and testing two control approaches in a test rig, as well as reproducing and validating the measured results in a black box system model. This work highlighted that an AEGR SOFC system can be advantageously operated with natural gas using an advanced control scheme, which is reactive to the current natural gas state, achieving a good realization of the fuel utilization factor of the stack ($U_{\mathrm{f,S}}$) and oxygen-to-carbon ratio (Φ) set points. Therefore, the risks of carbon deposition, partial depletion of fuel inside the stack and harmful system conditions are limited.

In chapter 2, three different SOFC system approach options were compared. The AEGR option was chosen for further evaluation, due to the superior efficiency potential. For a constant voltage level and $U_{\mathrm{f,S}}$ of 0.75, the AEGR option achieved approximately 9 to 10 %-points higher gross electrical efficiencies than the external water supply approach. Additionally, the governing system equations of an AEGR SOFC system were outlined. The four main characteristic system parameters were Φ, $U_{\mathrm{f,S}}$, the recirculation ratio and the fuel utilization factor of the system. For a designated Φ and $U_{\mathrm{f,S}}$, as well as a known natural gas quality, the corresponding recirculation ratio and fuel utilization factor of the system can be uniquely determined and the related mass and molar flow rate balance can be distinctly solved. As a result, fluctuating natural gas quality imposes challenging environments for SOFC system control strategies relying on the predetermination of designated flow rate set points, using the analytic mass and molar flow rate balance. Without access to a natural gas quality determination, the designated Φ and $U_{\mathrm{f,S}}$ set points can not be ideally realized and vary in correspondence to the natural gas composition.

In chapter 3, the regulatory framework of natural gas and the natural gas quality fluctuations in Europe were outlined. Eight different temporally resolved natural gas data sets from seven countries, which provided approximately 35000 individual measurements, were compared. The analyzed data base comprised of only six major species: Methane, ethane, propane, butane, carbon dioxide and nitrogen, where the butane contents represented the sum of all higher hydrocarbons containing at least four carbon atoms. Methane and ethane contents were the most volatile fractions, having 95 % confidence domains from 86.5 to 97.5 % and 0.9 to 10.2 %, respectively. The propane, butane and carbon dioxide contents were very stable with a high density of values below approximately 2.0 %. Lastly, nitrogen contents displayed intermediate fluctuation domains with 95 % confidence regions of up to 3.5 %. As a result, it was outlined that the natural gas quality in Europe was highly volatile, having variable magnitudes in different locations. Nevertheless, except approximately 500 data points from one location, which had above average carbon dioxide contents, the entire data base fulfilled the German regulatory framework. Additionally, the data base covered a significant area of the permitted domain in Germany, providing the basis for the derivation and validation of general constraints. Even though none of the natural gas data sets included any hydrogen contents, hydrogen was further considered as a possible natural gas fraction, representing potential additions to the grid.

Five general natural gas coefficients were derived, which classified the amount of carbon, oxygen, hydrogen or nitrogen atoms or releasable electrons contained in the respective natural gas mixture. In correspondence to the governing system equations, the natural gas coefficients were used to exactly cluster different natural gas mixtures, which cause analogous SOFC system responses. The reoccurring coefficients in the governing system equations are the carbon (K_{C}), oxygen (K_{O}) and electron ($K_{\mathrm{e^-}}$) gas coefficients. The three coefficients had 95 % confidence domains from 1.01 to 1.16, 0.00 to 0.11 and 7.85 to 8.89, respectively. As a result, the gas coefficients provided a more feasible evaluation criteria, due to the replacement of all composition constraints in the governing equations. The gas coefficients were further used to derive interrelations between the natural gas coefficients and corresponding relations to other

natural gas properties. The electron coefficient was analytically expressed as a function of the higher heating value, where the linear dependency was validated using the natural gas data base. Additionally, two reoccurring coefficients in the governing system equations were the change in molar quantity coefficient ($K_{\triangle \mathrm{an}}$) and the oxygen-to-carbon ratio combined gas coefficient (K_{Φ}), which outlined distinct relations to K_{C} and K_{O} or Φ, K_{C} and K_{O}, respectively. Both coefficients were expressed as a regression function of $K_{\mathrm{e^-}}$, displaying sufficient accuracy. Consequently, the complete governing system equations were related to a single natural gas quality indicator, the electron coefficient or higher heating value, ultimately providing the basis for the development of advanced reactive control strategies.

In chapter 4, the designed control strategy for the AEGR SOFC test rig, with a rated nominal power output of 13 kW, was outlined. The control logic included: the adjustment of the fuel flow rate to match a designated power output while keeping the fuel utilization factor of the stack constant; the control of the recirculation gas flow rate to keep the oxygen-to-carbon ratio at a designated value; the adjustment of the total air flow rate and bypass air flow rate to control the cathode inlet temperature and stack temperature; and the control of the temperature at the recirculation gas blower inlet by providing sufficient cooling air in a heat exchanger upstream of the blower. The basic fuel control strategy during natural gas operation was denoted as the natural gas mass flow rate control scheme 1 ($\mathrm{NM_1}$). In the $\mathrm{NM_1}$, the natural gas mass flow rate and reformer inlet volume flow rate are kept constant in relation to a defined reference natural gas composition, as well as the three designated leading system set points, $U_{\mathrm{f,S}}$, Φ and the electric current. In parallel, an ideal control scheme ($\mathrm{IC_0}$) was introduced as the baseline for perfect system behavior.

Furthermore, a black box model was developed in MATLAB to evaluate the effect of varying natural gas quality on the characteristic parameters of an AEGR SOFC system for the designated control approach at atmospheric pressure. The model inputs were the three leading system set points, the number of cells inside the stack, the air utilization factor, the designated reference natural gas composition, the fluctuating natural gas data, as well as the equilibrium temperatures in the reformer and SOFC stack. The outputs of the model included the flow rates and gas compositions for both the $\mathrm{NM_1}$ and $\mathrm{IC_0}$ at nine specified system positions. The modeling methodology also included an inherent validation of the mass balance and species conservation.

The black box model was used to evaluate the effect of varying natural gas quality on the AEGR SOFC system at nominal operation using the eight different temporally resolved natural gas data sets. The set points of $U_{\mathrm{f,S}}$, Φ and the electric current at nominal operation were 0.75, 2 and 24 A, respectively. The corresponding approximated equilibrium temperatures in the reformer and stack were 600 and 810 °C. For each individual natural gas data set, the corresponding average was used as the reference natural gas composition. The evaluation in the model outlined that the application of the $\mathrm{NM_1}$ can result in high $U_{\mathrm{f,S}}$ and Φ deviations from the designated set points, whereas the $\mathrm{IC_0}$ yielded perfect system responses without any deviations. The corresponding 95 % confidence intervals of $U_{\mathrm{f,S}}$ and Φ in the $\mathrm{NM_1}$ ranged from 0.70 to 0.91 and from 1.90 to 2.26, respectively. Both large positive and negative deviations from the $U_{\mathrm{f,S}}$ and Φ set points are undesirable, due to lower system efficiencies or increasing risks of enhanced degradation and harmful conditions for system components. However, in the designated setup location of the SOFC test rig in Renningen, the predicted deviations of the characteristic parameters were barely tolerable based upon the data from 2013. The corresponding 95 % confidence intervals of $U_{\mathrm{f,S}}$ and Φ ranged from 0.71 to 0.78 and from 1.93 to 2.06, respectively. As a result, the $\mathrm{NM_1}$ was used as the basic control approach for experimental testing, due to the simplicity of the implementation in the control logic and the tolerable simulation results.

For the purpose of gas composition quantification, the SOFC test rig was equipped with a gas chromatography system (GC) connected to four system sampling positions. The discontinuous GC analysis allowed for a complete system state characterization every two hours. As a result,

the $U_{f,S}$ and Φ were indirectly measured based upon the GC quantification. Additionally, the measured natural gas composition and indirectly determined $U_{f,S}$ and Φ were used to analytically solve the complete SOFC system balance to compute the corresponding system flow rates. The indirectly measured $U_{f,S}$ and Φ, as well as the measurement based computed flow rates were used for a comparison with the modeling outputs for the quantified natural gas composition.

The SOFC test rig was operated with the $NM_{\mathbf{1}}$ using natural gas from the grid between October 2016 and February 2017 for 12 individual periods. For the application of the $NM_{\mathbf{1}}$, the Renningen 2013 data set average was used as the reference natural gas composition. Compared to the chosen reference state, the natural gas quality fluctuations were significant during the individual testing periods, due to K_C, K_O and K_{e^-} displaying deviations from -1.6 to 1.8 %, -69.4 to 89.9 % and -0.4 to 1.0 %, respectively. However, the outlined fluctuations did not exceed the expectations, due to the similarity to the Renningen 2013 data set.

The 2016 data portion outlined that the mass flow controller (MFC) did not keep the natural gas mass flow rate constant, due to the calibration of the MFC to pure methane. Consequently, the major basic constraint of the $NM_{\mathbf{1}}$ was not realized. The measured results were not reproducible with the black box system model and the measured $U_{f,S}$ and Φ significantly deviated from the simulated values. Consequently, the 2016 data portion was used to derive an MFC scaling logic. It was outlined that the ratio between the measurement based calculated natural gas mass flow rate and the specified methane MFC mass flow rate set point can be expressed as a linear function of the specific heat capacity ratio of methane and natural gas at the measured MFC inlet temperature. The linear correlation achieved a high accuracy with a coefficient of determination of approximately 0.98. The derived regression was used to correctly realize any given natural gas mass flow rate set point by scaling the MFC set point, using a multi gas analyzer to continuously determine the specific heat capacity of natural gas.

In 2017, the derived MFC scaling was implemented, providing a fulfillment of the basic constraint of the $NM_{\mathbf{1}}$. The characteristic system states and gas compositions at the reformer inlet, reformer outlet and anode outlet were accurately reproduced with the $NM_{\mathbf{1}}$ modeling approach. The agreement between the calculated and measured mole fractions was strong, due to 95 % of the corresponding absolute deviations ranging between approximately -0.006 and +0.009.

In the $NM_{\mathbf{1}}$ testing period, the measured $U_{f,S}$ fluctuated approximately between 0.68 to 0.76 at nominal operation. The corresponding measured Φ covered a domain from approximately 1.82 to 2.11. Consequently, during the $NM_{\mathbf{1}}$ testing period, the carbon deposition risk was temporarily too high, whereas the risk of stack damage, due to the partial depletion of fuel inside single cells, was low. In summary, the $NM_{\mathbf{1}}$ was successfully implemented and tested in the SOFC test rig. Additionally, the derived analytic equations of the $NM_{\mathbf{1}}$ and the modeling approach were validated and the derived MFC scaling logic was effectively tested, providing the basis for the accurate control of any given natural gas mass flow rate.

In chapter 5, 23 modified control scheme options were derived and compared to the $NM_{\mathbf{1}}$ and IC_0. Analogous to the $NM_{\mathbf{1}}$, 22 modified control schemes were defined by changing the related pair of controlled flow rate set points. The considered control positions included a mass or volume flow rate control at the natural gas inlet, inside the recirculation loop, at the reformer inlet, at the reformer outlet and at the anode outlet. Additionally, the recirculation ratio was considered controllable, using at least two separate control elements. The combination of two set points was used to characterize a control scheme. Consequently, basic and additional control scheme constraints were defined in relation to the designated reference natural gas state to derive analytic equations. Furthermore, an advanced control scheme option was designed, which relied on the quantification of K_{e^-} and the corresponding regression based estimation of $K_{\triangle an}$ and K_Φ to adjust the system flow rates in relation to the detected natural gas state.

In addition to the $NM_{\mathbf{1}}$ and IC_0, all 23 derived modified control scheme options were implemented in the modeling. The effects of fluctuating natural gas quality on the control schemes

were evaluated in the model using two natural gas data sets. In addition to the $U_{f,S}$ and Φ domains of each individual control scheme options at nominal operation, the robustness towards changing reference natural gas composition and hydrogen addition to the natural gas data base were evaluated. Furthermore, the implementation feasibility and projected costs were considered. Each of the six criteria were used to rate the control schemes on an arbitrary integer scale, between one and five. The rating intervals for the $U_{f,S}$, Φ, reference natural gas composition and hydrogen robustness were defined in relation to the corresponding deviation magnitudes and domain sensitivities. For the implementation feasibility and projected costs, the corresponding ratings were quantitatively justified according to technical specifications. The arithmetic averaging of the six defined ratings allowed for the comparison of all control scheme options.

The evaluation outlined that the natural gas electron coefficient control scheme (NC_0) was the only option that achieved a total rating above 4, with a score of 4.4 out of 5.0. In comparison, the $NM_{\mathbf{1}}$ reached a score of just 2.9 and therefore, was beneath the intermediate rated options. The NC_0 achieved flawless scores in the $U_{f,S}$ and Φ robustness, due to the marginal deviations of $U_{f,S}$ and Φ from the corresponding set points of less than 1 %. Additionally, the NC_0 reached a perfect score in the reference natural gas composition robustness, due to the independence from the reference natural gas composition. Furthermore, the NC_0 achieved a flawless score in the hydrogen robustness, due to negligible shifts of the $U_{f,S}$ and Φ domain averages by less than -0.1 %-points and approximately +0.02, respectively. The implementation feasibility and projected cost ratings of the NC_0 reached average scores of approximately 3, due to challenging implementation and high costs of a K_{e^-} detection unit. Nevertheless, the NC_0 outlined an overall superior performance and was chosen for experimental testing.

The NC_0 was implemented in the SOFC test rig control logic and experimentally tested in January and February 2017 for three separate periods. The major adjustment of the SOFC control logic was the implementation of the multi gas analyzer outputs to continuously determine K_{e^-}, as well as the corresponding regression based estimation of $K_{\triangle an}$ and K_{Φ}. Analogous to the $NM_{\mathbf{1}}$ testing period, the natural gas quality fluctuations during the NC_0 evaluation were significant, due to K_C, K_O and K_{e^-} displaying deviations from the Renningen 2013 averages between -1.5 to 1.6 %, -65.2 to 72.7 % and -0.2 to 0.7 %, respectively. In contrast to the $NM_{\mathbf{1}}$, the measured $U_{f,S}$ and Φ outlined stable progressions and were in good agreement with the respective set points and simulated values. The $U_{f,S}$ and Φ domains covered a spectrum from 0.754 to 0.763 and 1.97 to 2.03, whereas the $NM_{\mathbf{1}}$ simulated $U_{f,S}$ and Φ in the corresponding period ranged from 0.703 to 0.761 and 1.91 to 2.02. As a result, excessively low Φ values were successfully prevented by the implementation of the NC_0 and therefore, the risk of carbon formation was significantly decreased. The correct implementation of the NC_0 in the modeling environment was proven by the strong match between the calculated equilibrium mole fractions and the measured data, due to 95 % of the corresponding absolute deviations ranging between approximately -0.004 and +0.007. In summary, the NC_0 achieved a superior performance during natural gas quality fluctuations with stable $U_{f,S}$ progressions, due to the adjustment of the system flow rates in relation to the detected natural gas quality indicator.

Lastly, to extend and intensify the understanding of the fluctuating natural gas quality effects on SOFC systems, the following research activities should focus on:

- The evaluation of the dynamic behavior of SOFC systems in transient operating modes under the influence of fluctuating natural gas quality.
- The development and testing of cheap, small, accurate and low-maintenance natural gas quality detection units to effectively implement advanced SOFC control strategies in competitive products. The sensors should only have marginal drifts to prohibit a steady re-calibration in the field.

- The detailed physical modeling of natural gas grids to estimate the composition at the point of consumption using preexisting natural gas quality and flow rate measurements inside the natural gas grid, where the control of grid connected devices could be coupled to the simulated composition.
- The improvement of the flow rate determination using the characteristic compressor map modeling approach to increase the accuracy and applicability to a wider range of blowers.
- The development of cheap, small, accurate and low-maintenance sensor units to quantify the characteristic SOFC system parameters, for instance with an electrochemical based detection.
- The large-scale evaluation of SOFC system data to identify dependencies between fluctuating natural gas quality and corresponding system responses, ultimately allowing for improvements and adjustments of the derived control strategies or the indirect determination of characteristic SOFC system parameters.
- The evaluation of the effects of oxygen contents in natural gas on the governing system equations and control scheme options, including the determination of the corresponding robustness towards oxygen fractions.

6 Zusammenfassung und Ausblick

In dieser Dissertation wurde die Auswirkungen schwankender Erdgasqualität auf das Betriebsverhalten von oxidkeramischen Brennstoffzellensystemen (SOFC) mit Anodenabgasrezirkulation (AEGR) untersucht. Hierzu wurden zwei Betriebsstrategien in einem Versuchssystem implementiert und die aufgezeichneten experimentellen Daten mit Hilfe eines entwickelten 0D-Modells evaluiert und validiert. Als ein Hauptergebnis wurde gezeigt, dass ein SOFC-System mit AEGR vorteilhaft mit einer erweiterten Regelstrategie betrieben werden kann, welche auf die aktuelle Erdgasqualität reagiert. Folglich werden die Sollwerte des Stackbrennstoffnutzungsgrades ($U_{\mathrm{f,S}}$) und des Sauerstoff-zu-Kohlenstoff-Verhältnisses (Φ) zielgerichtet umgesetzt und somit die Verkokungsneigung und das Risiko der Brennstoffverarmung in einzelnen Zellen der Stacks reduziert, sowie das Erreichen schädlicher Betriebszustände limitiert.

In Kapitel 2 wurden drei unterschiedliche SOFC-Systemansätze verglichen, wobei die Variante mit AEGR aufgrund des herausragenden Effizienzpotentials als Basis für die nachfolgenden Bewertungen ausgewählt wurde. Im Vergleich zu einem System mit externer Wasserzufuhr erreicht die Variante mit AEGR eine um ungefähr 9 bis 10 Prozentpunkte höhere elektrische Bruttoeffizienz bei einem angenommenen konstanten Spannungsniveau und einem $U_{\mathrm{f,S}}$ von 0,75. Zusätzlich wurden die bestimmenden Systemgleichungen und Zusammenhänge für die Variante mit AEGR auf Basis vier charakteristischer Hauptparameter - dem Φ, dem $U_{\mathrm{f,S}}$, der Rezirkulationsrate und dem Systembrennstoffnutzungsgrad - beschrieben. Hierbei können die Rezirkulationsrate und der Systembrennstoffnutzungsgrad für gegebene Φ, $U_{\mathrm{f,S}}$ und bekannte Gasqualitäten eindeutig bestimmt werden, sowie die verknüpfte Massen- und Stoffbilanz exakt gelöst werden. Deshalb führt eine schwankende Erdgasqualität bei Regelstrategien, welche auf der Bestimmung von Durchflusssollwerten durch Lösung der analytischen Massen- und Stoffbilanz beruhen, zu herausfordernden Betriebsphasen, da die Sollwerte des Φ und $U_{\mathrm{f,S}}$ ohne eine kontinuierliche Erdgasqualitätsanalyse nicht ideal umgesetzt werden und folglich in Abhängigkeit von der momentanen Erdgaszusammensetzung schwanken.

In Kapitel 3 wurden aktuelle regulatorische und gesetzliche Rahmenbedingungen für Erdgas vorgestellt, sowie eine Bewertung der schwankenden Erdgasqualität in Europa anhand des Vergleichs von acht zeitlich aufgelösten Erdgasdatensätzen aus sieben Ländern mit einer Gesamtanzahl von ungefähr 35000 einzelnen Erdgasanalysen durchgeführt. Die evaluierten Datensätze enthielten jeweils nur sechs Hauptkomponenten: Methan, Ethan, Propan, Butan, Kohlenstoffdioxid und Stickstoff, wobei die Butananteile die Summe aller höherwertigen Kohlenwasserstoffe mit mindestens vier gebunden Kohlenstoffatomen repräsentierten. Methan und Ethan waren die volatilsten Komponenten mit Schwankungsbreiten der zugehörigen 95 % Konfidenzintervalle zwischen 86,5 und 97,5 % sowie 0,9 und 10,2 %. Hingegen waren die Propan-, Butan- und Kohlenstoffdioxidanteile sehr stabil mit einer großen Datendichte unterhalb von ungefähr 2,0 %, während die obere 95 % Konfidenzintervallgrenze von Stickstoff einen Wert von bis zu 3,5 % erreichte und folglich eine mittelmäßige Schwankung indizierte. Zusammenfassend wurde durch den Vergleich herausgestellt, dass die Erdgasqualität im Betrachtungszeitraum in Europa äußerst volatil war und unterschiedliche Größenordnungen in verschiedenen Standorten erreichte. Dennoch erfüllten nahezu alle 35000 Erdgasanalysen die regulatorischen Rahmenbedingungen in Deutschland, wobei lediglich rund 500 Datenpunkte eines Standortes mit überdurchschnittlicher Kohlenstoffdioxidkonzentration die Grenzwerte überschritten. Außerdem deckten die Erdgasdatensätze einen signifikanten Bereich des zulässigen Erdgasspektrums in Deutschland ab und konnten somit als Basis für die Herleitung und Validierung von allgemeinen Zusammenhängen verwendet werden. Wasserstoff wurde zwar nicht als Hauptbestandteil der Erdgaszusammensetzung in Europa identifiziert, dennoch wurde er im Rahmen einer möglichen zukünftigen Einspeisung ins Erdgasnetz in dieser Dissertation als Erdgasbestandteil angesehen.

Aus den Erdgashauptkomponenten wurden fünf allgemeine Gaskoeffizienten abgeleitet, welche die Anzahl an Kohlenstoff-, Sauerstoff-, Wasserstoff- und Stickstoffatomen sowie die Anzahl der elektrochemisch freisetzbaren Elektronen in der zugehörigen Erdgasmischung beschreiben. In Bezug auf die bestimmenden Systemgleichungen wurden die Gaskoeffizienten eingeführt, um Erdgasmischungen, welche ein analoges SOFC-Systemverhalten hervorrufen, zu gruppieren. Die wiederkehrenden Gaskoeffizienten sind der Kohlenstoff- (K_{C}), Sauerstoff- (K_{O}) und Elektronengaskoeffizient (K_{e^-}), wobei sich die Schwankungsbreiten der jeweiligen 95 % Konfidenzintervalle zwischen 1,01 und 1,16, 0,00 und 0,11 und 7,85 und 8,89 erstreckten. Durch die Einführung der Gaskoeffizienten wurden die Erdgaskonzentrationsterme in den bestimmenden Systemgleichungen vorteilhaft ersetzt und dadurch die Vergleichbarkeit und Bewertungsgrundlage verbessert. Darüber hinaus wurden Wechselbeziehungen zwischen den Gaskoeffizienten sowie Abhängigkeiten zu weiteren Erdgaseigenschaften abgeleitet. Folglich konnte der Elektronengaskoeffizient als eine analytische Funktion des Brennwertes dargestellt werden, wobei die lineare Abhängigkeit mit Hilfe der Erdgasdatenbasis validiert wurde. Als zwei weitere wiederkehrende Koeffizienten in den bestimmenden Systemgleichungen wurden der molare Veränderungskoeffizient ($K_{\triangle\mathrm{an}}$) und der Sauerstoff-zu-Kohlenstoff-Verhältnis abhängige verknüpfte Gaskoeffizient (K_{Φ}) abgeleitet, wobei beide Koeffizienten eine direkte Abhängigkeit vom K_{C} und K_{O} oder vom K_{C}, K_{O} und Φ aufwiesen. Ebenfalls konnten beide Koeffizienten durch eine Regressionsfunktion basierend auf dem Elektronengaskoeffizient mit ausreichender Genauigkeit beschrieben werden. Folglich wurde die Abhängigkeiten der bestimmenden Systemgleichungen auf nur einen Erdgasqualitätsindikator, den Elektronengaskoeffizient oder den Brennwert, reduziert und somit die Basis für die Entwicklung von anwendbaren, adaptiven Betriebsstrategien gelegt.

In Kapitel 4 wurde die Betriebsstrategie für das SOFC-Versuchssystem mit AEGR mit einer Nennleistung von 13 kW beschrieben. Das Regelungsprinzip basierte auf der Anpassung des Brennstoffdurchflusses, um eine gegebene Leistungsanforderung bei konstantem Stackbrennstoffnutzungsgrad zu bedienen; der Regelung der Rezirkulationsmenge zur Gewährleistung eines festgelegten Sauerstoff-zu-Kohlenstoff-Verhältnisses; der Einstellung des Haupt- und Bypassluftvolumenstroms zur Regelung der Kathodeneintritts- und Stacktemperatur; und der Anpassung

des Luftvolumenstroms zur Regelung der Rezirkulationsgebläseeintrittstemperatur durch Kühlung des Rezirkulationsgases in einem Wärmeübertrager stromaufwärts des Gebläses. In der Basiserdgasbetriebsstrategie, als Erdgasmassendurchflussregelungsschema 1 (NM_1) bezeichnet, wurde der Erdgasmassendurchfluss und der Reformereintrittsvolumenstrom in Bezug zu einer festgelegten Erdgasreferenzkonzentration und den drei führenden Systemsollwerten - $U_{f,S}$, Φ und dem elektrischen Strom - konstant gehalten. Darüber hinaus wurde parallel ein ideales Erdgasregelungsschema (IC_0) als konzeptioneller Basisvergleich für perfektes Systemverhalten eingeführt.

Zusätzlich wurde zur Evaluierung der Auswirkung schwankender Erdgaszusammensetzung auf die charakteristischen Parameter eines atmosphärischen SOFC-Systems mit AEGR mit einer ausgewählten Betriebsstrategie ein 0D-Model in MATLAB entwickelt. Als Modelleingangsgrößen dienten die drei führenden Systemsollwerte, die Zellzahl im Stack, der Luftnutzungsgrad, die festgelegte Erdgasreferenzkonzentration, ein fluktuierender Erdgasdatensatz, sowie die Gleichgewichtstemperaturen im Reformer und SOFC-Stack. Die Modellausgangsgrößen umfassten die Durchflüsse und Zusammensetzungen an neun festgelegten Systempositionen für das NM_1 und IC_0. Außerdem wurde in der Modellmethodik eine inhärente Validierung der Massen- und Stoffbilanzen hinterlegt.

Die Modellumgebung wurde weiter verwendet, um die Auswirkungen schwankender Erdgasqualität auf das nominale Betriebsverhalten des SOFC-Systems mit AEGR anhand der acht zeitlich aufgelösten Erdgasdatensätze zu bewerten. Die zugehörigen Systemsollwerte für den $U_{f,S}$, das Φ und den elektrischen Strom am nominalen Betriebspunkt waren 0,75, 2 und 24 A, wobei die Gleichgewichtstemperaturen im Reformer und Stack mit 600 und 810 °C abgeschätzt wurden. Die Erdgasreferenzkonzentration wurde für jeden der acht Erdgasdatensätze individuell aus dem jeweiligen Mittelwert bestimmt. Die Bewertung zeigte, dass der Einsatz des NM_1 zu hohen $U_{f,S}$ und Φ Sollwertabweichungen führte, während das IC_0 perfekt auf die Erdgasqualitätsschwankungen reagierte und eine ideale Systemantwort ohne Sollwertabweichungen realisierte. Im NM_1 erstreckten sich die Schwankungsbreiten der jeweiligen 95 % Konfidenzintervalle des $U_{f,S}$ und Φ zwischen 0,70 und 0,91 sowie 1,90 und 2,26. Sowohl hohe positive als auch negative Sollwertabweichungen des $U_{f,S}$ und Φ sind unerwünscht, da möglicherweise die Systemeffizienz verringert, die Degradation beschleunigt und das Risiko, schädliche Betriebszustände zu erreichen, gesteigert werden kann. Dennoch zeigte die Bewertung des Erdgasdatensatzes aus Renningen aus dem Jahr 2013, dass die vorhergesagten $U_{f,S}$ und Φ Sollwertabweichungen am Versuchssystemstandort gerade noch tolerierbar waren, da sich die Schwankungsbreiten der jeweiligen 95 % Konfidenzintervalle des $U_{f,S}$ und Φ nur zwischen 0,71 und 0,78 sowie 1,93 und 2,06 erstreckten. Folglich wurde das NM_1 aufgrund seiner einfachen Implementierbarkeit in die Regelungslogik und der erzielten tolerierbaren Modellergebnisse als Basiserdgasbetriebsstrategie im Versuchssystem eingesetzt.

Darüber hinaus wurde das SOFC-Versuchssystem mit einem Gaschromatographen verbunden, um die Zusammensetzung an vier Systempositionen zu quantifizieren. Die diskontinuierlichen Gasanalysen ermöglichten eine vollständige Systemcharakterisierung in einer Zykluszeit von zwei Stunden, wobei der $U_{f,S}$ und das Φ indirekt aus der Quantifizierung bestimmt werden konnten. Die zugehörigen Systemdurchflüsse wurden anschließend durch Lösen der analytischen Systembilanzen basierend auf den indirekt gemessenen $U_{f,S}$ und Φ, sowie den direkten Analysen der Erdgaszusammensetzung bestimmt. Die errechneten Systemdurchflüsse und die indirekt bestimmten charakteristischen Parameter, der $U_{f,S}$ und das Φ, wurden zur Validierung mit den Modellausgangsgrößen, welche basierend auf den nominalen Systemsollwerten und gemessenen Erdgaskonzentrationen berechnet wurden, verglichen.

Das NM_1 wurde zwischen Oktober 2016 und Februar 2017 in 12 individuellen Zeitabschnitten am SOFC-Versuchssystem im Erdgasbetrieb getestet, wobei zur Implementierung des NM_1 der Mittelwert des Erdgasdatensatzes von Renningen 2013 als Referenzerdgaskonzentration ver-

wendet wurde. Im Vergleich zum gewählten Referenzzustand waren die Erdgasqualitätsschwankungen im Versuchszeitraum signifikant, da die K_{C}, K_{O} und $K_{\mathrm{e^-}}$ von -1,6 bis 1,8 %, -69,4 bis 89,9 % und -0,4 bis 1,0 % von der Referenz abwichen. Dennoch wurden die Annahmen über die auftretenden Erdgasqualitätsschwankungen nur geringfügig überschritten, da das erfasste Erdgasspektrum eine hohe Ähnlichkeit zum Renningen 2013 Erdgasdatensatz aufwies.

Die Analyse der im Jahr 2016 aufgezeichneten experimentellen Daten zeigte, dass der Massendurchflussregler (MFC), hingegen den zuvor getroffenen Annahmen, den Massendurchfluss an Erdgas nicht konstant einstellte, da die werksseitige Kalibrierung mit reinem Methan durchgeführt wurde. Folglich wurde ein Grundkriterium des NM_1 nicht korrekt umgesetzt und die experimentellen Daten konnten nicht in der Modellumgebung reproduziert werden. Die Abweichungen zwischen den indirekt gemessenen und berechneten $U_{\mathrm{f,S}}$ und Φ waren demnach hoch. Deshalb wurde basierend auf den aufgezeichneten experimentellen Daten eine MFC-Skalierung abgeleitet, wobei gezeigt wurde, dass das Verhältnis aus dem auf Basis von Messdaten bestimmten Erdgasmassendurchfluss und dem MFC-Massendurchflusssollwert als lineare Funktion des spezifischen Wärmekapazitätsverhältnisses zwischen Methan und Erdgas bei der gemessenen MFC-Eintrittstemperatur ausgedrückt werden kann. Die lineare Korrelation erreichte eine sehr hohe Genauigkeit mit einem Bestimmtheitsmaß von ungefähr 0,98. Anschließend wurde die spezifische Wärmekapazität des Erdgases kontinuierlich mit einem Multigasanalysator erfasst, um den Erdgasmassendurchfluss durch Skalierung des MFC-Sollwertes basierend auf der abgeleiteten linearen Korrelation eindeutig umzusetzen.

Im anschließenden Messzeitraum wurden durch den Einsatz der MFC-Skalierung beide Grundkriterien des NM_1 erfüllt und die charakteristischen Systemparameter und Gaszusammensetzungen am Reformereintritt, Reformer- und Anodenaustritt konnten mit Hilfe der Modellumgebung reproduziert werden. Hierbei waren die Übereinstimmungen zwischen den berechneten und gemessenen Gaszusammensetzungen besonders hoch, denn 95 % der zugehörigen absoluten Abweichungen schwankten lediglich zwischen -0,006 und +0,009.

Während der gesamten NM_1-Testphase fluktuierten die indirekt gemessenen $U_{\mathrm{f,S}}$ und Φ in Domänen zwischen 0,68 und 0,76, sowie 1,82 und 2,11. Folglich war das Risiko der Bildung von Kohlenstoffablagerungen innerhalb der Testphase zeitweise sehr hoch, während das Brennstoffverarmungsrisiko in einzelnen Zellen der Stacks gering war. Somit lässt sich zusammenfassend festhalten, dass das NM_1 erfolgreich im Versuchssystem implementiert und getestet wurde. Zusätzlich konnten die analytisch abgeleiteten Gleichungen und Zusammenhänge des NM_1, sowie der Modellansatz validiert werden. Hierbei bildete die empirisch hergeleitete MFC-Skalierung den Grundstein für die effektive und genaue Umsetzung eines gewünschten Erdgasmassendurchflusses.

In Kapitel 5 wurden 23 weitere Regelungsschemas abgeleitet und mit dem NM_1 und IC_0 verglichen. In Analogie zum NM_1 wurden 22 Regelungsschemas durch die Veränderung der zugehörigen geregelten Durchflusspaare bestimmt, wobei die betrachteten Stellpositionen die Massen- oder Volumendurchflüsse am Erdgaseintritt, im Rezirkulationskreis, am Reformereintritt, sowie am Reformer- und Anodenaustritt umfassten. Zusätzlich wurde die Rezirkulationsrate durch den Einsatz von zwei separaten Stellelementen als regelbar eingestuft. Abschließend wurde die Kombination aus jeweils zwei Regelelementen verwendet, um ein neues Regelungsschema zu charakterisieren. Die resultierenden Grundkriterien jedes Regelungsschemas wurden verwendet, um die jeweiligen analytische Gleichungen unter Verwendung des zugehörigen Referenzfalles abzuleiten. Zusätzlich wurde ein adaptives Regelungsschema entwickelt, welches eine Quantifizierung des Elektronenkoeffizienten und die zugehörige regressionsbasierte Abschätzung von $K_{\triangle\mathrm{an}}$ und K_{Φ} nutzte, um die Systemdurchflüsse kontinuierlich und zielgerichtet an die detektierte Erdgasqualität anzupassen.

Die Modellumgebung wurde zusätzlich zum NM_1 und IC_0 um die 23 entwickelten Regelungsschemas erweitert und die Auswirkungen schwankender Erdgasqualität wurde anhand von zwei

ausgewählten Erdgasdatensätzen bewertet. Neben den resultierenden Domänen des $U_{f,S}$ und Φ wurden auch die Robustheit gegenüber einer geänderten Erdgasreferenzkonzentration und die zusätzliche Netzeinspeisung von Wasserstoff für alle Regelungsschemas am nominalen Betriebspunkt als Vergleichskriterien verwendet. Darüber hinaus wurden zusätzlich die Implementierbarkeit und die projizierten Kosten bewertet. Jedes der sechs Einzelkriterien wurde für das jeweilige Regelungsschema basierend auf einer festgelegten Skala mit Werten zwischen eins und fünf benotet. Hierbei wurden die Bewertungsintervalle für die Robustheit des $U_{f,S}$ und Φ, sowie gegenüber der geänderten Referenzgaskonzentration und der Wasserstoffeinspeisung in Relation zu den auftretenden Größenordnungen der absoluten Abweichungen und Sensitivitäten der Domänen festgelegt. Für die Implementierbarkeit und projizierten Kosten wurden die erzielten Bewertungen mit Hilfe von technischen Spezifikationen quantitativ begründet. Die Bildung des arithmetischen Mittelwertes der sechs Einzelkriterien ermöglichte einen intuitiven Gesamtvergleich aller Regelungsschemas.

Der Gesamtvergleich zeigte, dass lediglich eine einzige Option, das adaptive Regelungsschema, eine Gesamtbewertung höher als 4 erreichte. Hierbei erzielte das so bezeichnete Erdgaselektronenkoeffizientenregelungsschema (NC_0) mit einer Gesamtbewertung von 4,4 aus möglichen 5,0 die beste Benotung. Das NM_1 erreichte lediglich eine Gesamtbewertung von 2,9 und reihte sich somit sogar unterhalb des mittleren Notendurchschnitts ein. Das NC_0 erhielt makellose Bewertungen in der Robustheit des $U_{f,S}$ und Φ, da die zugehörigen Domänen jeweils weniger als 1 % von den festgelegten Sollwerten abwichen. Zusätzlich war das NC_0 unabhängig von der Veränderung der Referenzgaskonzentration und das NC_0 erzielte in diesem Kriterium ebenfalls eine makellose Bewertung. Die Einspeisung von Wasserstoff führte beim NC_0 lediglich zu vernachlässigbaren Verschiebungen der Mittelwerte der $U_{f,S}$ und Φ Domänen im Bereich von weniger als -0,1 Prozentpunkten und +0,02. Somit wurde auch die Robustheit gegenüber Wasserstoffeinspeisung mit einer Note von 5,0 bewertet. Hingegen erreichte das NC_0 bei der Implementierbarkeit und den projizierten Kosten lediglich mittlere Bewertungen von ungefähr 3, da der Installationsaufwand und die Kosten für einen kontinuierlichen Erdgasanalysator als hoch eingeschätzt wurden. Trotzdem erzielte das NC_0 herausragende Ergebnisse und wurde für eine nachfolgende Implementierung und experimentelle Untersuchung im SOFC-Versuchssystem ausgewählt.

Das NC_0 wurde im Januar und Februar 2017 in 3 individuellen Zeitabschnitten am SOFC-Versuchssystem im Erdgasbetrieb getestet. Die Hauptanpassungen in der Regelungslogik bestanden aus der zielgerichteten Verwendung der Ausgangsgrößen des Multigasanalysators zur Bestimmung des Elektronenkoeffizienten und die zugehörige regressionsbasierte Abschätzung von $K_{\triangle an}$ und K_Φ. Die Erdgasqualitätsschwankungen im Versuchszeitraum erreichten ähnliche Größenordnungen wie während der NM_1-Testphase, da die K_C, K_O und K_{e^-} von -1,5 bis 1,6 %, -65,2 bis 72,7 % und -0,2 bis 0,7 % vom Mittelwert des Renningen 2013 Erdgasdatensatzes abwichen. Im Gegensatz zu den NM_1 Ergebnissen erreichten die indirekt gemessenen $U_{f,S}$ und Φ stabile Verläufe und hohe Übereinstimmungen mit den zugehören Sollwerten und simulierten Daten. Die indirekt gemessenen $U_{f,S}$ und Φ schwankten lediglich in Domänen zwischen 0,754 und 0,763 sowie 1,97 und 2,03, während die parallel modellierten Werte des NM_1 im Vergleichszeitraum zwischen 0,703 und 0,761 sowie 1,92 und 2,02 fluktuierten. Folglich wurden das Risiko der Bildung von Kohlenstoffablagerungen durch die Implementierung des NC_0 signifikant reduziert, da niedrige Φ-Werte erfolgreich verhindert wurden. Die richtige Umsetzung und Implementierung des NC_0 in der Modellumgebung wurde durch die hohen Übereinstimmungen zwischen den berechneten und gemessenen Gaszusammensetzungen validiert, wobei 95 % der zugehörigen absoluten Abweichungen lediglich zwischen -0,004 und +0,007 schwankten. Zusammenfassend führte die Implementierung des adaptiven NC_0 zu einem herausragenden Betriebsverhalten unter schwankender Erdgasqualität mit stabilen Verläufen der $U_{f,S}$ basierend auf der zielgerichteten Anpassung von Systemdurchflüssen durch die kontinuierliche Detektion des Elektronenkoeffizienten über einen Multigasanalysator.

Zur Erweiterung und Intensivierung des Verständnisses der Auswirkung schwankender Erdgasqualität auf SOFC-Systeme sollten anschließende Forschungsaktivitäten die nachfolgenden Themenfelder adressieren:

- Die Untersuchung des dynamischen Verhaltens von SOFC-Systemen in transienten Betriebsphasen unter dem Einfluss schwankender Erdgasqualität.
- Die Entwicklung und experimentelle Evaluierung von kostengünstigen, kleinen, präzisen und wartungsarmen Erdgasqualitätsdetektoren zur effektiven Implementierung von adaptiven SOFC-Betriebsstrategien in wettbewerbsfähigen Produkten. Die entwickelten Sensoren sollten hierbei nur minimale Drifts aufweisen, um eine Rekalibrierung im Feld zu vermeiden.
- Die detaillierte physikalische Modellierung von Erdgasnetzen zur Abschätzung der Erdgaszusammensetzung am Verbrauchspunkt basierend auf den bereits vorhandenen Erdgasqualitätsbestimmungen und Durchflussmessungen im Erdgasnetz, wobei die Betriebsstrategie von netzbetriebenen Geräten direkt mit der simulierten Erdgaskonzentration gekoppelt werden könnte.
- Die Verbesserung der modellbasierten Ermittlung von Volumenströmen auf Basis charakteristischer Kompressorkennfelder zur Erhöhung der Genauigkeit sowie zur Erweiterung der Anwendbarkeit auf eine Vielzahl von Gebläsen.
- Die Entwicklung und experimentelle Evaluierung von kostengünstigen, kleinen, präzisen und wartungsarmen Sensor zur Bestimmung charakteristischer SOFC-Systemparameter, beispielsweise mit Hilfe elektrochemischer Sensorik.
- Die großflächige Analyse von SOFC-Systemdaten zur Identifizierung von Abhängigkeiten zwischen schwankender Erdgasqualität und den zugehörigen Systemantworten, welche eine Verbesserung und Anpassung von bereits vorhandenen Betriebsstrategien oder die indirekte Bestimmung charakteristischer SOFC-Systemparameter ermöglichen könnten.
- Die Evaluierung des Einflusses von Sauerstoffanteilen im Erdgas auf die bestimmenden Systemgleichungen und Regelungsschemas, sowie die Bewertung der Robustheit gegenüber Sauerstoffanteilen.

Literaturverzeichnis

[1] United Nations: *Paris Agreement - Status of Ratification*, Accessed in July 2017. URL: *http://unfccc.int/paris_agreement/items/9444.php*

[2] United Nations: *Paris Agreement*, United Nations, 2015.

[3] Federal Ministry for the Environment, Nature Conservation, Building and Nuclear Safety (BMUB): *Climate Action in Figures 2017 - Facts, Trends and Incentives for German Climate Policy*, BMUB, 2017.

[4] International Energy Agency (IEA): *World Energy Outlook 2016 - Executive Summary*, IEA Publications, 2016.

[5] U.S. Energy Information Administration (EIA): *International Energy Outlook 2016 - With Projections to 2040*, EIA, 2016.

[6] BP p.l.c: *BP Energy Outlook - 2017 Edition*, BP p.l.c, 2017.

[7] T. K. Ghosh, M. A. Prelas: *Energy Resources and Systems - Volume 1: Fundamentals and Non-Renewable Resources*, Springer Netherlands, 2009. ISBN: 978–90–481–2382–7

[8] J. Larminie, A. Dicks: *Fuel Cell Systems Explained.* 2nd Edition, John Wiley & Sons Ltd., 2003. ISBN: 978–0–470–84857–9

[9] J. A. Kent: *Handbook of Industrial Chemistry and Biotechnology.* 12th Edition, Vol. 1, Springer US, 2012. ISBN: 978–1–4614–4258–5

[10] R. van Basshuysen: *Natural Gas and Renewable Methane for Powertrains - Future Strategies for a Climate-Neutral Mobility*, Springer International Publishing, 2016. ISBN: 978–3–319–23224–9

[11] DIN Deutsches Institut für Normung e. V.: *DIN EN 16726 - Gas infrastructure - Quality of gas - Group H*, Beuth Verlag GmbH, 2016.

[12] S. J. McPhail, V. Cigolotti, A. Moreno: *Fuel Cells in the Waste-to-Energy Chain: Distributed Generation Through Non-Conventional Fuels and Fuel Cells.* 1st Edition, Springer-Verlag London, 2012. ISBN: 978–1–4614–4258–5

[13] A. Demirbas: *Biofuels: Securing the Planet's Future Energy Needs*, Springer-Verlag London, 2009. ISBN: 978–1–84882–010–4

[14] W. Osterhage: *Die Energiewende: Potenziale bei der Energiegewinnung*, Springer Fachmedien Wiesbaden, 2015. ISBN: 978–3–658–10244–9

[15] H. Watter: *Regenerative Energiesysteme: Grundlagen, Systemtechnik und Analysen ausgeführter Beispiele nachhaltiger Energiesysteme*, Springer Fachmedien Wiesbaden, 2015. ISBN: 978–3–658–09637–3

[16] A. Wellinger, J. D. Murphy, D. Baxter: *The Biogas Handbook: Science, Production and Applications*, Elsevier Science, 2013. ISBN: 978–0–857–09498–8

[17] A. Demirbas: *Biohydrogen: For Future Engine Fuel Demands*, Springer-Verlag London, 2009. ISBN: 978–1–84882–510–9

[18] M. Lehner, R. Tichler, H. Steinmüller, M. Koppe: *Power-to-Gas: Technology and Business Models.* 1st Edition, Springer International Publishing, 2014. ISBN: 978–3–319–03994–7

[19] H. Krause, M. Werschy, S. Franke, A. Giese, J. Benthin, H. Dörr: *Untersuchungen der Auswirkungen von Gasbeschaffenheitsänderungen auf industrielle und gewerbliche Anwendungen*, DVGW Deutscher Verein des Gas- und Wasserfaches e.V., 2014.

[20] K. Kendall, M. Kendall: *High-temperature Solid Oxide Fuel Cells for the 21st Century: Fundamentals, Design and Applications.* 2nd Edition, Elsevier Science, 2016. ISBN: 978–0–12–410453–2

[21] K. Huang, J. B. Goodenough: *Solid Oxide Fuel Cell Technology: Principles, Performance and Operations*, Elsevier Science, 2009. ISBN: 978–1–8456–9628–3

[22] J. T. Irvine, P. Connor: *Solid Oxide Fuels Cells: Facts and Figures*. 1st Edition, Springer-Verlag London, 2013. ISBN: 978–1–4471–4456–4

[23] J. Milewski, K. Swirski, M. Santarelli, P. Leone: *Advanced Methods of Solid Oxide Fuel Cell Modeling*. 1st Edition, Springer-Verlag London, 2011. ISBN: 978–0–85729–261–2

[24] M. Boaro, A. A. Salvatore: *Advances in Medium and High Temperature Solid Oxide Fuel Cell Technology*. 1st Edition, Springer International Publishing, 2017. ISBN: 978–3–319–46145–8

[25] S. Wahl: *Verfahrenstechnische Optimierung und Leistungsskalierung eines Festoxid-Brennstoffzellensystems mit Hilfe multiphysikalischer Modellierung und experimenteller Daten*, Verlag Dr. Hut, 2015. ISBN: 978–3–8439–2371–2

[26] M. Hering: *Untersuchung der Skalierbarkeit von SOFC-Systemen durch die Verschaltung von Brennstoffzellenstacks bei Kraft-Wärme-Kopplungsanlagen*, Hochschule Ulm, 2013.

[27] M. Carré, R. Brandenburger, W. Friede, F. Lapicque, U. Limbeck, P. da Silva: *Feed-forward control of a solid oxide fuel cell system with anode offgas recycle*, Journal of Power Sources 282 (2015) 498 – 510. ISSN: 0378–7753
URL: *http://www.sciencedirect.com/science/article/pii/S0378775315002761*

[28] A. Gallet Segarra: *Robust Control of a Solid Oxide Fuel Cell for Combined Heat and Power Applications*, University Stuttgart, 2017.

[29] M. Carré: *Modeling and control of a solid oxide fuel cell system with anode offgas recycle for residential combined heat and power generation*, Der Andere Verlag, 2012. ISBN: 978–3–86247–255–0

[30] S. C. Singhal, K. Kendall: *High Temperature and Solid Oxide Fuel Cells: Fundamentals, Design and Applications*. 1st Edition, Elsevier Science, 2003. ISBN: 978–1–85617–387–2

[31] DVGW Deutscher Verein des Gas- und Wasserfaches e.V.: *Technische Regel - Arbeitsblatt DVGW G 260 - Gasbeschaffenheit*, DVGW e.V., 2013.

[32] Bosch Thermotechnologie SAS: *Natural gas composition data set of Saint-Thegonnec in France for January to December 2014*. Internal communications with Bosch Thermotechnologie SAS regarding natural gas measurements in Saint-Thegonnec, 2015.

[33] REN - Redes Energéticas Nacionais, SGPS, S.A.: *Natural Gas Quality - Gas year 2014 - 2016*, Accessed in July 2016.
URL: *https://www.ign.ren.pt/en/monitorizacao-da-qualidade-do-gn?p_p_id=listAllocationYear_WAR_renatrportlet&p_p_lifecycle=0&_listAllocationYear_WAR_renatrportlet_implicitModel=true*

[34] EnBW Energie Baden-Württemberg AG: *Gasanalysen des Gasjahres 2013 - Standort Renningen*, 2013.

[35] Energinet.dk: *Hourly natural gas composition data set of Egtved in Denmark for January to December 2014*. Internal communications with Energinet.dk's Senior Systems Analyst Jesper Bruun regarding natural gas measurements in Denmark, 2015.

[36] Fluxys Belgium NV/SA: *Hourly natural gas composition data set of Gent area in Belgium for January 2014*. Internal communications with Fluxys Belgium NV/SA Key Account Manager Eric Van Gysel regarding natural gas measurements in Belgium, 2015.

[37] Gasum Oy: *Gas composition at Imatra, historical data at daily level*, Accessed in July 2016.
URL: *http://www.gasum.com/transmission-portal/Finlands-gas-network/Gas-composition/imatra-daily-values/*

[38] FGSZ Ltd.: *Hourly natural gas composition data set of Hungary for January to December 2014*. Internal communications with FGSZ's Head of Metrology József Balla regarding natural gas measurements in Hungary, 2015.

[39] DIN Deutsches Institut für Normung e. V.: *DIN EN 437 - Test gases - Test pressures - Appliance categories*, Beuth Verlag GmbH, 2009.

[40] S. C. Bhattacharyya: *Energy Economics - Concepts, Issues, Markets and Governance*, Springer London, 2011. ISBN: 978–0–85729–267–4

[41] D. Papurello, A. Lanzini, S. Fiorilli, F. Smeacetto, R. Singh, M. Santarelli: *Sulfur poisoning in Ni-anode solid oxide fuel cells (SOFCs): Deactivation in single cells and a stack*, Chemical Engineering Journal 283 (2016) 1224 – 1233. ISSN: 1385–8947
URL: *http://www.sciencedirect.com/science/article/pii/S1385894715011730*

[42] G. Nurk, T. Huthwelker, A. Braun, C. Ludwig, E. Lust, R. Struis: *Redox dynamics of sulphur with Ni/GDC anode during SOFC operation at mid- and low-range temperatures: An operando S K-edge XANES study*, Journal of Power Sources 240 (2013) 448 – 457. ISSN: 0378–7753
URL: *http://www.sciencedirect.com/science/article/pii/S0378775313006009*

[43] H. Madi, S. Diethelm, C. Ludwig, J. V. Herle: *Organic-sulfur poisoning of solid oxide fuel cell operated on bio-syngas*, International Journal of Hydrogen Energy 41 (28) (2016) 12231 – 12241. ISSN: 0360–3199
URL: *http://www.sciencedirect.com/science/article/pii/S0360319915302688*

[44] F. P. Nagel, T. J. Schildhauer, J. Sfeir, A. Schuler, S. M. Biollaz: *The impact of sulfur on the performance of a solid oxide fuel cell (SOFC) system operated with hydrocarboneous fuel gas*, Journal of Power Sources 189 (2) (2009) 1127 – 1131. ISSN: 0378–7753
URL: *http://www.sciencedirect.com/science/article/pii/S0378775308024713*

[45] W. Tan, H. Yan, D. Xu, Q. Zhong: *Electrochemical behaviors of Y-doped $La_{0.7}Sr_{0.3}CrO_{3-\delta}$ anode in sulfur-containing fuel SOFC*, International Journal of Hydrogen Energy 38 (36) (2013) 16552 – 16557. ISSN: 0360–3199
URL: *http://www.sciencedirect.com/science/article/pii/S0360319913020958*

[46] H. Chen, F. Wang, W. Wang, D. Chen, S.-D. Li, Z. Shao: *H_2S poisoning effect and ways to improve sulfur tolerance of nickel cermet anodes operating on carbonaceous fuels*, Applied Energy 179 (2016) 765 – 777. ISSN: 0306–2619
URL: *http://www.sciencedirect.com/science/article/pii/S0306261916309692*

[47] A. L. Vincent, J.-L. Luo, K. T. Chuang, A. R. Sanger: *Promotion of activation of CH_4 by H_2S in oxidation of sour gas over sulfur tolerant SOFC anode catalysts*, Applied Catalysis B: Environmental 106 (1 - 2) (2011) 114 – 122. ISSN: 0926–3373
URL: *http://www.sciencedirect.com/science/article/pii/S0926337311002220*

[48] F.-Y. Wang, G.-B. Zhong, S. Luo, L. Xia, L.-H. Fang, X. Song, X. Hao, G. Yan: *Porous $Sr_2MgMo_{1-x}V_xO_{6-d}$ ceramics as anode materials for SOFCs using biogas fuel*, Catalysis Communications 67 (2015) 108 – 111. ISSN: 1566–7367
URL: *http://www.sciencedirect.com/science/article/pii/S156673671500165X*

[49] DIN Deutsches Institut für Normung e. V.: *DIN EN ISO 6976 - Calculation of calorific values, density, relative density and Wobbe index from composition*, Beuth Verlag GmbH, 2005.

[50] Council of the European Union, European Parliament: *Regulation (EC) No 715/2009 of the European Parliament and of the Council of 13 July 2009 on conditions for access to the natural gas transmission networks and repealing Regulation (EC) No 1775/2005*, Official Journal of the European Union L211/36 (2009) 36 – 54.

[51] GRTgaz: *Part A2 - Technical Requirements applicable to GRTgaz's transmission pipelines and to gas transmission, distribution and storage installations connected to the GRTgaz network*, GRTgaz, 2011.

[52] Entidade Reguladora dos Serviços Energéticos (ERSE): *Regulamento da Qualidade de Serviço do Setor do Gás Natural*, ERSE, 2013.

[53] Agilent Technologies, Inc.: *Data sheet: Agilent 7890B Gas Chromatograph*, 2013.
URL: *http://www.agilent.com/cs/library/datasheets/public/5991-1436EN.pdf*

[54] Gasum Oy: *Finland's Gas Transmission Network*, Accessed in July 2016.
URL: *http://www.gasum.com/transmission-portal/Finlands-gas-network/*

[55] REN - Redes Energéticas Nacionais, SGPS, S.A.: *Information about LNG Terminal in Sines - Portugal*, Accessed in July 2016.
URL: *https://www.ign.ren.pt/en/terminal-de-gnl3*

[56] Fluxys Belgium NV/SA: *Belgium Natural Gas Grid Infrastructure*, Accessed in July 2016.
URL: *http://www.fluxys.com/belgium/en/About%20Fluxys/Infrastructure/Infrastructure*

[57] H. Wang, X. You, A. V. Joshi, S. G. Davis, A. Laskin, F. Egolfopoulos, C. K. Law: *USC Mech Version II. High-Temperature Combustion Reaction Model of H2/CO/C1-C4 Compounds*, University of Southern California, 2007.
URL: *http://ignis.usc.edu/USC_Mech_II.htm*

[58] D. G. Goodwin, H. K. Moffat, R. L. Speth: *Cantera: An Object-oriented Software Toolkit for Chemical Kinetics, Thermodynamics, and Transport Processes*, 2016.
URL: *http://www.cantera.org*

[59] K. Sasaki, Y. Teraoka: *Equilibria in Fuel Cell Gases: II. The C-H-O Ternary Diagrams*, Journal of The Electrochemical Society 150 (7) (2003) A885–A888.
URL: *http://jes.ecsdl.org/content/150/7/A885.abstract*

[60] W. Y. Lee, J. Hanna, A. F. Ghoniem: *On the Predictions of Carbon Deposition on the Nickel Anode of a SOFC and Its Impact on Open-Circuit Conditions*, Journal of The Electrochemical Society 160 (2) (2013) F94–F105.
URL: *http://jes.ecsdl.org/content/160/2/F94.abstract*

[61] V. Subotić, C. Schluckner, C. Hochenauer: *An experimental and numerical study of performance of large planar ESC-SOFCs and experimental investigation of carbon depositions*, Journal of the Energy Institute 89 (1) (2016) 121 – 137. ISSN: 1743–9671
URL: *//www.sciencedirect.com/science/article/pii/S174396711420242X*

[62] G. Bae, J. Bae, P. Kim-Lohsoontorn, J. Jeong: *Performance of SOFC coupled with n-C_4H_{10} autothermal reformer: Carbon deposition and development of anode structure*, International Journal of Hydrogen Energy 35 (22) (2010) 12346 – 12358. ISSN: 0360–3199
URL: *//www.sciencedirect.com/science/article/pii/S0360319910017647*

[63] H. Sumi, P. Puengjinda, H. Muroyama, T. Matsui, K. Eguchi: *Effects of crystal Structure of yttria- and scandia-stabilized zirconia in nickel-based SOFC anodes on carbon deposition and oxidation behavior*, Journal of Power Sources 196 (15) (2011) 6048 – 6054. ISSN: 0378–7753
URL: *//www.sciencedirect.com/science/article/pii/S0378775311007075*

[64] S.-H. Cui, J.-H. Li, A. Jayakumar, J.-L. Luo, K. T. Chuang, J. M. Hill, L.-J. Qiao: *Effects of H_2S and H_2O on carbon deposition over $La_{0.4}Sr_{0.5}Ba_{0.1}TiO_3$/YSZ perovskite anodes in methane fueled SOFCs*, Journal of Power Sources 250 (2014) 134 – 142. ISSN: 0378–7753
URL: *//www.sciencedirect.com/science/article/pii/S0378775313017904*

[65] S. A. Taher, S. Mansouri: *Optimal PI controller design for active power in grid-connected SOFC DG system*, International Journal of Electrical Power & Energy Systems 60 (0) (2014) 268 – 274. ISSN: 0142–0615
URL: *http://www.sciencedirect.com/science/article/pii/S0142061514000738*

[66] L. Zhang, X. Li, J. Jiang, S. Li, J. Yang, J. Li: *Dynamic modeling and analysis of a 5-kW solid oxide fuel cell system from the perspectives of cooperative control of thermal safety and high efficiency*, International Journal of Hydrogen Energy 40 (1) (2015) 456 – 476. ISSN: 0360–3199
URL: *http://www.sciencedirect.com/science/article/pii/S0360319914030754*

[67] L. Zhang, J. Jiang, H. Cheng, Z. Deng, X. Li: *Control strategy for power management, efficiency-optimization and operating-safety of a 5-kW solid oxide fuel cell system*, Electrochimica Acta 177 (2015) 237 – 249. ISSN: 0013–4686
URL: *http://www.sciencedirect.com/science/article/pii/S0013468615003229*

[68] S. Hajimolana, S. Tonekabonimoghadam, M. Hussain, M. Chakrabarti, N. Jayakumar, M. Hashim: *Thermal stress management of a solid oxide fuel cell using neural network predictive control*, Energy 62 (2013) 320 – 329. ISSN: 0360–5442
URL: *http://www.sciencedirect.com/science/article/pii/S0360544213007068*

[69] S. Lee, O. Kwon, J. H. Park: *Predictive control for sector bounded nonlinear model and its application to solid oxide fuel cell systems*, Applied Mathematics and Computation 218 (18) (2012) 9296 – 9304. ISSN: 0096–3003
URL: *http://www.sciencedirect.com/science/article/pii/S0096300312002408*

[70] M. Nayeripour, M. Hoseintabar: *A new control strategy of solid oxide fuel cell based on coordination between hydrogen fuel flow rate and utilization factor*, Renewable and Sustainable Energy Reviews 27 (2013) 505 – 514. ISSN: 1364–0321
URL: *http://www.sciencedirect.com/science/article/pii/S1364032113004310*

[71] P. Vijay, A. Samantaray, A. Mukherjee: *A bond graph model-based evaluation of a control scheme to improve the dynamic performance of a solid oxide fuel cell*, Mechatronics 19 (4) (2009) 489 – 502. ISSN: 0957–4158
URL: *http://www.sciencedirect.com/science/article/pii/S095741580800192X*

[72] A. Chaisantikulwat, C. Diaz-Goano, E. Meadows: *Dynamic modelling and control of planar anode-supported solid oxide fuel cell*, Computers & Chemical Engineering 32 (10) (2008) 2365 – 2381. ISSN: 0098–1354
URL: *http://www.sciencedirect.com/science/article/pii/S009813540700302X*

[73] J. Yang, X. Li, H.-G. Mou, L. Jian: *Control-oriented thermal management of solid oxide fuel cells based on a modified Takagi-Sugeno fuzzy model*, Journal of Power Sources 188 (2) (2009) 475 – 482. ISSN: 0378–7753
URL: *http://www.sciencedirect.com/science/article/pii/S0378775308023318*

[74] J. Yang, X. Li, H.-G. Mou, L. Jian: *Predictive control of solid oxide fuel cell based on an improved Takagi-Sugeno fuzzy model*, Journal of Power Sources 193 (2) (2009) 699 – 705. ISSN: 0378–7753
URL: *http://www.sciencedirect.com/science/article/pii/S0378775309007071*

[75] Z. Deng, H. Cao, X. Li, J. Jiang, J. Yang, Y. Qin: *Generalized predictive control for fractional order dynamic model of solid oxide fuel cell output power*, Journal of Power Sources 195 (24) (2010) 8097 – 8103. ISSN: 0378–7753
URL: *http://www.sciencedirect.com/science/article/pii/S0378775310012760*

[76] H. Cao, Z. Deng, X. Li, J. Yang, Y. Qin: *Dynamic modeling of electrical characteristics of solid oxide fuel cells using fractional derivatives*, International Journal of Hydrogen Energy 35 (4) (2010) 1749 – 1758. ISSN: 0360–3199
URL: *http://www.sciencedirect.com/science/article/pii/S0360319909018734*

[77] L. Tsikonis, J. Albrektsson, J. V. herle, D. Favrat: *The effect of bias in gas temperature measurements on the control of a Solid Oxide Fuel Cells system*, Journal of Power Sources 245 (2014) 19 – 26. ISSN: 0378–7753
URL: *http://www.sciencedirect.com/science/article/pii/S0378775313010720*

[78] D. Georgis, S. S. Jogwar, A. S. Almansoori, P. Daoutidis: *Design and control of energy integrated SOFC systems for in situ hydrogen production and power generation*, Computers & Chemical Engineering 35 (9) (2011) 1691 – 1704. ISSN: 0098–1354
URL: *http://www.sciencedirect.com/science/article/pii/S0098135411000688*

[79] X.-J. Wu, X.-J. Zhu, G.-Y. Cao, H.-Y. Tu: *Predictive control of SOFC based on a GA-RBF neural network model*, Journal of Power Sources 179 (1) (2008) 232 – 239. ISSN: 0378–7753
URL: *http://www.sciencedirect.com/science/article/pii/S0378775307028005*

[80] A. Sorce, A. Greco, L. Magistri, P. Costamagna: *FDI oriented modeling of an experimental SOFC system, model validation and simulation of faulty states*, Applied Energy 136 (0) (2014) 894 – 908. ISSN: 0306–2619
URL: *http://www.sciencedirect.com/science/article/pii/S0306261914003146*

[81] A. Greco, A. Sorce, R. Littwin, P. Costamagna, L. Magistri: *Reformer faults in SOFC systems: Experimental and modeling analysis, and simulated fault maps*, International Journal of Hydrogen Energy 39 (36) (2014) 21700 – 21713. ISSN: 0360–3199
URL: *http://www.sciencedirect.com/science/article/pii/S0360319914026226*

[82] Y. Komatsu, S. Kimijima, J. Szmyd: *Numerical analysis on dynamic behavior of solid oxide fuel cell with power output control scheme*, Journal of Power Sources 223 (2013) 232 – 245. ISSN: 0378–7753
URL: *http://www.sciencedirect.com/science/article/pii/S0378775312014693*

[83] M. Sorrentino, C. Pianese, Y. G. Guezennec: *A hierarchical modeling approach to the simulation and control of planar solid oxide fuel cells*, Journal of Power Sources 180 (1) (2008) 380 – 392. ISSN: 0378–7753
URL: *http://www.sciencedirect.com/science/article/pii/S0378775308002930*

[84] Y. Li, J. Shen, J. Lu: *Constrained model predictive control of a solid oxide fuel cell based on genetic optimization*, Journal of Power Sources 196 (14) (2011) 5873 – 5880. ISSN: 0378–7753
URL: *http://www.sciencedirect.com/science/article/pii/S0378775311005295*

[85] A. M. Murshed, B. Huang, K. Nandakumar: *Estimation and control of solid oxide fuel cell system*, Computers & Chemical Engineering 34 (1) (2010) 96 – 111. ISSN: 0098–1354
URL: *http://www.sciencedirect.com/science/article/pii/S0098135409001665*

[86] X. Zhang, S. Chan, H. Ho, J. Li, G. Li, Z. Feng: *Nonlinear model predictive control based on the moving horizon state estimation for the solid oxide fuel cell*, International Journal of Hydrogen Energy 33 (9) (2008) 2355 – 2366. ISSN: 0360–3199
URL: *http://www.sciencedirect.com/science/article/pii/S0360319908002243*

[87] G. D'Andrea, M. Gandiglio, A. Lanzini, M. Santarelli: *Dynamic model with experimental validation of a biogas-fed SOFC plant*, Energy Conversion and Management 135 (2017) 21 – 34. ISSN: 0196–8904
URL: *http://www.sciencedirect.com/science/article/pii/S0196890416311499*

[88] L. Barelli, G. Bidini, A. Ottaviano: *Solid oxide fuel cell modelling: Electrochemical performance and thermal management during load-following operation*, Energy 115, Part 1 (2016) 107 – 119. ISSN: 0360–5442
URL: *http://www.sciencedirect.com/science/article/pii/S0360544216312208*

[89] F. Mueller, F. Jabbari, R. Gaynor, J. Brouwer: *Novel solid oxide fuel cell system controller for rapid load following*, Journal of Power Sources 172 (1) (2007) 308 – 323. ISSN: 0378–7753
URL: *http://www.sciencedirect.com/science/article/pii/S0378775307011408*

[90] A. Pohjoranta, M. Halinen, J. Pennanen, J. Kiviaho: *Model predictive control of the solid oxide fuel cell stack temperature with models based on experimental data*, Journal of Power Sources 277 (2015) 239 – 250. ISSN: 0378–7753
URL: *http://www.sciencedirect.com/science/article/pii/S0378775314019831*

[91] A. Pohjoranta, M. Halinen, J. Pennanen, J. Kiviaho: *Solid oxide fuel cell stack temperature estimation with data-based modeling - Designed experiments and parameter identification*, Journal of Power Sources 277 (2015) 464 – 473. ISSN: 0378–7753
URL: *//www.sciencedirect.com/science/article/pii/S0378775314014074*

[92] B. J. Spivey, T. F. Edgar: *Dynamic modeling, simulation, and MIMO predictive control of a tubular solid oxide fuel cell*, Journal of Process Control 22 (8) (2012) 1502 – 1520. ISSN: 0959–1524
URL: *http://www.sciencedirect.com/science/article/pii/S0959152412000182*

[93] Y. Inui, N. Ito, T. Nakajima, A. Urata: *Analytical investigation on cell temperature control method of planar solid oxide fuel cell*, Energy Conversion and Management 47 (15 - 16) (2006) 2319 – 2328. ISSN: 0196–8904
URL: *http://www.sciencedirect.com/science/article/pii/S0196890405003122*

[94] R. Kandepu, L. Imsland, B. A. Foss, C. Stiller, B. Thorud, O. Bolland: *Modeling and control of a SOFC-GT-based autonomous power system*, Energy 32 (4) (2007) 406 – 417. ISSN: 0360–5442
URL: *http://www.sciencedirect.com/science/article/pii/S036054420600209X*

[95] A. S. Martinez, J. Brouwer, G. S. Samuelsen: *Feasibility study for SOFC-GT hybrid locomotive power: Part I. Development of a dynamic 3.5 MW SOFC-GT FORTRAN model*, Journal of Power Sources 213 (0) (2012) 203 – 217. ISSN: 0378–7753
URL: *http://www.sciencedirect.com/science/article/pii/S0378775312007550*

[96] Z. Jia, J. Sun, H. Dobbs, J. King: *Feasibility study of solid oxide fuel cell engines integrated with sprinter gas turbines: Modeling, design and control*, Journal of Power Sources 275 (0) (2015) 111 – 125. ISSN: 0378–7753
URL: *http://www.sciencedirect.com/science/article/pii/S0378775314018229*

[97] X.-J. Wu, X.-J. Zhu: *Multi-loop control strategy of a solid oxide fuel cell and micro gas turbine hybrid system*, Journal of Power Sources 196 (20) (2011) 8444 – 8449. ISSN: 0378–7753
URL: *http://www.sciencedirect.com/science/article/pii/S0378775311011013*

[98] X.-J. Wu, Q. Huang, X.-J. Zhu: *Power decoupling control of a solid oxide fuel cell and micro gas turbine hybrid power system*, Journal of Power Sources 196 (3) (2011) 1295 – 1302. ISSN: 0378–7753
URL: *http://www.sciencedirect.com/science/article/pii/S0378775310013182*

[99] M. L. Ferrari: *Advanced control approach for hybrid systems based on solid oxide fuel cells*, Applied Energy 145 (2015) 364 – 373. ISSN: 0306–2619
URL: *http://www.sciencedirect.com/science/article/pii/S0306261915002366*

[100] T. Kaneko, J. Brouwer, G. Samuelsen: *Power and temperature control of fluctuating biomass gas fueled solid oxide fuel cell and micro gas turbine hybrid system*, Journal of Power Sources 160 (1) (2006) 316 – 325. ISSN: 0378–7753
URL: *http://www.sciencedirect.com/science/article/pii/S037877530600098X*

[101] D. McLarty, J. Brouwer, S. Samuelsen: *Fuel cell-gas turbine hybrid system design part II: Dynamics and control*, Journal of Power Sources 254 (2014) 126 – 136. ISSN: 0378–7753
URL: *http://www.sciencedirect.com/science/article/pii/S0378775313019757*

[102] T. Gonzalez Baquet, S. Wahl: *Internal Report AEB-4265: Entwicklung eines 10 kW SOFC-Systems*, Robert Bosch GmbH, 2015.

[103] T. Gonzalez Baquet, S. Wahl: *Internal Report AEB-4267: Konzeption des Gasprozessors für ein 10 kW SOFC-Systems*, Robert Bosch GmbH, 2015.

[104] T. Gonzalez Baquet, S. Wahl: *Internal Report AEB-4984: Inbetriebnahme und Versuchsauswertung des 10 kW SOFC-Systems*, Robert Bosch GmbH, 2017.

[105] T. Danne, S. Wahl, P. Horstmann, T. Gonzalez Baquet, R. Meise, M. Hering: *Patent Application 102016220978.7 (previously undisclosed): Brennstoffzellenvorrichtung*, Robert Bosch GmbH, 2016.

[106] P. Horstmann, T. Danne, M. Hering: *Internal Report AEB-5064: Regelung des 10 kW SOFC Prototypen*, Robert Bosch GmbH, 2017.

[107] G. P. Smith, D. M. Golden, M. Frenklach, N. W. Moriarty, B. Eiteneer, M. Goldenberg, C. T. Bowman, R. K. Hanson, S. Song, J. William C. Gardiner, V. V. Lissianski, Z. Qin: *GRI-Mech 3.0 - An optimized mechanism designed to model natural gas combustion, including NO formation and reburn chemistry*, University of California Berkeley, 2000.
URL: *http://www.me.berkeley.edu/gri_mech/*

[108] A. Dicks, T. Connor, J. Bradley, A. Lashtabeg: *Impact of Australian natural gas and coal bed methane composition on PEM fuel cell performance*, International Journal of Hydrogen Energy 34 (21) (2009) 8892 – 8904. ISSN: 0360–3199
URL: *http://www.sciencedirect.com/science/article/pii/S0360319909012518*

[109] J. Warnatz, U. Maas, R. W. Dibble: *Combustion - Physical and Chemical Fundamentals, Modeling and Simulation, Experiments, Pollutant Formation.* 4th Edition, Springer-Verlag Berlin Heidelberg, 2006. ISBN: 978–3–540–25992–3

[110] Bürkert GmbH & Co. KG: *Data sheet: Mass flow controller type 8626*, 2017.
URL: *https://www.buerkert.de/de/Media/plm/DTS/DS/DS8626-Standard-EU-EN.pdf?id=DTS0000000000000001000011124ENN*

[111] EA Elektro-Automatik GmbH & Co. KG: *Data sheet: Programmable electronic DC loads with energy recovery - EA-ELR 9000*, 2017.
URL: *http://shop.elektroautomatik.de/shop/dos2/Web/Datenblaetter/datasheet_elr9000.pdf*

[112] UNION Instruments GmbH: *Data sheet: Multi-gas analyzer INCA 1051*, 2016.
URL: *http://www.union-instruments.com/images/downloads/Datenblaetter/en/INCA1051_eng_small.pdf*

[113] B. J. McBride, S. Gordon, M. A. Reno: *NASA Technical Memorandum 4513 - Coefficients for Calculating Thermodynamic and Transport Properties of Individual Species*, National Aeronautics and Space Administration (NASA), 1993.

[114] E. Lemmon, M. McLinden, D. Friend: *Thermophysical Properties of Fluid Systems in NIST Chemistry WebBook.* NIST Standard Reference Database Number 69, Eds. P.J. Linstrom and W.G. Mallard, National Institute of Standards and Technology, Gaithersburg MD, 20899, Accessed in November 2016.
URL: *http://webbook.nist.gov*

[115] K. Heidebrecht: *Internal communications with VAIREX air systems.* VRB8[2] and VRB32-2 measured data set, 2015.

[116] T. Grohmann: *Internal communications with AIRTECH Europe GmbH.* ASV_P2 measured data set, 2016.

[117] T. Carolus: *Ventilatoren - Aerodynamischer Entwurf, Schallvorhersage, Konstruktion.* 3rd Edition, Springer Vieweg, 2013. ISBN: 978–3–8348–2471–4

Appendix

A Gross efficiency calculation for different system design options

The gross efficiency related to $U_{\mathrm{f,S}}$ can be computed for each of the three individual system design options by applying the corresponding relation between $U_{\mathrm{f,Sys}}$ and $U_{\mathrm{f,S}}$ to equation (2.41). For the EWS option, $U_{\mathrm{f,Sys}}$ and $U_{\mathrm{f,S}}$ are identical and for the AEGR system, $U_{\mathrm{f,Sys}}$ can be expressed using equation (2.3), ultimately yielding equations (A.1) and (A.2), respectively.

$$\eta_{\mathrm{Gross,EWS}} = \frac{E_{\mathrm{Cell}}\, U_{\mathrm{f,S}}\, F\, K_{\mathrm{e^-}}}{h_{\mathrm{i,NG}}} \tag{A.1}$$

$$\eta_{\mathrm{Gross,AEGR}} = \frac{E_{\mathrm{Cell}}\, F\, (U_{\mathrm{f,S}}\, K_{\mathrm{e^-}} + 2\,(\Phi\, K_{\mathrm{C}} - K_{\mathrm{O}})\,(1 - U_{\mathrm{f,S}}))}{h_{\mathrm{i,NG}}} \tag{A.2}$$

For the CPOX option, the utilization of the electrons due to the partial oxidation of methane in the reformer has to be considered for the calculation of the relation between $U_{\mathrm{f,Sys}}$ and $U_{\mathrm{f,S}}$. The partial oxidation of methane is shown in the chemical equation (A.3), clarifying that for a stoichiometric conversion, half a mole of oxygen is utilized per one mole of methane. Therefore, the resulting molar flow rate of releasable electrons at the anode inlet can be computed by relating the molar flow rate of oxygen to the molar flow rate of methane. Additionally, the molar flow rate of supplied oxygen can be expressed using the definition of Φ, where for Φ equal to 1, the reaction is stoichiometric. In combination with the definition of the utilized electrons in the stack, derived from equation (2.24), both relations can be applied to the calculation of the fuel utilization factor, previously introduced in equation (2.26). As a result, $U_{\mathrm{f,Sys}}$ can be expressed as a function of $U_{\mathrm{f,S}}$, Φ and the electron coefficient, outlined in equation (A.4). The derived relation is applied to equation (2.41), yielding a function expressing the gross efficiency of the CPOX option, as highlighted in equation (A.5). It should be noted that for the CPOX case, all derived equations are only valid for a pure methane feed.

$$\mathrm{CH_4} + \frac{1}{2}\,\mathrm{O_2} \rightarrow 2\,\mathrm{H_2} + \mathrm{CO} \tag{A.3}$$

$$\begin{aligned} U_{\mathrm{f,S}} &= \frac{\dot{n}_{\mathrm{e^-,S,uti}}}{\dot{n}_{\mathrm{e^-,an,in}}} = \frac{\dot{n}_{\mathrm{e^-,S,uti}}}{\dot{n}_{\mathrm{e^-,CH_4,in}} - \dot{n}_{\mathrm{e^-,O_2,in}}} = \frac{\dot{n}_{\mathrm{CH_4}}\, U_{\mathrm{f,Sys}}\, K_{\mathrm{e^-}}}{\dot{n}_{\mathrm{CH_4}}\, K_{\mathrm{e^-}} - \dot{n}_{\mathrm{CH_4}}\, \Phi\, \frac{4}{2}} = U_{\mathrm{f,Sys}} \left(\frac{K_{\mathrm{e^-}}}{K_{\mathrm{e^-}} - 2\,\Phi} \right) \\ &\rightarrow U_{\mathrm{f,Sys}} = U_{\mathrm{f,S}} \left(1 - \frac{2\,\Phi}{K_{\mathrm{e^-}}} \right) \end{aligned} \tag{A.4}$$

$$\eta_{\mathrm{Gross,CPOX}} = \frac{E_{\mathrm{Cell}}\, U_{\mathrm{f,S}}\, F\, (K_{\mathrm{e^-}} - 2\,\Phi)}{h_{\mathrm{i,NG}}} \tag{A.5}$$

B Permitted H-gas domains in Europe

In Table B.1, the permitted H-gas domains for Germany, France and Portugal are listed. It should be noted that the permitted relative density domain in Germany is adjusted to the newer standard DIN EN 16726 with a value between 0.555 and 0.700 [11].

Tabelle B.1: Permitted H-gas domain in Germany, France and Portugal

	Unit	Germany	France	Portugal
Wobbe-index	MJ m^{-3}	49.0 - 56.5	49.1 - 56.5	48.2 - 57.7
Higher heating value	MJ m^{-3}	36.3 - 47.2	38.5 - 46.1	35.9 - 48.2
Relative density	-	0.55 - 0.75	0.56 - 0.70	0.56 - 0.70
Reference	-	[31]	[51]	[52]

C Derivation of gas coefficient constraints

C.1 Sum of all mole fractions

As shown in equation (C.1), by rearranging the sum of mole fractions, it can be expressed using the gas coefficients based upon equations (3.3), (3.4), (3.5) and (3.6).

$$\begin{aligned}\sum_i x_{\mathrm{NG},i} = 1 &= x_{\mathrm{NG,CH_4}} + x_{\mathrm{NG,C_2H_6}} + x_{\mathrm{NG,C_3H_8}} + x_{\mathrm{NG,C_4H_{10}}} + x_{\mathrm{NG,CO_2}} + x_{\mathrm{NG,N_2}} + x_{\mathrm{NG,H_2}} \\ &= \left(\frac{4\,x_{\mathrm{NG,CH_4}} + 6\,x_{\mathrm{NG,C_2H_6}} + 8\,x_{\mathrm{NG,C_3H_8}} + 10\,x_{\mathrm{NG,C_4H_{10}}} + 2\,x_{\mathrm{NG,H_2}}}{2}\right) - (x_{\mathrm{NG,CH_4}} \\ &\quad + 2\,x_{\mathrm{NG,C_2H_6}} + 3\,x_{\mathrm{NG,C_3H_8}} + 4\,x_{\mathrm{NG,C_4H_{10}}} + x_{\mathrm{NG,CO_2}}) + 2\,x_{\mathrm{NG,CO_2}} + x_{\mathrm{NG,N_2}} \\ &= \frac{K_\mathrm{H}}{2} - K_\mathrm{C} + K_\mathrm{O} + \frac{K_\mathrm{N}}{2}\end{aligned} \tag{C.1}$$

C.2 Electron coefficient as a function of hydrogen, carbon and oxygen coefficients

The electron gas coefficient can be expressed using the hydrogen, carbon and oxygen gas coefficients, as derived in equation (C.2) based upon equations (3.3), (3.4), (3.5) and (3.7).

$$\begin{aligned}K_\mathrm{H} + 4\,K_\mathrm{C} - 2\,K_\mathrm{O} &= 4\,x_{\mathrm{NG,CH_4}} + 6\,x_{\mathrm{NG,C_2H_6}} + 8\,x_{\mathrm{NG,C_3H_8}} + 10\,x_{\mathrm{NG,C_4H_{10}}} + 2\,x_{\mathrm{NG,H_2}} \\ &\quad + 4\,(x_{\mathrm{NG,CH_4}} + 2\,x_{\mathrm{NG,C_2H_6}} + 3\,x_{\mathrm{NG,C_3H_8}} + 4\,x_{\mathrm{NG,C_4H_{10}}} + x_{\mathrm{NG,CO_2}}) \\ &\quad - 2\,(2\,x_{\mathrm{NG,CO_2}}) \\ &= 8\,x_{\mathrm{NG,CH_4}} + 14\,x_{\mathrm{NG,C_2H_6}} + 20\,x_{\mathrm{NG,C_3H_8}} + 26\,x_{\mathrm{NG,C_4H_{10}}} + 2\,x_{\mathrm{NG,H_2}} = K_{\mathrm{e^-}}\end{aligned} \tag{C.2}$$

C.3 Molar mass

As shown in equation (C.3), the molar mass of natural gas can be calculated using the mole fraction and corresponding molar masses of each individual species. The molar masses are listed in Table 4.5.

$$\begin{aligned}M_\mathrm{NG} = {} & M_{\mathrm{CH_4}}\,x_{\mathrm{NG,CH_4}} + M_{\mathrm{C_2H_6}}\,x_{\mathrm{NG,C_2H_6}} + M_{\mathrm{C_3H_8}}\,x_{\mathrm{NG,C_3H_8}} + M_{\mathrm{C_4H_{10}}}\,x_{\mathrm{NG,C_4H_{10}}} \\ & + M_{\mathrm{CO_2}}\,x_{\mathrm{NG,CO_2}} + M_{\mathrm{N_2}}\,x_{\mathrm{NG,N_2}} + M_{\mathrm{H_2}}\,x_{\mathrm{NG,H_2}}\end{aligned} \tag{C.3}$$

The molar masses of each individual species can be substituted using the corresponding molar masses of the contained carbon, hydrogen, oxygen and nitrogen atoms, yielding equation (C.4).

$$\begin{aligned} M_{\mathrm{NG}} &= (M_{\mathrm{C}} + 4\,M_{\mathrm{H}})\,x_{\mathrm{NG,CH_4}} + (2\,M_{\mathrm{C}} + 6\,M_{\mathrm{H}})\,x_{\mathrm{NG,C_2H_6}} + (3\,M_{\mathrm{C}} + 8\,M_{\mathrm{H}})\,x_{\mathrm{NG,C_3H_8}} + (4\,M_{\mathrm{C}} \\ &\quad +10\,M_{\mathrm{H}})\,x_{\mathrm{NG,C_4H_{10}}} + (M_{\mathrm{C}} + 2\,M_{\mathrm{O}})\,x_{\mathrm{NG,CO_2}} + (2\,M_{\mathrm{N}})\,x_{\mathrm{NG,N_2}} + (2\,M_{\mathrm{H}})\,x_{\mathrm{NG,H_2}} \\ &= M_{\mathrm{C}}\,(x_{\mathrm{NG,CH_4}} + 2\,x_{\mathrm{NG,C_2H_6}} + 3\,x_{\mathrm{NG,C_3H_8}} + 4\,x_{\mathrm{NG,C_4H_{10}}} + x_{\mathrm{NG,CO_2}}) \\ &\quad + M_{\mathrm{H}}\,(4\,x_{\mathrm{NG,CH_4}} + 6\,x_{\mathrm{NG,C_2H_6}} + 8\,x_{\mathrm{NG,C_3H_8}} + 10\,x_{\mathrm{NG,C_4H_{10}}} + 2\,x_{\mathrm{NG,H_2}}) \\ &\quad + M_{\mathrm{O}}\,(2\,x_{\mathrm{NG,CO_2}}) + M_{\mathrm{N}}\left(2\,x_{\mathrm{NG,N_2}}\right) \end{aligned} \tag{C.4}$$

Applying the definition of the gas coefficients to equation (C.4), yields equation (C.5) based upon equations (3.3), (3.4), (3.5) and (3.6).

$$M_{\mathrm{NG}} = M_{\mathrm{C}}\,K_{\mathrm{C}} + M_{\mathrm{H}}\,K_{\mathrm{H}} + M_{\mathrm{O}}\,K_{\mathrm{O}} + M_{\mathrm{N}}\,K_{\mathrm{N}} \tag{C.5}$$

The nitrogen gas coefficient can be eliminated by applying a rearranged form of equation (3.8) to equation (C.5), yielding equation (C.6).

$$M_{\mathrm{NG}} = M_{\mathrm{C}}\,K_{\mathrm{C}} + M_{\mathrm{H}}\,K_{\mathrm{H}} + M_{\mathrm{O}}\,K_{\mathrm{O}} + M_{\mathrm{N}}\,(2 - K_{\mathrm{H}} + 2\,K_{\mathrm{C}} - 2\,K_{\mathrm{O}}) \tag{C.6}$$

Lastly, the hydrogen coefficient can be substituted using a rearranged form of equation (3.9), as outlined in equation (C.7).

$$M_{\mathrm{NG}} = (M_{\mathrm{C}} - 4\,M_{\mathrm{H}} + 6\,M_{\mathrm{N}})\,K_{\mathrm{C}} + (M_{\mathrm{H}} - M_{\mathrm{N}})\,K_{\mathrm{e^-}} + (M_{\mathrm{O}} + 2\,M_{\mathrm{H}} - 4\,M_{\mathrm{N}})\,K_{\mathrm{O}} + 2\,M_{\mathrm{N}} \tag{C.7}$$

D Coefficients of regression approaches for natural gas coefficient correlations

D.1 Coefficients a_1 to a_8 of the linear, quadratic and power regression approach of the electron coefficient and change in molar quantity coefficient

The coefficients a_1 to a_8 of the linear, quadratic and power regression between the electron and change in molar quantity coefficient are listed in Table D.1.

Tabelle D.1: Coefficients a_1 to a_8 of linear, quadratic and power regression approach between electron and change in molar quantity coefficient

Regression	Linear		Quadratic			Power		
Coefficient	a_1	a_2	a_3	a_4	a_5	a_6	a_7	a_8
Value	3.16E-01	-5.12E-01	5.30E-02	-5.78E-01	3.26E+00	2.14E-04	3.80E+00	1.45E+00

D.2 Coefficients a_9 to a_{12} of the multiple linear regression approach of the electron coefficient and oxygen-to-carbon ratio dependent combined gas coefficient

The coefficients a_9 to a_{12} of the multiple linear regression approach between electron and oxygen-to-carbon ratio dependent combined gas coefficient are listed in Table D.2.

Tabelle D.2: Coefficients a_9 to a_{12} of multiple linear regression approach between electron and oxygen-to-carbon ratio dependent combined gas coefficient

Regression	Multiple linear			
Coefficient	a_9	a_{10}	a_{11}	a_{12}
Value	-2.07E-01	2.23E-02	-1.52E-01	1.47E-01

E Derivation of cathode outlet composition as function of air utilization factor

The oxygen fraction at the cathode outlet can generally be expressed as the quotient of the molar flow rate of oxygen divided by the total molar flow rate at the cathode outlet. The total molar flow rate can also be written as the sum of the molar flow rate of nitrogen and oxygen, considering both as the only present species at the cathode inlet and outlet. The resulting general constraint is shown in equation (E.1).

$$x_{\mathrm{ca,out,O_2}} = \frac{\dot{n}_{\mathrm{ca,out,O_2}}}{\dot{n}_{\mathrm{ca,out}}} = \frac{\dot{n}_{\mathrm{ca,out,O_2}}}{\dot{n}_{\mathrm{ca,out,N_2}} + \dot{n}_{\mathrm{ca,out,O_2}}} \tag{E.1}$$

By considering the molar flow rate of nitrogen, between the cathode inlet and outlet, invariant and expressing the molar flow rate of oxygen at the cathode outlet as a function of the molar flow rate at the cathode inlet and transferred flow rate of oxygen, equation (E.1) can be rewritten into equation (E.2). Lastly, by expressing the molar flow rates at the cathode inlet as the product of the individual mole fraction and total air flow rate, as well as by applying the definition of the transferred molar flow rate of oxygen, equation (E.1) can be further rewritten using equations (2.24) and (2.5). Consequently, the mole fraction of oxygen at the cathode outlet can be solely expressed as a function of the air utilization factor and cathode inlet composition.

$$x_{\mathrm{ca,out,O_2}} = \frac{\dot{n}_{\mathrm{ca,in,O_2}} - \dot{n}_{\mathrm{O_2,tr}}}{\dot{n}_{\mathrm{ca,in,N_2}} + \dot{n}_{\mathrm{ca,in,O_2}} - \dot{n}_{\mathrm{O_2,tr}}} = \frac{x_{\mathrm{ca,in,O_2}}\,(1 - U_{\mathrm{a}})}{x_{\mathrm{ca,in,N_2}} + x_{\mathrm{ca,in,O_2}}\,(1 - U_{\mathrm{a}})} \tag{E.2}$$

F USC-Mech II - List of species

The 111 considered species of the USC-Mech II with the number of carbon, oxygen, hydrogen, nitrogen atoms and number of releasable electrons are listed in Table F.1 [57].

Tabelle F.1: Number of carbon, oxygen, hydrogen and nitrogen atoms, as well as releasable electrons of USC-Mech II species

Species i	Number of carbon atoms $N_{\mathrm{C,i}}$	Number of oxygen atoms $N_{\mathrm{O,i}}$	Number of hydrogen atoms $N_{\mathrm{H,i}}$	Number of nitrogen atoms $N_{\mathrm{N,i}}$	Number of releasable electrons $N_{\mathrm{e^-,i}}$
AR	0	0	0	0	0
N_2	0	0	0	2	0
H	0	0	1	0	1
O	0	1	0	0	-2
OH	0	1	1	0	-1
HO_2	0	2	1	0	-3

Species i	Number of carbon atoms $N_{\mathrm{C,i}}$	Number of oxygen atoms $N_{\mathrm{O,i}}$	Number of hydrogen atoms $N_{\mathrm{H,i}}$	Number of nitrogen atoms $N_{\mathrm{N,i}}$	Number of releasable electrons $N_{\mathrm{e^-,i}}$
H_2	0	0	2	0	2
H_2O	0	1	2	0	0
H_2O_2	0	2	2	0	-2
O_2	0	2	0	0	-4
C	1	0	0	0	4
CH	1	0	1	0	5
CH_2	1	0	2	0	6
CH_2^*	1	0	2	0	6
CH_3	1	0	3	0	7
CH_4	1	0	4	0	8
HCO	1	1	1	0	3
CH_2O	1	1	2	0	4
CH_3O	1	1	3	0	5
CH_2OH	1	1	3	0	5
CH_3OH	1	1	4	0	6
CO	1	1	0	0	2
CO_2	1	2	0	0	0
C_2O	2	1	0	0	6
C_2H	2	0	1	0	9
C_2H_2	2	0	2	0	10
H_2CC	2	0	2	0	10
C_2H_3	2	0	3	0	11
C_2H_4	2	0	4	0	12
C_2H_5	2	0	5	0	13
C_2H_6	2	0	6	0	14
HCCO	2	1	1	0	7
HCCOH	2	1	2	0	8
CH_2CO	2	1	2	0	8
CH_3CO	2	1	3	0	9
CH_2CHO	2	1	3	0	9
CH_2OCH	2	1	3	0	9
CH_3CHO	2	1	4	0	10
CH_2OCH_2	2	1	4	0	10
C_3H_3	3	0	3	0	15
pC_3H_4	3	0	4	0	16
aC_3H_4	3	0	4	0	16
cC_3H_4	3	0	4	0	16
aC_3H_5	3	0	5	0	17
CH_3CCH_2	3	0	5	0	17

Species i	Number of carbon atoms $N_{\mathrm{C,i}}$	Number of oxygen atoms $N_{\mathrm{O,i}}$	Number of hydrogen atoms $N_{\mathrm{H,i}}$	Number of nitrogen atoms $N_{\mathrm{N,i}}$	Number of releasable electrons $N_{\mathrm{e^-,i}}$
CH_3CHCH	3	0	5	0	17
C_3H_6	3	0	6	0	18
nC_3H_7	3	0	7	0	19
iC_3H_7	3	0	7	0	19
C_3H_8	3	0	8	0	20
CH_2CHCO	3	1	3	0	13
C_2H_3CHO	3	1	4	0	14
CH_3CHOCH_2	3	1	6	0	16
CH_3CH_2CHO	3	1	6	0	16
CH_3COCH_3	3	1	6	0	16
C_4H_2	4	0	2	0	18
nC_4H_3	4	0	3	0	19
iC_4H_3	4	0	3	0	19
C_4H_4	4	0	4	0	20
nC_4H_5	4	0	5	0	21
iC_4H_5	4	0	5	0	21
C_4H_5-2	4	0	5	0	21
$c-C_4H_5$	4	0	5	0	21
C_4H_6	4	0	6	0	22
$C_4H_6(1,2)$	4	0	6	0	22
C_4H_6-2	4	0	6	0	22
C_4H_7	4	0	7	0	23
iC_4H_7	4	0	7	0	23
$C_4H_8(1)$	4	0	8	0	24
$C_4H_8(2)$	4	0	8	0	24
iC_4H_8	4	0	8	0	24
pC_4H_9	4	0	9	0	25
sC_4H_9	4	0	9	0	25
iC_4H_9	4	0	9	0	25
tC_4H_9	4	0	9	0	25
C_4H_{10}	4	0	10	0	26
iC_4H_{10}	4	0	10	0	26
H_2C_4O	4	1	2	0	16
C_4H_4O	4	1	4	0	18
$CH_2CHCHCHO$	4	1	5	0	19
$CH_3CHCHCO$	4	1	5	0	19
$C_2H_3CHOCH_2$	4	1	6	0	20
$C_4H_6O(2,3)$	4	1	6	0	20
$CH_3CHCHCHO$	4	1	6	0	20

Species i	Number of carbon atoms $N_{C,i}$	Number of oxygen atoms $N_{O,i}$	Number of hydrogen atoms $N_{H,i}$	Number of nitrogen atoms $N_{N,i}$	Number of releasable electrons $N_{e^-,i}$
$C_4H_6O(2,5)$	4	1	6	0	20
C_5H_4O	5	1	4	0	22
$C_5H_5O(1,3)$	5	1	5	0	23
$C_5H_5O(2,4)$	5	1	5	0	23
C_5H_4OH	5	1	5	0	23
C_5H_5OH	5	1	6	0	24
C_5H_5	5	0	5	0	25
C_5H_6	5	0	6	0	26
lC_5H_7	5	0	7	0	27
C_6H_2	6	0	2	0	26
C_6H_3	6	0	3	0	27
$l-C_6H_4$	6	0	4	0	28
$o-C_6H_4$	6	0	4	0	28
C_6H_5	6	0	5	0	29
C_6H_6	6	0	6	0	30
$C_6H_5CH_2$	7	0	7	0	35
$C_6H_5CH_3$	7	0	8	0	36
$C_6H_5C_2H$	8	0	6	0	38
C_6H_5O	6	1	5	0	27
C_6H_5OH	6	1	6	0	28
$C_6H_4O_2$	6	2	4	0	24
C_6H_5CO	7	1	5	0	31
C_6H_5CHO	7	1	6	0	32
$C_6H_5CH_2OH$	7	1	8	0	34
$OC_6H_4CH_3$	7	1	7	0	33
$HOC_6H_4CH_3$	7	1	8	0	34
$C_6H_4CH_3$	7	0	7	0	35

G Volume flow rate estimation based upon characteristic blower map modeling

The methodology for the estimation of volume flow rates as a function of the measured blower speed, pressure and temperature is based upon the accurate reproduction of the characteristic blower maps using detailed manufacturer's data. As a result, the volume flow rates can be indirectly measured and a direct measurement with flow rate sensors is redundant. Therefore, investment costs are reduced and possible system shutdowns due to the malfunction of the flow rate sensors are precluded. The methodology is applied to the two main blowers in the system, the air and recirculation gas blower.

The used air and recirculation blower data base includes 35 and 39 data records at 7 and 8 different reference speed levels, respectively [115, 116]. The individual reference speed levels and corresponding data points are displayed in Figure G.1 for the air and recirculation blower, respectively. Linear regression is applied to each individual reference speed level to express the volume flow rate as a function of the pressure difference, as outlined in equation (G.1).

$$\dot{V}_{\mathrm{Std}} = B \triangle p_{\mathrm{Std}} + C \tag{G.1}$$

The derived regression coefficients B and C for each individual reference speed include 14 or 18 individual coefficients for the air and recirculation gas blower, respectively. Additionally, the individual coefficients of the reference speed levels can be expressed as functions of the rotational speed. As a result, a single function is derived to describe the entire compressor map based upon the pressure difference and rotational speed. As shown in equations (G.2) and (G.3) for the air and recirculation blower, a power or cubic regression approach is used to express coefficient B, whereas coefficient C is computed based upon a linear regression approach, respectively. The individual coefficients B_1 to B_6 and C_1 to C_4 are listed in Table G.1. The approximated regression curves for the reference speed levels are also displayed in Figure G.1. The blower maps of the air and recirculation gas blower can be accurately reproduced using the modified linear regression approaches, as outlined by the high match between the data base and the fitted regression curves.

$$\dot{V}_{\mathrm{Std,a,blower}} = B_1\, n^{B_2} \triangle p_{\mathrm{Std}} + (C_1\, n + C_2) \tag{G.2}$$

$$\dot{V}_{\mathrm{Std,rec,blower}} = \left(B_3\, n^3 + B_4\, n^2 + B_5\, n + B_6\right) \triangle p_{\mathrm{Std}} + (C_3\, n + C_4) \tag{G.3}$$

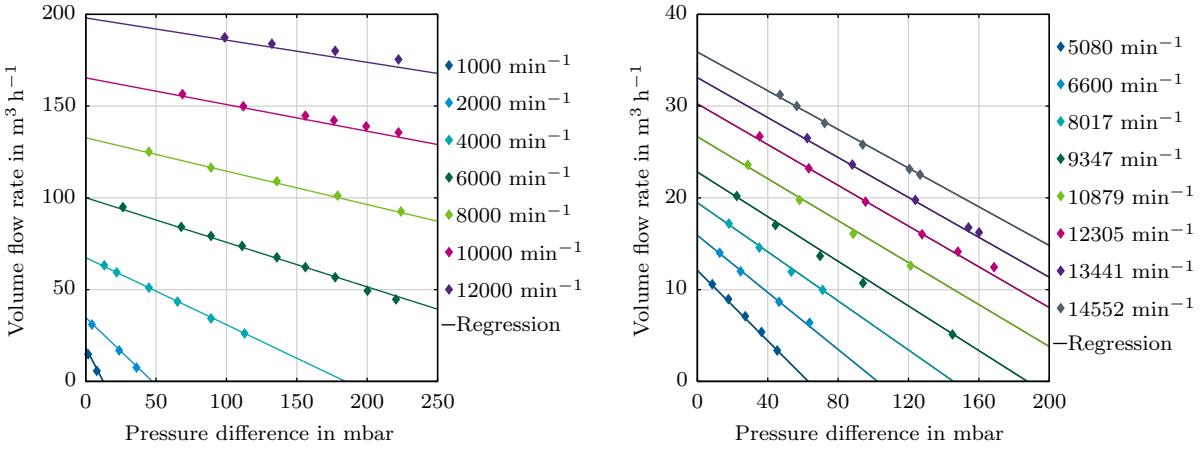

(a) Air blower

(b) Recirculation gas blower

Abbildung G.1: Characteristic blower map modeling

The laws of similitude, for geometrical, kinematic and dynamic similar blowers, can be applied in connection with the ideal gas law to express the relation between a reference and any new state for a constant speed level [117]. For the purpose of simplification, the reference state is label as the standard (Std) case, since the reference blower data base was scaled to the designated standard conditions with a temperature and pressure level of 273.15 K and 101325 Pa, respectively. The new state is referred to as the measured (Msd) case based upon the relation

Tabelle G.1: Regression coefficients of characteristic blower map modeling

Air blower			Recirculation gas blower		
Coefficient	Unit	Value	Coefficient	Unit	Value
B_1	$\mathrm{m^3\,min\,h^{-1}\,mbar^{-1}}$	-1.542E+03	B_3	$\mathrm{m^3\,min^3\,h^{-1}\,mbar^{-1}}$	1.657E-13
B_2	-	-1.006E+00	B_4	$\mathrm{m^3\,min^2\,h^{-1}\,mbar^{-1}}$	-6.211E-09
C_1	$\mathrm{m^3\,min\,h^{-1}}$	1.632E-02	B_5	$\mathrm{m^3\,min\,h^{-1}\,mbar^{-1}}$	7.945E-05
C_2	$\mathrm{m^3\,h^{-1}}$	2.158E+00	B_6	$\mathrm{m^3\,h^{-1}\,mbar^{-1}}$	-4.569E-01
			C_3	$\mathrm{m^3\,min\,h^{-1}}$	2.512E-03
			C_4	$\mathrm{m^3\,h^{-1}}$	-6.632E-01

to the experimental gas conditions, which deviate from the designated standard conditions. As outlined in equation (G.4), the reference pressure difference can be expressed as a function of the pressure, temperature and molar mass of both states, as well as the pressure difference of the new state [117]. It should be noted, that both reference blower data bases were recorded with air. Therefore, the reference or standard molar mass is defined using the molar mass of dry air with a value of 28.85 $\mathrm{g\,mol^{-1}}$.

$$\triangle p_{\mathrm{Std}} = \left(\frac{p_{\mathrm{Std}}}{p_{\mathrm{Msd}}}\right)\left(\frac{T_{\mathrm{Msd}}}{T_{\mathrm{Std}}}\right)\left(\frac{M_{\mathrm{Std}}}{M_{\mathrm{Msd}}}\right)\triangle p_{\mathrm{Msd}} \tag{G.4}$$

Applying equation (G.4) to equations (G.2) and (G.3) yields equations (G.5) and (G.6) using the corresponding labels of the blowers and measured process values, defined in section 4.2. As a result, the volume flow rate related to standard conditions can be determined based upon the measured pressure, temperature and rotational speed. It should be noted that the molar mass of the gas mixture at the recirculation gas blower inlet is estimated based upon an ideal system balance, as outlined in equation (H.6). The molar mass of air of the experimental state is assumed to be equal to the defined standard molar mass of dry air. Therefore, the molar mass quotient is eliminated in equation (G.5).

$$\begin{aligned}\dot{V}_{202,\mathrm{PV}} = {} & B_1\, n_{201,\mathrm{PV}}^{(B_2)}\left(\frac{p_{\mathrm{Std}}}{p_{\mathrm{amb,PV}} + p_{201,\mathrm{PV}}}\right)\left(\frac{\vartheta_{201,\mathrm{PV}} + 273.15\,\mathrm{K}}{T_{\mathrm{Std}}}\right)(p_{202,\mathrm{PV}} - p_{201,\mathrm{PV}}) \\ & + (C_1\, n_{201,\mathrm{PV}} + C_2)\end{aligned} \tag{G.5}$$

$$\begin{aligned}\dot{V}_{102,\mathrm{PV}} = {} & \left(B_3\, n_{101,\mathrm{PV}}^3 + B_4\, n_{101,\mathrm{PV}}^2 + B_5\, n_{101,\mathrm{PV}} + B_6\right)\left(\frac{p_{\mathrm{Std}}}{p_{\mathrm{amb,PV}} + p_{101,\mathrm{PV}}}\right) \\ & \left(\frac{\vartheta_{101,\mathrm{PV}} + 273.15\,\mathrm{K}}{T_{\mathrm{Std}}}\right)\left(\frac{M_{\mathrm{a}}}{M_{101,\mathrm{SP}}}\right)(p_{102,\mathrm{PV}} - p_{101,\mathrm{PV}}) + (C_3\, n_{101,\mathrm{PV}} + C_4)\end{aligned} \tag{G.6}$$

H Set point and process value calculation of applied control strategy

H.1 Computation of set points

By applying equations (2.3) and (4.1) to equation (2.4), the volume flow rate set points of natural gas can be obtained as shown in equation (H.1).

$$\dot{V}_{007,\mathrm{SP}} = \frac{I_{\mathrm{SP}}\, N_{\mathrm{Cell}}\, v_{\mathrm{m,Std}}}{F\left(U_{\mathrm{f,S,SP}}\, K_{\mathrm{e^-,R}} + 2\left(\Phi_{\mathrm{SP}}\, K_{\mathrm{C,R}} - K_{\mathrm{O,R}}\right)\left(1 - U_{\mathrm{f,S,SP}}\right)\right)} \tag{H.1}$$

As outlined in equation (H.2), by applying equation (4.1) to equation (2.4), the system fuel utilization factor set point can be calculated using the volume flow rate set point of natural gas.

$$U_{\mathrm{f,Sys,SP}} = \frac{I_{\mathrm{SP}}\, N_{\mathrm{Cell}}\, v_{\mathrm{m,Std}}}{\dot{V}_{007,\mathrm{SP}}\, F\, K_{\mathrm{e^-,R}}} \tag{H.2}$$

By applying equation (2.3) and (4.1) to equation (2.18), the designated volume flow rate set point at the reformer inlet $\left(\dot{V}_{102,\mathrm{SP,des}}\right)$ can be obtained, as shown in equation (H.3). However, as outlined in equation (H.4), the two limiting volume flow rates $\dot{V}_{102,\mathrm{min}}$ and $\dot{V}_{106,\mathrm{min}}$ have to be considered to compute the final set point.

$$\dot{V}_{102,\mathrm{SP,des}} = \frac{\dot{V}_{007,\mathrm{SP}}\left(U_{\mathrm{f,Sys,SP}}\left(1 - U_{\mathrm{f,S,SP}}\right) + K_{\triangle\mathrm{an,R}}\left(U_{\mathrm{f,Sys,SP}} - U_{\mathrm{f,S,SP}}\right)\right)}{U_{\mathrm{f,S,SP}}\left(1 - U_{\mathrm{f,Sys,SP}}\right)} \tag{H.3}$$

$$\dot{V}_{102,\mathrm{SP}} = \max\left(\max\left(\dot{V}_{102,\mathrm{SP,des}}, \dot{V}_{106,\mathrm{min}}\right), \dot{V}_{102,\mathrm{min}}\right) \tag{H.4}$$

As shown in equation (H.5), the recirculation ratio set point can be calculated by rearranging and applying equations (2.14), (2.15), (2.18), (2.19) and (4.1) to equation (2.2).

$$r_{\mathrm{SP}} = \frac{\dot{V}_{102,\mathrm{SP}} - \dot{V}_{007,\mathrm{SP}}}{\dot{V}_{102,\mathrm{SP}} + \dot{V}_{007,\mathrm{SP}}\, K_{\triangle\mathrm{an,R}}} \tag{H.5}$$

By using equations (2.4), (2.8), (2.13), (2.18) and (4.1), the molar mass set point at the recirculation blower can be estimated, as outlined in equation (H.6). It should be noted, that the molar mass at the reformer and blower inlets are equal since the gas compositions are identical.

$$M_{101,\mathrm{SP}} = \frac{4\, F\, \dot{V}_{007,\mathrm{SP}}\, M_{\mathrm{NG,in,R}} + r_{\mathrm{SP}}\, I_{\mathrm{SP}}\, N_{\mathrm{Cell}}\, M_{\mathrm{O_2}}\, v_{\mathrm{m,Std}}}{4\, F\, \dot{V}_{007,\mathrm{SP}}\left(1 + r_{\mathrm{SP}}\, K_{\triangle\mathrm{an,R}}\right)} \tag{H.6}$$

The scaling of the cathode inlet volume flow rate set point, due to a minimal allowed volume flow rate $\left(\dot{V}_{207,\mathrm{SP,limit}}\right)$, based upon a maximal tolerable air utilization factor, is outlined in equation (H.7) using equations (2.5) and (4.1).

$$\dot{V}_{207,\mathrm{SP}'} = \max\left(\dot{V}_{207,\mathrm{SP}}, \left(\dot{V}_{207,\mathrm{SP,limit}} = \frac{I_{\mathrm{SP}}\, N_{\mathrm{Cell}}\, v_{\mathrm{m,Std}}}{4\, U_{\mathrm{a,max}}\, F\, x_{\mathrm{O_2,a}}}\right)\right) \tag{H.7}$$

The final cathode inlet temperature set point is subjected to two temperature limitations $\triangle T_{\mathrm{an,ca,max,SP}}$ and $\triangle T_{\mathrm{S,ca,max,SP}}$. As shown in equation (H.8), those limitations have to be considered for the adjustment of the designated cathode inlet temperature set point, based upon the measured process value of the anode inlet temperature ($\vartheta_{106,\mathrm{PV}}$) and maximum stack temperature to prevent thermal stress inside the stack.

$$\vartheta_{207,\mathrm{SP}'} = \min(\vartheta_{207,\mathrm{SP}}, (\vartheta_{106,\mathrm{PV}} + \triangle T_{\mathrm{an,ca,max,SP}}), (\vartheta_{\mathrm{S,max,PV}} + \triangle T_{\mathrm{S,ca,max,SP}})) \tag{H.8}$$

The volume flow rate set point of natural gas to the start up burner is calculated based upon the designated heat flow rate set point and the lower heating value of the reference natural gas, as outlined in equation (H.9).

$$\dot{V}_{009,\mathrm{SP}} = \frac{\dot{Q}_{\mathrm{sbu,SP}}\, v_{\mathrm{m,Std}}}{h_{\mathrm{i,NG,R}}} \tag{H.9}$$

As shown in equation (H.10), based upon equation (2.7), the volume flow rate set point of air supplied to the start up burner can be determined using the natural gas volume flow rate and air-to-fuel equivalence ratio set points.

$$\dot{V}_{241,\mathrm{SP}} = \frac{\lambda_{\mathrm{sbu,SP}}\,\dot{V}_{009,\mathrm{SP}}\,K_{\lambda,\mathrm{NG,R}}}{x_{\mathrm{O_2,a}}} \tag{H.10}$$

H.2 Computation of process values

By applying equation (4.1) to equation (2.24), the volume flow rate of transferred oxygen inside the stack can be computed, as shown in equation (H.11)

$$\dot{V}_{\mathrm{O_2,tr,PV}} = \frac{I_{\mathrm{PV}}\,N_{\mathrm{Cell}}\,v_{\mathrm{m,Std}}}{4\,F} \tag{H.11}$$

The recirculation ratio process value is calculated by applying equations (2.14), (2.15), (2.18), (2.19) and (4.1) to equation (2.2), as outlined in equation (H.12). The calculation methodology of $\dot{V}_{102,\mathrm{PV}}$ is shown in equation (G.6).

$$r_{\mathrm{PV}} = \frac{\dot{V}_{102,\mathrm{PV}} - \dot{V}_{007,\mathrm{PV}}}{\dot{V}_{102,\mathrm{PV}} + \dot{V}_{007,\mathrm{PV}}\,K_{\triangle\mathrm{an,R}}} \tag{H.12}$$

By applying equations (2.30), (2.33), (2.34) and (4.1) to equation (2.1), the process value of the oxygen-to-carbon ratio can be computed, as shown in equation (H.13).

$$\Phi_{\mathrm{PV}} = \frac{\dot{n}_{\mathrm{O},102}}{\dot{n}_{\mathrm{C},102}} = \frac{\dot{V}_{007,\mathrm{PV}}\,K_{\mathrm{O}} + 2\,r_{\mathrm{PV}}\,\dot{V}_{\mathrm{O_2,tr,PV}}}{\dot{V}_{007,\mathrm{PV}}\,K_{\mathrm{C}}} \tag{H.13}$$

The system fuel utilization factor process value is calculated by applying equation (4.1) to equation (2.24), as outlined in equation (H.14).

$$U_{\mathrm{f,Sys,PV}} = \frac{4\,\dot{V}_{\mathrm{O_2,tr,PV}}}{\dot{V}_{007,\mathrm{PV}}\,K_{\mathrm{e^-,R}}} \tag{H.14}$$

By applying equations (2.3) and (4.1) to equation (2.24), the fuel utilization factor of the stack process value can be obtained, as shown in equation (H.15).

$$U_{\mathrm{f,S,PV}} = \frac{4\,(1 - r_{\mathrm{PV}})\,\dot{V}_{\mathrm{O_2,tr,PV}}}{\dot{V}_{007,\mathrm{PV}}\,K_{\mathrm{e^-,R}} - 4\,r_{\mathrm{PV}}\,\dot{V}_{\mathrm{O_2,tr,PV}}} \tag{H.15}$$

The air-to-fuel equivalence ratio process value of the start-up burner can be calculated using the flow rate process values of natural gas and air, as shown in equation (H.16) based upon equation (2.7).

$$\lambda_{\mathrm{sbu,PV}} = \frac{\dot{V}_{241,\mathrm{PV}}\,x_{\mathrm{O_2,a}}}{\dot{V}_{009,\mathrm{PV}}\,K_{\lambda,\mathrm{NG,R}}} \tag{H.16}$$

The air-to-fuel equivalence ratio process value of the burner can be obtained via an oxygen balance including the complete supply of oxygen to the system, the internal transport of oxygen from the cathode to the anode side, as well as the utilization inside the start up burner and anode channel, since all separate flows are ultimately merged inside the burner. Therefore, as shown in equation (H.17), $\lambda_{\mathrm{bu,PV}}$ can be solely calculated as a function of the total air volume

flow rate, volume flow rate of transferred oxygen inside the stack, as well as the volume flow rates of natural gas to the start up burner and anode flow path. The calculation methodology of $\dot{V}_{202,\mathrm{PV}}$ is shown in equation (G.5).

$$\lambda_{\mathrm{bu,PV}} = \frac{\dot{V}_{202,\mathrm{PV}}\, x_{\mathrm{O_2,a}} - \dot{V}_{\mathrm{O_2,tr,PV}} - \dot{V}_{009,\mathrm{PV}}\, K_{\lambda,\mathrm{NG,R}}}{\dot{V}_{007,\mathrm{PV}}\, K_{\lambda,\mathrm{NG,R}} - \dot{V}_{\mathrm{O_2,tr,PV}}} \tag{H.17}$$

The process value of the volume flow rate at the cathode inlet is calculated by subtracting the volume flow rate of air to the start up burner from the complete supplied volume flow rate of air, as shown in equation (H.18). The process values of the volume flow rates in the remaining air bypasses, $\dot{V}_{221,\mathrm{PV}}$ and $\dot{V}_{231,\mathrm{PV}}$, are not considered in the computation since both are fed back to the cathode inlet.

$$\dot{V}_{207,\mathrm{PV}} = \dot{V}_{202,\mathrm{PV}} - \dot{V}_{241,\mathrm{PV}} \tag{H.18}$$

By applying equations (2.24) and (4.1) to (2.5), the process value of the air utilization factor can be calculated using a constant mole fraction of oxygen in air, the cathode inlet volume flow rate and the volume flow rate of transferred oxygen inside the stack, as outlined in equation (H.19).

$$U_{\mathrm{a,PV}} = \frac{\dot{V}_{\mathrm{O_2,tr,PV}}}{\dot{V}_{207,\mathrm{PV}}\, x_{\mathrm{O_2,a}}} \tag{H.19}$$

I Measurement overview during methane operation

The time frames, sample sizes, fuel utilization factor and oxygen-to-carbon ratio set points, as well as the reformer and anode outlet temperatures, including the corresponding minima and maxima of the measurements, from the methane operating periods are listed in Table I.1.

Tabelle I.1: CH_4 operating period - Overview of measurement data

Time frame	Samples	Φ			$U_{\mathrm{f,S}}$			$\vartheta_{\mathrm{ref,out}}$ in °C		$\vartheta_{\mathrm{an,out}}$ in °C	
		SP	Min	Max	SP	Min	Max	Min	Max	Min	Max
23.09. - 24.09.2016	10	2.00	2.12	2.17	0.750	0.739	0.762	578.8	581.3	799.1	802.1
12.10. - 13.10.2016	10	2.00	2.07	2.13	0.750	0.741	0.754	576.4	587.0	797.2	802.7
13.10. - 17.10.2016	46	2.00	2.11	2.16	0.725	0.710	0.721	579.3	581.8	802.3	802.9
17.10. - 19.10.2016	23	2.00	2.14	2.20	0.700	0.677	0.689	573.0	583.2	801.6	805.1
17.10. - 24.10.2016	57	2.00	2.10	2.17	0.750	0.740	0.750	576.4	584.6	799.6	803.1
24.10. - 25.10.2016	14	2.10	2.24	2.29	0.750	0.739	0.749	576.7	578.9	801.9	802.6
07.11. - 11.11.2016	45	2.00	2.13	2.19	0.750	0.746	0.757	583.7	590.2	800.3	801.9
25.11. - 28.11.2016	32	2.00	2.11	2.15	0.750	0.749	0.757	585.3	589.9	799.5	801.7
11.01. - 16.01.2017	53	2.00	2.10	2.19	0.750	0.741	0.757	580.9	588.3	793.5	802.4
03.02. - 06.02.2017	31	2.00	2.13	2.16	0.750	0.751	0.759	584.8	585.7	799.1	799.7
15.02. - 17.02.2017	19	2.00	2.04	2.07	0.750	0.765	0.773	588.5	590.3	794.8	797.9

J Measurement overview during natural gas operation with $\mathrm{NM_1}$

The time frames, sample sizes, set points of the leading system variables, utilization of the MFC scaling and the application of the arbitrary safety scaling factor of the recirculation flow rate for

the individual testing periods of the NM_1 are listed in Table J.1. Additionally, the corresponding measured minima and maxima of the oxygen-to-carbon ratio, fuel utilization factor of the stack and temperatures at the reformer and anode outlet are shown in Table J.2.

Tabelle J.1: NM_1 testing period - Overview of measurement data I

Time frame	Samples	I_{SP}	$U_{f,S,SP}$	Φ_{SP}	MFC scaling	Safety scaling factor of recirculation flow rate
25.10. - 26.10.2016	11	24	0.75	2	Off	On
26.10. - 27.10.2016	13	20	0.75	2	Off	On
27.10. - 28.10.2016	8	18	0.75	2	Off	On
28.10. - 31.10.2016	33	24	0.75	2	Off	On
31.10. - 31.10.2016	4	22	0.75	2	Off	On
02.11. - 03.11.2016	13	22	0.75	2	Off	On
03.11. - 07.11.2016	42	24	0.75	2	Off	On
11.11. - 15.11.2016	47	24	0.75	2	Off	On
15.11. - 25.11.2016	114	24	0.70	2	Off	On
17.01. - 27.01.2017	113	24	0.75	2	On	Off
17.02. - 23.02.2017	67	24	0.75	2	On	Off
23.02. - 28.02.2017	59	24	0.70	2	On	Off

Tabelle J.2: NM_1 testing period - Overview of measurement data II

Time frame	I	Φ			$U_{f,S}$			$\vartheta_{ref,out}$ in °C		$\vartheta_{an,out}$ in °C	
	SP	SP	Min	Max	SP	Min	Max	Min	Max	Min	Max
25.10. - 26.10.2016	24	2	1.97	2.02	0.75	0.69	0.70	585.9	595.7	801.0	807.0
26.10. - 27.10.2016	20	2	1.94	1.97	0.75	0.70	0.71	575.6	582.9	799.5	804.1
27.10. - 28.10.2016	18	2	1.90	1.96	0.75	0.70	0.71	564.8	567.7	800.9	802.2
28.10. - 31.10.2016	24	2	1.97	2.01	0.75	0.68	0.70	591.1	595.9	800.0	805.0
31.10. - 31.10.2016	22	2	1.94	1.95	0.75	0.69	0.70	588.8	591.3	803.3	804.4
02.11. - 03.11.2016	22	2	1.92	1.96	0.75	0.68	0.70	589.8	591.8	803.2	804.3
03.11. - 07.11.2016	24	2	1.97	2.09	0.75	0.69	0.73	592.2	596.3	802.1	805.2
11.11. - 15.11.2016	24	2	1.99	2.11	0.75	0.70	0.74	587.7	593.0	801.0	804.2
15.11. - 25.11.2016	24	2	2.04	2.16	0.70	0.63	0.69	586.8	596.0	803.8	806.4
17.01. - 27.01.2017	24	2	1.82	1.95	0.75	0.70	0.73	589.1	599.0	799.1	804.2
17.02. - 23.02.2017	24	2	1.90	2.04	0.75	0.72	0.76	592.1	598.9	797.3	799.4
23.02. - 28.02.2017	24	2	1.97	2.09	0.70	0.67	0.72	592.4	603.6	798.5	804.2

The reference values, as well as averages, minima and maxima of the measured data base of K_C, K_O, K_{e^-} and $M_{NG,in}$, including the deviations between the averages, minima and maxima to the corresponding reference values, are listed in Table J.3.

Tabelle J.3: NM_1 testing period - Natural gas characteristics

	K_C	K_O	K_{e-}	$M_{NG,in}$
Reference value	1.0384	0.0190	8.1245	17.237
Average value of measurement	1.0379	0.0189	8.1389	17.008
Minimum value of measurement	1.0216	0.0058	8.0961	16.562
Maximum value of measurement	1.0571	0.0361	8.2044	17.492
Deviation between average and reference in %	-0.0475	-0.3403	0.1766	-1.331
Deviation between minimum and reference in %	-1.6178	-69.412	-0.3502	-3.9155
Deviation between maximum and reference in %	+1.7952	+89.943	+0.9834	+1.4791

K Derivation of indirectly measured fuel utilization factor

As shown in equation (K.1), equation (2.26) can be rewritten by applying equation (2.27) and an adjusted form of equation (2.25).

$$U_{f,S} = \frac{\dot{n}_{e^-,S,uti}}{\dot{n}_{e^-,an,in}} = \frac{\dot{n}_{e^-,an,in} - \dot{n}_{e^-,an,out}}{\dot{n}_{e^-,an,in}} = \frac{\dot{n}_{an,in}\, K_{e^-,an,in} - \dot{n}_{an,out}\, K_{e^-,an,out}}{\dot{n}_{an,in}\, K_{e^-,an,in}} \tag{K.1}$$

Analogous to equation (3.7), the corresponding electron gas coefficients can be calculated based upon the measured composition and the respective number of releasable electrons of the species, listed in Table F.1. Therefore, equation (K.1) can be further rewritten by applying equations (K.2) and (K.3), yielding equation (K.4).

$$\begin{aligned} K_{e^-,an,in} = \sum_i x_{an,in,i}\, N_{e^-,i} = 8\, x_{an,in,CH_4} + 14\, x_{an,in,C_2H_6} + 20\, x_{an,in,C_3H_8} + 26\, x_{an,in,C_4H_{10}} \\ + 2\, x_{an,in,H_2} + 2\, x_{an,in,CO} \end{aligned} \tag{K.2}$$

$$\begin{aligned} K_{e^-,an,out} = \sum_i x_{an,out,i}\, N_{e^-,i} = 8\, x_{an,out,CH_4} + 14\, x_{an,out,C_2H_6} + 20\, x_{an,out,C_3H_8} \\ + 26\, x_{an,out,C_4H_{10}} + 2\, x_{an,out,H_2} + 2\, x_{an,out,CO} \end{aligned} \tag{K.3}$$

$$U_{f,S} = \frac{\dot{n}_{an,in} \sum_i x_{an,in,i}\, N_{e^-,i} - \dot{n}_{an,out} \sum_i x_{an,out,i}\, N_{e^-,i}}{\dot{n}_{an,in} \sum_i x_{an,in,i}\, N_{e^-,i}} \tag{K.4}$$

Analogous to the derivation of the change in molar quantity coefficient of natural gas, introduced in section 2.2.2.2, the change in the molar flow rate can also be related to the anode inlet flow rate and composition using the molar quantity coefficient of the anode, listed in Table 2.4. The result is shown in equation (K.5), which can be used to express the molar flow rate at the anode outlet solely based upon anode inlet conditions.

$$\triangle\dot{n}_{an} = \dot{n}_{an,in} \sum_i x_{an,in,i}\, \triangle\dot{n}_{an,i} \rightarrow \dot{n}_{an,out} = \dot{n}_{an,in} + \triangle\dot{n}_{an} = \dot{n}_{an,in} \left(1 + \sum_i x_{an,in,i}\, \triangle\dot{n}_{an,i}\right) \tag{K.5}$$

By applying equation (K.5) to equation (K.4), the fuel utilization factor of the stack can be expressed solely as a function of the inlet and outlet compositions, as outlined in equation (K.6).

$$U_{f,S} = 1 - \frac{(1 + \sum_i x_{an,in,i}\, \triangle\dot{n}_{an,i}) \sum_i x_{an,out,i}\, N_{e^-,i}}{\sum_i x_{an,in,i}\, N_{e^-,i}} \tag{K.6}$$

L Coefficients y_1 to y_5 for calculation of molar heat capacity

The coefficients for the calculation of the molar heat capacity for each individual species, defined by McBride et al. [113] at a pressure level of 100 kPA, are listed in Table L.1.

Tabelle L.1: Coefficients for calculation of molar heat capacity

	T < 1000 K					T ≥ 1000 K				
Species	y_1	y_2 in $\frac{1}{K}$	y_3 in $\frac{1}{K^2}$	y_4 in $\frac{1}{K^3}$	y_5 in $\frac{1}{K^4}$	y_1	y_2 in $\frac{1}{K}$	y_3 in $\frac{1}{K^2}$	y_4 in $\frac{1}{K^3}$	y_5 in $\frac{1}{K^4}$
CH_4	5.1	-1.4E-02	4.9E-05	-4.8E-08	1.7E-11	1.6	1.0E-02	-3.4E-06	5.3E-10	-3.2E-14
C_2H_6	4.3	-5.5E-03	6.0E-05	-7.1E-08	2.7E-11	4.0	1.5E-02	-5.5E-06	8.8E-10	-5.2E-14
C_3H_8	4.2	1.7E-03	7.1E-05	-9.2E-08	3.6E-11	6.7	2.1E-02	-7.4E-06	1.2E-09	-7.1E-14
C_4H_{10}	6.1	1.6E-04	9.7E-05	-1.3E-07	5.0E-11	9.4	2.6E-02	-9.2E-06	1.5E-09	-8.9E-14
CO_2	2.4	9.0E-03	-7.1E-06	2.5E-09	-1.4E-13	4.6	2.7E-03	-1.0E-06	1.6E-10	-9.2E-15
N_2	3.5	-1.2E-04	-5.0E-07	2.4E-09	-1.4E-12	3.0	1.4E-03	-4.9E-07	7.9E-11	-4.6E-15
H_2	2.3	8.0E-03	-1.9E-05	2.0E-08	-7.4E-12	2.9	8.3E-04	-1.5E-07	1.5E-11	-6.9E-16
CO	3.6	-6.1E-04	1.0E-06	9.1E-10	-9.0E-13	3.0	1.4E-03	-4.9E-07	7.9E-11	-4.7E-15
H_2O	4.2	-2.0E-03	6.5E-06	-5.5E-09	1.8E-12	2.7	3.0E-03	-7.7E-07	9.4E-11	-4.3E-15
O_2	3.8	-3.0E-03	9.8E-06	-9.7E-09	3.2E-12	3.7	6.6E-04	-1.4E-07	2.1E-11	-1.3E-15

M Sensitivity analysis for NM_1 - Variation of electric current

The variation of I_{SP} between 8 and 24 A is depicted in Figure M.1 for both the Saint-Thegonnec 2014 and Renningen 2016 data sets.

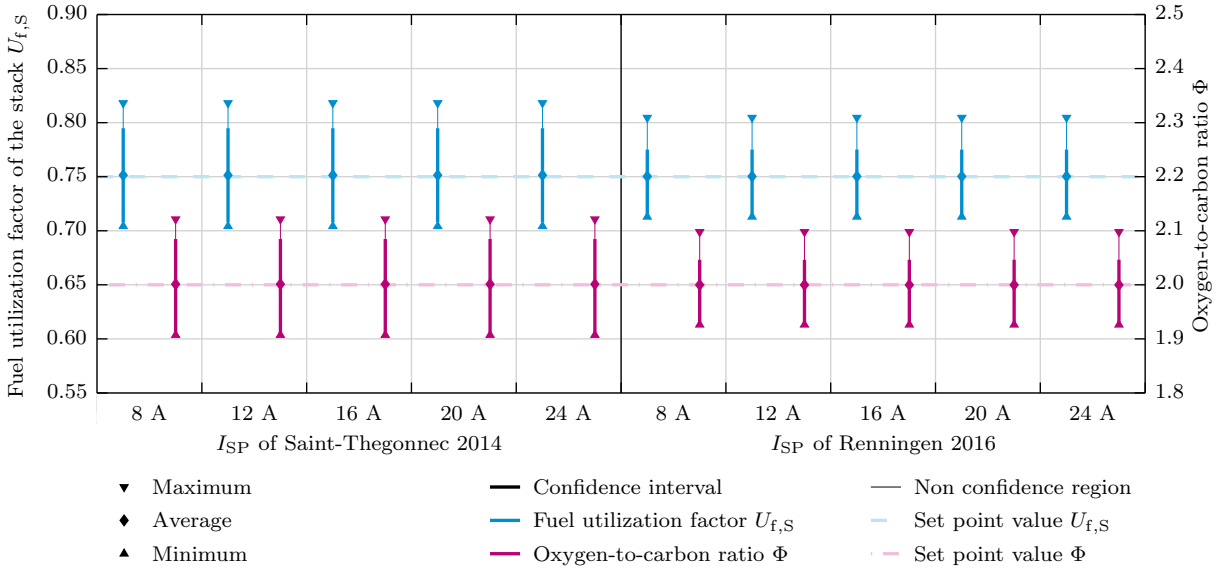

Abbildung M.1: Sensitivity analysis for NM_1 - Variation of electric current set point for Saint-Thegonnec 2014 and Renningen 2016 data set

N Derivation of natural gas mass flow rate control schemes

N.1 General fuel utilization factor equation

As shown in equation (N.1), the fuel utilization factor of the fluctuating state can be calculated by applying equations (2.3) and (2.4) to the constant natural gas mass flow rate constraint between the fluctuating and reference state, as outlined in equation (N.2).

$$\begin{gathered}\dot{m}_{\mathrm{NG,in,F}} = \dot{m}_{\mathrm{NG,in,R}} \\ \frac{\left(1 - r_{\mathrm{F}}\left(1 - U_{\mathrm{f,S,F}}\right)\right) I\, N_{\mathrm{Cell}}\, M_{\mathrm{NG,in,F}}}{U_{\mathrm{f,S,F}}\, F\, K_{\mathrm{e^-,F}}} = \frac{\left(1 - r_{\mathrm{R}}\left(1 - U_{\mathrm{f,S,R}}\right)\right) I\, N_{\mathrm{Cell}}\, M_{\mathrm{NG,in,R}}}{U_{\mathrm{f,S,R}}\, F\, K_{\mathrm{e^-,R}}}\end{gathered} \tag{N.1}$$

$$U_{\mathrm{f,S,F}} = \frac{U_{\mathrm{f,S,R}}\, K_{\mathrm{e^-,R}}\, M_{\mathrm{NG,in,F}}\left(1 - r_{\mathrm{F}}\right)}{K_{\mathrm{e^-,F}}\, M_{\mathrm{NG,in,R}}\left(1 - r_{\mathrm{R}}\left(1 - U_{\mathrm{f,S,R}}\right)\right) - r_{\mathrm{F}}\, U_{\mathrm{f,S,R}}\, K_{\mathrm{e^-,R}}\, M_{\mathrm{NG,in,F}}} \tag{N.2}$$

N.2 Recirculation ratio equations

N.2.1 Natural gas mass flow rate CS 1

First, the constant natural gas mass flow rate constraint is used to express the natural gas molar flow rate of the fluctuating state as a function of the molar flow rate of the reference state, using the natural gas molar masses of both states, as shown in equation (N.3).

$$\dot{m}_{\mathrm{NG,in,F}} = \dot{m}_{\mathrm{NG,in,R}} \rightarrow \dot{n}_{\mathrm{NG,in,F}} = \frac{\dot{m}_{\mathrm{NG,in,F}}}{M_{\mathrm{NG,in,F}}} = \frac{\dot{m}_{\mathrm{NG,in,R}}}{M_{\mathrm{NG,in,F}}} = \frac{\dot{n}_{\mathrm{NG,in,R}}\, M_{\mathrm{NG,in,R}}}{M_{\mathrm{NG,in,F}}} \tag{N.3}$$

Second, the molar flow rate balance equation (2.18) is applied to the constant reformer inlet molar flow rate constraint, as shown in equation (N.4).

$$\dot{n}_{\mathrm{ref,in,F}} = \frac{\dot{n}_{\mathrm{NG,in,F}}\left(1 + r_{\mathrm{F}}\, K_{\triangle\mathrm{an,F}}\right)}{\left(1 - r_{\mathrm{F}}\right)} = \frac{\dot{n}_{\mathrm{NG,in,R}}\left(1 + r_{\mathrm{R}}\, K_{\triangle\mathrm{an,R}}\right)}{\left(1 - r_{\mathrm{R}}\right)} = \dot{n}_{\mathrm{ref,in,R}} \tag{N.4}$$

Lastly, by applying equation (N.3) to equation (N.4), the equation can be solved for the recirculation ratio of the fluctuating state, as outlined in equation (N.5).

$$r_{\mathrm{F}} = \frac{M_{\mathrm{NG,in,F}}\left(1 + r_{\mathrm{R}}\, K_{\triangle\mathrm{an,R}}\right) - M_{\mathrm{NG,in,R}}\left(1 - r_{\mathrm{R}}\right)}{M_{\mathrm{NG,in,F}}\left(1 + r_{\mathrm{R}}\, K_{\triangle\mathrm{an,R}}\right) + K_{\triangle\mathrm{an,F}}\, M_{\mathrm{NG,in,R}}\left(1 - r_{\mathrm{R}}\right)} \tag{N.5}$$

N.2.2 Natural gas mass flow rate CS 2

First, the constant natural gas mass flow rate constraint is used to express the natural gas molar flow rate of the fluctuating state as a function of the molar flow rate of the reference state, using the natural gas molar masses of both states, as shown in equation (N.6).

$$\dot{m}_{\mathrm{NG,in,F}} = \dot{m}_{\mathrm{NG,in,R}} \rightarrow \dot{n}_{\mathrm{NG,in,F}} = \frac{\dot{m}_{\mathrm{NG,in,F}}}{M_{\mathrm{NG,in,F}}} = \frac{\dot{m}_{\mathrm{NG,in,R}}}{M_{\mathrm{NG,in,F}}} = \frac{\dot{n}_{\mathrm{NG,in,R}}\, M_{\mathrm{NG,in,R}}}{M_{\mathrm{NG,in,F}}} \tag{N.6}$$

Second, the molar flow rate balance equation (2.18) is applied to the constant recirculation gas molar flow rate constraint, as shown in equation (N.7).

$$\dot{n}_{\mathrm{rec,F}} = \frac{r_{\mathrm{F}}\, \dot{n}_{\mathrm{NG,in,F}}\left(1 + K_{\triangle\mathrm{an,F}}\right)}{\left(1 - r_{\mathrm{F}}\right)} = \frac{r_{\mathrm{R}}\, \dot{n}_{\mathrm{NG,in,R}}\left(1 + K_{\triangle\mathrm{an,R}}\right)}{\left(1 - r_{\mathrm{R}}\right)} = \dot{n}_{\mathrm{rec,R}} \tag{N.7}$$

Lastly, by applying equation (N.6) to equation (N.7), the equation can be solved for the recirculation ratio of the fluctuating state, as outlined in equation (N.8).

$$r_{\mathrm{F}} = \frac{r_{\mathrm{R}}\, M_{\mathrm{NG,in,F}}\,(1 + K_{\triangle \mathrm{an,R}})}{r_{\mathrm{R}}\, M_{\mathrm{NG,in,F}}\,(1 + K_{\triangle \mathrm{an,R}}) + M_{\mathrm{NG,in,R}}\,(1 - r_{\mathrm{R}})(1 + K_{\triangle \mathrm{an,F}})} \tag{N.8}$$

N.2.3 Natural gas mass flow rate CS 3

The application of the constant natural gas mass flow rate and constant transferred oxygen mass flow rate constraints to the anode outlet, reformer inlet, reformer outlet or recirculation gas mass flow rate balance yields an identical result, in particular a constant recirculation ratio between the fluctuating and reference states. The mass flow rate constraint equations (N.9) and (N.10) are applied to one of the mass flow rate balance constraint equations (N.11), (N.12) or (N.13), ultimately yielding the recirculation ratio of the fluctuating state, as shown in equation (N.14).

$$\dot{m}_{\mathrm{NG,in,F}} = \dot{m}_{\mathrm{NG,in,R}} \tag{N.9}$$

$$\dot{m}_{\mathrm{O_2,tr,F}} = \dot{m}_{\mathrm{O_2,tr,R}} \tag{N.10}$$

$$\dot{m}_{\mathrm{an,out,F}} = \frac{\dot{m}_{\mathrm{NG,in,F}} + \dot{m}_{\mathrm{O_2,tr,F}}}{1 - r_{\mathrm{F}}} = \frac{\dot{m}_{\mathrm{NG,in,R}} + \dot{m}_{\mathrm{O_2,tr,R}}}{1 - r_{\mathrm{R}}} = \dot{m}_{\mathrm{an,out,R}} \tag{N.11}$$

$$\dot{m}_{\mathrm{ref,in/out,F}} = \frac{\dot{m}_{\mathrm{NG,in,F}} + r_{\mathrm{F}}\, \dot{m}_{\mathrm{O_2,tr,F}}}{1 - r_{\mathrm{F}}} = \frac{\dot{m}_{\mathrm{NG,in,R}} + r_{\mathrm{R}}\, \dot{m}_{\mathrm{O_2,tr,R}}}{1 - r_{\mathrm{R}}} = \dot{m}_{\mathrm{ref,in/out,R}} \tag{N.12}$$

$$\dot{m}_{\mathrm{rec,F}} = \frac{r_{\mathrm{F}}\,(\dot{m}_{\mathrm{NG,in,F}} + \dot{m}_{\mathrm{O_2,tr,F}})}{1 - r_{\mathrm{F}}} = \frac{r_{\mathrm{R}}\,(\dot{m}_{\mathrm{NG,in,R}} + \dot{m}_{\mathrm{O_2,tr,R}})}{1 - r_{\mathrm{R}}} = \dot{m}_{\mathrm{rec,R}} \tag{N.13}$$

$$r_{\mathrm{F}} = r_{\mathrm{R}} \tag{N.14}$$

An identical result can be obtained by applying the constant recirculation gas mass flow rate constraint to either the reformer inlet, reformer outlet or anode outlet mass flow rate balance. As shown in equation (N.15), the mass flow rate balance equation (2.10) is used to rewrite the mass flow rate constraint. By applying equation (N.15) to one of the equations (N.11) or (N.12), a constant recirculation ratio and constant natural gas mass flow rate are obtained.

$$\begin{aligned} &\dot{m}_{\mathrm{rec,F}} = \dot{m}_{\mathrm{rec,R}} \\ \rightarrow\ &\dot{m}_{\mathrm{NG,in,F}} = \frac{\dot{m}_{\mathrm{NG,in,R}}\,(1 - r_{\mathrm{F}}) + \dot{m}_{\mathrm{O_2,tr,R}}\,(r_{\mathrm{R}} - r_{\mathrm{F}})}{1 - r_{\mathrm{R}}} \end{aligned} \tag{N.15}$$

Another possibility, obtaining an identical result with a constant natural gas mass flow rate, is the application of the constant recirculation ratio constraint equation (N.14) to either the reformer inlet, reformer outlet, anode outlet or recirculation gas mass flow rate constraint equations (N.11), (N.12) or (N.13).

N.2.4 Natural gas mass flow rate CS 4

First, the constant natural gas mass flow rate constraint is used to express the natural gas molar flow rate of the fluctuating state as a function of the molar flow rate of the reference state, using the natural gas molar masses of both states, as shown in equation (N.16).

$$\dot{m}_{\mathrm{NG,in,F}} = \dot{m}_{\mathrm{NG,in,R}} \rightarrow \dot{n}_{\mathrm{NG,in,F}} = \frac{\dot{m}_{\mathrm{NG,in,F}}}{M_{\mathrm{NG,in,F}}} = \frac{\dot{m}_{\mathrm{NG,in,R}}}{M_{\mathrm{NG,in,F}}} = \frac{\dot{n}_{\mathrm{NG,in,R}}\, M_{\mathrm{NG,in,R}}}{M_{\mathrm{NG,in,F}}} \tag{N.16}$$

Second, the molar flow rate balance equation (2.19) is applied to the constant anode outlet molar flow rate constraint, as shown in equation (N.17).

$$\dot{n}_{\mathrm{an,out,F}} = \frac{\dot{n}_{\mathrm{NG,in,F}}\,(1 + K_{\triangle\mathrm{an,F}})}{(1 - r_{\mathrm{F}})} = \frac{\dot{n}_{\mathrm{NG,in,R}}\,(1 + K_{\triangle\mathrm{an,R}})}{(1 - r_{\mathrm{R}})} = \dot{n}_{\mathrm{an,out,R}} \tag{N.17}$$

Lastly, by applying equation (N.16) to equation (N.17), the equation can be solved for the recirculation ratio of the fluctuating state, as outlined in equation (N.18).

$$r_{\mathrm{F}} = 1 - \frac{M_{\mathrm{NG,in,R}}\,(1 - r_{\mathrm{R}})(1 + K_{\triangle\mathrm{an,F}})}{M_{\mathrm{NG,in,F}}\,(1 + K_{\triangle\mathrm{an,R}})} \tag{N.18}$$

O Derivation of natural gas volume flow rate control schemes

O.1 General fuel utilization factor equation

As shown in equation (O.2), the fuel utilization factor of the fluctuating state can be calculated by applying equations (2.3) and (2.4) to the constant natural gas molar flow rate constraint between the fluctuating and reference state, as outlined in equation (O.1).

$$\begin{gathered} \dot{n}_{\mathrm{NG,in,F}} = \dot{n}_{\mathrm{NG,in,R}} \\ \frac{(1 - r_{\mathrm{F}}\,(1 - U_{\mathrm{f,S,F}}))\, I\, N_{\mathrm{Cell}}}{U_{\mathrm{f,S,F}}\, F\, K_{\mathrm{e^-,F}}} = \frac{(1 - r_{\mathrm{R}}\,(1 - U_{\mathrm{f,S,R}}))\, I\, N_{\mathrm{Cell}}}{U_{\mathrm{f,S,R}}\, F\, K_{\mathrm{e^-,R}}} \end{gathered} \tag{O.1}$$

$$U_{\mathrm{f,S,F}} = \frac{U_{\mathrm{f,S,R}}\, K_{\mathrm{e^-,R}}\,(1 - r_{\mathrm{F}})}{K_{\mathrm{e^-,F}}\,(1 - r_{\mathrm{R}}\,(1 - U_{\mathrm{f,S,R}})) - r_{\mathrm{F}}\, U_{\mathrm{f,S,R}}\, K_{\mathrm{e^-,R}}} \tag{O.2}$$

O.2 Recirculation ratio equations

O.2.1 Natural gas volume flow rate CS 1

The molar flow rate balance equation (2.18) is applied to the constant reformer inlet molar flow rate constraint, as shown in equation (O.3). Analogously, the recirculation gas molar flow rate balance can be used as a basic constraint, since it is connected to the reformer inlet molar flow rate via the natural gas molar flow rate. Equation (2.18) is applied to the constant recirculation gas molar flow rate constraint, ultimately yielding equation (O.4).

$$\dot{n}_{\mathrm{ref,in,F}} = \frac{\dot{n}_{\mathrm{NG,in,F}}\,(1 + r_{\mathrm{F}}\, K_{\triangle\mathrm{an,F}})}{(1 - r_{\mathrm{F}})} = \frac{\dot{n}_{\mathrm{NG,in,R}}\,(1 + r_{\mathrm{R}}\, K_{\triangle\mathrm{an,R}})}{(1 - r_{\mathrm{R}})} = \dot{n}_{\mathrm{ref,in,R}} \tag{O.3}$$

$$\dot{n}_{\mathrm{rec,F}} = \frac{r_{\mathrm{F}}\, \dot{n}_{\mathrm{NG,in,F}}\,(1 + K_{\triangle\mathrm{an,F}})}{(1 - r_{\mathrm{F}})} = \frac{r_{\mathrm{R}}\, \dot{n}_{\mathrm{NG,in,R}}\,(1 + K_{\triangle\mathrm{an,R}})}{(1 - r_{\mathrm{R}})} = \dot{n}_{\mathrm{rec,R}} \tag{O.4}$$

By applying the constant natural gas molar flow rate constraint to equation (O.3) or (O.4), both equations can be solved for the recirculation ratio of the fluctuating state yielding an identical result, which is outlined in equation (O.5).

$$r_{\mathrm{F}} = \frac{r_{\mathrm{R}}\,(1 + K_{\triangle\mathrm{an,R}})}{1 + K_{\triangle\mathrm{an,F}} + r_{\mathrm{R}}\,(K_{\triangle\mathrm{an,R}} - K_{\triangle\mathrm{an,F}})} \tag{O.5}$$

An identical result can be obtained by applying the constant recirculation gas molar flow rate constraint to the reformer inlet molar flow rate balance. As shown in equation (O.6), the molar flow rate balance equation (2.20) is used to rewrite the constant recirculation gas molar flow rate constraint. The application of equation (O.6) to equation (O.4) also results in equation (O.5).

$$\begin{aligned} &\dot{n}_{\mathrm{rec,F}} = \dot{n}_{\mathrm{rec,R}} \\ \rightarrow\ &\dot{n}_{\mathrm{NG,in,F}} = \frac{r_{\mathrm{R}}\,\dot{n}_{\mathrm{NG,in,R}}\,(1 + K_{\triangle\mathrm{an,R}})\,(1 - r_{\mathrm{F}})}{r_{\mathrm{F}}\,(1 - r_{\mathrm{R}})\,(1 + K_{\triangle\mathrm{an,F}})} \end{aligned} \tag{O.6}$$

O.2.2 Natural gas volume flow rate CS 3

First, the constant natural gas molar flow rate constraint is used to express the natural gas mass flow rate of the fluctuating state as a function of the mass flow rate of the reference state, using the natural gas molar masses of both states, as shown in equation (O.7).

$$\dot{n}_{\mathrm{NG,in,F}} = \dot{n}_{\mathrm{NG,in,R}} \rightarrow \dot{m}_{\mathrm{NG,in,F}} = \dot{n}_{\mathrm{NG,in,F}}\,M_{\mathrm{NG,in,F}} = \frac{\dot{m}_{\mathrm{NG,in,R}}\,M_{\mathrm{NG,in,F}}}{M_{\mathrm{NG,in,R}}} \tag{O.7}$$

Second, the transferred mass flow rate of oxygen inside the stack is expressed as a function of the reference state in accordance to equations (2.13) and (2.3), as outlined in equation (O.8).

$$\dot{m}_{\mathrm{O_2,tr,F}} = \dot{m}_{\mathrm{O_2,tr,R}} = \frac{\dot{m}_{\mathrm{NG,in,R}}\,U_{\mathrm{f,S,R}}\,K_{\mathrm{e^-,R}}\,M_{\mathrm{O_2}}}{4\,M_{\mathrm{NG,in,R}}\,(1 - r_{\mathrm{R}}\,(1 - U_{\mathrm{f,S,R}}))} \tag{O.8}$$

Third, the mass flow rate balance equation (2.10) is applied to the constant recirculation gas mass flow rate constraint, as shown in equation (O.9).

$$\dot{m}_{\mathrm{rec,F}} = \frac{r_{\mathrm{F}}\,(\dot{m}_{\mathrm{NG,in,F}} + \dot{m}_{\mathrm{O_2,tr,F}})}{1 - r_{\mathrm{F}}} = \frac{r_{\mathrm{R}}\,(\dot{m}_{\mathrm{NG,in,R}} + \dot{m}_{\mathrm{O_2,tr,R}})}{1 - r_{\mathrm{R}}} = \dot{m}_{\mathrm{rec,R}} \tag{O.9}$$

Lastly, by applying equations (O.7) and (O.8) to equation (O.9), the equation can be solved for the recirculation ratio of the fluctuating state, as outlined in equation (O.10).

$$r_{\mathrm{F}} = \frac{r_{\mathrm{R}}\left(4\,M_{\mathrm{NG,in,R}}\,(1 - r_{\mathrm{R}}\,(1 - U_{\mathrm{f,S,R}})) + U_{\mathrm{f,S,R}}\,K_{\mathrm{e^-,R}}\,M_{\mathrm{O_2}}\right)}{U_{\mathrm{f,S,R}}\,K_{\mathrm{e^-,R}}\,M_{\mathrm{O_2}} + 4\,(1 - r_{\mathrm{R}}\,(1 - U_{\mathrm{f,S,R}}))\,(M_{\mathrm{NG,in,F}} + r_{\mathrm{R}}\,(M_{\mathrm{NG,in,R}} - M_{\mathrm{NG,in,F}}))} \tag{O.10}$$

O.2.3 Natural gas volume flow rate CS 4

The molar flow balance equation (2.19) is applied to the constant anode outlet molar flow rate constraint, as outlined in equation (O.11).

$$\dot{n}_{\mathrm{an,out,F}} = \frac{\dot{n}_{\mathrm{NG,in,F}}\,(1 + K_{\triangle\mathrm{an,F}})}{(1 - r_{\mathrm{F}})} = \frac{\dot{n}_{\mathrm{NG,in,R}}\,(1 + K_{\triangle\mathrm{an,R}})}{(1 - r_{\mathrm{R}})} = \dot{n}_{\mathrm{an,out,R}} \tag{O.11}$$

By applying the constant natural gas molar flow rate constraint to equation (O.11), the equation can be solved for the recirculation ratio of the fluctuating state, as shown in equation (O.12).

$$r_{\mathrm{F}} = 1 - \frac{(1 - r_{\mathrm{R}})\,(1 + K_{\triangle \mathrm{an,F}})}{(1 + K_{\triangle \mathrm{an,R}})} \tag{O.12}$$

O.2.4 Natural gas volume flow rate CS 5

First, the constant natural gas molar flow rate constraint is used to express the natural gas mass flow rate of the fluctuating state as a function of the mass flow rate of the reference state, using the natural gas molar masses of both states, as shown in equation (O.13).

$$\dot{n}_{\mathrm{NG,in,F}} = \dot{n}_{\mathrm{NG,in,R}} \rightarrow \dot{m}_{\mathrm{NG,in,F}} = \dot{n}_{\mathrm{NG,in,F}}\, M_{\mathrm{NG,in,F}} = \frac{\dot{m}_{\mathrm{NG,in,R}}\, M_{\mathrm{NG,in,F}}}{M_{\mathrm{NG,in,R}}} \tag{O.13}$$

Second, the transferred mass flow rate of oxygen inside the stack is expressed as a function of the reference state in accordance to equations (2.13) and (2.3), as outlined in equation (O.14).

$$\dot{m}_{\mathrm{O_2,tr,F}} = \dot{m}_{\mathrm{O_2,tr,R}} = \frac{\dot{m}_{\mathrm{NG,in,R}}\, U_{\mathrm{f,S,R}}\, K_{\mathrm{e^-,R}}\, M_{\mathrm{O_2}}}{4\, M_{\mathrm{NG,in,R}}\,(1 - r_{\mathrm{R}}\,(1 - U_{\mathrm{f,S,R}}))} \tag{O.14}$$

Third, the mass flow rate balance equation (2.9) is applied to the constant anode outlet mass flow rate constraint, as shown in equation (O.15). Analogously, the reformer inlet or reformer outlet mass flow rate balance can be used as a basic constraint, since both are connected to the anode outlet mass flow rate via the transferred mass flow rate of oxygen inside the stack, which is outlined in equation (O.16).

$$\dot{m}_{\mathrm{an,out,F}} = \frac{\dot{m}_{\mathrm{NG,in,F}} + \dot{m}_{\mathrm{O_2,tr,F}}}{1 - r_{\mathrm{F}}} = \frac{\dot{m}_{\mathrm{NG,in,R}} + \dot{m}_{\mathrm{O_2,tr,R}}}{1 - r_{\mathrm{R}}} = \dot{m}_{\mathrm{an,out,R}} \tag{O.15}$$

$$\dot{m}_{\mathrm{ref,in/out,F}} = \frac{\dot{m}_{\mathrm{NG,in,F}} + r_{\mathrm{F}}\, \dot{m}_{\mathrm{O_2,tr,F}}}{1 - r_{\mathrm{F}}} = \frac{\dot{m}_{\mathrm{NG,in,R}} + r_{\mathrm{R}}\, \dot{m}_{\mathrm{O_2,tr,R}}}{1 - r_{\mathrm{R}}} = \dot{m}_{\mathrm{ref,in/out,R}} \tag{O.16}$$

Lastly, by applying equations (O.13) and (O.14) to equation (O.15) or equation (O.16), both equations can be analogously solved for the recirculation ratio of the fluctuating state, as outlined in equation (O.17).

$$r_{\mathrm{F}} = \frac{4\,(1 - r_{\mathrm{R}}\,(1 - U_{\mathrm{f,S,R}}))\,(M_{\mathrm{NG,in,R}} + M_{\mathrm{NG,in,F}}\,(r_{\mathrm{R}} - 1)) + r_{\mathrm{R}}\, U_{\mathrm{f,S,R}}\, K_{\mathrm{e^-,R}}\, M_{\mathrm{O_2}}}{U_{\mathrm{f,S,R}}\, K_{\mathrm{e^-,R}}\, M_{\mathrm{O_2}} + 4\, M_{\mathrm{NG,in,R}}\,(1 - r_{\mathrm{R}}\,(1 - U_{\mathrm{f,S,R}}))} \tag{O.17}$$

P Derivation of reformer inlet volume flow rate control schemes

P.1 General fuel utilization factor equation

As outlined in equation (P.1), by solving the constant reformer inlet molar flow rate constraint between the fluctuating and reference state using equations (2.3) and (2.4), the fuel utilization factor of the fluctuating state can be calculated, as shown in equation (P.2).

$$\begin{gathered}
\dot{n}_{\mathrm{ref,in,F}} = \frac{\dot{n}_{\mathrm{NG,in,F}}\,(1 + r_{\mathrm{F}}\, K_{\triangle \mathrm{an,F}})}{(1 - r_{\mathrm{F}})} = \frac{\dot{n}_{\mathrm{NG,in,R}}\,(1 + r_{\mathrm{R}}\, K_{\triangle \mathrm{an,R}})}{(1 - r_{\mathrm{R}})} = \dot{n}_{\mathrm{ref,in,R}} \\
\frac{I\, N_{\mathrm{Cell}}\,(1 - r_{\mathrm{F}}\,(1 - U_{\mathrm{f,S,F}}))\,(1 + r_{\mathrm{F}}\, K_{\triangle \mathrm{an,F}})}{U_{\mathrm{f,S,F}}\, F\, K_{\mathrm{e^-,F}}\,(1 - r_{\mathrm{F}})} = \frac{I\, N_{\mathrm{Cell}}\,(1 - r_{\mathrm{R}}\,(1 - U_{\mathrm{f,S,R}}))\,(1 + r_{\mathrm{R}}\, K_{\triangle \mathrm{an,R}})}{U_{\mathrm{f,S,R}}\, F\, K_{\mathrm{e^-,R}}\,(1 - r_{\mathrm{R}})}
\end{gathered} \tag{P.1}$$

$$U_{\mathrm{f,S,F}} = \frac{U_{\mathrm{f,S,R}}\, K_{\mathrm{e^-,R}}\, (1 - r_{\mathrm{R}})\, (1 - r_{\mathrm{F}})\, (1 + r_{\mathrm{F}}\, K_{\triangle \mathrm{an,F}})}{\left(\begin{array}{r} K_{\mathrm{e^-,F}}\, (1 - r_{\mathrm{F}})\, (1 - r_{\mathrm{R}}\, (1 - U_{\mathrm{f,S,R}}))\, (1 + r_{\mathrm{R}}\, K_{\triangle \mathrm{an,R}}) \\ - r_{\mathrm{F}}\, U_{\mathrm{f,S,R}}\, K_{\mathrm{e^-,R}}\, (1 - r_{\mathrm{R}})\, (1 + r_{\mathrm{F}}\, K_{\triangle \mathrm{an,F}}) \end{array} \right)} \tag{P.2}$$

P.2 Recirculation ratio equation of reformer inlet volume flow rate CS 1

First, the constant reformer inlet molar flow rate constraint is used to express the natural gas mass flow rate of the fluctuating state as a function of the mass flow rate of the reference state, using the natural gas molar masses of both states, as shown in equation (P.4) based upon the modification of the molar flow rate balance constraint equation (P.3).

$$\dot{n}_{\mathrm{ref,in,F}} = \frac{\dot{n}_{\mathrm{NG,in,F}}\, (1 + r_{\mathrm{F}}\, K_{\triangle \mathrm{an,F}})}{(1 - r_{\mathrm{F}})} = \frac{\dot{n}_{\mathrm{NG,in,R}}\, (1 + r_{\mathrm{R}}\, K_{\triangle \mathrm{an,R}})}{(1 - r_{\mathrm{R}})} = \dot{n}_{\mathrm{ref,in,R}} \tag{P.3}$$

$$\dot{m}_{\mathrm{NG,in,F}} = \frac{\dot{m}_{\mathrm{NG,in,R}}\, M_{\mathrm{NG,in,F}}\, (1 + r_{\mathrm{R}}\, K_{\triangle \mathrm{an,R}})\, (1 - r_{\mathrm{F}})}{M_{\mathrm{NG,in,R}}\, (1 - r_{\mathrm{R}})\, (1 + r_{\mathrm{F}}\, K_{\triangle \mathrm{an,F}})} \tag{P.4}$$

Second, the transferred mass flow rate of oxygen inside the stack is expressed as a function of the reference state in accordance to equations (2.13) and (2.3), as outlined in equation (P.5).

$$\dot{m}_{\mathrm{O_2,tr,F}} = \dot{m}_{\mathrm{O_2,tr,R}} = \frac{\dot{m}_{\mathrm{NG,in,R}}\, U_{\mathrm{f,S,R}}\, K_{\mathrm{e^-,R}}\, M_{\mathrm{O_2}}}{4\, M_{\mathrm{NG,in,R}}\, (1 - r_{\mathrm{R}}\, (1 - U_{\mathrm{f,S,R}}))} \tag{P.5}$$

Third, the mass flow rate balance equation (2.10) is applied to the constant recirculation gas mass flow rate constraint, as shown in equation (P.6).

$$\dot{m}_{\mathrm{rec,F}} = \frac{r_{\mathrm{F}}\, (\dot{m}_{\mathrm{NG,in,F}} + \dot{m}_{\mathrm{O_2,tr,F}})}{1 - r_{\mathrm{F}}} = \frac{r_{\mathrm{R}}\, (\dot{m}_{\mathrm{NG,in,R}} + \dot{m}_{\mathrm{O_2,tr,R}})}{1 - r_{\mathrm{R}}} = \dot{m}_{\mathrm{rec,R}} \tag{P.6}$$

Lastly, by applying equations (P.4) and (P.5) to equation (P.6), the equation can be solved for the recirculation ratio of the fluctuating state, yielding a quadratic equation, as outlined in equation (P.7). The coefficients α, β and γ of the quadratic equation are shown in equations (P.8), (P.9) and (P.10).

$$\alpha_{\mathrm{R_iV_1}}\, (r_{\mathrm{F}})^2 + \beta_{\mathrm{R_iV_1}}\, r_{\mathrm{F}} + \gamma_{\mathrm{R_iV_1}} = 0 \tag{P.7}$$

$$\begin{aligned} \alpha_{\mathrm{R_iV_1}} = {} & 4\, (1 - r_{\mathrm{R}}\, (1 - U_{\mathrm{f,S,R}}))\, (M_{\mathrm{NG,in,F}}\, (1 + r_{\mathrm{R}}\, K_{\triangle \mathrm{an,R}}) - r_{\mathrm{R}}\, K_{\triangle \mathrm{an,F}}\, M_{\mathrm{NG,in,R}}) \\ & - U_{\mathrm{f,S,R}}\, K_{\triangle \mathrm{an,F}}\, K_{\mathrm{e^-,R}}\, M_{\mathrm{O_2}} \end{aligned} \tag{P.8}$$

$$\begin{aligned} \beta_{\mathrm{R_iV_1}} = {} & (K_{\triangle \mathrm{an,F}} - 1)\, \left(4\, r_{\mathrm{R}}\, M_{\mathrm{NG,in,R}}\, (1 - r_{\mathrm{R}}\, (1 - U_{\mathrm{f,S,R}})) + r_{\mathrm{R}}\, U_{\mathrm{f,S,R}}\, K_{\mathrm{e^-,R}}\, M_{\mathrm{O_2}}\right) \\ & - 4\, M_{\mathrm{NG,in,F}}\, (1 + r_{\mathrm{R}}\, K_{\triangle \mathrm{an,R}})\, (1 - r_{\mathrm{R}}\, (1 - U_{\mathrm{f,S,R}})) - U_{\mathrm{f,S,R}}\, K_{\mathrm{e^-,R}}\, M_{\mathrm{O_2}}\, (1 - r_{\mathrm{R}}) \end{aligned} \tag{P.9}$$

$$\gamma_{\mathrm{R_iV_1}} = 4\, r_{\mathrm{R}}\, M_{\mathrm{NG,in,R}}\, (1 - r_{\mathrm{R}}\, (1 - U_{\mathrm{f,S,R}})) + r_{\mathrm{R}}\, U_{\mathrm{f,S,R}}\, K_{\mathrm{e^-,R}}\, M_{\mathrm{O_2}} \tag{P.10}$$

The quadratic formula is applied to obtain a solution for the recirculation ratio of the fluctuating state, as outlined in equation (P.11). It should be noted that only the negative solution yields physical valid results with a recirculation ratio between 0 and 1.

$$r_{\mathrm{F}} = \frac{-\beta_{\mathrm{R_iV_1}} - \sqrt{(\beta_{\mathrm{R_iV_1}})^2 - 4\, \alpha_{\mathrm{R_iV_1}}\, \gamma_{\mathrm{R_iV_1}}}}{2\, \alpha_{\mathrm{R_iV_1}}} \tag{P.11}$$

Q Derivation of reformer outlet volume flow rate control schemes

Q.1 General fuel utilization factor equation

As outlined in equation (2.26), the utilized flow rate of electrons can be calculated using the fuel utilization factor of the stack and the anode inlet electron flow rate, which is identical to the reformer outlet flow rate. By using the constant reformer outlet molar flow rate constraint and assuming an identical utilization of electrons for the fluctuating and reference state, the fuel utilization factor of the fluctuating state can be derived, as shown in equation (Q.2) using equation (Q.1). In equation (Q.2), the electron coefficients at the reformer outlet of the fluctuating and reference states are a both functions of the corresponding equilibrium composition and the related number of releasable electrons per species, as outlined in Table 3.2.

$$\dot{n}_{\mathrm{ref,out,F}} = \dot{n}_{\mathrm{ref,out,R}} \tag{Q.1}$$

$$\begin{aligned} \dot{n}_{\mathrm{e^-,S,uti,F}} &= \dot{n}_{\mathrm{e^-,S,uti,R}} \\ U_{\mathrm{f,S,F}}\, \dot{n}_{\mathrm{ref,out,F}}\, K_{\mathrm{e^-,ref,out,F}} &= U_{\mathrm{f,S,R}}\, \dot{n}_{\mathrm{ref,out,R}}\, K_{\mathrm{e^-,ref,out,R}} \\ \rightarrow U_{\mathrm{f,S,F}} &= U_{\mathrm{f,S,R}}\, \frac{K_{\mathrm{e^-,ref,out,R}}}{K_{\mathrm{e^-,ref,out,F}}} \end{aligned} \tag{Q.2}$$

Q.2 Recirculation ratio equations

Q.2.1 Reformer outlet volume flow rate CS 1

For the designated recirculation ratio constraint equation (Q.3), the fuel utilization constraint equation (Q.2) is iteratively solved, using the corresponding reformer outlet equilibrium state, until the reformer outlet molar flow rate constraint and the complete mass balance are valid.

$$r_{\mathrm{F}} = r_{\mathrm{R}} \tag{Q.3}$$

Q.2.2 Reformer outlet volume flow rate CS 2

The constant natural gas mass flow rate constraint equation (Q.4) and transferred mass flow of oxygen constraint equation (Q.5) are used to iteratively solve the fuel utilization constraint equation (Q.2), using the corresponding reformer outlet equilibrium state and the rewritten recirculation ratio, shown in equation (Q.6), based upon equations (2.2), (2.8) and (2.9), until the reformer outlet molar flow rate constraint and the complete mass balance are valid.

$$\dot{m}_{\mathrm{NG,in,F}} = \dot{m}_{\mathrm{NG,in,R}} \tag{Q.4}$$

$$\dot{m}_{\mathrm{O_2,tr,F}} = \dot{m}_{\mathrm{O_2,tr,R}} \tag{Q.5}$$

$$r_{\mathrm{F}} = \frac{\dot{m}_{\mathrm{ref,out,F}} - \dot{m}_{\mathrm{NG,in,F}}}{\dot{m}_{\mathrm{ref,out,F}} + \dot{m}_{\mathrm{O_2,tr,F}}} = \frac{\dot{n}_{\mathrm{ref,out,F}}\, M_{\mathrm{ref,out,F}} - \dot{m}_{\mathrm{NG,in,R}}}{\dot{n}_{\mathrm{ref,out,F}}\, M_{\mathrm{ref,out,F}} + \dot{m}_{\mathrm{O_2,tr,R}}} \tag{Q.6}$$

Q.2.3 Reformer outlet volume flow rate CS 3

The constant natural gas molar flow rate constraint equation (Q.7) and transferred mass flow of oxygen constraint equation (Q.8) are used to iteratively solve the fuel utilization constraint equation (Q.2), using the corresponding reformer outlet equilibrium state and the rewritten recirculation ratio, shown in equation (Q.9), based upon equations (2.2), (2.8) and (2.9), until the reformer outlet molar flow rate constraint and the complete mass balance are valid.

$$\dot{n}_{\mathrm{NG,in,F}} = \dot{n}_{\mathrm{NG,in,R}} \tag{Q.7}$$

$$\dot{m}_{\mathrm{O_2,tr,F}} = \dot{m}_{\mathrm{O_2,tr,R}} \tag{Q.8}$$

$$r_{\mathrm{F}} = \frac{\dot{m}_{\mathrm{ref,out,F}} - \dot{m}_{\mathrm{NG,in,F}}}{\dot{m}_{\mathrm{ref,out,F}} + \dot{m}_{\mathrm{O_2,tr,F}}} = \frac{\dot{n}_{\mathrm{ref,out,F}}\, M_{\mathrm{ref,out,F}} - \dot{n}_{\mathrm{NG,in,R}}\, M_{\mathrm{NG,in,F}}}{\dot{n}_{\mathrm{ref,out,F}}\, M_{\mathrm{ref,out,F}} + \dot{m}_{\mathrm{O_2,tr,R}}} \tag{Q.9}$$

Q.2.4 Reformer outlet volume flow rate CS 4

The constant anode outlet mass flow rate constraint equation (Q.10) and transferred mass flow of oxygen constraint equation (Q.11) are used to iteratively solve the fuel utilization constraint equation (Q.2), using the corresponding reformer outlet equilibrium state and the rewritten recirculation ratio, shown in equation (Q.12), based upon equations (2.2), (2.8) and (2.9), until the reformer outlet molar flow rate constraint and the complete mass balance are valid. The natural gas mass flow rate of the fluctuating state, used in equation (Q.12), is calculated at the end of each iterative step with the help of the computed fuel utilization factor and recirculation ratio of the previous iterative step.

$$\dot{m}_{\mathrm{an,out,F}} = \dot{m}_{\mathrm{an,out,R}} \tag{Q.10}$$

$$\dot{m}_{\mathrm{O_2,tr,F}} = \dot{m}_{\mathrm{O_2,tr,R}} \tag{Q.11}$$

$$r_{\mathrm{F}} = \frac{\dot{m}_{\mathrm{ref,out,F}} - \dot{m}_{\mathrm{NG,in,F}}}{\dot{m}_{\mathrm{an,out,F}}} = \frac{\dot{m}_{\mathrm{an,out,R}} - \dot{m}_{\mathrm{O_2,tr,R}} - \dot{m}_{\mathrm{NG,in,F}}}{\dot{m}_{\mathrm{an,out,R}}} \tag{Q.12}$$

Additionally, using the constant reformer inlet mass flow rate constraint equation (Q.13) instead of the constant anode outlet mass flow rate constraint equation (Q.10) yields an identical result, since both constraints are correlated by mass balance equations (2.8) and (2.9).

$$\dot{m}_{\mathrm{ref,in,F}} = \dot{m}_{\mathrm{ref,in,R}} \tag{Q.13}$$

Q.2.5 Reformer outlet volume flow rate CS 5

The constant anode outlet molar flow rate constraint equation (Q.14) is used to iteratively solve the fuel utilization constraint equation (Q.2), using the corresponding reformer outlet and anode outlet equilibrium states, as well as the rewritten recirculation ratio, shown in equation (Q.15), based upon equations (2.2) and (2.8), until the reformer outlet molar flow rate constraint and the complete mass balance are valid. The natural gas mass flow rate of the fluctuating state,

used in equation (Q.15), is calculated at the end of each iterative step with the help of the computed fuel utilization factor and recirculation ratio of the previous iterative step.

$$\dot{n}_{\mathrm{an,out,F}} = \dot{n}_{\mathrm{an,out,R}} \tag{Q.14}$$

$$r_{\mathrm{F}} = \frac{\dot{m}_{\mathrm{ref,out,F}} - \dot{m}_{\mathrm{NG,in,F}}}{\dot{m}_{\mathrm{an,out,F}}} = \frac{\dot{n}_{\mathrm{ref,out,F}}\, M_{\mathrm{ref,out,F}} - \dot{m}_{\mathrm{NG,in,F}}}{\dot{n}_{\mathrm{an,out,R}}\, M_{\mathrm{an,out,F}}} \tag{Q.15}$$

Q.2.6 Reformer outlet volume flow rate CS 6

The constant recirculation gas mass flow rate constraint equation (Q.16) and transferred mass flow of oxygen constraint equation (Q.17) are used to iteratively solve the fuel utilization constraint equation (Q.2), using the corresponding reformer outlet equilibrium state and the rewritten recirculation ratio, shown in equation (Q.18), based upon equations (2.2), (2.8) and (2.9), until the reformer outlet molar flow rate constraint and the complete mass balance are valid.

$$\dot{m}_{\mathrm{rec,F}} = \dot{m}_{\mathrm{rec,R}} \tag{Q.16}$$

$$\dot{m}_{\mathrm{O_2,tr,F}} = \dot{m}_{\mathrm{O_2,tr,R}} \tag{Q.17}$$

$$r_{\mathrm{F}} = \frac{\dot{m}_{\mathrm{rec,F}}}{\dot{m}_{\mathrm{ref,out,F}} + \dot{m}_{\mathrm{O_2,tr,F}}} = \frac{\dot{m}_{\mathrm{rec,R}}}{\dot{n}_{\mathrm{ref,out,F}}\, M_{\mathrm{ref,out,F}} + \dot{m}_{\mathrm{O_2,tr,R}}} \tag{Q.18}$$

R Derivation of anode outlet mass flow rate control schemes

R.1 General fuel utilization factor equation

First, the constant anode outlet mass flow rate constraint between the fluctuating and reference state is rewritten using equations (2.3) and (2.4), resulting in equation (R.1).

$$\begin{aligned}
\dot{m}_{\mathrm{an,out,F}} &= \frac{\dot{m}_{\mathrm{NG,in,F}} + \dot{m}_{\mathrm{O_2,tr,F}}}{1 - r_{\mathrm{F}}} = \frac{\dot{m}_{\mathrm{NG,in,R}} + \dot{m}_{\mathrm{O_2,tr,R}}}{1 - r_{\mathrm{R}}} = \dot{m}_{\mathrm{an,out,R}} \\
&\rightarrow (1 - r_{\mathrm{R}}) \left(\frac{(1 - r_{\mathrm{F}}\,(1 - U_{\mathrm{f,S,F}}))\, I\, N_{\mathrm{Cell}}\, M_{\mathrm{NG,in,F}}}{U_{\mathrm{f,S,F}}\, F\, K_{\mathrm{e^-,F}}} + \dot{m}_{\mathrm{O_2,tr,F}} \right) \\
&= (1 - r_{\mathrm{F}}) \left(\frac{(1 - r_{\mathrm{R}}\,(1 - U_{\mathrm{f,S,R}}))\, I\, N_{\mathrm{Cell}}\, M_{\mathrm{NG,in,R}}}{U_{\mathrm{f,S,R}}\, F\, K_{\mathrm{e^-,R}}} + \dot{m}_{\mathrm{O_2,tr,R}} \right)
\end{aligned} \tag{R.1}$$

Second, the transferred mass flow rate of oxygen inside the stack is expressed as a function of the reference state in accordance to equations (2.13) and (2.3), as outlined in equation (R.2).

$$\dot{m}_{\mathrm{O_2,tr,F}} = \dot{m}_{\mathrm{O_2,tr,R}} = \frac{\dot{m}_{\mathrm{NG,in,R}}\, U_{\mathrm{f,S,R}}\, K_{\mathrm{e^-,R}}\, M_{\mathrm{O_2}}}{4\, M_{\mathrm{NG,in,R}}\, (1 - r_{\mathrm{R}}\,(1 - U_{\mathrm{f,S,R}}))} \tag{R.2}$$

Lastly, by applying equation (R.2) to equation (R.1), the equation is solved for the fuel utilization factor of the fluctuating state, as outlined in equation (R.3).

$$U_{\mathrm{f,S,F}} = \frac{4\, U_{\mathrm{f,S,R}}\, K_{\mathrm{e^-,R}}\, M_{\mathrm{NG,in,F}}\, (1 - r_{\mathrm{R}})\, (1 - r_{\mathrm{F}})}{\left(\begin{array}{r} 4\, K_{\mathrm{e^-,F}}\, M_{\mathrm{NG,in,R}}\, (1 - r_{\mathrm{F}} - r_{\mathrm{R}}\,(1 - r_{\mathrm{F}})\,(1 - U_{\mathrm{f,S,R}})) \\ + U_{\mathrm{f,S,R}}\, K_{\mathrm{e^-,R}} \left(K_{\mathrm{e^-,F}}\, M_{\mathrm{O_2}}\, (r_{\mathrm{R}} - r_{\mathrm{F}}) - 4\, r_{\mathrm{F}}\, M_{\mathrm{NG,in,F}}\, (1 - r_{\mathrm{R}}) \right) \end{array} \right)} \tag{R.3}$$

R.2 Recirculation ratio equations

R.2.1 Anode outlet mass flow rate CS 1

First, the constant anode outlet mass flow rate constraint is used to express the natural gas molar flow rate of the fluctuating state as a function of the molar flow rate of the reference state, using the natural gas molar masses of both states, as shown in equation (R.5) based upon the modification of the molar flow rate balance constraint equation (R.4).

$$\dot{m}_{\mathrm{an,out,F}} = \frac{\dot{m}_{\mathrm{NG,in,F}} + \dot{m}_{\mathrm{O_2,tr,F}}}{1 - r_{\mathrm{F}}} = \frac{\dot{m}_{\mathrm{NG,in,R}} + \dot{m}_{\mathrm{O_2,tr,R}}}{1 - r_{\mathrm{R}}} = \dot{m}_{\mathrm{an,out,R}} \tag{R.4}$$

$$\dot{n}_{\mathrm{NG,in,F}} = \frac{\left(\dot{n}_{\mathrm{NG,in,R}}\, M_{\mathrm{NG,in,R}} + \dot{m}_{\mathrm{O_2,tr,R}}\right)(1 - r_{\mathrm{F}}) - \dot{m}_{\mathrm{O_2,tr,F}}\,(1 - r_{\mathrm{R}})}{M_{\mathrm{NG,in,F}}\,(1 - r_{\mathrm{R}})} \tag{R.5}$$

Second, the transferred mass flow rate of oxygen inside the stack is expressed as a function of the reference state in accordance to equations (2.13) and (2.3), as outlined in equation (R.6).

$$\dot{m}_{\mathrm{O_2,tr,F}} = \dot{m}_{\mathrm{O_2,tr,R}} = \frac{\dot{n}_{\mathrm{NG,in,R}}\, U_{\mathrm{f,S,R}}\, K_{\mathrm{e^-,R}}\, M_{\mathrm{O_2}}}{4\,(1 - r_{\mathrm{R}}\,(1 - U_{\mathrm{f,S,R}}))} \tag{R.6}$$

Third, the molar flow rate balance equation (2.18) is applied to the constant reformer inlet molar flow rate constraint, as shown in equation (R.7).

$$\dot{n}_{\mathrm{ref,in,F}} = \frac{\dot{n}_{\mathrm{NG,in,F}}\,(1 + r_{\mathrm{F}}\, K_{\triangle\mathrm{an,F}})}{(1 - r_{\mathrm{F}})} = \frac{\dot{n}_{\mathrm{NG,in,R}}\,(1 + r_{\mathrm{R}}\, K_{\triangle\mathrm{an,R}})}{(1 - r_{\mathrm{R}})} = \dot{n}_{\mathrm{ref,in,R}} \tag{R.7}$$

Lastly, by applying equations (R.5) and (R.6) to equation (R.7), the equation can be solved for the recirculation ratio of the fluctuating state, yielding a quadratic equation, as outlined in equation (R.8). The coefficients α, β and γ of the quadratic equation are shown in equations (R.9), (R.10) and (R.11).

$$\alpha_{\mathrm{AM_1}}\,(r_{\mathrm{F}})^2 + \beta_{\mathrm{AM_1}}\, r_{\mathrm{F}} + \gamma_{\mathrm{AM_1}} = 0 \tag{R.8}$$

$$\alpha_{\mathrm{AM_1}} = K_{\triangle\mathrm{an,F}}\left(4\, M_{\mathrm{NG,in,R}}\,(1 - r_{\mathrm{R}}\,(1 - U_{\mathrm{f,S,R}})) + U_{\mathrm{f,S,R}}\, K_{\mathrm{e^-,R}}\, M_{\mathrm{O_2}}\right) \tag{R.9}$$

$$\begin{aligned}\beta_{\mathrm{AM_1}} = {} & 4\,(1 - r_{\mathrm{R}}\,(1 - U_{\mathrm{f,S,R}}))\,(M_{\mathrm{NG,in,R}}\,(1 - K_{\triangle\mathrm{an,F}}) - M_{\mathrm{NG,in,F}}\,(1 + r_{\mathrm{R}}\, K_{\triangle\mathrm{an,R}})) \\ & + U_{\mathrm{f,S,R}}\, K_{\mathrm{e^-,R}}\, M_{\mathrm{O_2}}\,(1 - r_{\mathrm{R}}\, K_{\triangle\mathrm{an,F}})\end{aligned} \tag{R.10}$$

$$\gamma_{\mathrm{AM_1}} = 4\,(1 - r_{\mathrm{R}}\,(1 - U_{\mathrm{f,S,R}}))\,(M_{\mathrm{NG,in,F}}\,(1 + r_{\mathrm{R}}\, K_{\triangle\mathrm{an,R}}) - M_{\mathrm{NG,in,R}}) - r_{\mathrm{R}}\, U_{\mathrm{f,S,R}}\, K_{\mathrm{e^-,R}}\, M_{\mathrm{O_2}} \tag{R.11}$$

The quadratic formula is applied to obtain a solution for the recirculation ratio of the fluctuating state, as shown in equation (R.12). It should be noted that only the positive solution yields physical valid results with a recirculation ratio between 0 and 1.

$$r_{\mathrm{F}} = \frac{-\beta_{\mathrm{AM_1}} + \sqrt{(\beta_{\mathrm{AM_1}})^2 - 4\,\alpha_{\mathrm{AM_1}}\,\gamma_{\mathrm{AM_1}}}}{2\,\alpha_{\mathrm{AM_1}}} \tag{R.12}$$

An identical result can be obtained by rewriting the constant reformer outlet mass flow rate constraint, as outlined in equation (R.13) using the mass flow rate balance equation (2.8), and applying the rewritten equation and the transferred mass flow rate of oxygen constraint equation (R.6) to the constant reformer inlet molar flow rate constraint equation (R.7).

$$\begin{aligned} &\dot{m}_{\mathrm{ref,out,F}} = \dot{m}_{\mathrm{ref,out,R}} \\ \rightarrow\ &\dot{n}_{\mathrm{NG,in,F}} = \frac{\left(\dot{n}_{\mathrm{NG,in,R}}\, M_{\mathrm{NG,in,R}} + r_{\mathrm{R}}\, \dot{m}_{\mathrm{O_2,tr,R}}\right)\left(1 - r_{\mathrm{F}}\right) - r_{\mathrm{F}}\, \dot{m}_{\mathrm{O_2,tr,R}}\left(1 - r_{\mathrm{R}}\right)}{M_{\mathrm{NG,in,F}}\left(1 - r_{\mathrm{R}}\right)} \end{aligned} \tag{R.13}$$

R.2.2 Anode outlet mass flow rate CS 2

First, the constant anode outlet mass flow rate constraint is used to express the natural gas molar flow rate of the fluctuating state as a function of the molar flow rate of the reference state, using the natural gas molar masses of both states, as shown in equation (R.15) based upon the modification of the molar flow rate balance constraint equation (R.14).

$$\dot{m}_{\mathrm{an,out,F}} = \frac{\dot{m}_{\mathrm{NG,in,F}} + \dot{m}_{\mathrm{O_2,tr,F}}}{1 - r_{\mathrm{F}}} = \frac{\dot{m}_{\mathrm{NG,in,R}} + \dot{m}_{\mathrm{O_2,tr,R}}}{1 - r_{\mathrm{R}}} = \dot{m}_{\mathrm{an,out,R}} \tag{R.14}$$

$$\dot{n}_{\mathrm{NG,in,F}} = \frac{\left(\dot{n}_{\mathrm{NG,in,R}}\, M_{\mathrm{NG,in,R}} + \dot{m}_{\mathrm{O_2,tr,R}}\right)\left(1 - r_{\mathrm{F}}\right) - \dot{m}_{\mathrm{O_2,tr,F}}\left(1 - r_{\mathrm{R}}\right)}{M_{\mathrm{NG,in,F}}\left(1 - r_{\mathrm{R}}\right)} \tag{R.15}$$

Second, the transferred mass flow rate of oxygen inside the stack is expressed as a function of the reference state in accordance to equations (2.13) and (2.3), as outlined in equation (R.16).

$$\dot{m}_{\mathrm{O_2,tr,F}} = \dot{m}_{\mathrm{O_2,tr,R}} = \frac{\dot{n}_{\mathrm{NG,in,R}}\, U_{\mathrm{f,S,R}}\, K_{\mathrm{e^-,R}}\, M_{\mathrm{O_2}}}{4\left(1 - r_{\mathrm{R}}\left(1 - U_{\mathrm{f,S,R}}\right)\right)} \tag{R.16}$$

Third, the molar flow rate balance equation (2.18) is applied to the constant recirculation gas molar flow rate constraint, as shown in equation (R.17).

$$\dot{n}_{\mathrm{rec,F}} = \frac{r_{\mathrm{F}}\, \dot{n}_{\mathrm{NG,in,F}}\left(1 + K_{\triangle\mathrm{an,F}}\right)}{\left(1 - r_{\mathrm{F}}\right)} = \frac{r_{\mathrm{R}}\, \dot{n}_{\mathrm{NG,in,R}}\left(1 + K_{\triangle\mathrm{an,R}}\right)}{\left(1 - r_{\mathrm{R}}\right)} = \dot{n}_{\mathrm{rec,R}} \tag{R.17}$$

Lastly, by applying equations (R.15) and (R.16) to equation (R.17), the equation can be solved for the recirculation ratio of the fluctuating state, yielding a quadratic equation, as outlined in equation (R.18). The coefficients α, β and γ of the quadratic equation are shown in equations (R.19), (R.20) and (R.21).

$$\alpha_{\mathrm{AM_2}}\left(r_{\mathrm{F}}\right)^2 + \beta_{\mathrm{AM_2}}\, r_{\mathrm{F}} + \gamma_{\mathrm{AM_2}} = 0 \tag{R.18}$$

$$\alpha_{\mathrm{AM_2}} = \left(1 + K_{\triangle\mathrm{an,F}}\right)\left(4\, M_{\mathrm{NG,in,R}}\left(1 - r_{\mathrm{R}}\left(1 - U_{\mathrm{f,S,R}}\right)\right) + U_{\mathrm{f,S,R}}\, K_{\mathrm{e^-,R}}\, M_{\mathrm{O_2}}\right) \tag{R.19}$$

$$\begin{aligned} \beta_{\mathrm{AM_2}} = &-r_{\mathrm{R}}\, U_{\mathrm{f,S,R}}\, K_{\mathrm{e^-,R}}\, M_{\mathrm{O_2}}\left(1 + K_{\triangle\mathrm{an,F}}\right) \\ &- 4\left(1 - r_{\mathrm{R}}\left(1 - U_{\mathrm{f,S,R}}\right)\right)\left(r_{\mathrm{R}}\, M_{\mathrm{NG,in,F}}\left(1 + K_{\triangle\mathrm{an,R}}\right) + M_{\mathrm{NG,in,R}}\left(1 + K_{\triangle\mathrm{an,F}}\right)\right) \end{aligned} \tag{R.20}$$

$$\gamma_{\mathrm{AM_2}} = 4\, r_{\mathrm{R}}\, M_{\mathrm{NG,in,F}}\left(1 + K_{\triangle\mathrm{an,R}}\right)\left(1 - r_{\mathrm{R}}\left(1 - U_{\mathrm{f,S,R}}\right)\right) \tag{R.21}$$

The quadratic formula is applied to obtain a solution for the recirculation ratio of the fluctuating state, as shown in equation (R.22). It should be noted that only the positive solution yields physical valid results with a recirculation ratio between 0 and 1.

$$r_{\mathrm{F}} = \frac{-\beta_{\mathrm{AM_2}} + \sqrt{\left(\beta_{\mathrm{AM_2}}\right)^2 - 4\,\alpha_{\mathrm{AM_2}}\,\gamma_{\mathrm{AM_2}}}}{2\,\alpha_{\mathrm{AM_2}}} \tag{R.22}$$

An identical result can be obtained by rewriting the constant reformer inlet or reformer outlet mass flow rate constraint, as outlined in equation (R.23) using mass balance equation (2.8), and applying the rewritten equation and the transferred mass flow rate of oxygen constraint equation (R.16) to the constant recirculation gas molar flow rate constraint equation (R.17).

$$\begin{aligned} &\dot{m}_{\mathrm{ref,in,F}} = \dot{m}_{\mathrm{ref,out,F}} = \dot{m}_{\mathrm{ref,out,R}} = \dot{m}_{\mathrm{ref,in,R}} \\ &\qquad \rightarrow \dot{n}_{\mathrm{NG,in,F}} = \frac{\left(\dot{n}_{\mathrm{NG,in,R}}\,M_{\mathrm{NG,in,R}} + r_{\mathrm{R}}\,\dot{m}_{\mathrm{O_2,tr,R}}\right)\left(1 - r_{\mathrm{F}}\right) - r_{\mathrm{F}}\,\dot{m}_{\mathrm{O_2,tr,R}}\left(1 - r_{\mathrm{R}}\right)}{M_{\mathrm{NG,in,F}}\left(1 - r_{\mathrm{R}}\right)} \end{aligned} \tag{R.23}$$

S Derivation of anode outlet volume flow rate control schemes

S.1 General fuel utilization factor equation

As outlined in equation (S.1), by solving the constant anode outlet molar flow rate constraint between the fluctuating and reference state using equations (2.3) and (2.4), the fuel utilization factor of the fluctuating state can be calculated, resulting in equation (S.2).

$$\begin{aligned} \dot{n}_{\mathrm{an,out,F}} &= \frac{\dot{n}_{\mathrm{NG,in,F}}\left(1 + K_{\triangle\mathrm{an,F}}\right)}{\left(1 - r_{\mathrm{F}}\right)} = \frac{\dot{n}_{\mathrm{NG,in,R}}\left(1 + K_{\triangle\mathrm{an,R}}\right)}{\left(1 - r_{\mathrm{R}}\right)} = \dot{n}_{\mathrm{an,out,R}} \\ \frac{I\,N_{\mathrm{Cell}}\left(1 - r_{\mathrm{F}}\left(1 - U_{\mathrm{f,S,F}}\right)\right)\left(1 + K_{\triangle\mathrm{an,F}}\right)}{U_{\mathrm{f,S,F}}\,F\,K_{\mathrm{e^-,F}}\left(1 - r_{\mathrm{F}}\right)} &= \frac{I\,N_{\mathrm{Cell}}\left(1 - r_{\mathrm{R}}\left(1 - U_{\mathrm{f,S,R}}\right)\right)\left(1 + K_{\triangle\mathrm{an,R}}\right)}{U_{\mathrm{f,S,R}}\,F\,K_{\mathrm{e^-,R}}\left(1 - r_{\mathrm{R}}\right)} \end{aligned} \tag{S.1}$$

$$U_{\mathrm{f,S,F}} = \frac{U_{\mathrm{f,S,R}}\,K_{\mathrm{e^-,R}}\left(1 - r_{\mathrm{R}}\right)\left(1 - r_{\mathrm{F}}\right)\left(1 + K_{\triangle\mathrm{an,F}}\right)}{\left(\begin{array}{r} K_{\mathrm{e^-,F}}\left(1 - r_{\mathrm{F}}\right)\left(1 - r_{\mathrm{R}}\left(1 - U_{\mathrm{f,S,R}}\right)\right)\left(1 + K_{\triangle\mathrm{an,R}}\right) \\ - r_{\mathrm{F}}\,U_{\mathrm{f,S,R}}\,K_{\mathrm{e^-,R}}\left(1 - r_{\mathrm{R}}\right)\left(1 + K_{\triangle\mathrm{an,F}}\right) \end{array}\right)} \tag{S.2}$$

S.2 Recirculation ratio equations

S.2.1 Anode outlet volume flow rate CS 1

First, the constant anode outlet molar flow rate constraint is used to express the natural gas molar flow rate of the fluctuating state as a function of the molar flow rate of the reference state, as shown in equation (S.4) based upon the modification of the molar flow rate balance constraint equation (S.3).

$$\dot{n}_{\mathrm{an,out,F}} = \frac{\dot{n}_{\mathrm{NG,in,F}}\left(1 + K_{\triangle\mathrm{an,F}}\right)}{\left(1 - r_{\mathrm{F}}\right)} = \frac{\dot{n}_{\mathrm{NG,in,R}}\left(1 + K_{\triangle\mathrm{an,R}}\right)}{\left(1 - r_{\mathrm{R}}\right)} = \dot{n}_{\mathrm{an,out,R}} \tag{S.3}$$

$$\dot{n}_{\mathrm{NG,in,F}} = \frac{\dot{n}_{\mathrm{NG,in,R}}\left(1 - r_{\mathrm{F}}\right)\left(1 + K_{\triangle\mathrm{an,R}}\right)}{\left(1 - r_{\mathrm{R}}\right)\left(1 + K_{\triangle\mathrm{an,F}}\right)} \tag{S.4}$$

Second, the molar flow rate balance equation (2.18) is applied to the constant reformer inlet molar flow rate constraint, as shown in equation (S.5).

$$\dot{n}_{\mathrm{ref,in,F}} = \frac{\dot{n}_{\mathrm{NG,in,F}}\,(1 + r_{\mathrm{F}}\,K_{\triangle\mathrm{an,F}})}{(1 - r_{\mathrm{F}})} = \frac{\dot{n}_{\mathrm{NG,in,R}}\,(1 + r_{\mathrm{R}}\,K_{\triangle\mathrm{an,R}})}{(1 - r_{\mathrm{R}})} = \dot{n}_{\mathrm{ref,in,R}} \tag{S.5}$$

Lastly, by applying equation (S.4) to equation (S.5), the equation can be solved for the recirculation ratio of the fluctuating state, as outlined in equation (S.6).

$$r_{\mathrm{F}} = \frac{(1 + r_{\mathrm{R}}\,K_{\triangle\mathrm{an,R}})\,(1 + K_{\triangle\mathrm{an,F}}) - K_{\triangle\mathrm{an,R}} - 1}{K_{\triangle\mathrm{an,F}}\,(1 + K_{\triangle\mathrm{an,R}})} \tag{S.6}$$

S.2.2 Anode outlet volume flow rate CS 2

First, the constant anode outlet molar flow rate constraint is used to express the natural gas molar flow rate of the fluctuating state as a function of the molar flow rate of the reference state, as shown in equation (S.8) based upon the modification of the molar flow rate balance constraint equation (S.7).

$$\dot{n}_{\mathrm{an,out,F}} = \frac{\dot{n}_{\mathrm{NG,in,F}}\,(1 + K_{\triangle\mathrm{an,F}})}{(1 - r_{\mathrm{F}})} = \frac{\dot{n}_{\mathrm{NG,in,R}}\,(1 + K_{\triangle\mathrm{an,R}})}{(1 - r_{\mathrm{R}})} = \dot{n}_{\mathrm{an,out,R}} \tag{S.7}$$

$$\dot{n}_{\mathrm{NG,in,F}} = \frac{\dot{n}_{\mathrm{NG,in,R}}\,(1 - r_{\mathrm{F}})\,(1 + K_{\triangle\mathrm{an,R}})}{(1 - r_{\mathrm{R}})\,(1 + K_{\triangle\mathrm{an,F}})} \tag{S.8}$$

Second, the molar flow rate balance equation (2.18) is applied to the constant recirculation gas molar flow rate constraint, as shown in equation (S.9).

$$\dot{n}_{\mathrm{rec,F}} = \frac{r_{\mathrm{F}}\,\dot{n}_{\mathrm{NG,in,F}}\,(1 + K_{\triangle\mathrm{an,F}})}{(1 - r_{\mathrm{F}})} = \frac{r_{\mathrm{R}}\,\dot{n}_{\mathrm{NG,in,R}}\,(1 + K_{\triangle\mathrm{an,R}})}{(1 - r_{\mathrm{R}})} = \dot{n}_{\mathrm{rec,R}} \tag{S.9}$$

Lastly, by applying equation (S.8) to equation (S.9), the equation can be solved for the recirculation ratio of the fluctuating state, as outlined in equation (S.10), ultimately yielding a constant recirculation ratio between the fluctuating and reference state.

$$r_{\mathrm{F}} = r_{\mathrm{R}} \tag{S.10}$$

Another possibility to obtain an identical result, with a constant anode outlet molar flow rate, is the application of the constant recirculation ratio constraint equation (S.10) to the recirculation gas molar flow rate constraint equation (S.9).

S.2.3 Anode outlet volume flow rate CS 3

First, the constant anode outlet molar flow rate constraint is used to express the natural gas mass flow rate of the fluctuating state as a function of the mass flow rate of the reference state, using the natural gas molar masses of both states, as shown in equation (S.12) based upon the modification of the molar flow rate balance constraint equation (S.11).

$$\dot{n}_{\mathrm{an,out,F}} = \frac{\dot{n}_{\mathrm{NG,in,F}}\,(1 + K_{\triangle\mathrm{an,F}})}{(1 - r_{\mathrm{F}})} = \frac{\dot{n}_{\mathrm{NG,in,R}}\,(1 + K_{\triangle\mathrm{an,R}})}{(1 - r_{\mathrm{R}})} = \dot{n}_{\mathrm{an,out,R}} \tag{S.11}$$

$$\dot{m}_{\mathrm{NG,in,F}} = \frac{\dot{m}_{\mathrm{NG,in,R}}\, M_{\mathrm{NG,in,F}}\, (1 - r_{\mathrm{F}})\, (1 + K_{\triangle \mathrm{an,R}})}{M_{\mathrm{NG,in,R}}\, (1 - r_{\mathrm{R}})\, (1 + K_{\triangle \mathrm{an,F}})} \tag{S.12}$$

Second, the transferred mass flow rate of oxygen inside the stack is expressed as a function of the reference state in accordance to equations (2.13) and (2.3), as outlined in equation (S.13).

$$\dot{m}_{\mathrm{O_2,tr,F}} = \dot{m}_{\mathrm{O_2,tr,R}} = \frac{\dot{m}_{\mathrm{NG,in,R}}\, U_{\mathrm{f,S,R}}\, K_{\mathrm{e^-,R}}\, M_{\mathrm{O_2}}}{4\, M_{\mathrm{NG,in,R}}\, (1 - r_{\mathrm{R}}\, (1 - U_{\mathrm{f,S,R}}))} \tag{S.13}$$

Third, the mass flow rate balance equation (2.10) is applied to the constant recirculation gas mass flow rate constraint, as shown in equation (S.14).

$$\dot{m}_{\mathrm{rec,F}} = \frac{r_{\mathrm{F}}\, (\dot{m}_{\mathrm{NG,in,F}} + \dot{m}_{\mathrm{O_2,tr,F}})}{1 - r_{\mathrm{F}}} = \frac{r_{\mathrm{R}}\, (\dot{m}_{\mathrm{NG,in,R}} + \dot{m}_{\mathrm{O_2,tr,R}})}{1 - r_{\mathrm{R}}} = \dot{m}_{\mathrm{rec,R}} \tag{S.14}$$

Lastly, by applying equations (S.12) and (S.13) to equation (S.14), the equation can be solved for the recirculation ratio of the fluctuating state, yielding a quadratic equation, as outlined in equation (S.15). The coefficients α, β and γ of the quadratic equation are shown in equations (S.16), (S.17) and (S.18).

$$\alpha_{\mathrm{AV_3}}\, (r_{\mathrm{F}})^2 + \beta_{\mathrm{AV_3}}\, r_{\mathrm{F}} + \gamma_{\mathrm{AV_3}} = 0 \tag{S.15}$$

$$\alpha_{\mathrm{AV_3}} = \frac{M_{\mathrm{NG,in,F}}\, (1 + K_{\triangle \mathrm{an,R}})}{(1 - r_{\mathrm{R}})} \tag{S.16}$$

$$\begin{aligned} \beta_{\mathrm{AV_3}} = &- \frac{U_{\mathrm{f,S,R}}\, K_{\mathrm{e^-,R}}\, M_{\mathrm{O_2}}\, (1 + K_{\triangle \mathrm{an,F}})}{4\, (1 - r_{\mathrm{R}}\, (1 - U_{\mathrm{f,S,R}}))} \\ &- \frac{M_{\mathrm{NG,in,F}}\, (1 + K_{\triangle \mathrm{an,R}}) + r_{\mathrm{R}}\, (1 + K_{\triangle \mathrm{an,F}}) \left(M_{\mathrm{NG,in,R}} + \frac{U_{\mathrm{f,S,R}}\, K_{\mathrm{e^-,R}}\, M_{\mathrm{O_2}}}{4\, (1 - r_{\mathrm{R}}\, (1 - U_{\mathrm{f,S,R}}))} \right)}{(1 - r_{\mathrm{R}})} \end{aligned} \tag{S.17}$$

$$\gamma_{\mathrm{AV_3}} = \frac{r_{\mathrm{R}}\, (1 + K_{\triangle \mathrm{an,F}})}{(1 - r_{\mathrm{R}})} \left(M_{\mathrm{NG,in,R}} + \frac{U_{\mathrm{f,S,R}}\, K_{\mathrm{e^-,R}}\, M_{\mathrm{O_2}}}{4\, (1 - r_{\mathrm{R}}\, (1 - U_{\mathrm{f,S,R}}))} \right) \tag{S.18}$$

The quadratic formula is applied to obtain a solution for the recirculation ratio of the fluctuating state, as shown in equation (S.19). It should be noted that only the negative solution yields physical valid results with a recirculation ratio between 0 and 1.

$$r_{\mathrm{F}} = \frac{-\beta_{\mathrm{AV_3}} - \sqrt{(\beta_{\mathrm{AV_3}})^2 - 4\, \alpha_{\mathrm{AV_3}}\, \gamma_{\mathrm{AV_3}}}}{2\, \alpha_{\mathrm{AV_3}}} \tag{S.19}$$

S.2.4 Anode outlet volume flow rate CS 4

First, the constant anode outlet molar flow rate constraint is used to express the natural gas mass flow rate of the fluctuating state as a function of the mass flow rate of the reference state, using the natural gas molar masses of both states, as shown in equation (S.21) based upon the modification of the molar flow rate balance constraint equation (S.20).

$$\dot{n}_{\mathrm{an,out,F}} = \frac{\dot{n}_{\mathrm{NG,in,F}}\, (1 + K_{\triangle \mathrm{an,F}})}{(1 - r_{\mathrm{F}})} = \frac{\dot{n}_{\mathrm{NG,in,R}}\, (1 + K_{\triangle \mathrm{an,R}})}{(1 - r_{\mathrm{R}})} = \dot{n}_{\mathrm{an,out,R}} \tag{S.20}$$

$$\dot{m}_{\mathrm{NG,in,F}} = \frac{\dot{m}_{\mathrm{NG,in,R}}\, M_{\mathrm{NG,in,F}}\, (1 - r_{\mathrm{F}})\, (1 + K_{\triangle \mathrm{an,R}})}{M_{\mathrm{NG,in,R}}\, (1 - r_{\mathrm{R}})\, (1 + K_{\triangle \mathrm{an,F}})} \tag{S.21}$$

Second, the transferred mass flow rate of oxygen inside the stack is expressed as a function of the reference state in accordance to equations (2.13) and (2.3), as outlined in equation (S.22).

$$\dot{m}_{\mathrm{O_2,tr,F}} = \dot{m}_{\mathrm{O_2,tr,R}} = \frac{\dot{m}_{\mathrm{NG,in,R}}\, U_{\mathrm{f,S,R}}\, K_{\mathrm{e^-,R}}\, M_{\mathrm{O_2}}}{4\, M_{\mathrm{NG,in,R}}\, (1 - r_{\mathrm{R}}\, (1 - U_{\mathrm{f,S,R}}))} \tag{S.22}$$

Third, the molar flow rate balance equation (2.8) is applied to the constant reformer inlet or reformer outlet mass flow rate constraint, as shown in equation (S.23).

$$\dot{m}_{\mathrm{ref,in/out,F}} = \frac{\dot{m}_{\mathrm{NG,in,F}} + r_{\mathrm{F}}\, \dot{m}_{\mathrm{O_2,tr,F}}}{1 - r_{\mathrm{F}}} = \frac{\dot{m}_{\mathrm{NG,in,R}} + r_{\mathrm{R}}\, \dot{m}_{\mathrm{O_2,tr,R}}}{1 - r_{\mathrm{R}}} = \dot{m}_{\mathrm{ref,in/out,R}} \tag{S.23}$$

Lastly, by applying equations (S.21) and (S.22) to equation (S.23), the equation is solved for the recirculation ratio of the fluctuating state, as outlined in equation (S.24).

$$r_{\mathrm{F}} = \frac{\begin{pmatrix} r_{\mathrm{R}}\, U_{\mathrm{f,S,R}}\, K_{\mathrm{e^-,R}}\, M_{\mathrm{O_2}}\, (1 + K_{\triangle \mathrm{an,F}}) \\ \quad + 4\, (1 - r_{\mathrm{R}}\, (1 - U_{\mathrm{f,S,R}}))\, (M_{\mathrm{NG,in,R}}\, (1 + K_{\triangle \mathrm{an,F}}) - M_{\mathrm{NG,in,F}}\, (1 + K_{\triangle \mathrm{an,R}})) \end{pmatrix}}{\begin{pmatrix} U_{\mathrm{f,S,R}}\, K_{\mathrm{e^-,R}}\, M_{\mathrm{O_2}}\, (1 + K_{\triangle \mathrm{an,F}}) \\ \quad + 4\, (1 - r_{\mathrm{R}}\, (1 - U_{\mathrm{f,S,R}}))\, (M_{\mathrm{NG,in,R}}\, (1 + K_{\triangle \mathrm{an,F}}) - M_{\mathrm{NG,in,F}}\, (1 + K_{\triangle \mathrm{an,R}})) \end{pmatrix}} \tag{S.24}$$

T Derivation of natural gas electron coefficient control scheme

First, the initial value of the recirculation ratio is calculated based upon the quantified electron gas coefficient, the fuel utilization factor set point and by applying equation (3.14) to (2.2), ultimately yielding equation (T.1).

$$r_{\mathrm{ini}} = \left(U_{\mathrm{f,S,SP}} \left(\frac{K_{\mathrm{e^-,Msd}}}{2\, K_{\Phi,\mathrm{MLR}}} - 1 \right) + 1 \right)^{-1} \tag{T.1}$$

Second, the corresponding molar flow rates of natural gas and recirculation gas or reformer inlet gas are determined using equations (2.4), (2.3), (2.20) and (2.18), as shown in equations (T.2), (T.3) and (T.4). Both flow rates are considered as fixed set point values.

$$\dot{n}_{\mathrm{NG,in}} = \frac{I\, N_{\mathrm{Cell}}}{U_{\mathrm{f,Sys}}\, F\, K_{\mathrm{e^-,Msd}}} = \frac{I\, N_{\mathrm{Cell}}}{\frac{U_{\mathrm{f,S}}}{1 - r_{\mathrm{ini}}\, (1 - U_{\mathrm{f,S}})}\, F\, K_{\mathrm{e^-,Msd}}} = \frac{I\, N_{\mathrm{Cell}}\, (1 - r_{\mathrm{ini}}\, (1 - U_{\mathrm{f,S}}))}{U_{\mathrm{f,S}}\, F\, K_{\mathrm{e^-,Msd}}} \tag{T.2}$$

$$\dot{n}_{\mathrm{rec}} = \frac{r_{\mathrm{ini}}\, \dot{n}_{\mathrm{NG,in}}\, (1 + K_{\triangle \mathrm{an,QR}})}{(1 - r_{\mathrm{ini}})} \tag{T.3}$$

$$\dot{n}_{\mathrm{ref,in}} = \frac{\dot{n}_{\mathrm{NG,in}}\, (1 + r_{\mathrm{ini}}\, K_{\triangle \mathrm{an,QR}})}{(1 - r_{\mathrm{ini}})} \tag{T.4}$$

Third, the resulting recirculation ratio of the fluctuating state can be expressed as a function of the initial recirculation ratio, by rewriting equation (2.20) or (2.18) and applying equation (T.3) or (T.4), as outlined in equation (T.5).

$$r_{\mathrm{F}} = \frac{\dot{n}_{\mathrm{rec}}}{\dot{n}_{\mathrm{rec}} + \dot{n}_{\mathrm{NG,in}}\, (1 + K_{\triangle \mathrm{an}})} = \frac{\dot{n}_{\mathrm{ref,in}} - \dot{n}_{\mathrm{NG,in}}}{\dot{n}_{\mathrm{NG,in}}\, K_{\triangle \mathrm{an}} + \dot{n}_{\mathrm{ref,in}}} = \frac{r_{\mathrm{ini}}\, (1 + K_{\triangle \mathrm{an,QR}})}{r_{\mathrm{ini}}\, (K_{\triangle \mathrm{an,QR}} - K_{\triangle \mathrm{an}}) + 1 + K_{\triangle \mathrm{an}}} \tag{T.5}$$

Lastly, by applying the definition of the initial recirculation ratio, equation (T.1) can be solely related to the given set point values, as well as the quantified and estimated gas coefficients, as shown in equation (T.6).

$$r_{\mathrm{F}} = \frac{(1 + K_{\triangle\mathrm{an,QR}})}{(1 + K_{\triangle\mathrm{an,QR}}) + U_{\mathrm{f,S,SP}} \left(\frac{K_{\mathrm{e^-,Msd}}}{2\,K_{\Phi,\mathrm{MLR}}} - 1 \right) (1 + K_{\triangle\mathrm{an}})} \tag{T.6}$$

Additionally, the fuel utilization factor of the system of the initial and resulting state have to be considered identical, since the natural gas molar flow rate and the electron coefficient are invariant. Therefore, equation (2.3) can be used to express the fuel utilization factor of the fluctuating state, as outlined in equation (T.7).

$$\begin{aligned} U_{\mathrm{f,Sys,F}} &= \frac{U_{\mathrm{f,S,F}}}{1 - r_{\mathrm{F}}\,(1 - U_{\mathrm{f,S,F}})} = \frac{U_{\mathrm{f,S,SP}}}{1 - r_{\mathrm{ini}}\,(1 - U_{\mathrm{f,S,SP}})} = U_{\mathrm{f,Sys,ini}} \\ \rightarrow U_{\mathrm{f,S,F}} &= \frac{U_{\mathrm{f,S,SP}}\,(1 - r_{\mathrm{F}})}{1 - r_{\mathrm{ini}} + U_{\mathrm{f,S,SP}}\,(r_{\mathrm{ini}} - r_{\mathrm{F}})} \end{aligned} \tag{T.7}$$

By applying equation (T.1) to equation (T.7), the fuel utilization factor of the fluctuating state can be solely related to the given set point values, as well as the quantified and estimated gas coefficients, as shown in equation (T.8).

$$U_{\mathrm{f,S,F}} = \frac{(1 - r_{\mathrm{F}}) \left(U_{\mathrm{f,S,SP}}\,K_{\mathrm{e^-,Msd}} + 2\,K_{\Phi,\mathrm{MLR}}\,(1 - U_{\mathrm{f,S,SP}}) \right)}{K_{\mathrm{e^-,Msd}} - r_{\mathrm{F}} \left(U_{\mathrm{f,S,SP}}\,K_{\mathrm{e^-,Msd}} + 2\,K_{\Phi,\mathrm{MLR}}\,(1 - U_{\mathrm{f,S,SP}}) \right)} \tag{T.8}$$

Instead of the flow rate of recirculation or reformer inlet gas, the anode outlet flow rate can be used for the derivation of the recirculation ratio and fuel utilization factor of the fluctuating state. The molar flow rate set point at the anode outlet can be determined using the initial recirculation ratio, as shown in equation (T.9) based upon equation (2.19).

$$\dot{n}_{\mathrm{an,out}} = \frac{\dot{n}_{\mathrm{NG,in}}\,(1 + K_{\triangle\mathrm{an,QR}})}{(1 - r_{\mathrm{ini}})} \tag{T.9}$$

The resulting recirculation ratio of the fluctuating state can be expressed as a function of the initial recirculation ratio, by rewriting equation (2.19) and applying equation (T.9), as outlined in equation (T.10).

$$r_{\mathrm{F}} = \frac{\dot{n}_{\mathrm{an,out}} - \dot{n}_{\mathrm{NG,in}}\,(1 + K_{\triangle\mathrm{an}})}{\dot{n}_{\mathrm{an,out}}} = \frac{1 + K_{\triangle\mathrm{an,QR}} - (1 - r_{\mathrm{ini}})\,(1 + K_{\triangle\mathrm{an}})}{(1 + K_{\triangle\mathrm{an,QR}})} \tag{T.10}$$

Lastly by applying the definition of the initial recirculation ratio, equation (T.10) can be solely related to the given set point values, as well as the quantified and estimated gas coefficients, as shown in equation (T.11).

$$r_{\mathrm{F}} = 1 - \frac{U_{\mathrm{f,S,SP}}\,(1 + K_{\triangle\mathrm{an}}) \left(K_{\mathrm{e^-,Msd}} - 2\,K_{\Phi,\mathrm{MLR}} \right)}{(1 + K_{\triangle\mathrm{an,QR}}) \left(U_{\mathrm{f,S,SP}} \left(K_{\mathrm{e^-,Msd}} - 2\,K_{\Phi,\mathrm{MLR}} \right) + 2\,K_{\Phi,\mathrm{MLR}} \right)} \tag{T.11}$$

Analogously to the previous introduced case, the fuel utilization factor of the fluctuating state can be calculated as shown in equation (T.8).

Implementing the control scheme with a constant recirculation ratio also yields an equality of the resulting and initial or designated recirculation ratio and fuel utilization factor based upon equations (T.1) and (T.7). However, the recirculation ratio can not be directly measured and relies on advanced or combined sensor concepts for its detection.

U German H-gas domain with Renningen 2016 data and hydrogen addition

In Figure U.1, the Renningen 2016 data set, including a 4 % hydrogen addition, is compared to the permitted H-gas domain in Germany, using the volumetric higher heating value and Wobbe-index. The addition of hydrogen yields to a simultaneous reduction of both the volumetric higher heating value and Wobbe-index. Therefore, already a 4 % hydrogen addition to the Renningen 2016 data set results in natural gas data points that marginally exceed the permitted H-gas domain in Germany.

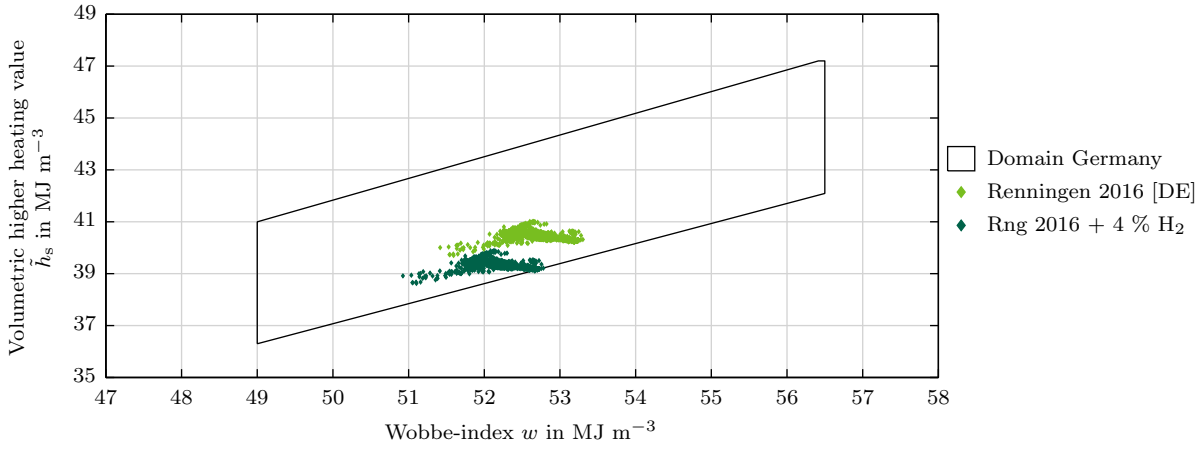

Abbildung U.1: Permitted H-gas domain in Germany with Renningen 2016 data set including 4 % hydrogen addition

V Rating intervals for control scheme comparison

Table V.1 displays the $U_{f,S}$ and Φ rating intervals, including the corresponding clear text labels, rating values and designated robustness domains.

Tabelle V.1: Fuel utilization factor and oxygen-to-carbon ratio robustness rating intervals

		Fuel utilization factor robustness	Oxygen-to-carbon ratio robustness
Category	Rating value	$\triangle U_{f,S,F} = \max(U_{f,S,F}) - U_{f,S,SP}$	$\triangle \Phi_F = \Phi_{SP} - \min(\Phi_F)$
Not tolerable	1	$\triangle U_{f,S,F} > 0.05$	$\triangle \Phi_F > 0.100$
Barely tolerable	2	$0.0375 < \triangle U_{f,S,F} \leq 0.05$	$0.075 < \triangle \Phi_F \leq 0.100$
Tolerable	3	$0.0250 < \triangle U_{f,S,F} \leq 0.0375$	$0.050 < \triangle \Phi_F \leq 0.075$
Acceptable	4	$0.0125 < \triangle U_{f,S,F} \leq 0.025$	$0.025 < \triangle \Phi_F \leq 0.050$
Negligible	5	$\triangle U_{f,S,F} \leq 0.0125$	$\triangle \Phi_F \leq 0.025$

The $x_{NG,R}$ robustness rating intervals, including the corresponding clear text labels, rating values and designated $U_{f,S}$ and Φ robustness domains are listed in Table V.2.

Tabelle V.2: Reference natural gas composition definition robustness rating intervals

Category	Rating value	Fuel utilization factor robustness $\triangle\overline{U_{\mathrm{f,S,F}}} = \left\lvert\overline{U_{\mathrm{f,S,F,1}}} - \overline{U_{\mathrm{f,S,F,2}}}\right\rvert$	Oxygen-to-carbon ratio robustness $\triangle\overline{\Phi_{\mathrm{F}}} = \left\lvert\overline{\Phi_{\mathrm{F,1}}} - \overline{\Phi_{\mathrm{F,2}}}\right\rvert$
Very low	1	$\triangle\overline{U_{\mathrm{f,S,F}}} > 0.015$	$\triangle\overline{\Phi_{\mathrm{F}}} > 0.04$
Low	2	$0.01125 < \triangle\overline{U_{\mathrm{f,S,F}}} \leq 0.015$	$0.03 < \triangle\overline{\Phi_{\mathrm{F}}} \leq 0.04$
Intermediate	3	$0.0075 < \triangle\overline{U_{\mathrm{f,S,F}}} \leq 0.01125$	$0.02 < \triangle\overline{\Phi_{\mathrm{F}}} \leq 0.03$
High	4	$0.00375 < \triangle\overline{U_{\mathrm{f,S,F}}} \leq 0.0075$	$0.01 < \triangle\overline{\Phi_{\mathrm{F}}} \leq 0.02$
Very high	5	$\triangle\overline{U_{\mathrm{f,S,F}}} \leq 0.00375$	$\triangle\overline{\Phi_{\mathrm{F}}} \leq 0.01$

Table V.3 depicts the H_2 robustness rating intervals, including the corresponding clear text labels, rating values and designated $U_{\mathrm{f,S}}$ and Φ robustness domains.

Tabelle V.3: Hydrogen robustness rating intervals

Category	Rating value	Fuel utilization factor robustness $\triangle\overline{U_{\mathrm{f,S,F}}} = \left\lvert\overline{U_{\mathrm{f,S,F,1}}} - \overline{U_{\mathrm{f,S,F,2}}}\right\rvert$	Oxygen-to-carbon ratio robustness $\triangle\overline{\Phi_{\mathrm{F}}} = \left\lvert\overline{\Phi_{\mathrm{F,1}}} - \overline{\Phi_{\mathrm{F,2}}}\right\rvert$
Very low	1	$\triangle\overline{U_{\mathrm{f,S,F}}} > 0.02$	$\triangle\overline{\Phi_{\mathrm{F}}} > 0.1$
Low	2	$0.015 < \triangle\overline{U_{\mathrm{f,S,F}}} \leq 0.02$	$0.075 < \triangle\overline{\Phi_{\mathrm{F}}} \leq 0.1$
Intermediate	3	$0.01 < \triangle\overline{U_{\mathrm{f,S,F}}} \leq 0.015$	$0.05 < \triangle\overline{\Phi_{\mathrm{F}}} \leq 0.075$
High	4	$0.005 < \triangle\overline{U_{\mathrm{f,S,F}}} \leq 0.01$	$0.025 < \triangle\overline{\Phi_{\mathrm{F}}} \leq 0.05$
Very high	5	$\triangle\overline{U_{\mathrm{f,S,F}}} \leq 0.005$	$\triangle\overline{\Phi_{\mathrm{F}}} \leq 0.025$

The clear text labels and corresponding rating values of the implementation feasibility and projected costs are listed in Table V.4. Additionally, Tables V.5 and V.6 display the chosen ratings for the implementation feasibility and projected costs for each individual control element position, including a justification of the determined values, respectively.

Tabelle V.4: Implementation feasibility and projected cost rating values

Implementation feasibility	Projected cost	Rating value
Very hard	Very high	1
Hard	High	2
Intermediate	Intermediate	3
Easy	Low	4
Very easy	Very low	5

Tabelle V.5: Implementation feasibility rating values and justification

Control element	Implementation rating	Justification of defined rating
$\dot{n}_{\mathrm{NG,in}}$	Easy	Many options for accurate volume flow rate detection at ambient temperatures, calibration to average natural gas composition necessary
$\dot{m}_{\mathrm{NG,in}}$	Easy	Many options for accurate mass flow rate detection at ambient temperatures, calibration to average natural gas composition necessary
$\dot{n}_{\mathrm{rec}}$	Easy	Many options for accurate volume flow rate detection at moderate temperatures, gas composition can be analytically determined

Control element	Implementation rating	Justification of defined rating
$\dot{m}_{\mathrm{rec}}$	Intermediate	Limited options for accurate mass flow rate detection at moderate temperatures, gas composition can be analytically determined
$\dot{n}_{\mathrm{ref,in}}$	Easy	Many options for accurate volume flow rate detection at moderate temperatures, gas composition can be analytically determined
$\dot{m}_{\mathrm{ref,in}}$	Intermediate	Limited options for accurate mass flow rate detection at moderate temperatures, gas composition can be analytically determined
$\dot{n}_{\mathrm{ref,out}}$	Very hard	Very limited options for accurate volume flow rate detection at high temperatures, gas composition depends on equilibrium state
$\dot{m}_{\mathrm{ref,out}}$	Very hard	Very limited options for accurate mass flow rate detection at high temperatures, gas composition depends on equilibrium state
$\dot{n}_{\mathrm{an,out}}$	Hard	Very limited options for accurate volume flow rate detection at elevated to high temperatures, gas composition can be analytically determined
$\dot{m}_{\mathrm{an,out}}$	Hard	Very limited options for accurate mass flow rate detection at elevated to high temperatures, gas composition can be analytically determined
r	Very hard	Very limited options for accurate flow rate detection at elevated to high temperatures, gas composition can be analytically determined, two signals are necessary for recirculation ratio determination

Tabelle V.6: Projected cost rating values and justification

Control element	Cost rating	Justification of defined rating
$\dot{n}_{\mathrm{NG,in}}$	Very low	Characteristic blower map modeling is possible, hardly no additional costs since compressors are inherently available
$\dot{m}_{\mathrm{NG,in}}$	Low	Ambient temperature mass flow meters have higher costs than characteristic blower map modeling
$\dot{n}_{\mathrm{rec}}$	Very low	Characteristic blower map modeling is possible, hardly no additional costs since compressors are inherently available
$\dot{m}_{\mathrm{rec}}$	Intermediate	Intermediate temperature mass flow meters have higher costs than ambient temperature mass flow meters
$\dot{n}_{\mathrm{ref,in}}$	Very low	Characteristic blower map modeling is possible, hardly no additional costs since compressors are inherently available
$\dot{m}_{\mathrm{ref,in}}$	Intermediate	Intermediate temperature mass flow meters have higher costs than ambient temperature mass flow meters
$\dot{n}_{\mathrm{ref,out}}$	High	High temperature volume flow meters have higher costs than intermediate temperature mass flow meters
$\dot{m}_{\mathrm{ref,out}}$	Very high	High temperature mass flow meters have very high costs
$\dot{n}_{\mathrm{an,out}}$	High	High temperature volume flow meters have higher costs than intermediate temperature mass flow meters
$\dot{m}_{\mathrm{an,out}}$	Very high	High temperature mass flow meters have very high costs
r	High	High temperature volume flow meters have higher costs than intermediate temperature mass flow meters, two signals are necessary for recirculation ratio determination

W Measurement overview during natural gas operation with NC_0

The time frames, sample sizes, set points of the leading system variables, utilization of the MFC scaling and the application of the arbitrary safety scaling factor of the recirculation flow rate for the individual testing periods of the NC_0 are listed in Table W.1. Additionally, the corresponding measured minima and maxima of the oxygen-to-carbon ratio, fuel utilization factor of the stack and temperatures at the reformer and anode outlet are shown in Table W.2.

Tabelle W.1: NC_0 testing period - Overview of measurement data I

Time frame	Samples	I_{SP}	$U_{f,S,SP}$	Φ_{SP}	MFC scaling	Safety scaling factor of recirculation flow rate
27.01. - 03.02.2017	81	24	0.75	2	On	Off
06.02. - 09.02.2017	34	24	0.75	2	On	Off
09.02. - 11.02.2017	21	24	0.70	2	On	Off

Tabelle W.2: NC_0 testing period - Overview of measurement data II

Time frame	I	Φ			$U_{f,S}$			$\vartheta_{ref,out}$ in °C		$\vartheta_{an,out}$ in °C	
	SP	SP	Min	Max	SP	Min	Max	Min	Max	Min	Max
25.10. - 26.10.2016	24	2	1.97	2.03	0.75	0.75	0.76	587.5	590.8	798.0	799.6
17.02. - 23.02.2017	24	2	2.00	2.03	0.75	0.76	0.76	587.3	589.4	799.1	799.6
23.02. - 28.02.2017	24	2	2.04	2.08	0.70	0.69	0.71	587.7	592.5	800.1	802.6

The reference values, as well as averages, minima and maxima of the measured data base of K_C, K_O, K_{e^-} and $M_{NG,in}$, including the deviations between the averages, minima and maxima to the corresponding reference values, are listed in Table W.3.

Tabelle W.3: NM_1 testing period - Natural gas characteristics

	K_C	K_O	K_{e^-}	$M_{NG,in}$
Reference value	1.0384	0.0190	8.1245	17.237
Average value of measurement	1.0398	0.0206	8.1425	17.072
Minimum value of measurement	1.0234	0.0066	8.1044	16.584
Maximum value of measurement	1.0553	0.0328	8.1845	17.491
Deviation between average and reference in %	0.1337	8.2468	0.2213	-0.9601
Deviation between minimum and reference in %	-1.4502	-65.154	-0.2481	-3.7899
Deviation between maximum and reference in %	+1.6298	+72.669	+0.7375	+1.4721